A Sheffield Hallam University thesis

Investigation of Induction-assisted Laser Metal Deposition of Crack Susceptible Coatings

Joshua Barras

A thesis submitted in partial fulfilment of the requirements of

Sheffield Hallam University

for the degree of Master of Philosophy

August 2023

Candidate Declaration

I hereby declare that:

1. I have been enrolled for another award of another academic organisation whilst undertaking my research degree. I am currently enrolled for the following award since 2022; Doctor of Philosophy from Brunel University London.

2. None of the material contained in the thesis has been used in any other submission for an academic award.

3. I am aware of and understand the University's policy on plagiarism and certify this thesis is my own work. The use of all published or other sources of material consulted have been properly and fully acknowledged.

4. The work undertaken towards the thesis has been conducted in accordance with the SHU Principles of Integrity in Research and the SHU Research Ethics Policy.

5. The word count of the thesis is 25,000

Name	Joshua Barras
Date	August 2023
Award	MPhil
Research Institute	Science, Engineering, Art and Design
Director(s) of Studies	Stephen Magowan

Abstract

Protecting components against severe wear and corrosion in high temperature environments is an ongoing challenge that is often resolved by applying an advanced functional coating. Environments like steam turbines present ever-evolving demands with industrial push to utilise higher operating temperatures that in turn increase power generation efficiencies.

Tribaloy T800 is a superior coating composition that presents challenges in processability due to its low toughness and crack susceptible nature. Weld overlay/ cladding processes based on fusion technology such as Laser Metal Deposition (LMD) (AKA Laser Cladding) offer significant benefits for the application of coating materials including a high strength metallurgical bond and a dense, defect free coating. LMD generates more rapid melting and solidification of the alloy compared to arc cladding, which produces a fine microstructure, but can lead to solidification cracking due to induced thermal stresses during the process and a lack of toughness in the coating material.

A small number of papers and published research projects have looked into LMD coatings of Tribaloy T800 with the ultimate aim to prove the feasibility of protecting components in high-temperature (600-1000°C) gas turbines, jet engines, shafts and pumps. Many of these studies conclude the findings of process optimisation, material characteristics and integrity, based on small-scale deposits. Small area deposits can present a lack of representation compared to full-scale coatings, including thermal control/accuracy, residual stresses, and even effects on dilution. In all circumstances, preheating was found to reduce or eliminate cracking by minimising the thermal shock and cooling rate of the alloy upon solidification.

In this study, part of the objectives was to review and ensure the relevance of the experiments and findings for transferability to full-scale components. Using Design of Experiments (DoE), experiments were constructed that evaluated the relationship between dilution, hardness and cracking response of the LMD deposited T800 against critical process variables including particularly induction heating temperature. One substrate alloy was investigated, 316L stainless steel, (although there was an intention to transfer developments to In718 nickel superalloy at a later stage). Through this process, it was determined that cracks form during solidification of the meltpool.

Another objective was to evaluate two methods of improving coatings speeds for the application of T800, 1) by implementing equipment adaptions to increase melt pool size and material feed rate and 2) to make initial assessment of a novel LMD technique known as Extreme High-speed Laser Application (EHLA).

Cracking was only eliminated in the large-scale undiluted coatings of T800 when using high levels of substrate heating (800-950°C) prior and during the coating operation by induction-assisted LMD. The resultant material behaviour of the deposited T800 showed promising results in terms of material integrity, and tribological and protective properties. Improvements in coating speeds were made when using laser defocus methods and increased deposition rate from 300 grams/hour to 600-1000grams/hour, though increased cracking was observed.

Trials using EHLA demonstrated unique process characteristics of high-speed thin coatings with promising cracking behaviour at lower preheat temperatures than required for LMD (200-500°C), ultra-low dilution and good material properties.

Contents

List of Abbreviations

Abbreviation	Definition
LMD	Laser Metal Deposition, also known as laser cladding or laser beam directed energy deposition
DED	Directed Energy Deposition
LC	Laser Cladding
DMD	Direct Metal Deposition
LENS	Laser Engineered Net Shaping
DoE	Design of Experiments
EHLA	Extreme High-speed Laser Application also known as ultra-high-speed laser cladding)
GMAW	Gas Metal Arc Welding
MIG	Metal Inert Gas
SAW	Submerged Arc Welding
HVOF	High Velocity Oxygen Fuel
HAZ	Heat Affected Zone
MFC	Magnetic Flux Controllers
LoF	Lack of Fusion
TRL	Technology Readiness Levels
HEA	High Entropy Alloys
fcc	Face centred cubic
bcc	Body centred cubic
WC	Tungsten Carbide
ODS	Oxide Dispersion Strengthened
LPT	Low Pressure Turbine
HIP	Hot Isostatic Pressing
SPS	Spark Plasma Sintering
EBM	Electron Beam Melting
SLM	Selective Laser Melting
PBF	Powder Bed Fusion
EDX	Energy Dispersive X-ray

Chapter 1

Introduction

1   Chapter 1 - Introduction

Tribaloy T800 is a hardfacing alloy developed as a galling wear and corrosion resistant coating in high temperature environments where lubrication is not feasible. The hardness of the material comes primarily from 50% hard intermetallic Laves phase and results in a low toughness that makes it extremely challenging to apply T800 crack free by many coating technologies. High levels of molybdenum and chromium generate the formation of the Laves phase and high levels of corrosion resistance. T800 is generally considered for applications where nickel-based superalloys are employed as base materials due to their high strength, corrosion, oxidation resistance at elevated temperatures.

The application of a hard facing material to the surface of a component is a common industrial process used to enhance wear resistance and commonly increase corrosion resistance. It can be applied using a range of different methods and materials, depending on a number of factors such as substrate size, complexity and access to a surface, coating thickness, performance, and cost. However, there is always a trade-off between speed of deposition and level of adhesion (which is directly proportional to the quality of coating). For example, a thermal sprayed coating has high coverage rate (125 cm^2/min (1)) but the bonding mechanism can be weak (mechanical interlocking with some diffusion) leading to poorer performance for the harsher environments. By contrast, Laser Metal Deposition (LMD) uses a focused laser beam to fully fuse powder to a substrate, giving a vastly superior coating (>99.9% dense, metallurgically fused and relatively defect free (1)), but applied at a much slower rate (25 cm^2/min (2)). Therefore, the first key driver for this research is to investigate the methodology behind producing high performance coatings with the superior quality of the LMD process. The second key driver is to investigate how to produce these LMD coatings in a more cost effective manner, primarily by increasing the area coverage and deposition rate.

1.1   Laser metal deposition

LMD is one of the Directed Energy Deposition (DED) family of technologies, and is often referred to by a number of names including Laser Cladding (LC), Direct Metal Deposition (DMD) and Laser Engineered Net Shaping (LENS). LMD is a technology that can be adapted to many applications including coatings, repair, feature addition and freeform additive manufacturing.

Laser Metal Deposition (LMD) can be a powder or wire fed process. The focus of this report is on the powder-fed variant. Figure 1 shows a schematic of the powder LMD process. An optical system above the powder nozzle controls the laser beam and focuses it onto the substrate at the desired stand –off distance of the nozzle. The laser creates a molten pool on the substrate and the nozzle feeds powder into the molten pool. A manipulation platform such as a robot and/or moving stage traverses the nozzle and/or substrate to produce a continuous coating or a freeform, multi-layered, deposit.
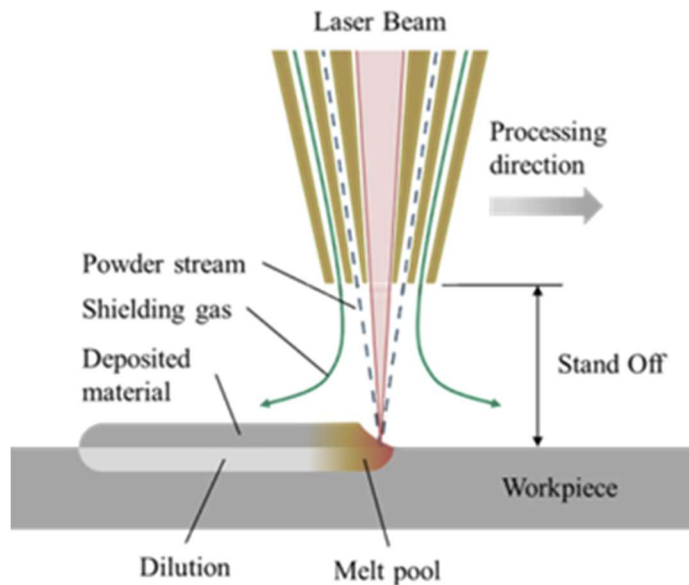
Figure 1 Schematic of the Laser Metal Deposition process using powder feedstock. (3)

The process typically results in a material utilisation of 60-95%. Track width can range from 0.5mm to more than 10mm and layer heights from 0.2mm to 2mm, depending significantly on equipment used but also the materials applied (4). LMD can be a net or very near net shape process in which small melt pools and track heights are used to create and control the geometrically accuracy and surface finish within the limitations of the process. This is considered similar to the surface finish that can be achieved in casting, approximately 10-20μm Ra (5). However the profiles of the tracks and overlapping zones of individual tracks on the single layer and multilayer planes, are what gives a waviness to the final deposits and which usually defines how much post processing is required, based on application specification. Where large tracks are used (several mm's wide and up to 2mm tall), this generally gives a lower quality surface finish particularly in surface waviness and final layer geometrical accuracy, in which case, LMD coatings and parts may require a secondary machining and/or finishing processes to achieve the final part geometry. However, in most scenarios, post process machining or finishing is required on functional surfaces.

Conventionally LMD was developed for coating applications and now spans across four applications of coatings, repair, feature addition, and freeform 3D manufacturing. These applications can sometimes intermix (for example a coating as a repair), but can generally be distinguished. Examples shown in figure 2.
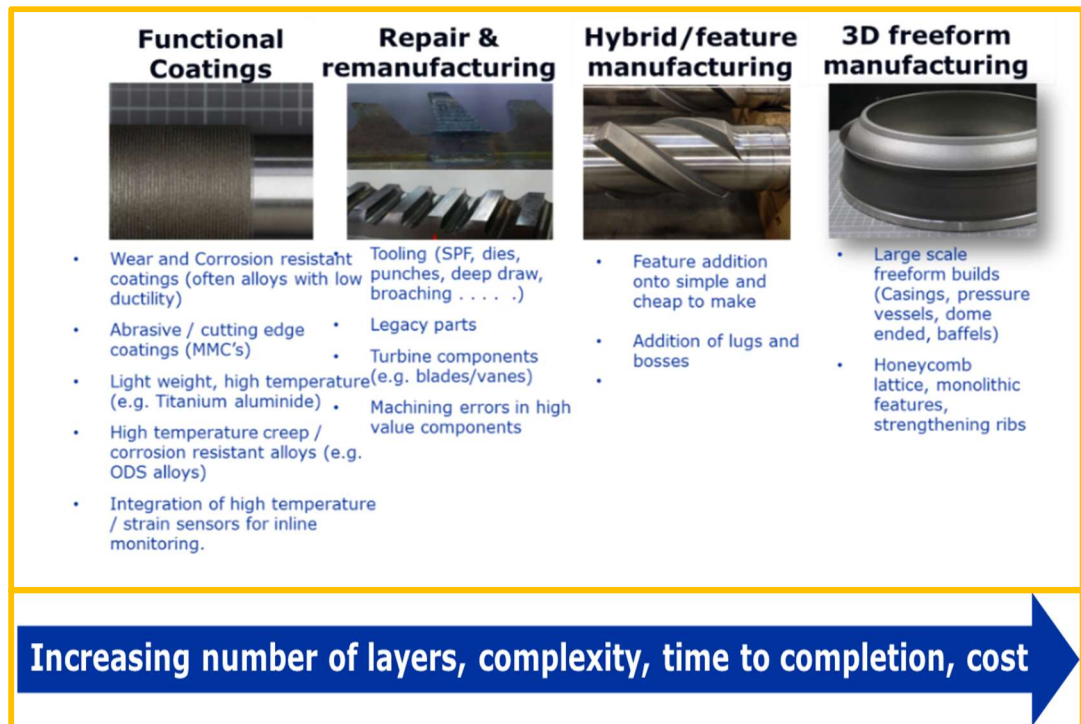
Figure 2 LMD application spaces and examples. Images for coatings, repair, and 3D, property of TWI, image hybrid features, property of Manufacturing Technology Centre.

There are a significant number of parameters that influence the LMD process, the exact number is argued but there is a common consensus that the number of variables is significantly beyond those summarised in Figure 3 (6). However, most of the key parameters are given in Figure 3. Each parameter has a different weighting of variability and effect on the deposit. However, strong interdependencies also means each parameter needs to be considered against all others in order to control the process and achieve an optimised quality of the deposit. Generally, the four most critically weighted parameters that influence conditions are laser power, scanning speed, feedstock rate, and shielding gas. The simplified effects of the major parameters can be seen in table 1 below. In this research, these critical parameters were fixed where possible and the focus of the work was in developing thermal control conditions via an induction heating process.

Table 1, key parameters and simplified effect on deposit characteristics.

Parameter change	Effect on clad bead width	Effect on clad bead height	Effect on penetration & dilution
Laser power ↑	↑	↑	↑
Traverse speed ↑	↓	↓	↓
Powder feed ↑	↓	↑	↓
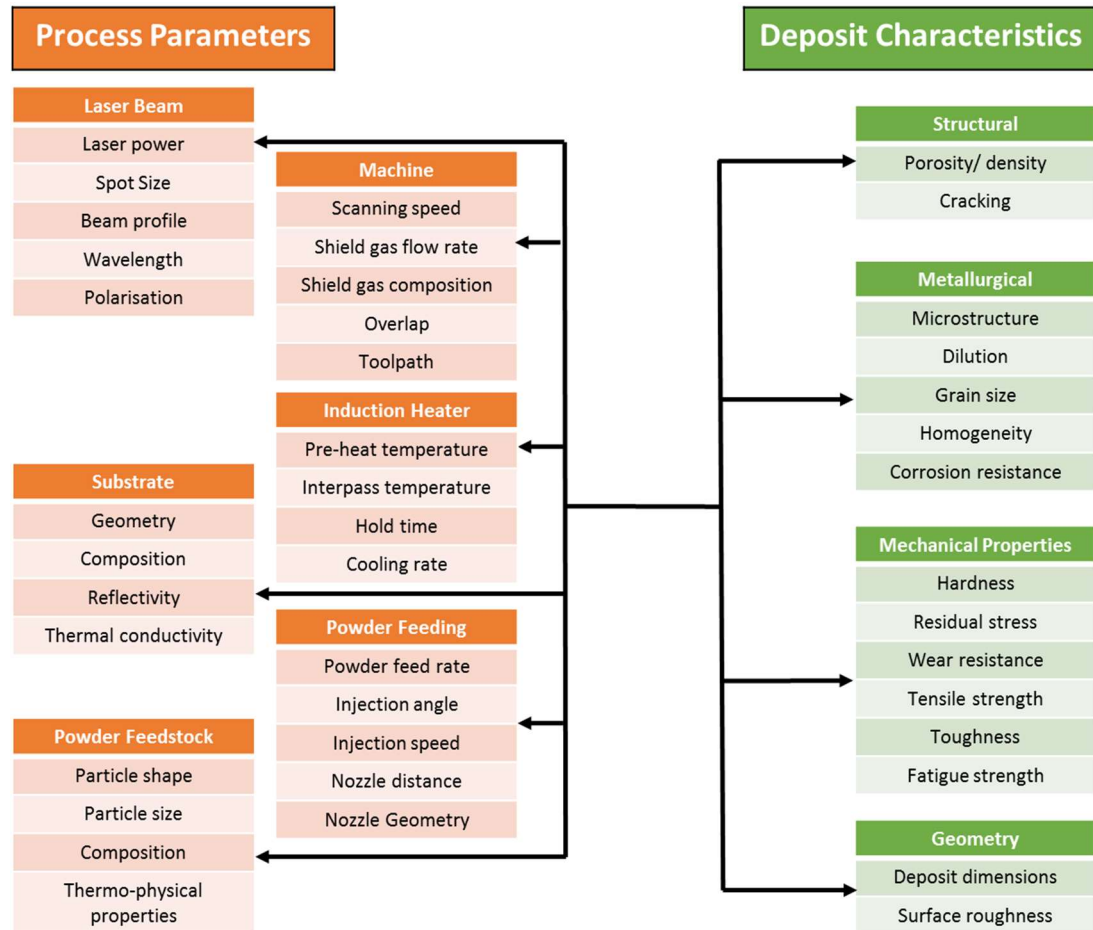
Figure 3 Summary of powder LMD process parameters and deposit characteristics.

1.2   Induction heating

Induction heating is the process of heating an object, through heat generated in the object by eddy currents, created by electromagnetic induction. Induction heating is highly effective on materials that are good conductors of electricity (7). The process works therefore on many industrially relevant substrates for coating applications such as steels.

Increasingly there is a need to have better performing coatings in industrial applications. To enable many of these high performance coatings, a technology or combination of technologies need to be capable of precisely controlling the thermal history of the coating throughout the stages of preheat, deposition, and post process cool down. LMD in combination with induction heating could provide a viable solution to this challenge.

1.3   Research Aim and Objectives

The aim of the research is to reduce or eliminate crack formation during LMD cladding in crack sensitive materials through the incorporation of induction heating.

The objectives of the research include:

In this study, part of the objectives was to review and ensure the relevance of the experiments and findings for transferability to full-scale components. Using Design of Experiments (DoE), experiments were constructed that evaluated the relationship between dilution, hardness and cracking response of the LMD deposited T800 against critical process variables including particularly induction heating temperature. One substrate alloy was investigated, 316L stainless steel, (although there was an intention to transfer developments to In718 nickel superalloy at a later stage). Through this process, it was determined that cracks form during solidification of the meltpool.

Another objective was to evaluate two methods of improving coatings speeds for the application of T800, 1) by implementing equipment adaptions to increase melt pool size and material feed rate and 2) to make initial assessment of a novel LMD technique known as Extreme High-speed Laser Application (EHLA).

Chapter 2

Literature and state-of-the-art review

2   Chapter 2 - Literature and State-of-the-art Review

2.1   State-of-the-art summary

Many commercial surface-coating technologies are well established for protecting against harsh environments such as wear, corrosion and oxidation. In the case of large surface area claddings, gas metal arc welding (GMAW also known as metal inert gas (MIG)), submerged arc welding (SAW) or thermal spray techniques are often chosen based on their high material deposition rates (8). However, the heat input involved for GMAW results in significant dilution of the clad material into the underlying substrate, high residual stresses, and component distortion (8). Conversely, thermal spray coatings only provide a mechanical bond to the substrate and can spall when subjected to impact, bending stresses or high loadings (1). How these technologies fit into wear and corrosion protection is shown in Figure 4 but is highly dependent on the application, however generally more than 20 µm and less than 1 mm of coating thickness is required to be fit for purpose (8, 9).
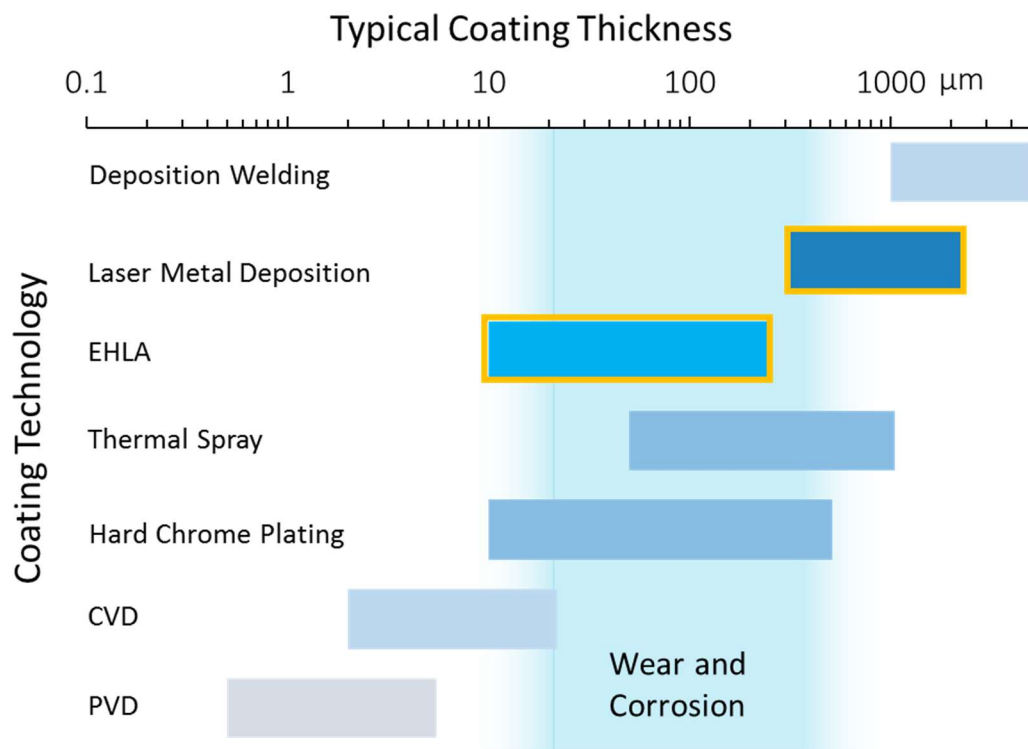
Figure 4 Process suitability based on typical coating thickness applied and typical requirements for wear and corrosion applications. Source Fraunhofer ILT (8).

LMD generally sits in a relatively narrow niche of economically viable applications requiring lower heat input, or higher choice of material solutions than deposition welding techniques while accepting the drop in deposition rate, but higher bond strength, thickness and performance than thermal spray techniques, again while being a slower process. LMD can somewhat be considered as a balance between many of the coating processes such as those presented in Table 2.
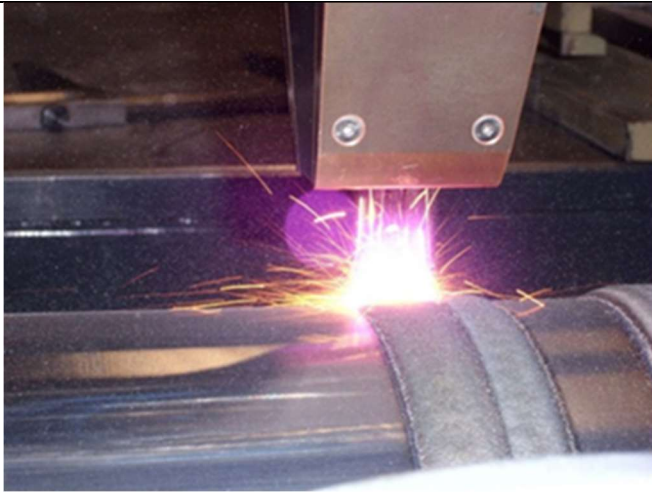
Table 2 State-of-the-art coating comparison table produced as guided values and comments

(key: Red=worse, Blue=okay, Green=better)

Deposition/ Coating Technology	Surface area coverage (cm²/min)	Coating linear speed (m/min)	Deposition rate (kg/hr)	Material yield efficiency (%)	Coating thickness/ layer (mm)	HAZ depth (µm)	Bond strength & mechanism	Material density (%)	Process stability (defect rate)
High Velocity Oxygen Fuel (HVOF) Thermal spray	100-150 (10)	0.5 – 5	1-3	<50% (10)	0.05-0.8	Low (0)	Low, Mechanical	85-97	High P <0.05
Submerged arc, Wire arc / GTAW	10-60	0.5 – 2	1-20	99.8%	1-3	High (1000-2000)	High, metallurgical	>99.9	Medium P <0.01
LMD/ laser cladding	10-40	0.5 – 2	0.5-12	>80%	0.3-2.0	Medium (500-2000)	High, metallurgical	>99.9	Low P <0.001
EHLA	100-1000	25-200	1-6	>80%	0.01-0.4	Low (5-50)	High, metallurgical	>99.8	Low P <0.001

In terms of some of the key features of coatings and deposition, LMD is a highly adaptable process and the most suitable equipment/setup is very much dependent on the particular requirements of the application. Two examples of the extreme variation in capabilities of different LMD techniques are shown in Table 3.

Table 3 SOTA LMD techniques

Thin coatings	Bulk deposition and thick coatings
Extreme high-speed laser application (EHLA) for low dilution and high area coverage.	Conventional laser metal deposition with diffractive optics or beam defocus for high bulk deposition rate.
Source Fraunhofer ILT (8)	Source Fraunhofer IWS (11)
Laser power 2-10kW +	Laser power 3-20kW+
20-300µm thick per layer	500-1500µm thick per layer
Coverage rate up to 1000cm^2/min	Coverage rate up to 40cm^2/min
1-6 kg/hr	1-12 kg/hr
HAZ 5-50µm	HAZ 500-1000µm
Disrupting conventional technologies of: thermal spray and electroplating	Disrupting conventional technologies of: arc-wire (submerged arc, TIG, MIG overlay).

In 2017, Fraunhofer ILT released a new nozzle technology that has been rapidly gaining research based and industrial interest. The extreme high-speed laser application (application, cladding, or metal deposition) (EHLA) nozzle is described as a step change for the LMD coatings technology. In the case of EHLA, the powder is injected into the laser beam and melted before it reaches the molten pool. This allows process speeds of several 100 m/min, conventionally 1-2m/min (8). The nozzle is in affect reducing the required layer thickness of the coating as it further reduces the dilution between the substrate and fused powder by minimising the energy input of the laser into the substrate and yet still maintaining a fusion bond. The key differences between conventional LMD and EHLA are

shown in Figure 5 below. With EHLA, multiple thin layers could be built up to equal a single layer thickness applied by LMD, this could lead to advantages in terms of substrate heat input, deposit microstructure, crack susceptibility, distortion and more. Further research in this topic could be very useful for informing best practices.
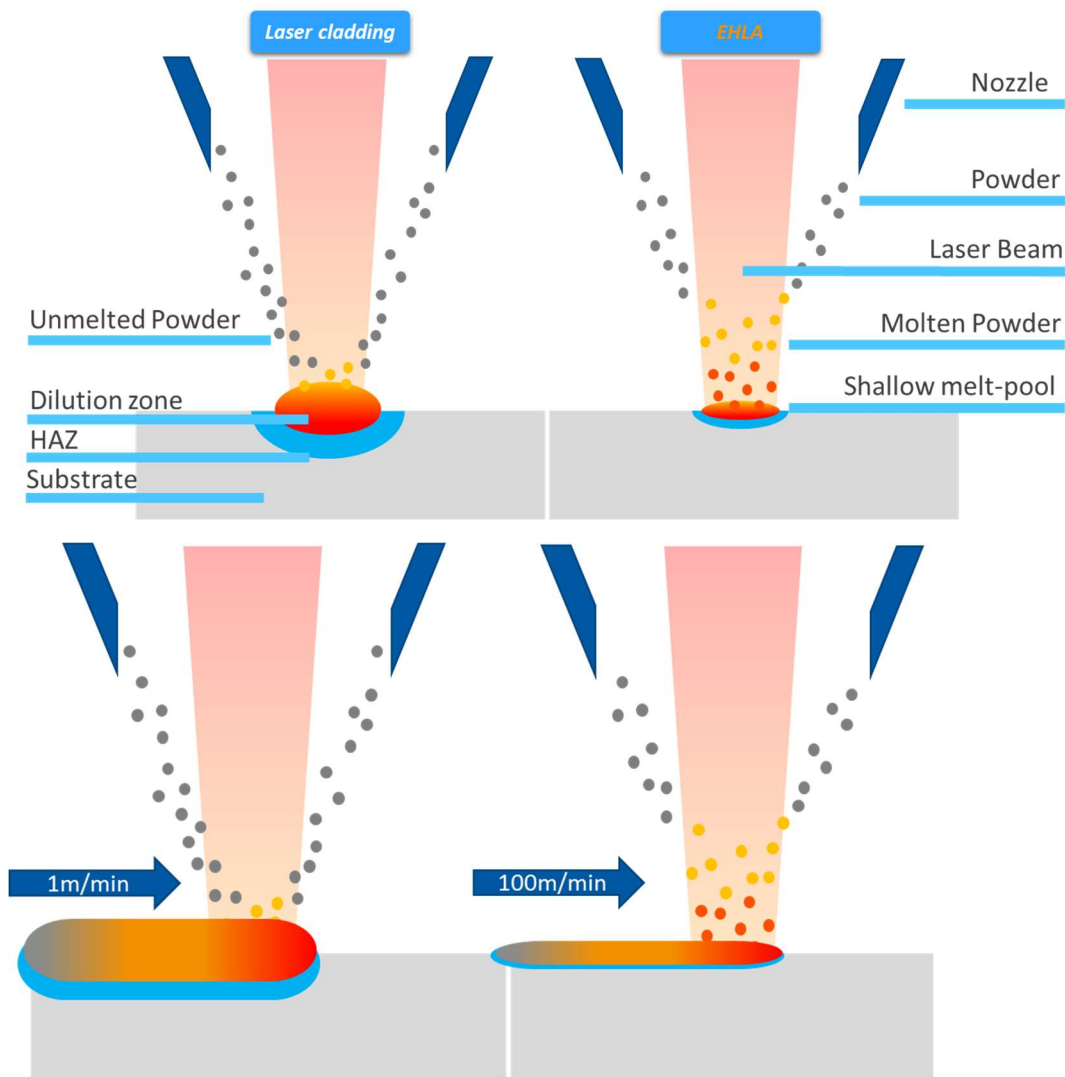
Figure 5 schematic of LMD and EHLA process specifics (Top image front view, bottom image side view).

2.1.1 Thermal control and induction heating of the substrate

Preheat is a well-established technique used just prior to cladding, to prevent cracking. By incorporating preheat into the process there is a reduction in the cooling rate of the deposition. This enables the deposition of harder materials without cracking, and reduces the effect of excessive hardening (especially within the HAZ). However, many techniques are limited for controlling the overall thermal history of the component production. For example applying a preheating step only using a furnace, provides a relatively good control for the starting temperature of the substrate but limits the thermal control once the deposition process has begun (12).

Increasingly there is a need to enhance coatings used in industrial applications. To enable many of these high performance coatings, a technology or combination of technologies need to be capable of precisely controlling the temperature of the substrate/coating throughout the stages of preheat, deposition, and post process cool down. LMD in combination with induction heating could provide a solution to this challenge.

Induction heating is the process of heating an object through heat generated in the object by a varying magnetic field known as eddy currents, created by electromagnetic induction. Essentially by creating an alternating current within a copper induction coil, a magnetic field is generated. The field is interrupted by the work piece metal placed inside the middle of the coil, and wraps itself around the work piece at a high rate. As the field continues to spin around the metal, it generates heat within the work piece. The heat is generated by the resistance within the work piece metal itself at the surface, acting as a "friction". Heat travels through the work piece by conduction. Induction heating is highly effective on materials that are good conductors of electricity. The process works therefore on many industrially relevant substrates for coating applications such as steels. D. Shim et al. 2017 concludes that induction preheating prior to using a deposition process results in a slower solidification rate, leading to grain coarsening from fine equiaxial to columnar dendrites, but no significant hardness reduction in the deposited M4 tool steel. The induction-heated samples had reduced residual stress, especially at the substrate to deposit interface, increasing tensile strength. Notable from the graphs in figure 6 is that the temperature range when depositing was significantly tighter when preheating the material. (7)
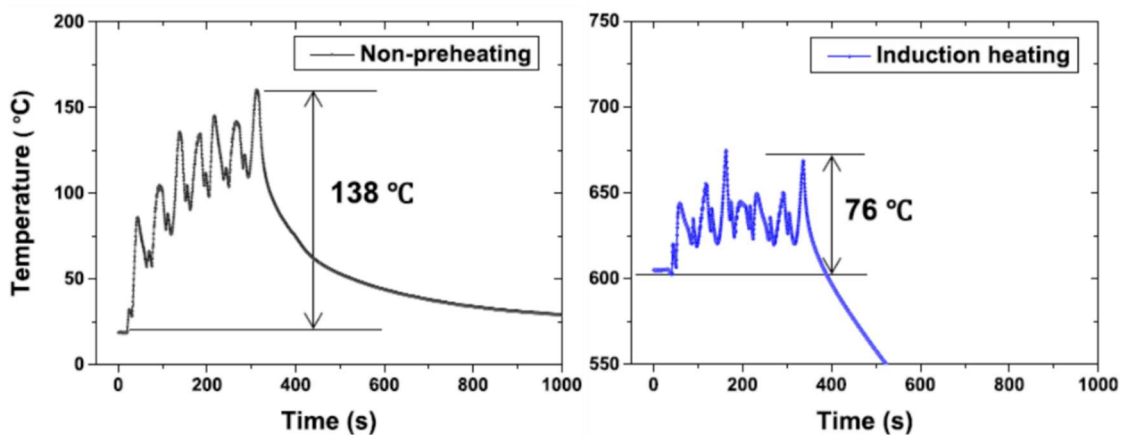
Figure 6 Temperature variation measured in the bulk substrate during deposition with and without induction preheating. Where high-temperature preheating (right) enables a completely difference thermal profile (7).

M. Dalaee et al. 2020 highlight the challenges of using induction heating with some ferromagnetic powder alloys that are susceptible to the effect of the magnetic field causing accumulation of powder that can disrupt the LMD process. Magnetic flux controllers (MFC) similar to the ones used in this project setup were used with success to direct the magnetic field more effectively than using a coil without MFC. (12)

2.1.2 State-of-the-art conclusions

LMD can be used as an advanced coating technology for the application of many metallic materials, providing a high integrity bond and surface engineering solution. LMD offers lower dilution than many conventional weld deposition technologies but struggles to compete in high volume markets where thin coatings of 10μm to a few hundred μm are applied. EHLA is a new branch of LMD with great potential but lacking in data and validation to back up the potential of the technology. Both technologies are suitable candidates for investigation into depositing crack susceptible materials such as some of the extreme hardfacing alloys detailed in section 2.5.2.

2.2 Key process considerations

2.2.1 Dilution

Dilution is a term used when welding two dissimilar alloys together – in terms of LMD when a base alloy is clad with a dissimilar coating alloy. To achieve a metallurgical bond, some mixing at the interface of the clad and the base material is required. The molten substrate and coating material mixes at the interface, resulting in a zone of diluted material chemistry. The hotter the weld pool and the longer it remains above the solidification transition temperatures of the alloys, the wider and deeper the dilution zone becomes. Dilution can be challenging to determine and measure. B. Song et al. 2016 found that different methods of measuring dilution gives highly variable results. No conclusion on the optimal method was made in that study. (13) It is common for the valve manufacturing industry to apply industry standard alloy Cobalt 6 (nominally 62Co 29Cr 4.5W 1.2C commonly called Stellite 6™) to their valve seating surfaces. Due to concerns about dilution, their typical cladding thickness specifies 3 mm to 8 mm. (14) Some processes require this thickness to ensure that the only the cladding composition remains in the upper surfaces and are not compromised by the base material elements. However, the more material added to the component by fusion technologies the greater the induced residual stresses and distortion, and the higher the filler material cost, the longer the deposition time and potentially the post process finishing time. LMD can minimize dilution with greater heat input control versus other DED technologies, ensuring full material properties of the clad are achieved within 0.25mm to 1mm of the deposit interface, and within 5µm to 50µm with EHLA. In many wear protection applications, chromium coatings are applied at only 30-250µm thickness to adequately protect the component for the intended lifespan. (9)

Table 4 – Table extracted from BS EN ISO 6158:2018; table shows typical coating thicknesses by plating techniques for discrete levels of severity of wear (9)

Typical thickness µm	Application
≥ 2 to ≤ 10	To reduce friction and for light wear resistance
> 10 to ≤ 30	For moderate wear resistance
> 30 to ≤ 60	For adhesive wear resistance
> 60 to ≤ 120	For severe wear resistance
> 120 to ≤ 250	For severe wear, abrasion and erosion resistance
> 250	For repair

Quantifying dilution from welding and deposition fusion processes seems to be rarely considered as a problem or issue needing further understanding and is often overlooked. However, it seems that commonly the definition is over-simplified and potentially incorrect in some cases. The approach idealises dilution as a distinct region below the coating layer within the substrate material. Figure 7 shows the generalised definition and equation, and figure 8 aims to closer represent reality of the graded dilution between the substrate and coating.
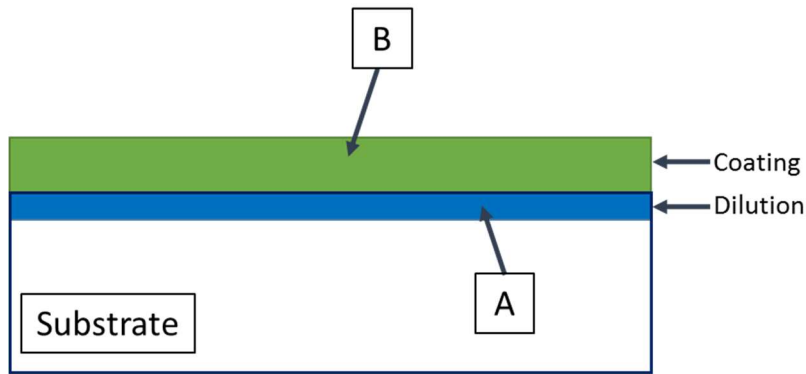
Figure 7 Conventional schematic diagram showing the clad layer in two parts, pure coating material (region B thickness), and melted substrate material (region A thickness). The dilution depth is often described as a percentage and given by A/(A+B).
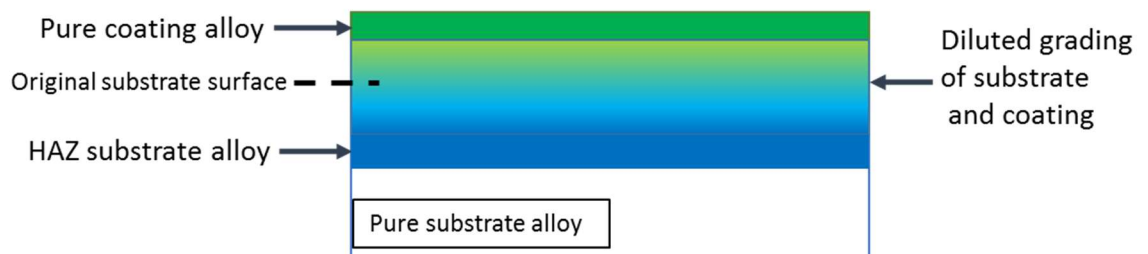
Figure 8 representation of the grading of dilution between the alloys between the coating and substrate, above and below the original substrate surface.

2.2.2 Key parameter interactions

The correlations of parameters found by experiments in Oliveira (15) were summarised into one chart Figure 10. Clad height (H) was calculated from the reciprocal relationship of travel speed over powder feed rate (S/F). The function of S/F is plotted against Power (W). The line at S/F = 0.047 is marked as the boundary to which all points right fulfill the condition α > 100°, angle alpha (known as the wetting angle) is the suggested criterion for the minimum wetting angle required for forming fully dense layers free of porosity. It is predicted that the angle forms a limiting factor when attempting to increase deposition rate (while maintaining non-porous, low diluted coatings), which may be resolved by using a larger laser spot size, increasing laser power and powder feed rate (i.e. keeping the overall energy density at a similar level to the desired condition). (15)
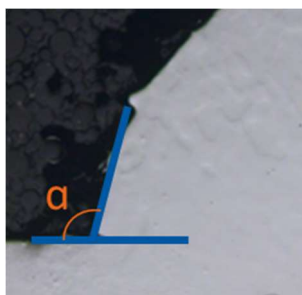
Figure 9 – Example of a LMD deposit wetting angle (α)

It is stated that dilution (D) is linearly controlled by the combined parameter $\sqrt{PS/F}$, the constant dilution curve will form a hyperbolic function. Curves for constant dilutions 5% and 30% are depicted by two solid curves. The experimental area limited by these two solid curves and by the vertical line from a left side reveals the practical processing window (shaded area). (15).
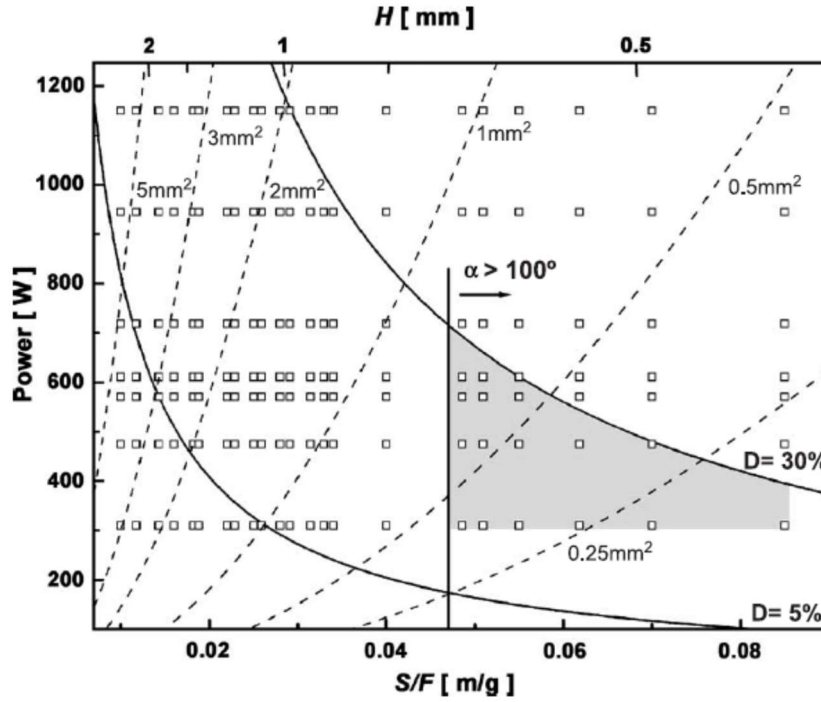
Figure 10 – Processing window for coaxial laser cladding in P vs. S/F representation. Points correspond to analysed laser track cross sections. Vertical solid line determines the clad angle condition required for continuous coating; two solid hyperbolas terminate an area of allowed dilution and the grey area shows the window, where an optimal clad layer can be formed. Dashed curves are isolines with denoted values of clad area (clad spot size). (15)

It is possible using analytical methods to calculate the required laser power required to melt both that of the substrate and powder. These equations could be useful in reducing the breadth of DoE for the practical trials as the analytical methods can give indications on the minimal power to heat the materials. The accuracy of the equations depends on the accuracy of the relations between the given parameter figures and the true values (which might not be measured due to lack of technology, or averaged due to complex variations, such as the differences caused by the range of powder particle sizes). (15) The power required to heat the material is defined by:

Substrate:

$$P_{ms} = \frac{\sqrt{\pi}k_s(T_{ms} - T_{is})}{2\beta\sqrt{\alpha_s t_{int}}}$$ *Equation 1*

Powder:

$$P_{\mathrm{mp}} = \frac{m_{\mathrm{p}} C_{\mathrm{p}} \left(T_{\mathrm{mp}} - T_{\mathrm{ip}} \right)}{\gamma}$$ *Equation 2*

Using:

$$\beta = \frac{A_{\mathrm{s}}}{S_{\mathrm{int}}} \exp \left(\frac{-\varepsilon F p_{\mathrm{d}}}{\pi \nu_{\mathrm{p}} \left(r_{\mathrm{n}}^2 + r_{\mathrm{n}} p_{\mathrm{d}} \tan \phi \right)} \right) + \frac{3 A_{\mathrm{pe}} F}{4 S_{\mathrm{p}} S_{\mathrm{int}} r_{\mathrm{p}} \rho_{\mathrm{p}}} \gamma$$ *Equation 3*

and:

$$\gamma = \frac{S_{\mathrm{p}} A_{\mathrm{p}}}{\pi \nu_{\mathrm{p}}} \int_{0}^{p_{\mathrm{d}}} \frac{1}{\left(r_{\mathrm{n}} + z \tan \phi \right)^2} \exp \left(\frac{-\varepsilon F z}{\pi \nu_{\mathrm{p}} \left(r_{\mathrm{n}}^2 + z r_{\mathrm{n}} \tan \phi \right)} \right) dz$$ *Equation 4*

Where

P_{ms} and P_{mp} are the power required to heat the substrate and powder to melting temperature respectively

T_{ms} and T_{mp} are substrate and powder melting temperature respectively

T_{is} and T_{ip} are substrate and powder initial temperature

K_{s} is the substrate thermal conductivity

α_{s} is the substrate thermal diffusivity

t_{int} is the laser beam interaction time with the substrate

m_{p} is the powder particle mass

C_{p} is the thermal heat capacity of the powder material

T_{mp} is the particle melting temperature

T_{ip} is the particle initial temperature

S_{int} is the laser beam/substrate interaction area

ε is the powder extinction coefficient ($\varepsilon = 3(1-A_{\mathrm{p}})/2\, \rho_{\mathrm{p}} r_{\mathrm{p}}$)

A_{s} is the substrate absorption coefficient

A_{p} is the particle absorption coefficient

A_{pe} is the powder cladding efficiency coefficient

ρ_{p} is the powder material density

r_{p} is the radius of the powder particle

v_{p} is the powder particle velocity

S_{p} is the particle cross section

(15)

2.2.3 Energy Density

Energy density is one way of assessing the combination of processing parameters. Caution should be taken when treating energy density as the solution for creating optimal processing conditions by LMD. The relationship between materials, laser power, spot size, travel speed and material feed rate creates a complex matrix of dependencies. LMD is used for a wide array of applications, from surface cladding to manufacture of near net shape 3D components. The varying requirements based on individual applications cause changes to the required parameters and therefore by extension, the required/optimal energy density. It is also possible to achieve matching energy densities by two very different combinations of parameters. Internal work at TWI, has shown that this can result in vastly different consolidated material, where equivalent energy densities can give "good" and "poor" quality deposition. It is therefore not advisable to focus on achieving specific energy densities, but there is still opportunity for further investigation to understand how the values are changing throughout the planned parameter windows.

$$Energy\ density\ (Joules/mm^3) = \frac{Laser\ power\ (W)}{Scan\ speed\ (mm/s) * Spot\ area\ (mm^2)}$$

Equation 3

$$Mass\ density\ (g/mm^3) = \frac{Powder\ feed\ rate\ (g/s)}{Scan\ speed\ (mm/s) * Spot\ area\ (mm^2)}$$

Equation 4

$$Specific\ energy\ density\ (Joules/g) = \frac{Laser\ power\ (W)}{Powder\ feed\ rate\ (g/s)}$$

Equation 5

2.3 Design of Experiments overview

Many methods of design of experiment (DoE) can be used to effectively investigate the interactions and behaviours of the process parameters. Taguchi is one example of a good statistical method for reducing the number of experiments. Factorials (full and fractional) are also well defined and useful methods, where the number of runs for a full factorial is the number of levels multiplied by the number of measurement levels. Modifying variants of these designs to fit the specific experimental need is also possible with careful planning. For the short experimental studies tested so far, process knowledge was used to design the experimental field, rather than standard DoE approaches, in the instance of experiment 2c, a variant of factorial was used. Further work on these materials could be benefited by DoE evaluation and deep dives into the responses.

2.4 Potential Processing Induced Defects

During manufacture, treatment, and service, defects may develop within the structure of the coating and affected substrate material. These defects are in the form of inclusions, undesirable phases, porosity, lack of fusion, and cracks.

2.4.1 Cracking

Cracks are particularly hazardous because of the high stress concentration at the crack tip, which will cause the crack to grow under an applied load until the component fails catastrophically, or in coatings, when a crack propagates from the coating surface into the substrate material, providing a route to corrosion and other major failures. Cracking can be classified by four key mechanisms:

- Solidification cracking;

- Grain boundary liquidation;

- Ductility dip and;

- Strain age cracking.

2.4.1.1 Solidification cracking

Solidification cracking or liquid-induced cracking, primarily originates in the HAZ adjacent to the deposit, caused by the dissolution of gain boundary phases under rapid heating. The dissolution of the grain boundary phases occurs at such a high rate that it forms of a low melting point eutectic along the grain boundary, which fails under applied tensile stress. This can be due to intergranular cracking or fracture, and due to several factors including eutectics often being more brittle and less strong than surrounding matrix, and often containing impurities or secondary phases. (16)

Fine grains in the deposit are able to withstand more strains developed during deposition. Additionally, the larger surface area of the grain boundary reduces the localised stress density along the grain boundary intersections, which are the most susceptible sites for crack nucleation. Finer grains also reduce the scale of elemental segregation during solidification, which results in thinner liquid films on the grain boundaries. (16)

These traits indicate that the state of the substrate microstructure prior to deposition can play an important role in the cracking behaviour. (16)

2.4.1.2 Grain boundary liquidation cracking

Typically initiating at the HAZ adjacent to the deposited material, due to dissolution of grain boundary phases under rapid heating. The thermal cycle is too fast for complete dissolution, forming a low melting point eutectic along the boundary which fails under stress. (16)

Solidification cracking and grain boundary liquidation cracking have some similarities but in summary, solidification cracking occurs when the weld metal solidifies and contracts, but is still hot and ductile, while grain boundary liquidation cracking occurs when the solidifying weld metal experiences localised melting and liquation at the grain boundaries.

2.4.1.3 Ductility dip cracking

Ductility dip cracking is a solid state mechanism that occurs due to loss of ductility within a certain temperature range below the materials solidus temperature. A combination of thermal and solidification stresses, including microscopic within the grain boundaries during precipitation of partially coherent carbide phases. This can cause melting and re-solidification at the grain boundaries. Typically seen in alloys with low melting temperature constituents. It is most likely to occur with high heat inputs and/or with slow cooling rates. (16)

2.4.1.4 Strain age cracking

Strain age cracking occurs during reheating or high temperature service. The particular defect nucleates as micro-cracking in either the HAZ or deposit, initiating at carbide sites. (16)

2.4.2 Porosity

Porosity is a common defect occurrence found in deposits and coatings applied by many technologies including LMD, HVOF, and Arc deposition. Porosity can have a number of origins and causes, understanding these causes can help to improve in reducing the amount of pores and size of individual pores. In powder fed LMD, porosity can occur and be affected by:

- Gas - shielding rates, type and purity

- Powder - entrapped porosity, shape, size, inclusions, oxidation, moisture

- Substrate - preparation and inclusions, oxidation, moisture

- Energy density (combination of laser power, spot size and travel speed)

  (16)

An optimised LMD process can readily achieve over 99.9% density. When density reaches higher levels, measuring density accurately becomes increasingly difficult and is often subject to the individual macro plane and sample measured.

Often small pores (i.e. <5μm) are introduced into the deposit from the source powder quality. Larger pores can more commonly be attributed to gas optimisation and energy density optimisation.

2.4.3 Lack of Fusion

Lack of fusion defects can sometimes be described under porosity defects, but it is important to differentiate the lack of fusion (LoF) defect from standard porosity. LoF defects are not spherical in shape. These defects generally occur when the energy density is too low, most commonly at the edge of the melt pool/deposit track where it overlaps adjacent tracks. LoF can also occur between the deposit and the underlying substrate or layer due to insufficient energy density.
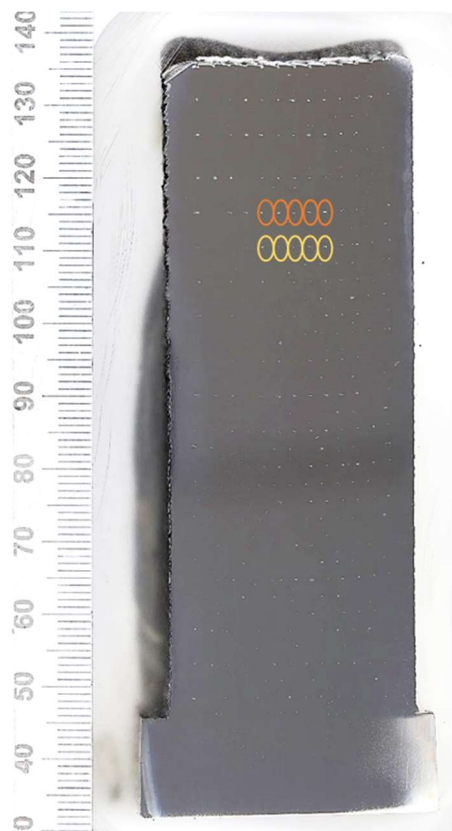
Figure 11 Macro cross section of titanium LMD powder deposit with lack of interrun fusion defects throughout (Source TWI Ltd). Individual defects are highlighted, from two deposited layers, each of 5 defects.

2.5 Industrial Challenges and Coating Applications

2.5.1 Industrial Challenges

The challenge of protecting components from wear, temperature (oxidation and thermal fatigue) and/or harsh environments is a significant long running problem within industry. Even when an adequate solution is found for extending the life of component, these solutions are often not optimised. New difficulties can come in to play, generally when environmental requirements change, such as increases in operating temperatures, or when material restrictions are issued and regulations are changed. Wear resistance provides common challenges within industry for component life extension, but within wear, there

are several particular modes, sometimes combined, such as abrasion, erosion, adhesion, impact, and corrosion.

2.5.1.1 Mechanisms of wear

There are a number of different wear mechanisms including adhesive, abrasive and fatigue. The key mechanism of interest in most of the investigated application is adhesive, followed by abrasive. Adhesive wear is usually a result of material transfer from one surface to another, i.e. metal to metal components surface contact. The extreme form of this is galling wear, in which the surfaces 'cold weld' together in seizure and material is torn from one surface (17).

Abrasive wear is the loss of material due to hard particles that are forced against a solid surface. Another more substantial from of abrasion is erosion, usually short motions of fast particle impacts, removing material in deformation and cutting actions (17).

2.5.2 High temperature wear and corrosion applications

Tribaloy T800 is an extremely wear and corrosion resistant material with excellent maintenance of corrosion and wear properties at high temperature (in the range operating range 600°C-1000°C). T800 has strong benefits as a coating in applications such as advanced and ultra-supercritical pressure steam turbine components, including stems and valves (18, 19 It is an extremely difficult alloy to deposit as a coating because of its limited weldability and susceptibility to cracking and brittle spalling. Its prime virtue is excellent hot hardness / wear resistance and it can maintain 58-60HRC up to 550-600°C and 31HRC at 760°C. Toughness and impact resistance are also important factors, reasons why ceramic materials may not be suitable. Hence, it is very suitable for application in high temperature applications, e.g. heavy-duty internal combustion engines, exhaust valves, seat faces, bushings etc. Tribaloy T800 consists of hard laves phase as displayed in figure 12. Laves phases are intermetallic phases that have a make up of usually hexagonal arrangement, and AB_2 composition, where A is ordered as diamond or hexagonal diamond structure, and B as tetrahedra around A. In Tribaloy the laves phases is known as C-14 type (MgZn2).The laves phases in a Tribaloy alloys are made up of mainly CoMoSi or Co3Mo2Si. (20)
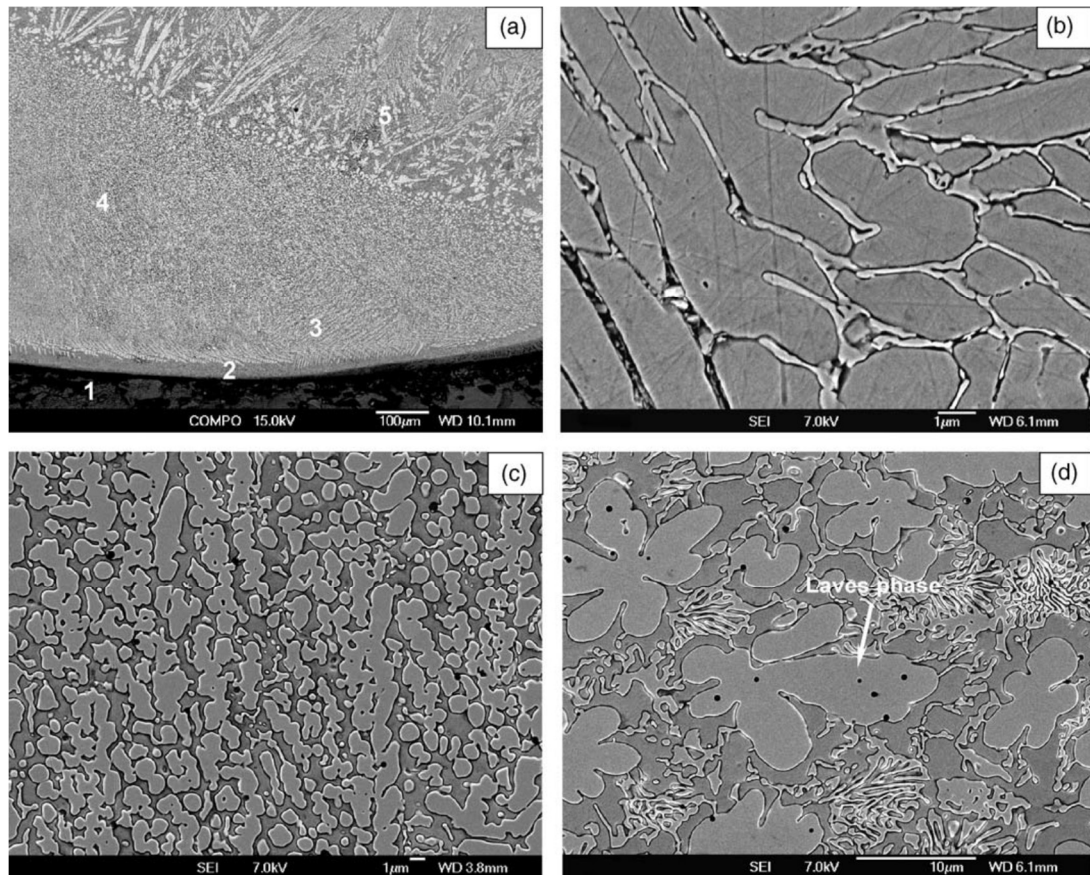
Figure 12 SEM morphologies of the laser clad layer: (a) back scattered electron image showing: (1) Bakelite mount; (2) planar crystallization region; (3) cellular growth zone; (4) fine dendritic microstructure; (5) overlap zone between tracks. Secondary electron images of: (b) a detail of the cellular structure near the planar crystallization; (c) the dendritic microstructure of the track centre zone; and (d) the morphology of the overlapping zone. (20)

Tribaloy T400C is a modified version of the Tribaloy alloy family. It is more oxidation resistant than T800, capable of high resistance to oxidation at 760°C. Like T400, T400C is less brittle and not quite as hardwearing, due to the approximate 10% increased Co, exchanged for Cr in T800, leading to a general hardness of >540Hv vs >700Hv for T800 and therefore has better weldability than T800, with hardness and wear resistance approximately 5% better than T400. T400C would make a good alternative material if T800 were found to be unfeasible to deposit crack free. The hardness of the final materials is greatly dependant on the process which they are applied with and the resultant microstructure. (20)

Zhang et al (21) 2011 investigated modification of Tribaloy T-800 material through the addition of minor alloying additions of either Y, or Al and Y. Such additions altered the microstructure of as-cast material and promoted refinement of the primary Laves phases and eutectic matrix. Casting provides relatively slow cooling and large grain growth, which might present differences to LMD deposits that are exposed to rapid solidification supressing grain growth. The alloying additions also exhibited superior high temperature oxidation resistance and may provide a good candidate for future coating material.

However, such compositions have not been deposited as coatings and are not readily available commercial powder for thermal spray or LMD.

In situations where less wear and corrosion resistance can be tolerated, Tribaloy T-400 can be used, which provides greater ductility and therefore is less prone to cracking when sprayed or fusion bonded. Yao et al (20) 2006 describe a new alloy designation of T-400C, which has been developed with enhanced corrosion and wear resistance. Manufacturer brochures' also reference Tribaloy T-401, with 'enhanced ductility with superior corrosion and wear resistance' which may be of interest when investigating potential alternative alloy systems. Due to the addition of 0.2% C, increase in chromium, and less silicon, T-401 does not contain large primary laves phase, primarily as silicon precipitates the laves phase and the new makeup results in a hypoeutectic structure alloy. Instead, the Laves phase is in the form of small particles in the eutectic region, and some carbides are present (22). A comparison of the Tribaloy 400 variants microstructures are shown in figure 13. Hypereutectic means that the alloy has a composition beyond the eutectic point, and the eutectic point is the maximum fraction that the primary alloying element is totally soluble in the substrate.

A summary table to compare the chemical makeup of Tribaloy alloys is shown below.

Table 5 chemistry comparison of the trademarked Tribaloy family of alloys.

Tribaloy Grade	Key Differentiators	Key Elements (approx. Wt.%)						Hardness (HRC)
		Co	Cr	Mo	Si	Ni	Others	
T800	High performance high temperature benchmark, highest hardness, high temp corrosion and wear resistance.	Bal.	17	29	3.7	1.5	~0.5	53-61
T900	T800 with added nickel for improved ductility/weldability but reduced hardness and temperature potential	Bal.	17	23	2.8	16	~0.5	48-55
T400	Increased weldability vs 800, and harder than T900, lower	Bal.	8.5	29	2.8	1.5	~0.5	51-57
T400C	Higher oxidation resistance than 400 and 800, slightly higher hardness and wear capabilities than 400	Bal.	14	27	2.6	1.5	~0.5	51-57
T401	Increased weldability vs T400C and better wear and corrosion res.	Bal.	17	22	1.3	1.5	~0.5	45-50
T700	Cobalt free (for Nuclear), lower temperature capabilities	0	16	32	3.4	Bal.	~0.5	45-52
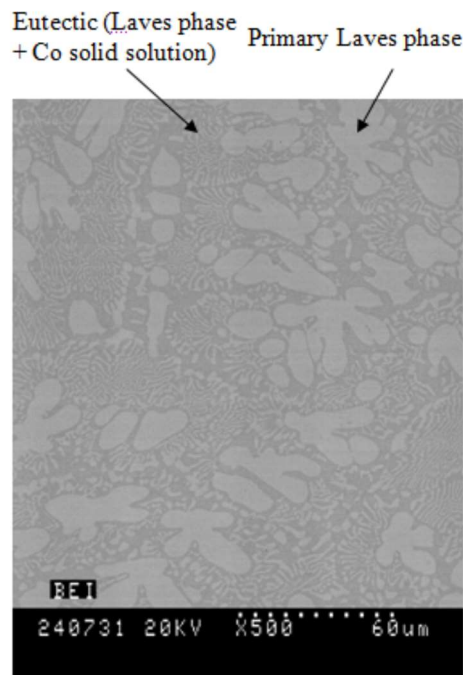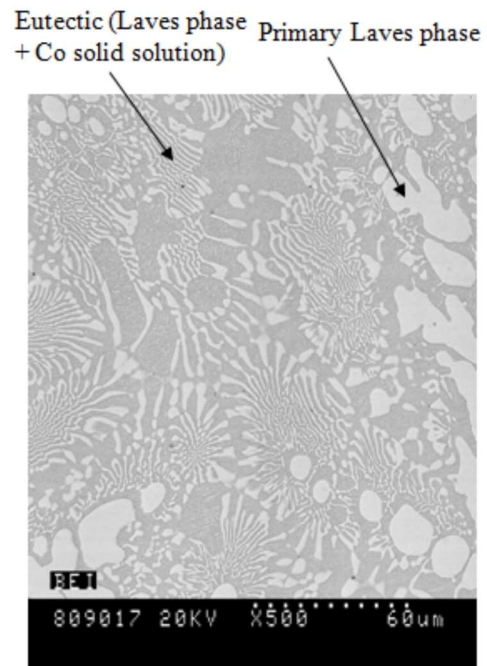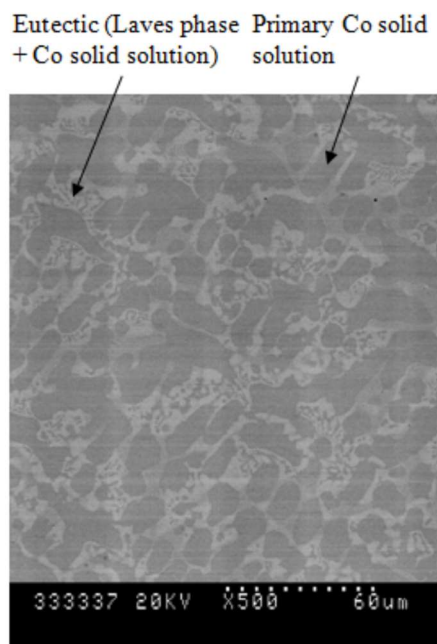
Figure 13 SEM microstructures of (a) T-400, (b) T-400C, and (C) T-401. (20)

Lower technology readiness level (TRL) coatings may become available, with promising results having been shown by so called High Entropy Alloys (HEAs) or Multi-Principal-Element-Alloys. Such alloys consist of at least five metallic elements alloyed in approximately equimolar concentrations which exhibit relatively simple face centred cubic (fcc) and/or body centred cubic (bcc) phases. While promising results have been published

of high temperature wear and oxidations resistance coating performance (23), commercial powder is not available and such coatings currently remain only of academic interest.

The most commonly used ceramic metal matrix coatings (aka cermet) for wear resistance are often based on cemented tungsten carbide (WC) compositions. Above 450-550°C such coatings start to degrade (due to changes in the surface morphology, changes in microstructural phases due to thermal expansion, and other effects). However, coatings based on Cr_3C_2 can provide adequate wear resistance up to 850-900°C (24). An investigation by Houdkova et al (25) 2014 compared the wear performance of a series of coatings, including Cr_3C_2-25%NiCr, Cr_3C_2-25%CoNiCrAlY, NiCrBSi and Stellite 6, with Cr_3C_2-NiCr exhibiting the best tribological performance.

Laser cladding can provide advantages compared with HVOF or other thermal spray techniques, such as increased adhesion strength due to the formation of metallurgical bonds with the substrate and the formation of fully dense microstructures. Both of these factors can result in increased wear resistance of coatings. A study by Kusmoko et al (26) 2014 compared the reciprocating wear performance of HVOF, plasma sprayed and laser clad coatings of Stellite 6 and found the laser clad coating to exhibit the lowest wear rates, linking the results to high density, high hardness and reasonable ductility.

T800 coatings have been successfully deposited onto stainless steel (AISI 304) by LMD (18, 19, 27). However, due to the brittle nature of T-800 and rapid solidification, cracking occurred transverse to the laser scan direction. A reasonably high level (10%) of dilution was used in the first layer applied, which resulted in the formation of fine lamellar eutectic structure, rather than the previously dendritic structure. However, this did not seem to affect the cracking response of the T-800. Increased substrate pre-heating may be a route to mitigate cracking. Alternatively, a more ductile coating material could be considered, such as T-900, which was successfully applied without cracking during the same study (19). However, switching to a more ductile coating resulted in an increased wear rate. As measured by pin-on-disc abrasion testing.

2.5.3   Nuclear wear and corrosion applications

Stellite™6 is a high performing and industrially proven alloy for applications in wear and corrosion environments, especially at elevated temperatures (~300°C), e.g. gate valve seats. When Stellite™6 wears, Co-59 is released, in nuclear systems with a flow path to the reactor, Co-59 can become activated to Co-60 by neutron capture (28). Cobalt 60 isotope ionisation is a concern in nuclear components as it causes significant operational problems through radiation damage, and then subsequent cost with equipment downtime. A move towards non-cobalt materials is urgently required. A number of alloys have been highlighted as potential replacements for Stellite™6, including Tristelle 5183, Norem 02, Tribaloy T700, and Delero 50/60.

Research undertaken by Ocken (28) 1995 evaluates the galling resistance of a range of iron based hardfacing alloys and compares the results with well-established cobalt- and nickel-based alloys. Ocken (28) uses pin-on-plate galling wear testing on a number of cobalt replacement alloys. It could be considered regular occurrence that these types of macro scale tests have questionable relativity to the conditions experienced in service, based on their selected environments, forces, interactions and durations. Differences can particularly be due to dynamical constraints of the test machine which are not true of the application

dynamics, which could be extremely expensive to simulate, and also differ from the standardised test methods.

Anthony (29) 1983 and Bhansali and Miller (30) 1982 have discussed the factors that contribute to galling wear resistance of alloys that crystallize in fcc crystal structures. Their view is that fracture at asperity junctions (i.e. local adhesion sites), rather than deformation, results in low friction and greater freedom from galling. Alloys in which the dislocation mobility is low and cleavage can occur should not gall; ductile alloys, where it is easy for dislocations to cross-slip over more than one plane, should be galling prone.

A number of the most galling-resistant iron-based alloys were found to consist of carbide precipitates and borides in an austenitic matrix (17, 29, 30, 31). This included modest additions of alloying constituents, mainly that of silicon, which consists a number of findings. It has been suggested by Laroudie et al (31) 1996 that the silicon carbides gives beneficial effects to improving wear resistance.

It is clear that even for material specialists the metallurgical factors affecting gall wear performance are not completely understood. (17)

An important factor when distinguishing why some materials are better suited than others at resisting galling wear, is the work hardening rate. Burdett (17) 1990 identifies that materials which harden slowly are more prone to galling than those which undergo rapid hardening and also goes on to comment that Tristelle 5183 contains a significant volume fraction of hard particles which appear to be beneficial for galling resistance. It was categorically stated that macroscopic hardness of materials does not dictate, and cannot be used as, a definitive indicator of a materials galling performance. The iron-base alloys tested compared well to the Stellite 6 results at both room temperature and an elevated 300°C. This comparison included EB 5183 (Tristelle 5183) alloy.

R. Smith et al (32) 2013 explores the tribological characteristics of the hardfacing alloys of Stellite 6 and Tristelle 5183 as well as Norem 02 (Fe based). The assessment included testing using the ASTM G98 pin-on-disc standard procedure for self-mated surfaces. The findings showed that all alloys performed well at ambient (25°C) temperature and the Tristelle performed the better of the three alloys at elevated temperature (350°C). It should be noted that the Tristelle 5183 sample could not be ground to the specified finish, thus affecting the results by unknown amount.

During a teleconference conducted on 20th September 2019, David Stewart of Rolls-Royce stated that iron-based hardfacing alloys struggle to achieve the established and renowned galling threshold of Stellite 6 at 300°C. This "threshold" does not seem to have a readily transferable value due to differences in test conditions, usually dictated by specific industrial environments. Also, it was mentioned that the ASTM G196 (33) galling test is an ideal test method material definition for the benchmarking of material for valve seats. Testing can be carried out wet or dry, ideal testing conditions are at 300°C and wet, however David Stewart mentions that a room temperature test will give initial indications of material performance. (Private communication – teleconference, D. Stewart 20/09/2019).

2.5.4 High temperature engines oxidation, creep and strength application

Improvements in cycle efficiencies of aerospace and power generation engines are commonly achieved by increasing the operating temperatures. Oxide dispersion strengthened (ODS) materials (highlighted in Figure 14) offer higher temperature oxidation stability, creep resistance and strength than conventional alloys (such as nickel-based superalloys), yet these materials can have lower temperature capability than some advanced ceramics. Gamma-titanium aluminide is a material with applications in blade technology for advanced aerospace engines (19). Further improvements to the temperature capability properties of the conventional GE48-2-2 TiAl were made by adding nano-yttria (Y_2O_3) to a purposely-designed variant of TiAl, Ti-45Al-3Nb, specifically designed for the application and additive manufacturing as part of the EU FP7 project OXIGEN (35). The OXIGEN project made significant leaps in designing and developing a new γTiAl material, and within that project, TWI developed parameters for processing the material by LMD. The Ti-45Al-3Nb + Y_2O_3 showed promising oxidation resistance and strength at 800°C but there were unanswered questions about the powder quality and suitability for processing by LMD. This work continues from where the OXIGEN project left off by performing further investigations into the processability of the developed material and suggest solutions for maximising the potential of the newly designed material (35).
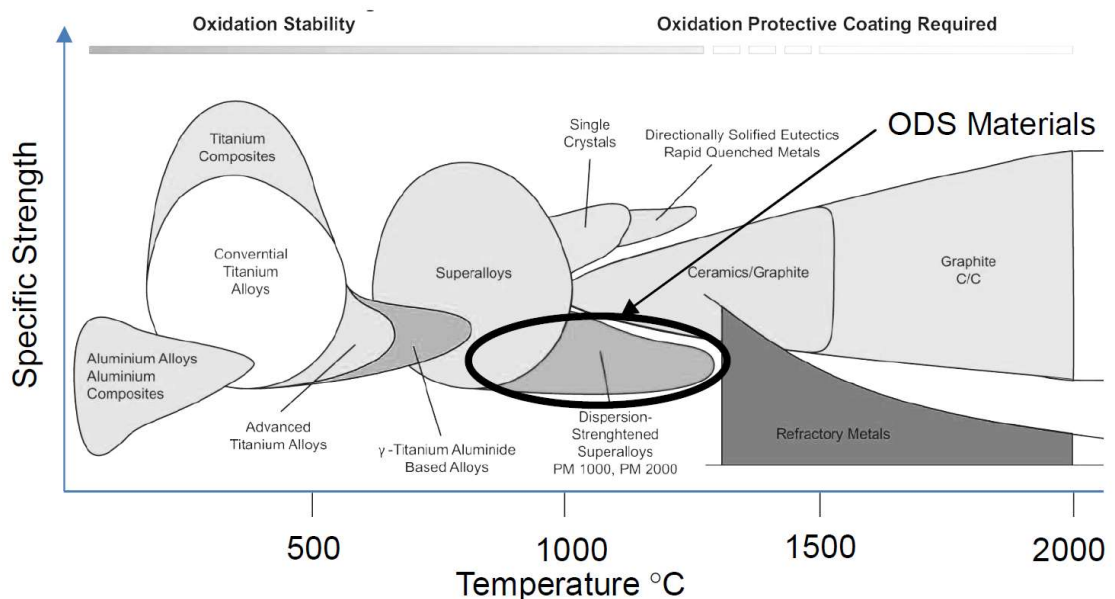
Figure 14 Chart of material groups in relation to specific strength at a given temperature (36).

Low-pressure turbine (LPT) blades used in gas turbine engines are widely made from Nickel based superalloys. The environment in gas turbine engines requires high temperature oxidation resistance, creep resistance, and strength. There is also a common call by engine producers for next generation engines to run at higher temperatures, leading to significant benefits of higher efficiency engines. The General Electric GEnx™ engines released in 2006 were the first commercial engines to feature TiAl (Ti-48Al-2Cr-2Nb). Two stages of TiAl LPT blades allow around 100 kg of weight to be removed from each engine. Reports by GE stipulate that the GEnx™ engine delivers a 20% reduction in fuel consumption, a 50% reduction in noise and an 80% reduction in NOx emission compared with prior engines in its

class. (37) The reported information suggests that a majority of the improvements come from the use of TiAl blades. However, it is not completely clear if other changes to the engine contributed to these improvements as well.

A number of manufacturers are incorporating TiAl into their next generation platforms including Rolls-Royce, SNECMA, Pratt and Whitney, and GKN among others. Third generation TiAl materials are intended to hold strength properties at higher temperatures, shown in figure 15.
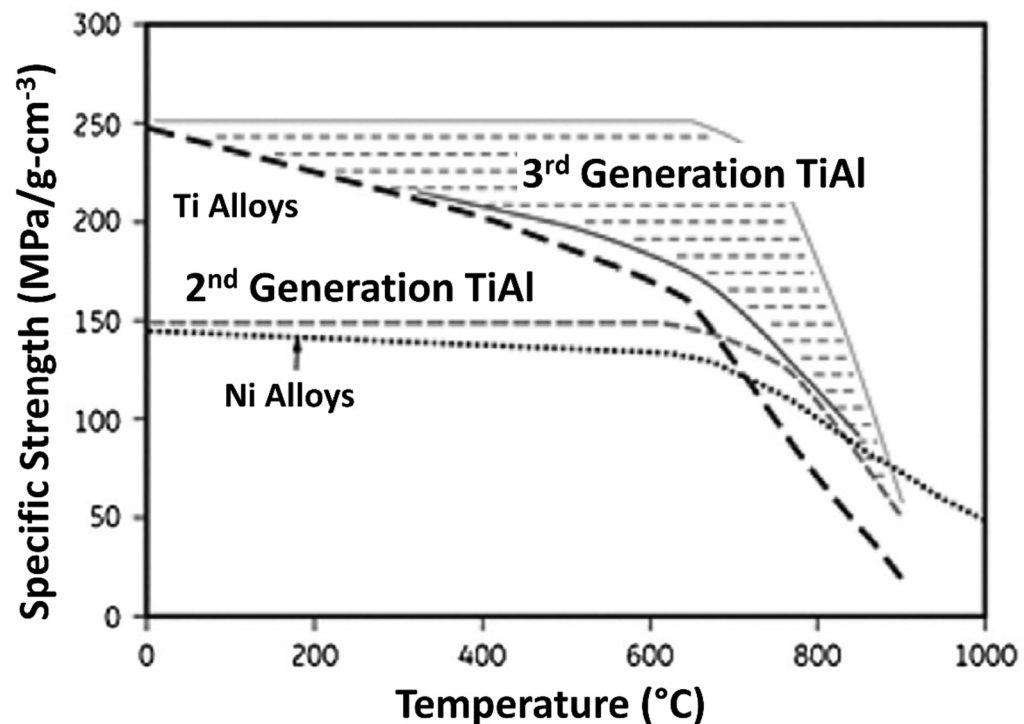
Figure 15 Specific strength capabilities of TiAl materials (35, 36).

2.5.4.1   Principles of TiAl alloys

There are three main phases of TiAl microstructure, fully or near α2/γ lamellar, an equiaxed γ structure, and a duplex structure of α2/γ lamellar colonies and single-phase γ grains. A duplex microstructure can enhance ductility and low cycle fatigue properties. (38, 39, 40, 41) Fully lamellar or near lamellar microstructures can enhance creep resistance and fatigue toughness.

The grain size of wrought alloys after hot working and heat treatment, with a duplex microstructure can be typically 20 μm, which is considerably smaller than the typical grain or colony size in as-cast lamellar structures where grains of several hundred micrometres are common, unless grain refiners, such as borides are incorporated. (40)

If the alloy is not hot worked, heat treatment approaches can be employed to refine the grain size. (TiAl alloys in commercial aircraft 6). The general practice is to hot isostatically press (HIP) TiAl castings to remove residual macro and micro porosity. The TiAl castings are

typically heat treated to convert the fully lamellar as-cast structure to a near fully lamellar, or duplex, structure, depending on the balance of properties that are required. The design of the correct heat treatment window that can provide acceptable microstructure throughout the whole component is extremely important. The selection of suitable heating rates, hold temperatures and times, and subsequent cooling rates are all parameters to which TiAl alloys can have strong sensitivity. (42)

2.5.4.2 Dispersion strengthened titanium aluminides

Strengthening by the addition of particles is known to have the potential to provide superior properties compared to the parent alloy, however only a limited number of studies have been published. Titanium aluminides have been produced in the past by many different manufacturing methods including, sintering, casting, extrusion, forging and laser electron beam based additive manufacturing. Today, casting and electron beam based additive manufacturing are the state-of-the-art processes to produce turbine blades for aero-engines. (43, 44).

Kenel 2016 emphasises that powder based processes have the potential to eliminate inherent problems of castings like macro-segregation, locally different mechanical properties, expensive homogenization heat treatments and limited part size (35, 45, 46). Kenel 2016 used spark plasma sintering (SPS) as a solid state sintering technique as a reference to compare the bulk material of additively manufactured parts by laser metal deposition. As SPS offers the capability to consolidate almost every material to full density it can therefore be used effectively as a baseline for material consolidation. Materials produced by SPS typically retain a fine microstructure with good mechanical properties. The TiAl ODS material designed by Kenel (35) 2016, was consolidated by LMD and produced 2x improvement in oxidation resistance than standard GE spec γ-TiAl also produced by LMD, and similar strength value potential at 800°C. Comparison of the two material microstructures are shown in Figure 16.
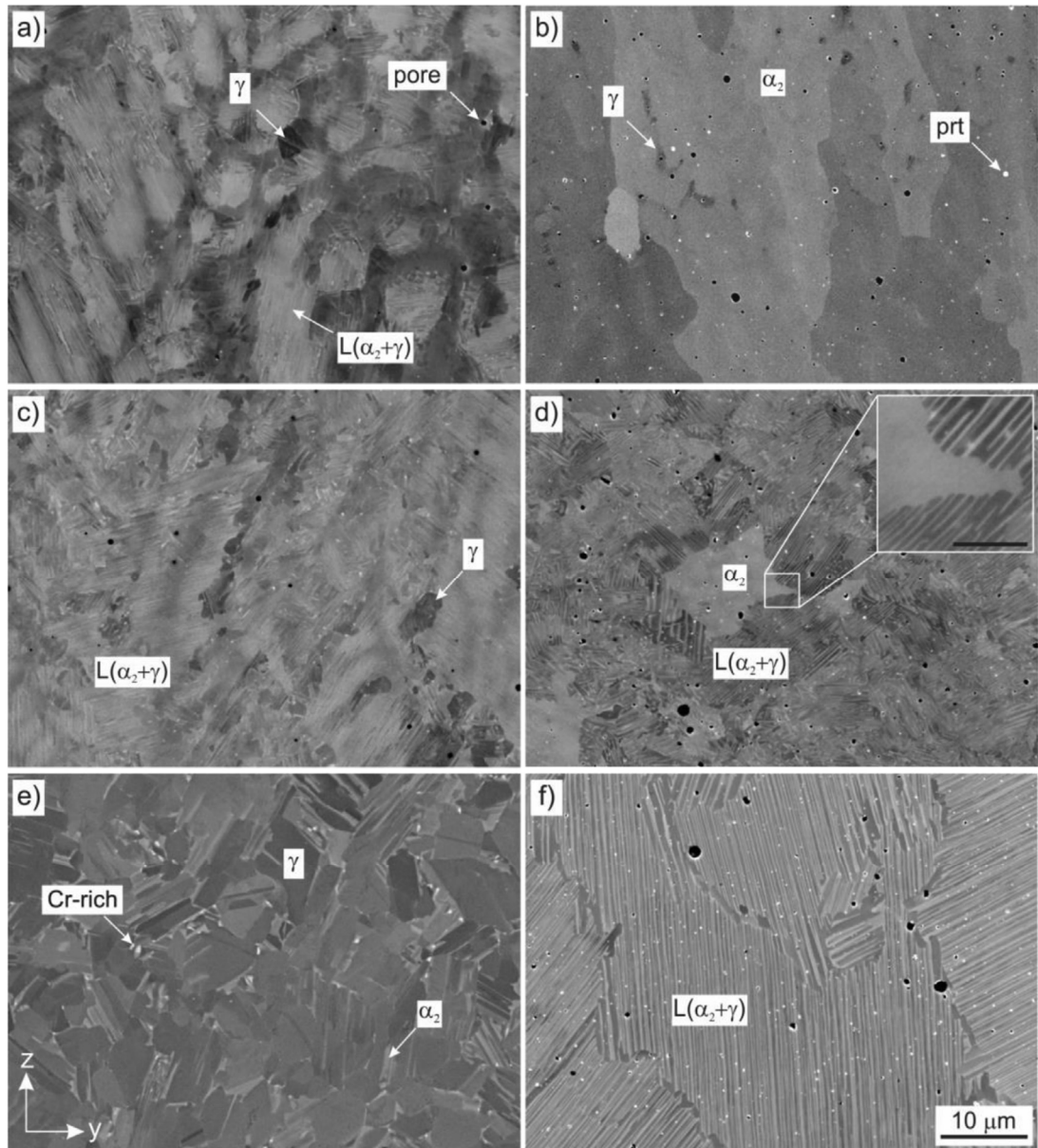
Figure 16 BSE SEM micrographs of LMD processed a, c, e) γTiAl GE48-2-2 (Ea = 179 J/mm^2) and b, d, f) γTiAl 45-3 ODS (Ea = 120 J/mm^2). (a, b) in the as processed state and after thermal annealing of (c, d) 1123 K/12 h and (e, f) 1573 K/15 min + 1123 K/12 h. The α2 and γ phase, pores and dispersoids (prt) are indicated. Bright spots in e) correspond to Cr rich areas. The scale bar in f) applies for all micrographs (inset: scale bar = 2 μm). The build direction (z) and the beam translation(y) are shown. The scanning direction (x) is out-of-plane. (45)

2.5.4.3 Additive manufacturing of titanium aluminides

Additive manufacturing of titanium aluminide alloys presents many challenges that contribute to the infancy of its adoption. Primarily, titanium aluminides are inherently brittle at low temperature due to the intermetallic structure that ensures desirable properties at elevated temperatures. At lower temperatures, the materials are highly susceptible to severe cracking when exposed to thermal stresses. Secondly, these alloys can

experience hot cracking, when the remaining liquid phase cannot sustain the thermal stresses imposed on the solidifying material. In addition, upon solidification and cooling, titanium aluminides undergo several solid state phase transformations. These transformations may alter or be suppressed at the typical cooling rates of laser based additive manufacturing techniques and metastable phase relations may be developed (44).

Usually preheating is applied alongside the process to achieve crack free titanium aluminide parts. Kenel 2016 states that the earliest manufacturing method for TiAl material was blown powder based LMD. (47). It was clearly shown that the obtained microstructure was dependant on the processing parameters and the subsequent heat treatment. (48). Srivastava et al (49) 2001 deposited Ti-48Al-2Mn-2Nb and observed a fine lamellar structure. Moll and McTierman (50) 2000 used a similar alloy Ti-47Al-2Cr-2Nb and obtained fully lamellar microstructures with comparable properties to cast material. Zhang et al. (51) 2001 applied the methodology to Ti-48Al-2Nb-0.4Ta and Ti-48Al-2Cr-2Nb and obtained microstructures rich in $\alpha2$. After heat treatment at 1173 K fine lamellar structures were observed. Lui and Dupont (52) 2004 reported preheating temperatures of 723 to 737 K as a stable range to obtain crack free deposits using LMD of Ti-48Al-2Cr-2Nb. It was clearly shown that although higher energy inputs during processing reduce the cracking frequency, this effect is limited and external preheating was always needed.

For powder bed based AM methods, electron beam melting (EBM) offers state-of-the-art preheating capabilities. Preheating to significant temperatures in powder bed fusion (PBF), also known as, selective laser melting (SLM), is more challenging and most of the work being conducted is using bespoke and retrofitted research machines. These research machines often have a significantly reduced build volume due to the heating technology and increased chamber protection.

A number of publications have stated successful (generally meaning crack free) AM production of various γTiAl alloys. All seem to have required preheating and generally within the temperature range of 1203-1323K. (53, 54, 55, 56, 57, 58, 59, 60, 61).

2.5.5 Extreme wear applications

White cast iron is a hard (>650Hv), brittle material with high abrasion wear resistance. This member of the cast iron family is different in which carbon is present only as carbide. White cast iron is not easily machined and is very difficult to weld. Conventional manufacturing of white cast iron components is often comprised of a casting process, which can often be the cause of major porosity and defects within a component. Components can be large and expensive to manufacture, scrapping components due to casting defects is highly uneconomical. In a personal communication with a mining castings supplier in June 2019, the following information was given. Manual weld overlay is used for repairing defective casting and requires preheating temperatures in the range of 800-1000°C prior to repair. Preheating is required because of the brittle nature of the substrate material. The preheating of some large >2m Ø components prior to manual weld overlay can take up to 48 hours. (Private communication – OpenHybrid project meeting, 20/06/2019).

To repair cast iron by powder fed – LMD, it is not possible to find high quality like for like powder material (primarily due to the fact the powder would rust and become risky and difficult to process), nor is it likely to be easy to deposit free from major cracking defects even with high quality feedstock, due to the nature of the material discussed previously. Therefore readily available powder materials with similar performance capabilities, such as

hardwearing tungsten carbides within a metal matrix, such as Ni-WC material, is a potentially useful material when attempting to repair. However the topic of white cast iron repair, particularly by LMD, is not well published and likely has limited research and exploration undertaken worldwide.

WC MMC materials such as Ni based –WC are prone to decarburisation when excessive heat is applied (thermal decomposition), which can occur in the melt-pool when being applied by the LMD process. Known as decarburisation or dissolution, where the WC particles loose carbon by diffusion and W2C eutectic phase forms, this phenomena causes embrittlement of the matrix, potentially leading to deposit and part failure via initiation of cracking.

P. Faramand et al 2014 found that using induction heating, increased micro hardness of Ni-WC (60%) to 1090Hv from 800Hv. It was reported that the detrimental effect of dissolution of WC into the matrix (decarburisation), was reduced by minimising the energy density of the laser deposition parameters in combination of using the induction heating technique. Additionally by adding nano-WC (5%) to Ni-WC (60%) MMC, the coating hardness increased to 1400Hv and, decreased cracking susceptibility. (62).

2.6 Process related specifics for key application

Wei Ya et al (63) 2018 observed an increase of dilution in the first layer of Tribaloy T-400 deposit from 21-45% when using preheating due to the extra energy input, increasing laser penetration, melting depth and molten duration, ultimately increased the mixing of deposit and substrate. As is common, the relationship between hardness, dilution and cracking was studied. It was commented that 15-20% dilution may be optimal as a balance between hardness properties and reduced tendency to crack.

One interesting aspect that was studied was the impact of the first deposit track vs subsequent tracks, with the dilution reducing to a rather steady state after the first two tracks. The exact conditions tested and relevance to other studies cannot be definitively extracted due to a number of unknowns, including preheat cooling between first and subsequent tracks.

It is summarised that preheating (250°C) during cladding reduces the tensile residual stresses and risk of cracking. (63) Furthermore, there were recommendations that heating a Ni-based superalloy substrate (IN718) to 500 °C in order to eliminate cracking in the Tribaloy T-400 coating. In the present work for the T-800—RENE 77 materials, a sole substrate volume pre-heating was not completely effective since cracks still appeared in the sample. A better solution was a combination of substrate volume pre-heating with a point laser heating having energy density within a range of 25 to 50 J/mm2. Therefore, by heating the substrate to a temperature of about 550 °C (by heating the working table and laser preheating) and by changing energy density during the fabrication of the coating, a coating with a good geometrical quality can be produced, which exhibits a minimal dilution zone with the substrate and is devoid of cracks. (63)

2.7 Literature Review Summary

Most if not all of the papers reviewed on LMD of crack susceptible materials, considered only small scale, sample deposits as a demonstration of the research and findings. This results in the conclusions of those works to be of a narrow field, lacking evidence of applicability for industrial scale. Additionally there is minimal discussion that could show an

understanding for the potential differences in the coating material behaviours from lab-scale to industrial scale.

Many of the practices discussed in this section provide useful insights about the processes, materials, and characteristics which can be utilised for informing the furthering of applied research in this area. However, in order to address the core concerns regarding upscaling, the methodologies of the process developments in particular need to be redesigned to maintain consistency from lab development to industrial scale. Specifically, evidence of sample scale T800 deposition will be expanded on to determine better the processability of the material.

Secondary heating processes have been shown to improve the processability of crack susceptible materials, primarily by reducing the cooling rate. Induction heating is capable of local heating of the deposit area as a pre-, during-, and post- process treatment. Developing further the understanding of combining induction with the deposition process will make up a critical part of the research.

Chapter 3

Methodology and Equipment Setup

3 Chapter 3 – Methodology and Equipment Setup

3.1 Materials and Equipment

3.1.1 Materials

The main powders listed in Table 6 were used for this work. The powders have been tested against the target specification of composition and inclusions. The powder test certificates are included in Appendix A. All powders were 45-90µm unless otherwise stated in the table below. Powder size influence was not studied.

Table 6 Experimental alloys and their applications

	Name	Industrial application	Key Elements (approx. Wt.%)						
Key development powders	Triballoy T800 Task 2a	Steam turbine valve stems	Co 50.8	Cr 17.5	Mo 28.4	Si 2.9			Others ~0.5
	Tristelle 5183 Tasks 2b & 2c	Nuclear gate valves and seats.	Fe 55	Cr 22	Ni 10	Nb 7.3	Si 3.1	C 2	Others ~0.5
	TiAl + ODS Task 2d. 45-106µm	Aerospace and power generation engines	Ti 61	Al 30.5	Nb 7.6	Y_2O_3 0.5			Others <1
	Ni-WC (60%) Task 2e. 45-106µm	Mining and extreme wear environments	WC 60	Ni 34.2	Cr 2.8	Si 1.44	B 0.62	C 2.5	Fe 0.96
Supplementary or comparative powders	NiCrSiB interlayer Task 2a. 45-125µm	Steam turbine valve stems	Ni 84.55	Cr 7.5	Si 3.5	B 1.7	Fe 2.5	C 0.25	
	Ti-48Al-2Nb-2Cr (conventional AM spec γTiAl) Task 2d	Aerospace and power generation engines	Ti 62	Al 34	Cr 2	Nb 2			
	Ti-6Al-4V Task 2d	Aerospace and power generation engines	Ti 90	Al 6	V 4				

The following materials were used as flat plate substrates for the initial developments in this work:

- 316L stainless steel 300x200x15mm length, width, thickness (Tasks 2a and 2b described in 3.4.1).

- Ti-6Al-4V 80x40x30mm length, width, thickness (Task 2d described in 3.4.1).

3.2 Equipment

3.2.1 Laser Metal Deposition

Figure 17 shows TWI's robotic cell setup for conventional laser metal deposition. The cell has been developed using TWI's laser processing experience and knowhow to ensure suitability for use in a wide range of process development tasks. Additionally, for Ti-6Al-4V deposition, TWI can use this system with an additional shielding setup via a flexible welding chamber to provide a fully enclosed environment that can be purged of oxygen and nitrogen by controlled filling of argon.

(a)

(b)

(c)

Figure 17 TWI's robotic LMD system:

a) Dedicated robotic LMD cell;

b) Trumpf deposition head with ILT 'three beam', coaxial, and side feed nozzle options.

c) Flexible welding/deposition enclosure purged with argon.

The robotic LMD system comprises the following elements:

- Trumpf Trudisk 8002 5.3kW disc laser.

- TruControl 1000 controller.

- Trumpf BEO D70 processing optics with motorised collimation.

- Reis RV60-40 robot (2.4m reach, 40kg max payload).

- Reis RDKVv05 two-axis manipulator (500kg max payload).

- Sulzer Metco 10-C powder feeder with dual 1.5kg hopper system.

3.2.2   In-process Thermal Control

Thermal control equipment is shown in figure 18. The equipment comprises of:

- Ceramic heating plate for small substrate/sample heating with a fixed temperature up to 400°C.

- 12kW dual-coil induction heating system capable of heating components or sections of components above 1000°C (material dependent). Developments have been made in the project to enable fully programmable temperature cycle control and pyrometer temperature measurements for pre-heating, in-process heating and post-process thermal control. Customised heating coils were manufactured for the application to improve heating efficiency.

- Pyrometers and thermocouples for temperature measurement and control.
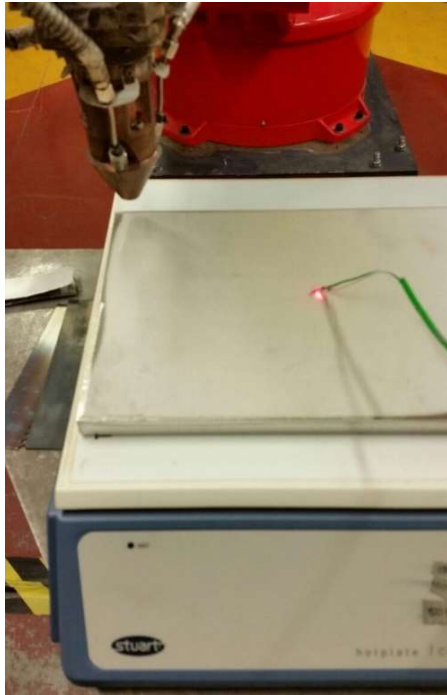
(a)

(b)

(c)

(d)

Figure 18 Thermal control equipment:

a) Preheating plate with thermocouple and pyrometer temperature feedback.

b) EFD induction heating unit 2x12kW coil outlets

c) 2x 12kW induction coils (specific coils pictured designed for flat plate heating)

d) Eurotherm control unit for temperature monitoring, control, and programming

3.3 Sample Characterisation Methods and Equipment

The samples were cross-sectioned perpendicular to their build direction and hot mounted into bakelite using a Struers LaboPress-1. The samples were then polished on a LabPol Duo8 polisher, using grit sizes ranging from 120 - 4000, followed by 0.06μm oxide polishing suspension (OPS). Light microscopy on an Olympus BX50 microscrope was used to undertake basic metallurgical inspection.

Hardness testing was performed using a Falcon 505 tester to BS EN ISO 6507-1:2005, with 0.2mm zig zag lines, and each indent 8 microns of vertical displacement from the starting position. Two line scans were carried out per sample and twelve to twenty indents were measured per line scan as displayed in figure 19. The indentations were carried out using 1kg load and a 10-second dwell time, at room temperature of around 24°C.
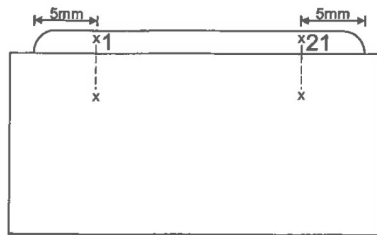
Figure 19 Hardness traverse schematic.

Semi quantitative chemical composition measurement by EDX analysis was carried out using TWI's SEM equipment. The main elements of the Task 2.1 materials were measured in seven samples. The results give a better understanding of the levels of dilution and material intermixing between the substrate and LMD coating. 25kV voltage was used consistently for the inspections on a Zeiss EVO LS15 SEM.

A number of etchants were trialled, for T800:

- Nital, dipped onto the specimen using a cotton swap, experimented between 10 seconds and one minute, until the proper etching was achieved, and

- electrolytic 1.5V, stainless steel electrodes, in 10mL nitric acid, 10mL hydrogen peroxide, and 100mL oxalic acid.

3.4 Approach

3.4.1 Overview

The scope of work untaken consisted of the following tasks:

- Task 1 – Induction heating development

- Task 2 – LMD process development:

  o 2a – Triabloy T800 (For high temperature wear application);

  o 2b – Tristelle 5183 (For nuclear wear application);

- o 2c – LMD productivity increase;

- o 2d – γTiAl ODS (For high temperature engines);

- o 2e – Ni-WC (60%) (For extreme wear applications).

3.4.2 Task 1: Induction heating development

Prior to the start of this work, TWI had acquired an induction heating system and combined it with the LMD process to provide preheat to materials that required reduced cooling rates when processed by LMD. No variations in coil design had been tested and only one of the two coils were usable at one time due to setup restrictions. The temperature was controlled by pyrometer feedback and temperature was adjusted manually by changing the target temperature.

The task was structured to develop the capability with the induction heating technology by improving the setup and implementation of the technology alongside LMD. This was initiated by working more closely with the equipment supplier. The key developments made include:

- ▪ Coils were designed to optimise the heating efficiency of flat top surface components, useful for parameter development and large component repair on flat substrates.

- ▪ The Eurotherm control unit was programmed to respond more rapidly to temperature changes measured by the pyrometers, enabling the equipment to hold the requested temperatures more accurately and adapt to changes more quickly.

- ▪ Simultaneous dual coil capability was enabled, with independent and combined programming options.

- ▪ The emissivity of the surface of a material is its effectiveness in emitting energy as thermal radiation was considered. The value of emissivity is given between 0 and 1, with 1 being the surface of a perfect black body. The material characteristics and surface preparation are important factors in dictating material emissivity. Pyrometers measures surface temperature by the thermal radiation. The emissivity value used throughout the project was 0.95.

Prior to initiating the LMD process development trials and design of experiments (DOE), it was necessary to develop a more efficient and advanced solution for in-process thermal control. TWI had already shown promising results prior to this project with the induction heating system as a supportive technology to LMD when processing crack sensitive alloys; but the equipment had no automation or programming solution and was generally inefficient at heating components using the generic supplied induction coils. Therefore application specific designs were made for the induction coils and implemented the capability and knowhow of a programmable induction heating system with preheating, in-process heating and post-process thermal control cycles. The arrangement and setup of the coils is shown in Figure 20.
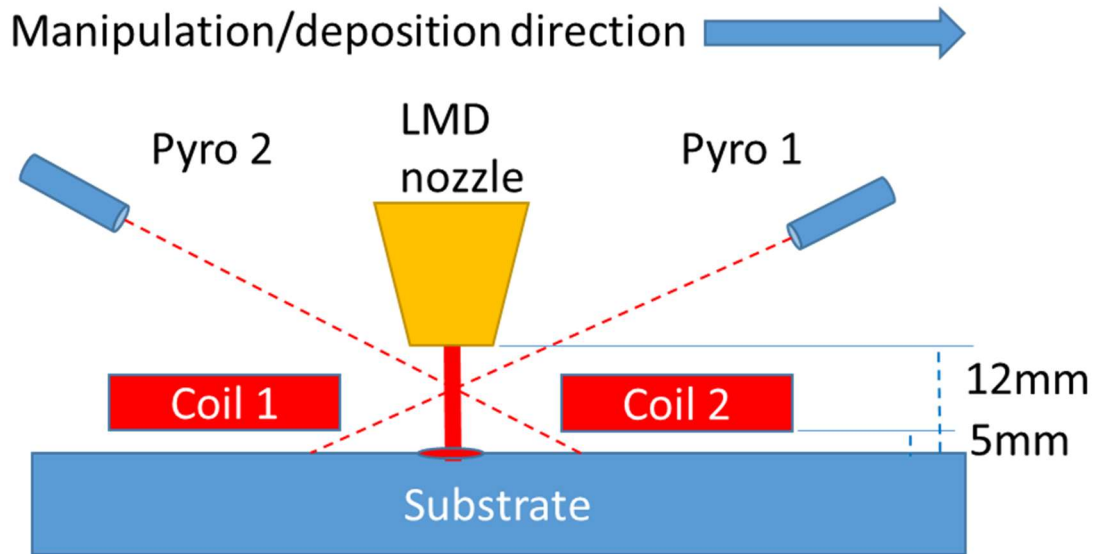
Figure 20 Induction coil location and pyrometer setup for in process thermal control

3.4.3   Task 2: LMD process development

LMD process development was carried out on a number of alloys and applications. Generally parameters were chosen using predefined baseline starting points and then refined using quality criteria of material density, optimal ratios of deposit width to height ratio of 3 to 1 or greater, and defect free consolidated material. Fully optimised parameters can be challenging to develop and justify, and need to be developed using test data feedback such as, hardness, chemistry, and wear and other performance criteria. There is still ongoing work to relate dilution, hardness, and performance of the deposited material, with the preheating conditions and energy density of the deposition process. Task 2 is broken down into 5 sub tasks.

3.4.3.1   Task 2a: Tribaloy T800

Firstly, deposition trials were carried out to establish suitable processing conditions for depositing dense, fused Tribaloy T800 onto 316L substrate, using historic parameter sets for similar material compositions. This was carried out without any additional heating source except the laser, and therefore, all samples in this first run were expected to form cracks in some way.

Using the sufficiently developed LMD parameters that are shown in table 7, a set of trials was then carried out to investigate the required pre-heating temperature (using induction coils) to reduce or eliminate cracking. Deposits were produced in multiple layers between two and four layers, so that the upper layers would be expected to be completely free from dilution, (as with diluted material, the deposit is likely to be more ductile through the entire diluted depth). Additionally the samples that were produced were relatively large, 190mm long x 30-50mm wide, to improve the representation of realistic stresses that would be created in a component production run, and reduce the effect of local heating with the laser when depositing in small areas. Overall attempting to create results that were sufficiently realistic of the final application requirements, without significantly increasing sample production cost and time.

Additional trials were carried out using a nickel interlayer material, NiCrSiB, applied in the non-preheated condition. T800 was then applied onto the nickel layer using the preheating approach.

Material analysis was carried out including metallography, hardness testing, and chemical analysis.

Table 7 LMD process parameters for Tribaloy T800.

Hardfacing material	Buffer layer material	Substrate material	Deposit No.	No. Buffer layer	No of hardfacing layers	Laser power (W)	Spot size (mm)	Traverse speed (mm/sec)	Powder flow rate hardfacing RPM %	Track separation (mm)	Layer height (mm)	Nozzle Shielding Gas (L/min)	Powder Carrier Gas (L/min)	Deposit area dimensions LxW (mm)	Pre + during heat hard-facing (°C)	Cool down rate (substrate) till 250°C and then uncontrolled air cooling Approx. K/min	Deposition Strategy
Tribaloy T800	NiCrSiB (metco 12C)	316L Stainless Steel 300x200x15mm (LxWxT)	101	0	2	600	1.5	11.25	6	1	0.4	6	2	190x50	0	Na	Unidirectional toolpath, staggered raster scanning, with distinct laser on/off (start and stop) at the end of each vector.
			102	0	4	600	1.5	11.25	6	1	0.4	6	2	190x50	0	Na	
			114	0	2	650	1.5	11.25	6	1	0.4	6	2	190x50	800	6	
			118	0	2	650	1.5	11.25	6	1	0.4	6	2	190x50	850	6	
			119	0	3	650	1.5	11.25	6	1	0.4	6	2	190x50	900	6	
			120	2	3	650	1.5	11.25	6	1	0.4	6	2	190x50	850	6	
			123	2	4	650	1.5	11.25	6	1	0.4	6	2	190x50	550	6	
			124	2	4	650	1.5	11.25	6	1	0.4	5	2	190x50	600	6	

3 jet nozzle with a 12mm standoff (tip distance from the workpiece).

3.4.3.2 Task 2b: Tristelle 5183

Process development trials were carried out using the Tristelle 5183 powder, deposited onto 316L substrate. The material was inspected after deposition; parameters were refined based on the quality of consolidated material, i.e. material without lack of fusion, without high concentrations of large pores (above 50μm) and free of cracking or other defects. Additional trials and material processing development were then further developed as part of Task 2c.

The Tristelle deposits were tested by ASTM G65 dry sand abrasion testing procedure A (64), and compared to LMD Stellite 6 material as a baseline. This test comprises a gravity sand feeder, rotating rubber wheel, and the sample mounted with a polished surface and forced against the rubber wheel under a set load. The weight of the sample is measured before and after the test. 6000 revolutions were carried out for each test. The sand was from the same batch of approved dry sand material. Two samples were tested for each material.

3.4.3.3 Task 2c: LMD Productivity Increase

3.4.3.3.1 Equipment capability mapping

Process trials were carried out to investigate the capability and limitations of the LMD equipment. The Trumpf D70 LMD optics uses a motorised collimation optic unit that can be modulated resulting in a change in the laser spot size. The goal of the experiments was to map out the range of achievable spot size. The spot size was measured using a beam profiler. To improve confidence in the results, trials were also conducted by energising the laser onto anodised aluminium using standard test laser powers and durations. The complete mapping DOE can be found in Appendix B, table B2.

3.4.3.3.2 Laser defocus approach with powder nozzle extension

In this task, a nozzle extension unit was designed and tested enabling the expansion of the beam diameter at the work piece. The motorised collimation optic unit in this system limits the largest spot size capable to 1.5-2mm. Therefore, a different approach was required for expanding the beam to a size that up to 5.3kW of power could be used with. It is reported by C. Zhong et al 2016 that 3kW laser power is sufficient for 3-4mm laser spots and will enable up to 2kg/hr deposition rate without significant comprise of deposition characteristics (65). The procedure for developing an expanded laser beam and optimised powder focus is shown in figure 21.
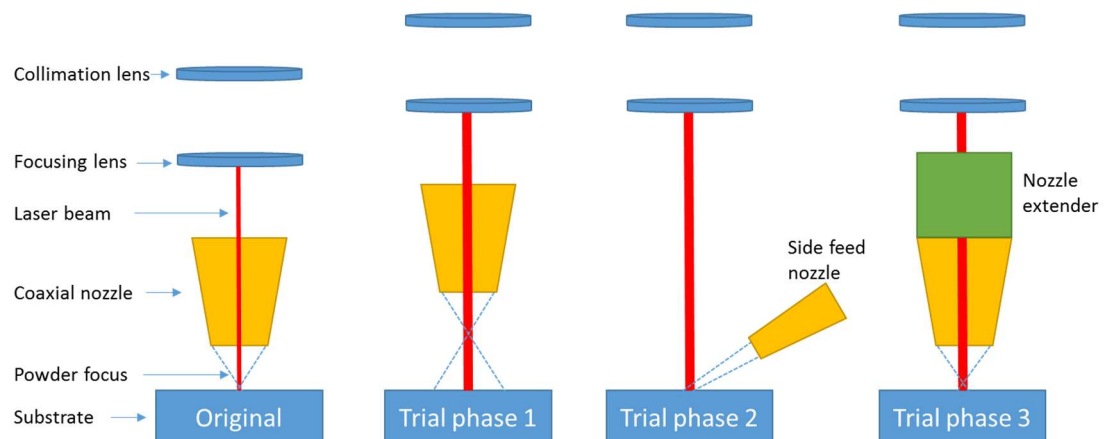
Figure 21 Phases of development for laser defocusing and deposition trials.

Initially the laser beam was defocused by lifting the processing head further away from the substrate in defined 10mm increments whilst using a side fed powder nozzle adjusted at each increment to maintain a standoff of 12mm from the melt pool; giving a focused stream of powder into the melt pool.

It was critical that any nozzle extension unit did not cause the wide spot to contact the internals of the nozzle and therefore was one of the limitations of the maximum spot size that was achievable. The second important limit of the spot size was the available laser power (5.3kW), required for developing a sufficiently large melt pool over the spot size diameter as well as creating dense consolidated material from the deposition process. Once this was properly understood, two nozzle extenders were designed and produced, one at +40mm standoff and one at +50mm standoff, to enable a theoretical spot size between 4mm and 7mm, while maintaining feeding the powder at the optimised 12mm standoff distance.

Deposition trials were carried out using the Tristelle 5183 powder and 316L substrate, application materials of Task 2.b. The deposition rate was compared with the results found in Task 2b.

Table 8 LMD process parameters for Tristelle 5183.

Hardfacing material	Substrate material	Deposit No.	Standoff distance (mm)	No of hardfacing layers	Laser power (W)	Spot size (mm)	Traverse speed (mm/sec)	Powder flow rate hardfacing RPM %	Track separation (mm)	Layer height (mm)	Nozzle Shielding Gas (L/min)	Powder Carrier Gas (L/min)	Deposit area dimensions (mm)	Pre + during heat hard-facing (°C)	Cool down rate (substrate) till 250°C and then uncontrolled air cooling Approx. K/min	Deposition Strategy
Tristelle 5183	316L Stainless Steel 300x200x15mm (LxWxT)	301	12	1	600	1.2	11.25	6	1	0.4	6	2	150x50	0	Na	Unidirectional toolpath, staggered raster scanning, with distinct laser on/off (start and stop) at the end of each vector.
		302	42 (30 extension + 12 nozzle)	1	1800	4-5	11.25	48	2.5	1.0	10	4	150x50	0	Na	

Coaxial D40 nozzle 12mm standoff (tip distance from the workpiece).

3.4.3.4 Task 2d: γTiAl ODS

TWI has developed LMD processing conditions for a bespoke version of the γTiAl ODS as part of EU FP7 project OXIGEN. During that project, the processability of the powder, or the challenges of the processing, was determined to be most likely caused by the powder quality without finding evidence of the route cause for significant porosity found in the consolidated material. The concern being specifically high contamination levels of oxygen in the powder formed by high-energy ball milling production process. The oxygen content in some chemical analysis tests were in excess of 1000ppm, which is significant, and usually specifications and recommendations for Titanium alloys specify material to be under 1000ppm. In this task, investigations were performed to look at the results of depositing the γTiAl ODS powder and comparing the results with the conventional GE spec γTiAl. To deposit any γTiAl without causing significant cracking, a preheating temperature of ~1000°C is required, with a controlled cool down post-deposition at around 4°C/min until 250°C, and then uncontrolled and not measured cooling in air. Since the substrate and deposit are sensitive to oxidation above 450°C, a fully argon shielded environment was required. In the setup shown in Figure 22, the environment can be purged down to below 10-ppm oxygen, using a calibrated oxygen measurement device known as weld purge monitors. Deposits were made of the γTiAl ODS and GE spec γTiAl to compare the resulting consolidated material characteristics and processability.
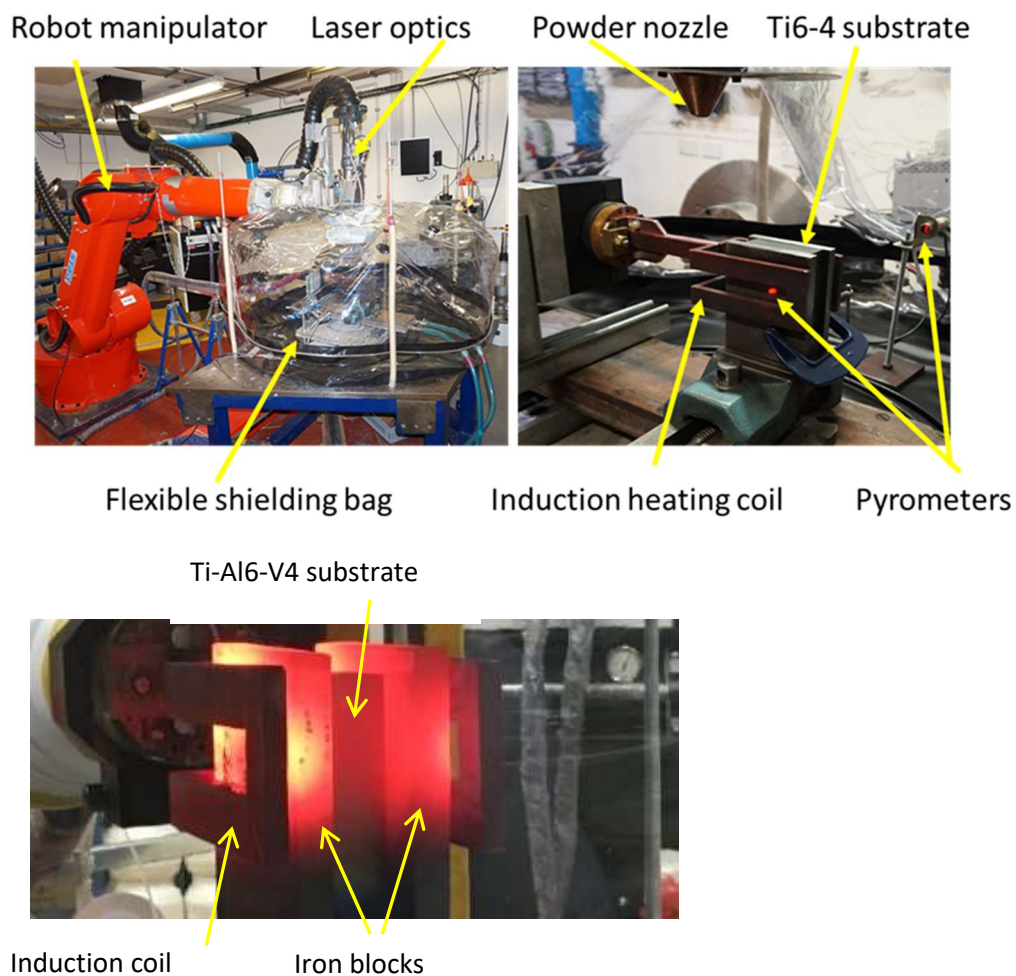
Figure 22 Inert shielding bag and induction heating setup for TiAl deposition.

Table 9 LMD process parameters for γTiAl materials.

Deposition	Substrate material	Laser power (W)	Spot size (mm)	Traverse speed (mm/sec)	Powder flow rate RPM %	Track separation (mm)	Layer height (mm)	Nozzle Shielding Gas (L/min)	Powder Carrier Gas (L/min)	Pre + during heat deposition (°C)	Cool down rate (substrate) till 250°C and then uncontrolled air cooling Approx. K/min	Deposition Strategy
γTiAl ODS	Ti-6Al-4V	225	1.2	8.3	5	1	0.2	3	3	1000	4	Unidirectional toolpath, staggered raster scanning, with distinct laser on/off (start and stop) at the end of each vector.
GE spec γTiAl	Ti-6Al-4V	225	1.2	8.3	5	1	0.2	3	3	1000	4	

3 beam nozzle 12mm standoff (tip distance from the workpiece).

3.4.3.5 Task 2e: Ni-WC (60%)

Information was provided of conventional manual weld repair techniques for the white cast iron material the industrial partner was given. The procedure for manual weld repairs showed that the substrate was subjected to pre-heating of 800-1000°C. The total time including the preheat, repair and post heat treatment for the conventional process is around 48 hours. There were requirements made from the industrial partner to find a suitable method of lowering the required pre-heating temperatures significantly, a suggested temperature, though without any disclosed evidence, theoretical or otherwise, was 400°C, though this was expected not to be feasible.

To find out the heating and processing requirements for the repair process, it was decided to split the issue into more distinguishable events that could be more closely monitored. The buffer layer of NiCrSiB (without WC), was deposited in trials onto the cast iron substrate as the first stage, the second stage was to deposit the NiCrSiB-WC onto the NiCrSiB.

To better understand the sequence of the cracking, cameras were used to monitor the area of interest throughout the deposit and during cool down. The knowledge of the sequencing was expected to help understand the cause of the cracking initiation, for example was the cracking occurring during deposition, immediately after, or at some point during the cool down period.

The pre-heating temperature was then increased in increments of 50°C until cracking was no longer found immediately after the deposition stopped. The next set of trials was intended to discover the required cooling regime and method by performing trials at different cooling rates, controlled by the induction coils.

Table 10 NiCrSiB-WC sample parameter development

Hardfacing material	Buffer layer material	Buffer layer deposit No.	No. Buffer layer	Hard facing sample No.	No of hardfacing layers	Laser power (W)	Spot size (mm)	Traverse speed (mm/sec)	Powder flow rate hardfacing (g/min)	Powder flow rate buffer (g/min)	Track separation (mm)	Layer height (mm)	Nozzle Shielding Gas (L/min)	Powder Carrier Gas (L/min)	Deposit area dimensions LxW (mm)	Pre + during Heat Buffer layers (°C)	Cool down rate to Approx k/min	Pre + during heat hard-facing (°C)	Cool down rate (substrate) till 250°C and then uncontrolled air cooling Approx. K/min	Deposition Strategy
NiCrSiB-WC	NiCrSiB (Metco 12C)	63	2	63A	4	550	1.5	11.25	5.5	3.8	1	0.4	4	2	30x30	550	6	500	6	Unidirectional toolpath, staggered raster scanning, with distinct laser on/off (start and stop) at the end of each vector.
		64	2	64A	4	550	1.5	11.25	5.5	3.8	1	0.4	4	2	30x30	550	6	450	6	
		65	2	65A	8	550	1.5	11.25	5.5	3.8	1	0.4	4	2	30x30	550	6	550	6	
		66	2	66A	8	550	1.5	11.25	5.5	3.8	1	0.4	4	2	30x30	550	6	650	6	
		67	2	67A	8	550	1.5	11.25	5.5	3.8	1	0.4	4	2	30x30	550	6	600	6	
		68	2	68A	8	550	1.5	11.25	5.5	3.8	1	0.4	4	2	30x30	550	6	600	6	
		69	2	69A	8	550	1.5	11.25	5.5	3.8	1	0.4	4	2	30x30	550	6	550	6	
		70	2	70A	8	550	1.5	11.25	5.5	3.8	1	0.4	4	2	30x30	550	6	650	6	
		71	2	71A	8	550	1.5	11.25	5.5	3.8	1	0.4	4	2	30x30	550	6	600	6	
		72	2	72A	8	550	1.5	11.25	5.5	3.8	1	0.4	4	2	30x30	550	6	640	6	
		73	2	73A	8	550	1.5	11.25	5.5	3.8	1	0.4	4	2	30x30	550	6	650	6	
		74	2	74A	8	550	1.5	11.25	5.5	3.8	1	0.4	4	2	30x30	550	6	650	6	

3 jet nozzle with a 12mm standoff (tip distance from the workpiece).

Table 11 NiCrSiB-WC larger area demonstration parameter development.

Hardfacing material	Buffer layer material	layer deposit No.	No. layers	Laser power (W)	Spot size (mm)	Traverse speed (mm/sec)	Powder flow rate (g/min)	Powder flow rate (%RPM)	Track separation (mm)	Layer height (mm)	Nozzle Shielding Gas (L/min)	Powder Carrier Gas (L/min)	Deposit area dimensions LxW (mm)	Pre + during Heat Buffer layers (°C)	Cool down rate to Approx k/min	Approx. cool down time to 250°C (then air cooled)
NiCrSiB-WC (60%)	NiCrSiB (Metco 12C)	76	2	550	1.5	11.25	3.8	6	1	0.4	4	2	100x40	600	6	1 hour
		76a	4	500	1.5	11.25	5.0	5	1	0.4	4	2	100x40	650	6	
		78	2	550	1.5	11.25	3.8	6	1	0.4	4	2	100x40	600	6	
		78a	4	400	1.5	11.25	4.9	5	1	0.4	4	2	100x40	600	6	
		79	2	550	1.5	11.25	3.8	6	1	0.4	4	2	120x60	600	6	
		79a	4	500	1.5	11.25	4.9	5	1	0.4	4	2	120x60	650	6	

3 jet nozzle with a 12mm standoff (tip distance from the workpiece).

Chapter 4

Results

4 Chapter 4 - Results

4.1 Overview

The results are presented below for the work completed in the project to date. The main results are from the following sections:

- Task 1 – Induction heating development

- Task 2 – LMD process development

    - 2a – Tribaloy T800

    - 2b – Tristelle 5183

    - 2c – LMD productivity increase;

    - 2d – γTiAl ODS

    - 2e – Ni-WC (60%).

4.2 Task 1: Induction heating development

The new twin induction coil design, shown in figure 23, provided a suitable solution for process development of the T800 alloy onto flat plate substrate. The bespoke coils (figure 23 (b)) have magnetic coatings that are designed and intended to direct the current into the flat substrate and improve heating efficiency and performance, usually coils are designed to wrap around a component to create an efficient field and heating. Additionally, being individually programmable coils provided better precision of the thermal input compared to single coil or even dual coil solutions that are fixed to apply the same amount current into the material.
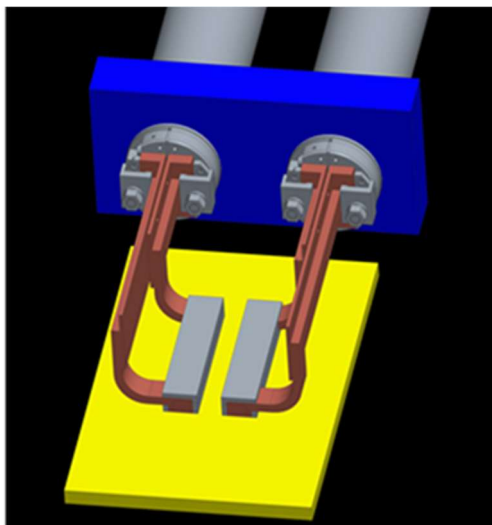
(a)

(b)

Figure 23 New induction heating coils:

a) Designs for flat plate dual induction coils

b) Image showing manufactured coils with magnetic coatings to reduce omnidirectional affect of the field and direct it down into the substrate, increasing unidirectional coil efficiency;
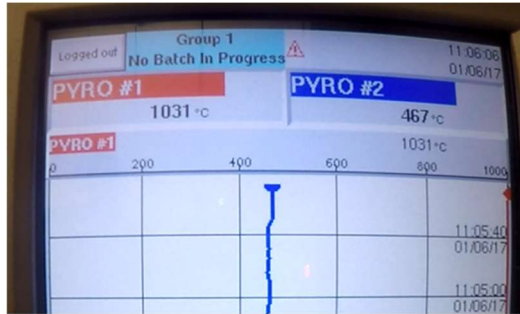
(c)
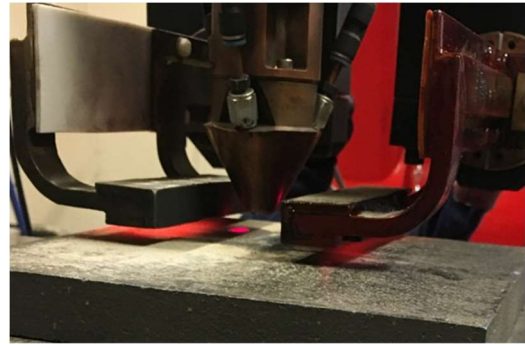
(d)

Figure 23 New induction heating coils:

c) Pyrometer controller showing temperature feedback examples of the two induction coil in a different setup to that used in the experiment, applying heat to different areas on the substrate independently and programmed to apply different temperatures, 1000°C and 450°C;

d) Coils preheating substrate prior to deposition (deposition direction goes from the left side of the image to the right side).

4.3   Task 2a: Tribaloy T800

The deposits without preheat showed significant macro cracking in multiple planes, shown in figure 24. For the undiluted T800 deposits cracking continued (identifiable on the surface visually, and by cross sectioning for greater detail regarding the depth of propagation) and only slightly reduced (in size and number of initiations) with increasing preheat temperature, until above approximately 850°C (with a controlled cool down) where the cracking reduced significantly. Samples were found to be crack free when applying preheating temperatures between 850-950°C. 850°C is a significantly high preheat to apply to most substrates and applications. Oxidation of the 316L substrates was observed in all samples produced with preheat above 800°C. There are risks associated with change of 316L material from its normal condition, such as mechanical property loss and sensitisation, where chromium carbides form along grain boundaries when subjected to 450-850°C. This substrate oxidation can be clearly seen in sample 118, shown in Appendix B, image B2. The cross sections and microstructure are shown in figure 25.
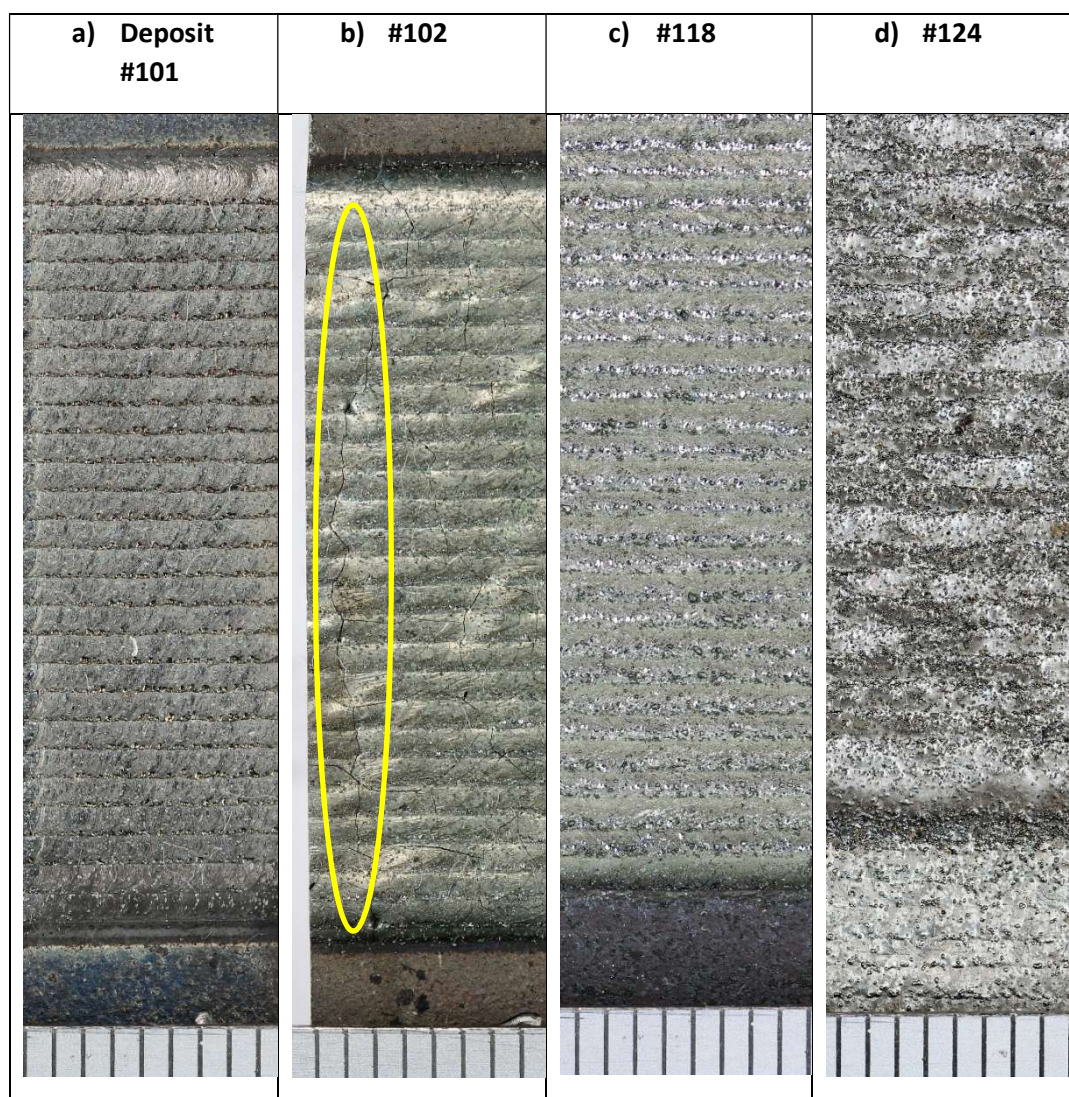
Figure 24 Coating surface views of T800 applied using different parameters.

a)   **#101** – no preheat, T800 2 layers (cracking observed in some of the cross sections)

b)   **#102** –no preheat, T800 4 layers (significant cracking on the surface & cross sections)

c)   **#118** - preheat >850°C, T800, 2 layers (no cracking observed)

d)   **#124** - preheat 550-700°C, NiCrSiB buffer 2 layers, T800 4 layers, (no cracking observed).
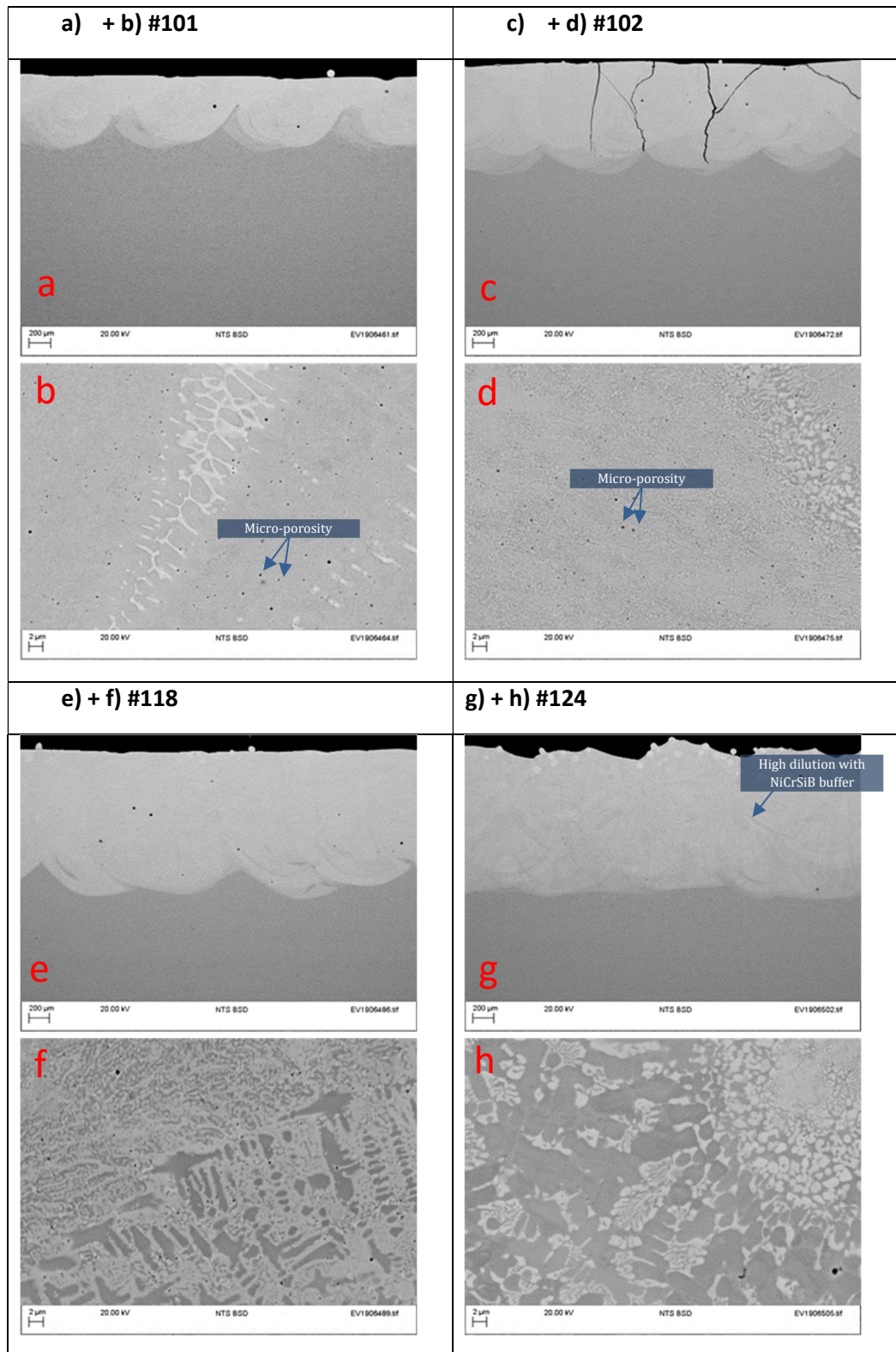
Figure 25 macro and micrographs of the T800 deposits taken in the etched condition using a Zeiss Sigma Field Emission Gun, which was also used as for EDX analysis. (b, d, f, & h, taken randomly from the etched coating)

a+b)   **#101** –   high visual dilution absent of cracking and evidence of randomly distributed micro pores (sub 1µm)

c+d)   **#102** – thicker deposit with significant cracking and evidence of micro pores (sub 1μm)

e+f)   **#118** – thicker deposit, absent of cracking and evidence of micro pores (sub 1μm)

g+h)   **#124** – thickest deposit, absent of cracking wth distinct evidence of multiple materials diluting (substrate, interface and upper coating). Less evidence of micro pores, and a mixture of microsctructures h) vs b), d), & f).

In all stainless steel 316L plates, there is a high content of ferrite (shown by visible dark strings in Figure 26), which as an austenitic stainless, could be caused by the production method of the stainless plate, including heat treatment and composition. This was identified as being the as received condition. From inspecting the full 15mm depth of substrate, there appears to be no difference worthy of note, in the microstructure before or after the application of the T800 coating. Additionally all samples appear to have a similar interface between the substrate and coating (figure 27). The time of deposition was also relatively short and so there was no major deterioration (carbides/sigma phase) of the microstructure. Longer deposition times may lead to the formation of undesirable phases or sensitisation, i.e. high ferrite content will promote sigma phase formation. Hardfacing with a buffer layer of NiCrSiB resulted in high mixing of both. The structure is much more eutectic which may suggest boron is supressing the melting point of the T800 compounds, forming fewer borides (responsible for high wear resistance of standalone NiCrSiB), hence hardness was also significantly lower.

Figure 26 relatively high Ferrite content in 316L substrate shown by visible dark strings, identified in the substrate after coating and also the untreated substrate.
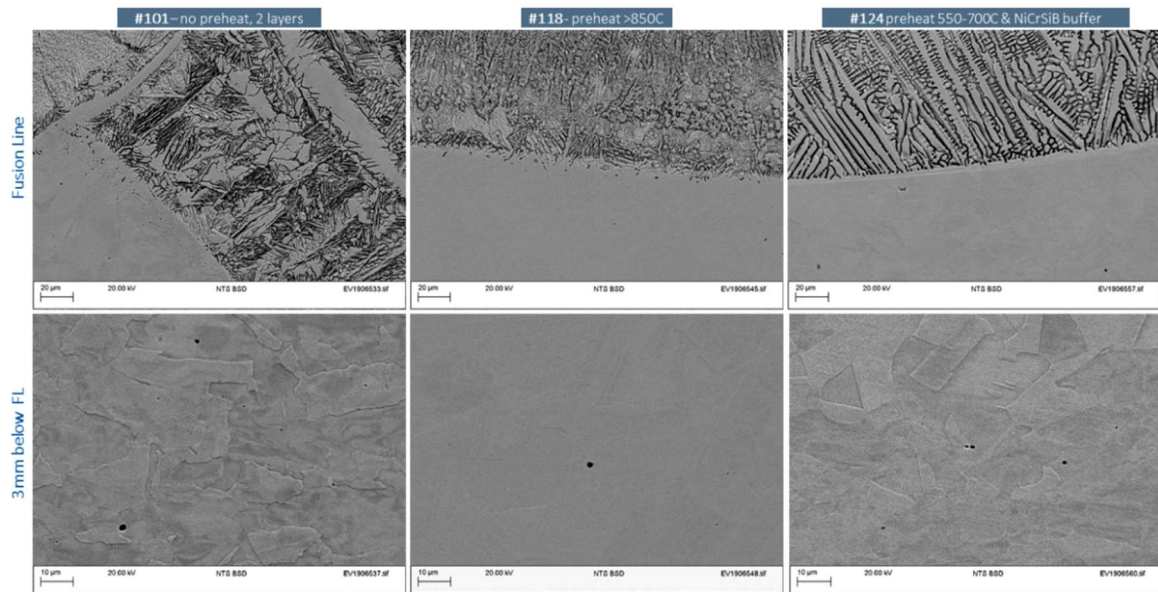
Figure 27 fusion line and substrate of samples 101, 118, and 124.

4.3.1   Hardness

From the literature, it is reported that T800 reaches peak hardness at around 14% iron dilution compared with pure T800. The peak hardness was found in sample 102, at 950Hv, which is generally in line with the results found in the iron-diluted literature (18). There is limited published data available on the material to gauge significant confidence in the results. It is clear that dilution plays a strong role on the resultant hardness. The level of dilution is extremely dependent on the processing conditions and can be difficult to predict for a new material requiring bespoke deposition parameters.

A number of different sample types were hardness tested using a line scan (figure 28). Samples 101 and 102 were produced with the same parameters and without any additional preheat. The only difference was that sample 101 had two layers and 102 had four layers. The significant difference in average hardness between the two samples is primarily down to the dilution of the substrate that is significantly present in the layers of sample 101 but is greatly reduced in the upper two layers of sample 102.

Samples 102 and 118 used the same processing conditions and number of layers; the only difference being that 118 was processed with roughly 850°C preheat and sample 102 was processed without any additional heating, other than from the laser. Sample 118, when compared to sample 102, had a lower hardness value of 750Hv mean and 850Hv peak.

Coating hardness varied across the deposits and the region between 'pure' coating alloy and diluted material is not clearly defined. Some of the deposits showed visual and other signs of significant dilution. Therefore, the minimum hardness of the coatings noted below, also takes into account this diluted region, yet still within the coating rather than the base material:

Sample No:

- 101: 385-625Hv

- 102: 560-950Hv

- 114: 370-920Hv

- 118: 510-855Hv

- 119: 430-690Hv

- 120: 225-375Hv

- 121: 225-310Hv

- 122: 325-515Hv

- 123: 230-510Hv

- 124: 340-550Hv
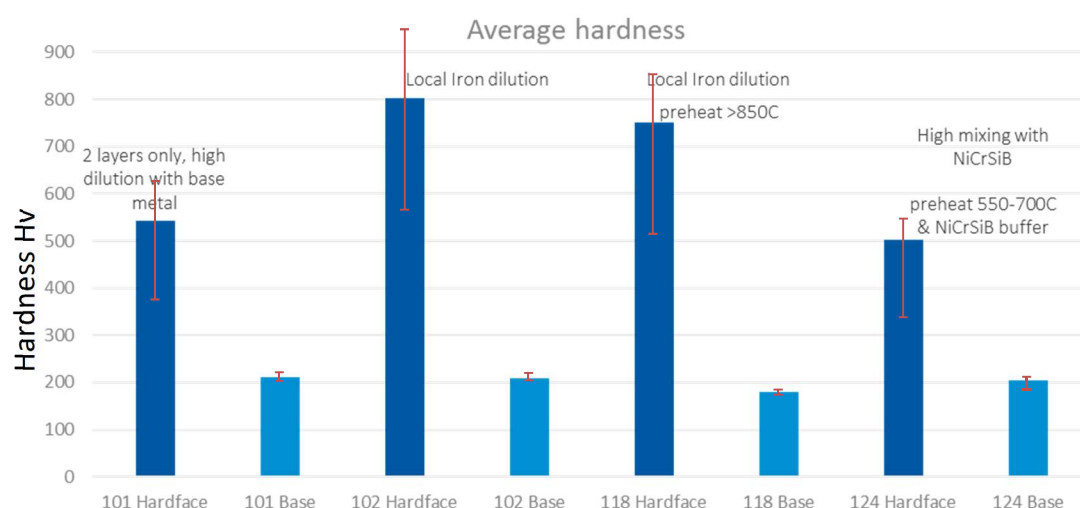
Figure 28 average hardness of T800 deposits. With approximate intention of 10 indents taken in the coating and 10 in the base for each of the two line scans recorded for each deposit. Lines are taken in a 0.2mm zig-zag spacing with overall coating height spacing between indents of 0.12mm. Lines scans taken 5mm from the edge of each sample at 1kg load and 10s dwell and starting approximately 0.1mm from the coating surface.

4.3.2   Chemical Composition EDX

The iron content increased in regions approaching the substrate in all samples. This is due to dilution between the deposited layers and substrate. It can also be observed in the measurement of samples that used the NiCrSiB buffer layer (samples 123 and 124). Here samples had a much higher nickel content throughout the depth of the coated layers. The chemical results (shown in figure 29 & 30) indicate that the dilution in these samples was extreme and not optimised for reaching the pure coating composition at the upper surface of the material. This extreme dilution was likely caused by the high pre-heat temperatures combined with the laser heat input. Full chemical analysis data points can be found in Appendix B, table B1.

Sample 118 showed slightly higher dilution of the substrate alloy compared with sample 102. Sample 118 was processed at 850°C preheat and 102 with zero preheat.
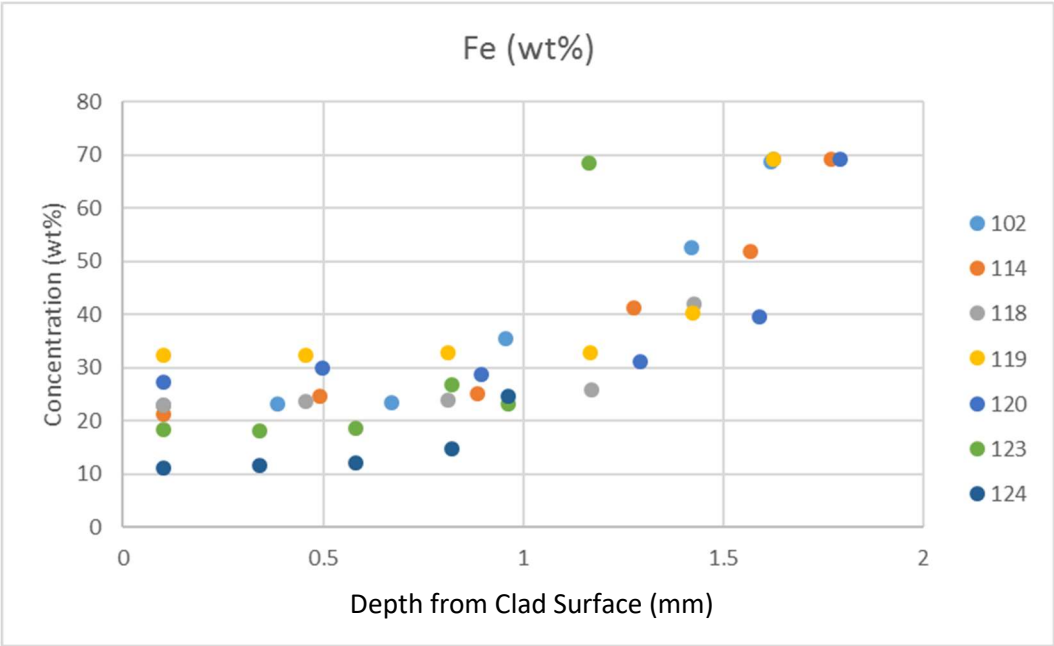
Figure 29 Energy dispersive X-ray spectroscopy (EDS) chemical analysis of iron content across depth of the deposited T800 and interface.
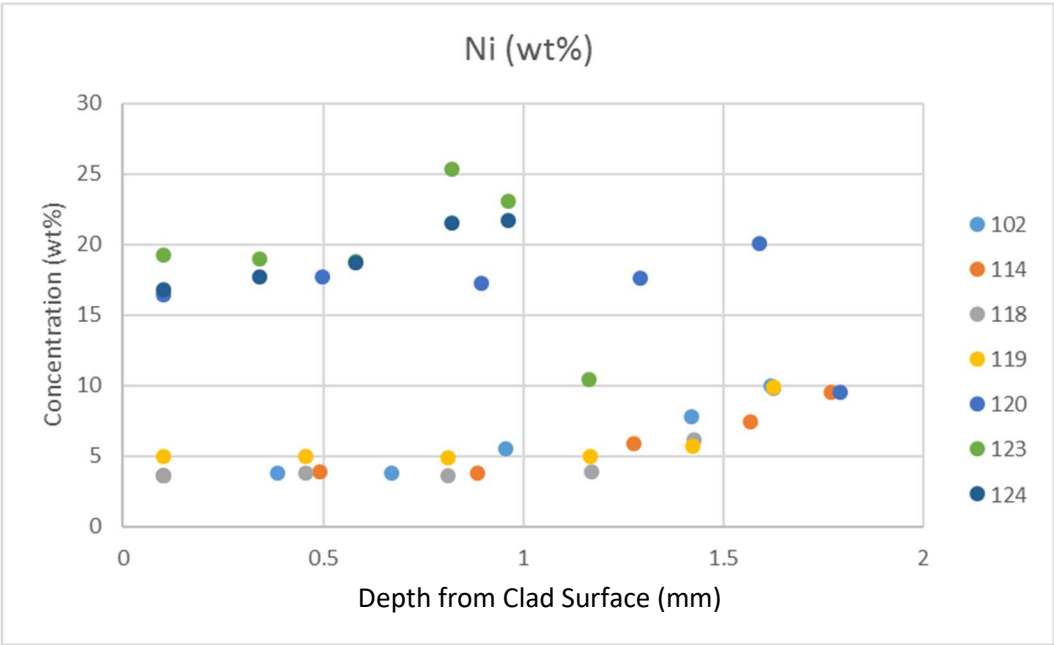
Figure 30 EDS Chemical analysis of nickel content across depth of the deposited T800 and interface.

4.4 Task 2b: Tristelle 5183

Parameters were developed for the iron based hardfacing alloy Tristelle 5183. Crack free deposits were achieved using preheating at 150°C and higher (figure 31). The deposits were defect free with high density and a sound bond to the substrate. Only small pores, generally less than 5μm and none larger than 50μm were found in cross sections when explored by light microscopy.
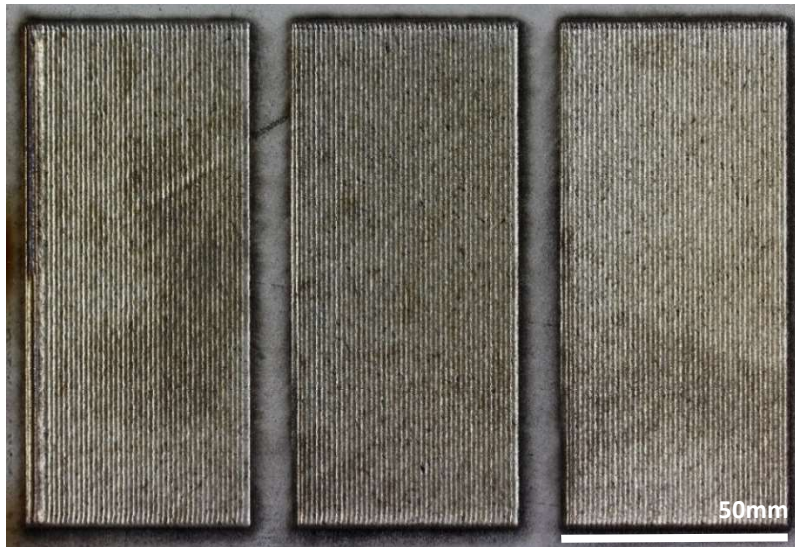
Figure 31 Tristelle 5183 crack free deposits.

LMD Tristelle 5183 samples were tested against Stellite 6 laser deposited samples using ASTM G65 dry sand abrasion testing (66). The results (figure 32) showed a decrease in the amount of material wear for Tristelle 5183 against Stellite 6. Sample wear uniformity on all tests were good and can be seen in Appendix B, image B17.
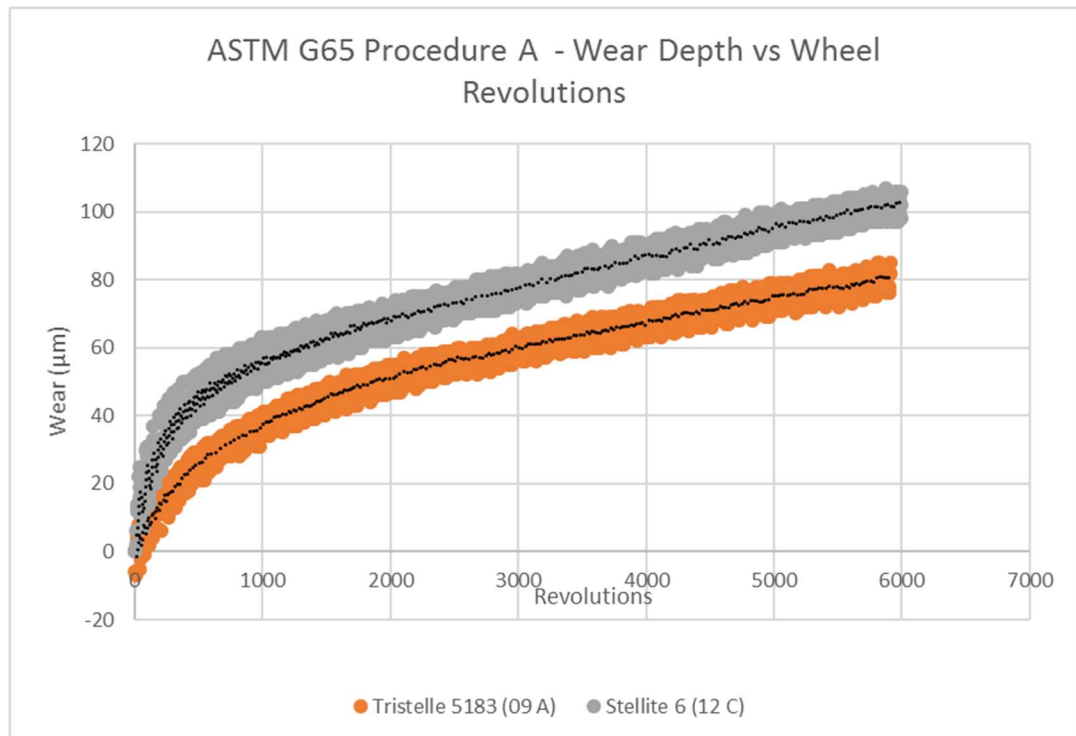
Figure 32 G65 dry sand abrasion test results comparing LMD Tristelle 5183 and Stellite 6. The black dotted line is the average of two tests per material.

4.5 Task 2c: LMD Productivity Increase

The results of the productivity task are provided in two sections. The robotic LMD system was a relatively new installation at the start of the project. Therefore, the first part of the task was completed by mapping out the laser spot size capability of the current equipment. Secondly, methods were trialled for increasing the laser beam size as a method of increasing deposition rate.

4.5.1 Equipment capability mapping

The beam mapping exercise (figure 33) revealed that with the standard fibre cable and optical arrangement, the maximum achievable beam spot diameter was less than 2mm (using 200W laser power).
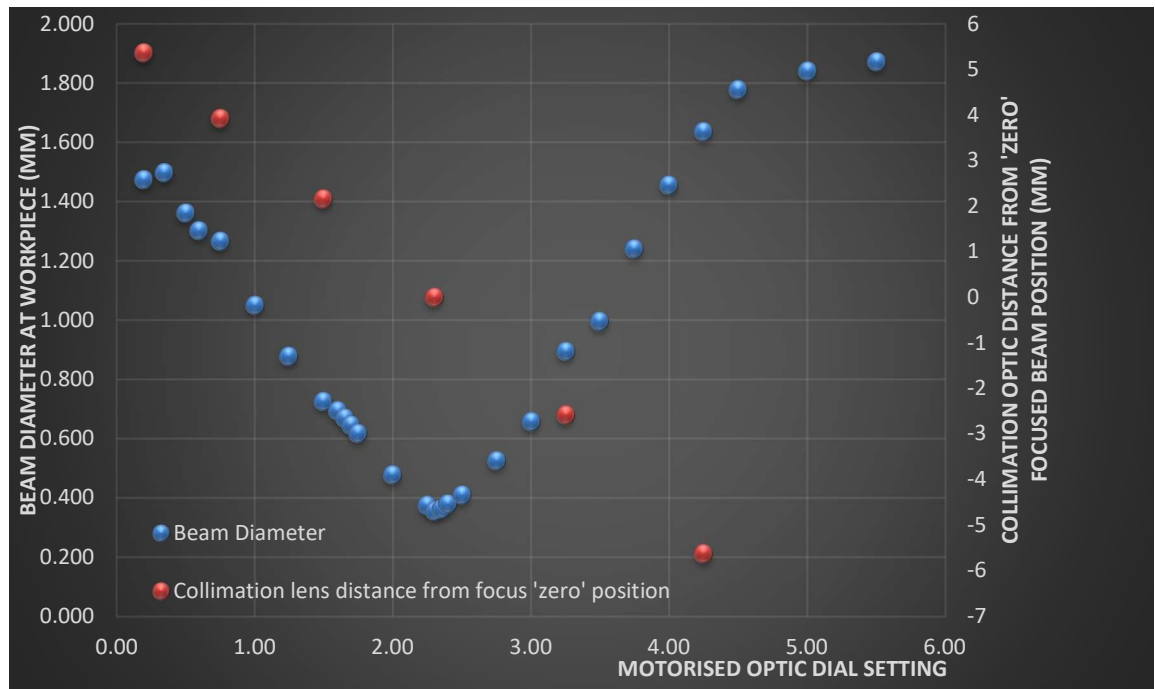
Figure 33 beam profile mapping results with Trumpf 8002 laser and D70 motorised optics.

Secondary tests using beam marking on anodised aluminium (figure 34a) and LMD deposited tracks (figure 34b) emphasised the beam size limitations of the equipment. The results from this task led to the approach taken in the second part of Task 2c.
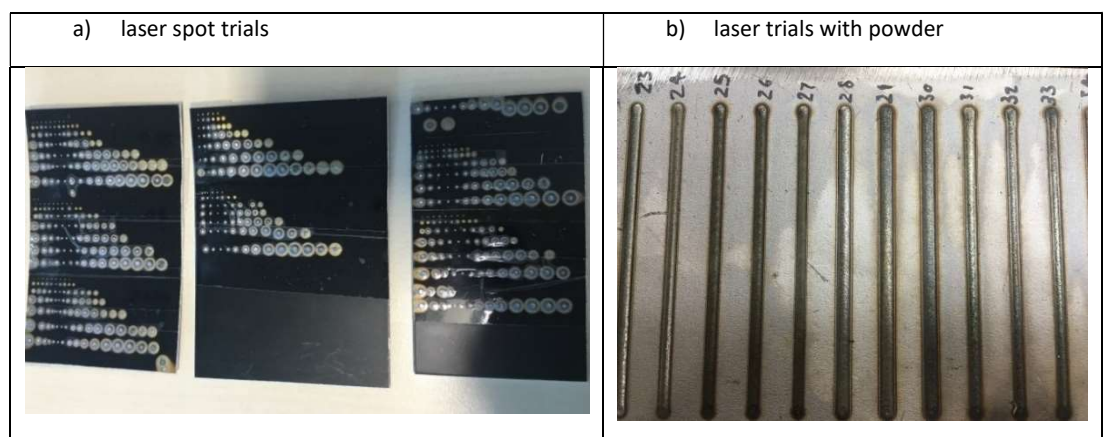
Figure 34 Laser spot size tests

a) Laser spot size variations with motorised optic adjustment;

b) Laser spot size trials with powder.

4.5.2   Laser defocus approach with powder nozzle extension

When investigating the response and defocusing the laser beam by moving the processing optics further away from the standard 12mm standoff, a standard coaxial or three beam nozzle arrangement would not provide efficient focusing of the powder.

Using a side feed nozzle resulted in a dramatic increase to the dilution between the powder and substrate (more than 70% dilution) through the excessive melting and almost keyholing effect of the substrate. Essentially less laser energy was absorbed by the inflight powder particles compared with energy absorbed by powder using a coaxial feed nozzle. It is expected that the powder fed from a coaxial nozzle process absorbs approximately 20% of the laser energy (8). The side feed nozzle was also inefficient with a poorly focused delivery of powder, resulting in a low yield (below 60%) capture efficiency, whereas a coaxial nozzle is usually 70-95% efficient.

The development of a nozzle extension unit (figure 35a) resulted in a cost effective method to defocus the laser beam, creating a larger laser spot while maintaining the correct standoff distance for optimal focus of the powder through the coaxial nozzle. It was not possible to measure the beam diameter at the new focus position on the substrate, primarily due to limitations with the standard beam profiling equipment available. Therefore, practical deposition trials were carried out with some promising results of the resultant deposit track widths (generally track widths are around 20-40% wider than the laser spot size). Laser power was capped at a safe 1800W (reducing the risk of damage to the nozzle) and produced deposit track widths of approximately 4mm (up from 2.4mm track widths as standard). With a different coaxial nozzle, designed for high laser powers, including better cooling, the next step would be to perform further trials to fully explore the new capabilities and find the limitations with the defocused laser and nozzle extension.

a) Nozzle extension (+40 mm)	b) Initial trials with nozzle extender, 4mm track width	c) Track without nozzle extender, 1.5mm track width.
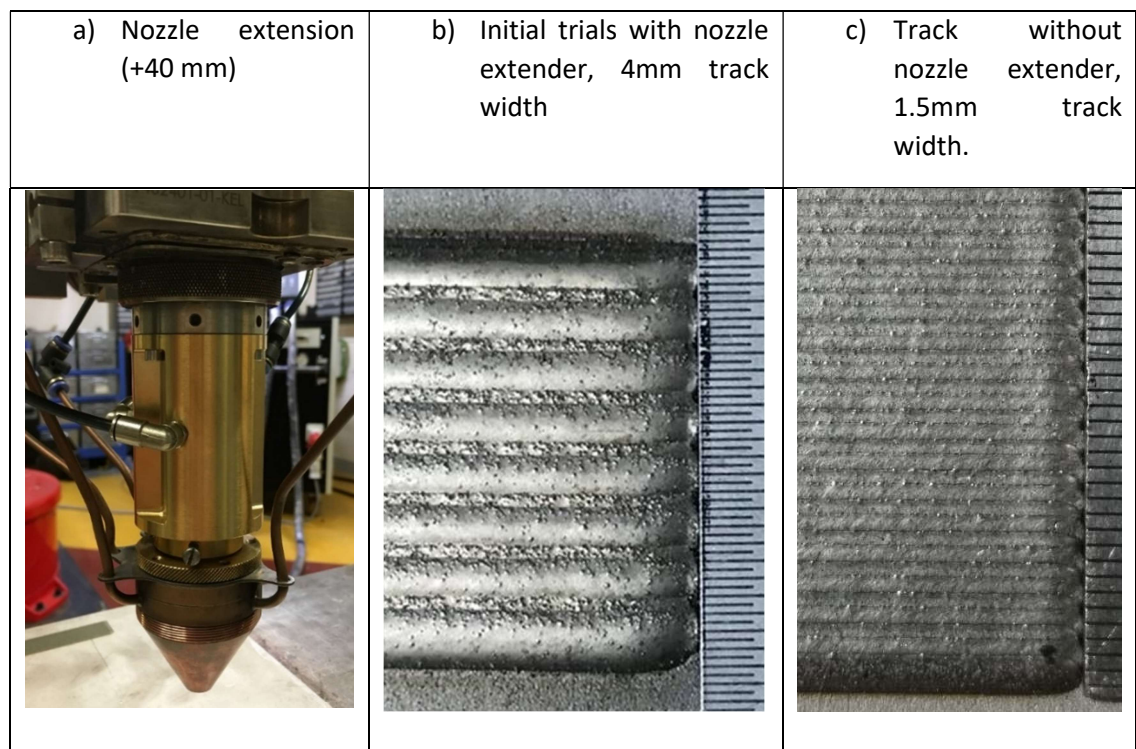
Figure 35 Developed nozzle extension and initial deposit results:

a) Nozzle extension unit;

b) Deposition tracks with nozzle extender causing laser defocus;

c) Deposition tracks without nozzle extender.

4.6 Task 2d: γTiAl ODS

The TiAl ODS material has applications as a high temperature capable coating for lower grade blades. It was not possible to acquire any TiAl substrate or blade material for the project. Therefore, basic Ti-6Al-4V blades were produced (figure 36) using powder bed fusion as a method of producing representative blades that will be coated in the project, (unfortunately coatings were not produced directly onto these blades within the project).

Task 2d Ti 64 blades produced by powder bed fusion AM to be coated with TiAl
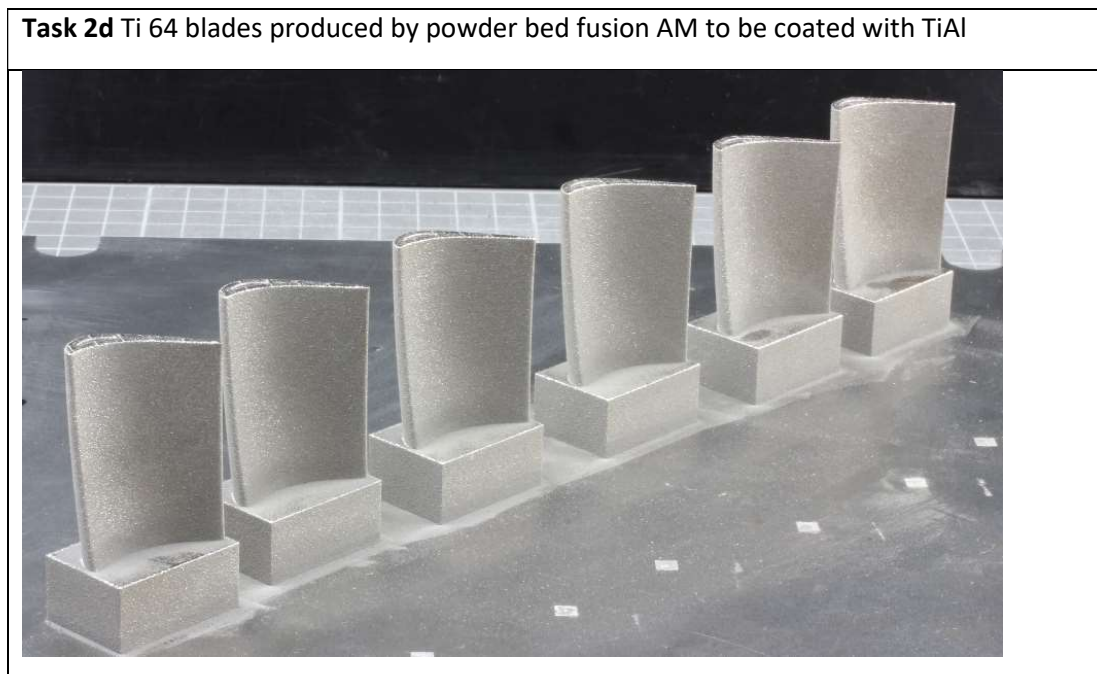
Figure 36 Ti64 representative blades produced by powder bed fusion to be coated with TiAl.

The TiAl ODS material has shown promising test results in previous testing. The initial results with the most densely consolidated material by LMD, showed a 2x improvement in oxidation resistance at 800°C and similar strength to conventional TiAl.

The deposited TiAl materials were inspected for porosity and defects by cross sectioning samples. It was clear from optical inspection that the TiAl ODS material had significant inclusions of gas-entrapped porosity in the deposits (figure 37b). The powder was tested for oxygen inclusions along with a number of other unwanted elements. The results showed an extremely high oxygen content present in the ODS variant, measuring 8788ppm. The non-ODS material contained 1516ppm O_2. The resultant quality of the samples produced by LMD suggests that the high inclusion of O_2 in the ODS powder has caused significant porosity and limited the performance potential for the consolidated material.

a) Ti-48Al-2Nb-2Cr At% material	b) Ti-45Al-3Nb+ 0.5Y$_2$O$_3$ At% material
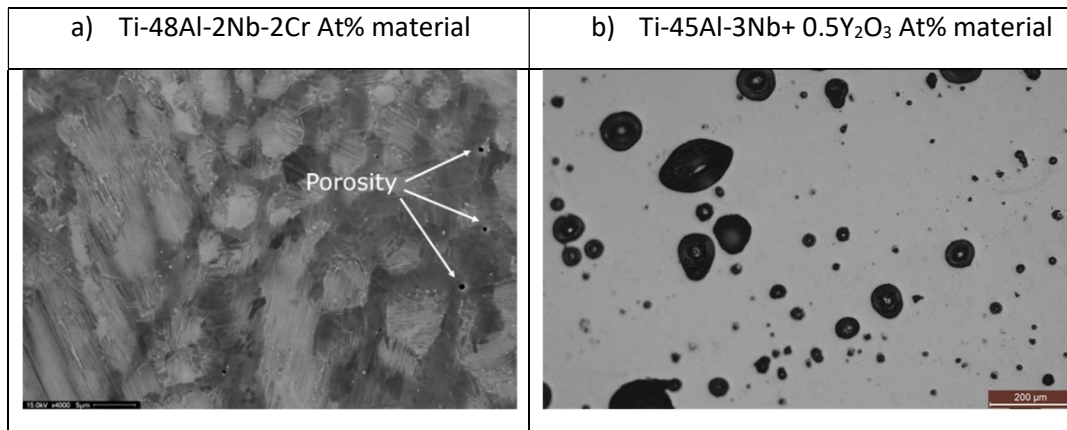
Figure 37 Cross sections of two TiAl materials deposited by LMD with independent parameters:

a) Conventional TiAl powder produced by high quality gas atomisation, with small pores (<1μm) and low concentrations;

b) Newly designed TiAl ODS powder produced by mechanical alloying, with large pores (10-200μm) in large concentrations.

4.6.1   Task 2e: Ni-WC (60%)

When deposits were made with high temperature pre-heat above 700°C, the powder (seen in the oversprayed material) went from a metallic silver to a golden colour. Another effect was that large black clumps of powder were found. Chemical analysis of the powder showed significant oxidation on the surface of the golden powder. Additionally the consolidated LMD material was significantly oxidised on the surface when exposed to excessive preheat above 700°C.

It was identified that the brittle white cast iron substrate was cracking when melted via the laser without adding any powder into the melt pool. This finding reinforced the understanding that the substrate required additional processes such as preheat to achieve a crack free result. This result also suggested that there was need for an intermediary 'buffer' material, between the substrate and WC repair material, the buffer material should be more compatible with the substrate than the direct application of the WC material. However, from the literature and available information the requirements for the peak input temperatures and the cooling rates were still unknown.

No macro crack free results were found for the deposits of the Ni-WC directly onto the substrate with preheating temperatures trialled up to around 900°C for samples of 30x30mm. During the trials, it was found that cracking was occurring in the substrate material at the corners of the interface between the buffer layer and the substrate, propagating down into the substrate in the Z direction (depth) and away from the deposit in the X and Y. The cracks were occurring in the same relative locations each time, at different heating temperatures, mainly at the final corner of the deposition sequence. The results of this were backed up by modelling of the deposition process (results not included in this report).

At lower preheat temperatures (such as 300-400°C), cracking was observed at the end of the deposit within the substrate immediately after the deposition, this was observed using a standard camera. It was also observed that with minimal preheat there was no observed surface macro cracking of the NiCrSiB buffer layers. At 550°C, there was a delay of 10 seconds after the laser switched off, before the initiation of the cracks. This indicated that the peak preheating temperature was sufficiently met and that cracking initiated because the cooling rate was not sufficiently controlled.

Chapter 5

Discussion

5 Discussion

5.1 Task 2a: Tribaloy T800

Laser metal deposition of Tribaloy T800 is very challenging due to the extremely brittle nature of the material, which was observed during the experiments and published by numerous sources (18, 19, 21, 27 and 67). This can occur as a result of thermal stresses that develop in the material due to the rapid heating and cooling that occurs during laser metal deposition. These stresses can cause the material to fracture, leading to cracks and other defects in the deposited layer. Materials like Tribaloy T800 tend to have poor ductility, which means that they do not stretch or deform easily under stress. This can make it difficult to achieve a uniform and crack-free deposit, particularly in areas of the part where there are high levels of stress or strain. However, by carefully controlling the deposition parameters, such as the laser power, scanning speed, and deposition temperature, it may be possible to minimize these issues and achieve high-quality deposits.

The limited published literature on LMD of T800 considers only the application of very small samples of deposited material and provides limited consideration to upscale issues associated with the overall processability of the material. Depositing small samples results in a smaller amount of residual stress, as well as, results in a unrepresentative heat input/thermal history that comes from the concentrated laser source, which can be argued does not represent the true behaviour of the material when applied to larger components (unless additional heating control is performed such as via additional heat sources, to account for the change). In this project, the size of the deposited area is expanded beyond that published by others (18, 19, 27), depositing areas of 150x50 mm, which is rarely considered large enough for full-scale components (which can require several square metres of deposit), but is more representative of industrial scale deposits. Meaning that the material response of this research should be much more realistic of what would be observed in component production.

Crack free deposits were produced using preheat temperatures of 850°C or higher with a controlled cool down (6°C/min for one hour until 250°C and then uncontrolled until room temperature). Sample numbers 123 and 124, produced with a NiCrSiB buffer layer, had significantly reduced hardness in the upper T800 layers (approximately 500Hv vs up to 1000Hv theoretical hardness (18, 27)) due to an observed high dilution with the buffer alloy, which can be witnessed in the macrographs of the deposits (figure 25), showing signs of excessive heat input due to the profiles of the interface of the beads/tracks, and is confirmed via the chemical analysis results.

Samples 102 and 118 used the same processing conditions and number of layers, the only difference was that 118 was processed with approximately 850°C preheat and sample 102 was processed without any additional heating besides the laser, i.e. zero intended preheat. Sample 118 did not have as high hardness values as sample 102. The chemical analysis results showed that sample 118 had higher dilution, caused by the increased heat input with the induction heating; additionally the molten deposit is expected to have solidified slower causing larger grain growth, although not directly measured this result can be seen in the side by side micrographs (Figure B6 and B7 in the appendix) which are the expected reasons for the reduction in hardness. The significance and impact of each effect has not been measured independently.

Copyright © TWI Ltd 2023

Comparing samples with and without a NiCrSiB inter/buffer layer, it is possible to see a number of differences. A key difference can be seen in the SEM images between 118 and 124 at the interface (figure 25). Sample 124 presents a strict boundary between the substrate and buffer layer, whereas 118 shows a segregated boundary. The microstructure of the buffer material in 124 is significantly different to the direct application of T800 and appears to be columnar dendrites. The direct application of T800 appears to produce fine cellular microstructure particularly near the interface leading up to fine dendrites further into the deposited material. This is in line with findings from Navas 2006 and Tobar 2008 (18, 27).

The microstructure of a material plays a critical role in determining its mechanical, physical, and chemical properties. Therefore, differences in microstructure can significantly impact the behaviour of a material. When it was observed that there was a significant difference in the microstructure of the buffer material in sample 124 compared to direct T800 deposition, this indicates that the buffer material is having a significant impact on the behaviour of the material. One possible reason for this difference in microstructure is that the NiCrSiB interlayer is promoting nucleation of the Tribaloy T800 material. The interlayer material may provide a suitable surface for nucleation of the T800 material, leading to a different microstructure compared to direct deposition. Alternatively, the interlayer material may provide a different thermal history during deposition, which can affect the microstructure of the T800 material. Understanding the impact of the buffer material on the microstructure of the Tribaloy T800 material can help to optimize the deposition process and improve the mechanical and physical properties of the deposited material. It can also provide insight into the fundamental mechanisms that govern the behaviour of the material, which can be useful for designing new materials and processes.

316L stainless steel is not generally regarded as the most relevant substrate for the application of Tribaloy T800. The 316L service temperature (to avoid sensitisation and sigma phase formation) is below 450°C; also the mechanical properties of 316L at temperatures of 450°C or above, are poor, e.g. creep at high temperatures. IN625 or 21-4N have been identified as a more applicable substrate material for T800 (compared with the 316L or NiCrSiB buffer materials). Alternatively IN625 or Ni-Cr alloy (e.g. filler 82) could be tested as a buffer material for 316L, to reduce the impacts of preheat, or explore lower preheat temperature requirements, i.e. below 450°C, or preheating above 450°C for short durations (less than a few hours to reduce the impact of sensitisation and other heat related effects). It is expected that if changes are made to the substrate materials then different parameters will be required for an optimal condition of crack-free deposition with minimal dilution of the T800 in the coating surface, primarily due to the difference in thermal expansion of the materials. For T800 and 21-4N substrate, IN625 or Ni-Cr could be applied as a buffer layer to mitigate cracking issues due to thermal mismatches. IN625, also known as Inconel 625, is a nickel-chromium-based superalloy that has excellent high-temperature strength and corrosion resistance. It also has good fatigue resistance, making it well-suited for use in aerospace and gas turbine applications. Its high melting point and thermal stability make it a suitable substrate for deposition of high-temperature coatings like Tribaloy T800. Additionally, the composition of IN625 is similar to Tribaloy T800, which means they have good compatibility when deposited on top of each other, resulting in a strong bond. 21-4N is a precipitation-hardening stainless steel that is often used in aerospace and petrochemical applications due to its high strength and corrosion resistance. It is also known for its excellent weldability and machinability. The precipitation-hardening process gives 21-

4N a combination of high strength and ductility, which makes it a good choice for coating with brittle materials like Tribaloy T800. The high strength of 21-4N also means that it can withstand the stresses and strains that can occur during the coating process. On the other hand, 316L is a commonly used stainless steel with good corrosion resistance and low carbon content, making it suitable for use in applications where welding type processes are required. However, its lower strength and inferior high-temperature performance compared to IN625 and 21-4N make it less suitable for use as a substrate for high-temperature applications and associated coatings like Tribaloy T800.

Another option for further development would be to change T800 to T400C or Stellite™ 12, which are somewhat more weldable/ processable alloys, but are generally less capable at resisting wear in such extreme environments.

5.2 Task 2b: Tristelle 5183

Crack free deposition of Tristelle 5183 was much less challenging than the Tribaloy T800 alloy. The material has relatively good toughness as indicated by its weldability. The hardness, dry abrasion and low temperature galling resistance of Tristelle 5183 are all promising traits of the alloy as a potential replacement for cobalt based Stellite 6, shown in the literature (17, 32). The dry abrasion results were presented in this report and at room temperature performed better than Stellite 6. There are questions from industry (12, 17) over the more suitable performance indicator of elevated temperature (350°C) galling performance in a wet environment, compared with Stellite 6. Another alternative alloy, potentially Norem 02 and Tribaloy T700, amongst others could be selected for a more rounded set of comparative trials (28, 32). Ultimately Tristelle 5183 requires further investigation aligned to industrial requirements, however it remains a contender as a replacement for Stellite 6 such as in environments which need similar performance characteristics but without the inclusions of cobalt, like the nuclear industry.

Dry abrasion resistance is a measure of a material's ability to withstand wear and damage caused by mechanical abrasion without the presence of a lubricating fluid. This property is important in applications where the material will be subjected to repeated contact with other surfaces, such as in machinery components or cutting tools. On the other hand, elevated temperature galling performance refers to a material's ability to resist damage caused by metal-to-metal contact at high temperatures, which can lead to seizure, scoring, or other types of damage. This property is critical in applications where components will be subjected to high temperatures and high pressures, such as in valves, pumps, and compressors. The fact that Tristelle 5183 shows promising results in dry abrasion tests at room temperature indicates that it could be a suitable replacement for Stellite 6 in applications that require good wear resistance but do not involve high temperatures. However, undisclosed industry experts have raised questions about its performance in elevated temperature galling, which suggests that more research and testing may be needed to determine its suitability for such applications. Overall, understanding the different properties and performance requirements for different applications is essential when selecting a material like Tristelle 5183, and it is important to consider the specific needs and conditions of each application in order to make an informed decision.

5.3 Task 2c: LMD Productivity Improvement

The productivity increase generated from the LMD trials were successful by increasing the deposition rate from 300g/hr to at least 500g/hr, with potential to go much higher (multiple

kg/hr expected) with further trials utilising up to 5.3kW of available laser power (up from the 1.8kW used as the benchmark starting point). Deposition rates in LMD can reach tens of kg/hr with the latest industrial lasers reaching 50kW and 35kg/hr (68). However, it may be difficult to process all materials at such higher rates, such as materials that are crack susceptible. Additionally, processing at such high rates will also increase heat input and may not be suitable for all substrates and application components.

To increase productivity further with the 5.3kW laser it was observed that additional equipment would be needed in order to manage the risks to equipment and safety. Having access to a beam profiler would aid these tests, allowing for proper characterisation and measurement of the beam at each setting. Increasing deposition rate can lead to a trade-off for a number of the LMD characteristics, including increased grain growth, higher defect rates and porosity inclusion, lower powder capture efficiency, and increased residual stress (69).

If a deposited material has a lower density and/or larger grain growth, it is expected that these traits will cause a detrimental effect to material properties and performance. Therefore, higher deposition rate developments should always be tested and compared with the optimal performance of materials found at more conservative deposition rates. With further development and demonstrated validation, simulation models may be accurate enough to advise without practical trails. However, it's important to note that simulation models must be validated with practical trials before they can be relied upon to guide decision-making in industrial applications. In industrial applications, the best production method will be dictated by a combination of economics, availability, and performance. Therefore sometimes it is impractical for the SOTA deposition rate systems that are mostly available within research labs, to be utilised (68).

5.4   Task 2d: γTiAl ODS

The promising test results from the previous work done in the OXIGEN project on the TiAl ODS material indicates that there is potential for the material to be deposited by the LMD process and achieve favourable properties for industry. The technical challenges of processing the extremely difficult material have been partially resolved and presented by Kenel C 2017 through complex development of the LMD process, coupling induction heating and a high purity argon shielding environment (35, 45, 46). It appears that the technical challenges when processing the TiAl ODS material were a cause of a combination of: the materials sensitivity to powder oxidation and it's the need for a high purity powder, the sensitivity of the shielding environment during the deposition process, and difficulties of high-temperature thermal management through preheating and controlled cooling.

Production of the ODS powder was done using a high-energy mechanical alloying technology, which has a number of process steps that can introduce oxygen into the material. The relatively low density of the consolidated material, supported by the powder testing results, indicates key issues with the quality of the powder, in particular the excessive oxygen content. To maximise the performance of the ODS variant, a higher quality powder needs to be produced and tested. A higher quality powder with lower traces of oxygen and nitrogen can be expected to result in a higher density of the final consolidated LMD material, therefore leading to better performance of the material especially in terms of strength, and creep resistance than reported by Kenel (35, 45, 46).

The representative Ti64 blades were not coated due to the deposit quality issues found during the process development trials. The significant quality issues of the deposit, including large pores, meant the demonstration activity was not completed and more development work (on generating new feedstock or process) would be required. New powder could be developed with lower oxidation, using purer methods such as better shielding to oxygen exposure from the production steps.

5.4.1 Task 2e: Ni-WC (60%)

The volume fraction of retained WC within the metal matrix was found to be relatively low, only around 16-20% as taken from EDX results (not shown due to confidentiality). Further process optimisation might allow the improvement the fraction of retained WC. However the challenges associated with WC deposition includes decarburisation of the particles into the matrix causes hardening of the matrix, reducing ductility, as reported by many (70, 71).

Decarburisation is not an acceptable effect for passing material specification for industrial application (for example in the mining industry). The reason for the low volume fraction and the decarburisation is expected to be caused due a number of process restrictions and challenges. The limited deposited layer thickness, due to the cracking susceptibility of the material, combined with large powder particles of WC (50μm to 150μm). An option for investigation could be to use smaller but much more numerous powder particles. Another option is to use pre-coated particles of WC, i.e. WC wrapped in protective matrix alloy. This can potentially lead to less heat input into the carbides and thus less decarburisation. Another approach could be to introduce the WC laterally, via a separate nozzle/ inject, therefore giving opportunity to reduce the laser energy input into the WC while maintaining sufficient melting for the matrix. There were no papers found which include the exact application, substrate, buffer layer, and deposit makeup. However, TiC can also be an alternative carbide which does not include the same challenges associated with decarburisation, and although has a lower hardness, may be applicable for exploration. (72)

The next set of trials which were not completed, were intended to discover the required cooling regime and method. The most promising selected method was to utilise the induction heating coils to apply a controlled thermal cooling. A relatively linear cooling approach was used from the peak temperature down to 250°C.

600°C preheat was used for the Ni-WC (60%) powder for the small samples of 30x30mm. When the deposits dimensions were increased to demonstration size of 120x60mm, the preheat was increased to 650°C to accommodate the increase in process induced stresses and the challenge of holding the required temperature over a larger area.

Chapter 6

Conclusions

6   Conclusions

The findings of the research are important for supporting the practicalities and approaches to resolving deposition of crack susceptible materials by LMD.

It was possible to increase the deposition rate of a standard powder fed laser metal deposition (LMD) machine, by increasing the laser spot size of a high quality, multi kW laser, by defocusing the beam in combination with effectively focusing the powder into the melt pool. The laser spot size was increased from 1.5mm to approximately 4mm and the deposition rate was increased (by 200%) to over 0.5kg/hr with evidence of opportunity to increase much higher with further equipment/setup revisions.

Combining induction heating with LMD provided additional thermal control and modulation compared to only LMD, which aided in generating crack free deposits of crack susceptible materials such as Tribaloy T800 which could not be created by LMD only.

Many different materials have been considered in this project, each with different characteristics, performance benefits and especially, behaviours while depositing by LMD. Commonly, one of the most critical and challenging aspects for depositing each material with some success and without detrimental cracking was in the selection of induction heating, or thermal control settings to an optimised state, mostly resolved by reducing the temperature differences in the substrate and molten pool, as well as by slowing down the cooling times post solidification.

Tribaloy T800 is an extremely challenging material to deposit by LMD without cracks forming. The inclusion of nickel to T800, resembling closer to T900, enhanced processability by creating a tougher material, but reduced the peak hardness to around 550Hv from a potential of >900Hv. T800 was deposited with 600-650W laser power, 1.5mm spot size, 11.25mm/sec traverse speed, and 6%RPM powder feed rate. Preheating above 850°C generated crack free results by direct application, and using interfacial layers aided in reducing detrimental impact the substrate and preheating temperatures.

Room temperature dry sand abrasion resistance of Tristelle 5183 deposited by LMD was measured to be at least on par with Stellite 6 deposited by LMD. The operating window for depositing Tristelle 5183 was found to be much wider than that of T800. Tristelle 5183 was deposited with 600W laser power, 1.2mm spot size, 11.25mm/min traverse speed, 6%RPM powder feed rate, and also an enhanced deposition rate by increasing the laser power to 1800W, approx. 4mm spot size, 11.25mm/min traverse speed, and 48%RPM powder feed rate.

Contamination by excessive oxidisation on the γTiAl ODS powder caused detrimental effects during the LMD process which impacted negatively the achievable density in the consolidated LMD material. To access the maximum potential of the newly designed γTiAl ODS material, a higher quality of feedstock powder would be required.

Overall it was shown that LMD is a capable process for depositing crack susceptible materials which are intended as high performance corrosion and wear protection coatings. Industry could use the results to gain confidence in adoption of induction-assisted LMD as a good solution for deposition high-performance crack susceptible materials. It can also be deduced that other heating – assisted methods (i.e. resistance, furnace, flame, laser, infrared) may be applicable to support LMD processing of crack susceptible alloys.

Chapter 7

Recommendations and Future Work

7 Recommendations and Future Work

7.1 Project recommendations

The following task recommendations are:

- The remainder of Task 2a and the associated demonstrator in Task 4 are completed with consideration to a high temperature demonstrator such as an IN625 component /substrate.

- Task 2b should be completed by comparing the Tristelle 5183 material with Norem 02 or other competing cobalt free alloy.

- Task 2c should be completed with the remaining planned trials of the nozzle extension. Measuring practically clipping risk of the nozzle is challenging and requires specialist beam profiling equipment. These tests were not conducted but are methods are being looked into for future work.

- Task 2d should be completed by testing the final batch of γTiAl ODS powder.

- Material performance testing should be completed in Task 3 for the developed coating materials, such as galling performance of the nuclear application using test method ASTM G196.

7.2 Future work

- Material testing and in-depth analysis of the applied coatings and deposits are required to understand more about process developments and materials. Performance testing of the final parameter developments will provide important information about the quality and characteristics of the developed processes and materials, and their potential relevance for industry. Therefore, performance testing should be relevant to the intended industrial applications.

- The Extreme High-speed Laser Application (EHLA) technology was highlighted in the state-of-the-art review as a new and emerging form of LMD technology for wear and corrosion coating applications. The technology is expected to offer a step change as a coating solution and should be investigated further for industrial application of high quality, high-speed LMD coatings. The EHLA technology creates a lower heat input and faster cooling rate for the material deposition, which is expected to provide an advantage when applying some challenging materials, and enabling new material combinations/interactions, potentially reducing or removing the need for additional thermal control such as the induction heating technology. Resource and equipment availability dependant, the EHLA technology should be trialled as a final output of this research programme for some of the promising application materials of interest.

- TWI has advanced modelling capabilities for coatings and additive manufacturing. The implementation of process modelling would benefit future projects by minimising the number of expensive physical trials for materials that are extremely challenging to process. This would benefit companies looking at feasibility and parameter development studies for new materials and applications.

- Integrating more advanced process monitoring and measurement equipment, such as meltpool measurement devices, could help in enabling greater understanding of the process, its consistency and traceability of issues and defects.

7.3 Relevant conferences, papers and dissemination contributions

Journal papers

- C. Kenel, K. Dawson, J. Barras, *'Microstructure and oxide particle stability in a novel ODS γ-TiAl alloy processed by spark plasma sintering and laser additive manufacturing'*, Intermetallics, Volume 90, 2017, Pages 63-73, ISSN 0966-9795.

- C. Kenel, J. Barras, et al, *'Mechanical performance and oxidation resistance of an ODS γ-TiAl alloy processed by spark plasma sintering and laser additive manufacturing'*, Intermetallics, Volume 91, 2017, Pages 169-180.

- R Lancaster, J Barras, et al, ADDMA_2019_1616 '*An Improved Methodology of Melt Pool Monitoring of Direct Energy Deposition Processes*'

Conference papers

- J. Barras, '*Induction assisted laser metal deposition of crack sensitive alloys.'* Materials & Engineering Research Institute Symposium 2018, Pages 6-7. Sheffield Hallam University

    - 1st place prize of Ph.D. presentation and article.

- Daniele Bassan, Josh Barras, et al *'ICME Assessment of Cladding Repair Processes',* 5th World Congress on Integrated Computational Materials Engineering (ICME 2019)

- Keynote; Josh Barras, 'Extreme High-speed Laser Application (EHLA); a step change in high speed coating technology' ILAS 2020 (May 2020).

Workshop Presentations

- J.Barras et al, *Openhybrid, 'Developing LMD and induction assisted process parameters for end use applications' September 2019, MTC* dissemination event to 100 industry and academic representatives

- *EHLA,* TWI AM symposium 2017 and 2019, to 120 industry representatives from aerospace, manufacturing, automotive and energy sectors

8   References

(1) Almeida NC, Candido LC, Faria GL, et al., 'Laser cladding and thermal spray coatings on steel pipe serving the oil and gas industry', Journal of Material Sciences & Engineering, 2169.0022 Voume 5 Issue 5, 10.4172/2169-0022.1000279. (2016)

(2) C Schmengler, A Hitzek, A Wank, 'Capability of high speed laser process with iron-based alloys', webpage resources gtv-mbh.de, https://www.gtv-mbh.de/_Resources/Persistent/a/8/e/7/a8e737951f8d6696e5d70b1b0c48c5ff16667ab8/High%20Speed%20Laser%20Cladding%20ITSC%202019.pdf accessed 20/03/2023.

(3) Zhichao Liu, Qiuhong Jiang, Fuda Ning, et al., 'Investigation of Energy Requirements and Environmental Performance for Additive Manufacturing Processes', MPDI Sustainability 10, 3606, doi:10.3390/su10103606. (2018).

(4) Staicu A R, 2012: 'Review of the Laser Cladding Technology'. (2012)

(5) Raquel Hidalgo, Jon Esnaola, Miren Larranage, Inigo Llavori, 'Influence of Surface Finish and Porosity on the Fatigue behaviour of A356 Aluminium Casting Alloy', Conference paper MATEC Web of Conferences, DOI: 10.1051/matecconf/201816514007, (2018).

(6) Vostrak M, Hruska M, Houdkova Š and Smazalova E, (2014): 'Coaxial laser cladding of Stellite: Analysis of process parameters'. New Technology Research Centre: University of West Bohema.

(7) D. Shim, 'Effect of substrate preheating by induction heater on direct energy deposition of AISI M4 powder' Elsevier, Materials Science and Engineering, 550-562, (2017)

(8) Thomas Schopphoven, Andres Gasser, Gerhard Backes, 'EHLA: Extreme High-Speed Laser Material Deposition', Laser Technik Journal Volume 14, Issue 4 p. 26-29, doi:10.1002/latj.201700020, (2017).

(9) ISO, '6158:2018 Metallic and other inorganic coatings — Electrodeposited coatings of chromium for engineering purposes', (2018-11)

(10) M. Riley, 'HVOF sprayed alternatives to hard chromium plating', TWI Members Report, (2006).

(11) J Tuominen, 'Laser cladding – applications and development trends', https://cris.tuni.fi/ws/portalfiles/portal/12505480/Esitys_Tuominen_25v_juhlaseminaari.pdf, accessed 15/10/2022. (2011).

(12) M. Dalaee, L. Gloor, C. Leinenbach, K. Wegener 'Experimental and numerical study of the influence of induction heating process on build rates Induction Heating-assisted laser Direct Metal Deposition (IH-DMD)' Elsevier, Surface & Coatings Technology, (2020).

(13) B. Song, T. Hussain, K.T. Voisey, 'Laser cladding of Ni50Cr: A parametric and dilution study', Elsevier Conference on Photonic Technologies, (2016).

(14) J.R. Davis, 'Stainless steel cladding and weld overlays', ASM International speciality handbook: Stainless steels, 06398G. (1994)

(15) Oliveira U and Oceh'k V: 'Analysis of coaxial laser cladding processing conditions'. Surface and Coatings Technology. 2005:127-36. (2005)

(16) P. A. McNutt, 'An investigation of cracking in laser metal deposited nickel superalloy CM247LC' EngD Thesis, University of Birmingham. (2015)

(17) Burdett W B: 'Development of cobalt-free wear resistant alloys for nuclear applications'. 1990:707-12. (1990)

(18) Tobar, M., Montero, C., Amado, J. M., Alvarex, C. and Yanez, A. (2006) 'Tribaloy-800 coatings on steel substrates by means of laser cladding: dilution effects on the microstructure and coating performance', ICALEO Congress Proceedings, pp. 257-261.

(19) Tobar, M., Montero, C., Amado, J. M., Alvarex, C. and Yanez, A. (2008) 'Characteristics of Tribaloy T-800 and T-900 coatings on steel substrates by laser cladding', Surface and Coatings Technology, 202(11), pp, 2297-2301.

(20) Yao, M., Wu, J., Yick, S., Xie, Y. and Lui, R. (2006) 'High temperature wear and corrosion resistance of a Laves phase strengthened Co-Mo-Cr-Si alloy', Materials Science and Engineering: A, 435, pp. 78-83.

(21) Zhang, Y.-D., Zhang, C., Lan, H., Hou, P. and Yang, Z.-G. (2011) 'Improvement of the oxidation resistance of Tribaloy T-800 alloy by the additions of yttrium and aluminium', Corrosion Science, 53(3), pp. 1035-1043.

(22) Yao M.X., Wu J.B.C. (2003) 'Ductile cobalt-based Laves phase alloys', US Patent US 7572408 B2, granted on August 11, 2009.

(23) Huang, P. K., Yeh, J. W., Shun, T. T. and Chen, S. K. (2004) 'Multi-principal-element alloys with improved oxidation and wear resistance for thermal spray coating', Advanced Engineering Materials, 6(1-2), pp. 74-78.

(24) Jones, M., Horlock, A., Shipway, P., Mcartney, D. and Wood, J. (2001) 'A comparison of the abrasive wear behaviour of HVOF sprayed titanium carbide-and titanium boride-based cermet coatings', Wear, 251(1), pp. 1009-1016.

(25) Houdkova, S., Kasperova, M,. Cesanek, Z., Schubert, J. and Plzen, C.Z. (2014) 'Wear resistant HVOF coatings for high temperature applications', Proceedings of the International Thermal Spray Conference, pp. 506-512.

(26) Kusmoko, A., Dunne, D. P. and Li, H. (2014) 'A comparative study for wear resistant of Stellite 6 coatings on nickel alloy substrate produced by laser cladding, HVOF and plasma spraying techniques'.

(27) Navas, C., Cadenas, M., Cuetos, J. and De Damborenea, J. (2006) 'Microstructure and sliding wear behaviour of Tribaloy T-800 coatings deposited by laser cladding' Wear, 260(7), pp. 838-846.

(28) Ocken H: 'The galling wear resistance of new iron-base hardfacing alloys: a comparison with established cobalt- and nickel-base alloys'. Surface and Coatings Technology. 1995:456-61. (1995)

(29) Anthony K C: 'Wear-resistant cobalt-base alloys'. 1983:52-60. (1983)

(30) Bhansali K J and Miller A E: 'The role of stacking fault energy on galling and wear behavior'. Wear. 1982:241. (1982)

(31) Laroudie F, Tassin C, Pons M and Lelait L: 'Improvement of the wear resistance of 316L stainless steel by laser surface alloying'. Surface and Coatings Technology. 1996;80(1-2):207-10. (1996)

(32) Ryan Smith J S, Gandy D and Babu S S: 'Tribolayer Formation by Strain-Induced Transformations in Hardfacing Alloys'. Advances in Materials Technology for Fossil Power Plants. 2013:482 - 90. (2013)

(33) ASTM G196-08(2016), Standard Test Method for Galling Resistance of Material Couples, ASTM International, West Conshohocken, PA, 2016, www.astm.org, DOI: 10.1520/G0196-08R16

(34) Franzén A and Karlsson J, 2010: 'γ-Titanium Aluminide Manufactured by Electron Beam Melting'.

(35) Kenel C, 2016: 'Development of Oxide Dispersion Strengthened Titanium Aluminides for Additive Manufacturing'. ETH-Zürich, 2016.

(36) Bewlay B P, Nag S, Suzuki A and Weimer M J: 'TiAl alloys in commercial aircraft engines'. Materials at High Temperatures.;33 (4-5):549-59, (2016)

(37) Hoadley A F A, Rappaz M and Zimmermann M: 'Heat-flow simulation of laser remelting with experimenting validation'. MTB. 1991;22(1):101-9. (1991)

(38) Clemens, H., Smarsly, W., Guther, V., and Mayer, S. (2015) 'Advanced intermetallic titanium aluminides', 13th World Titanium Conference Proceeding.

(39) Huang, S.-C., (1989) 'Titanium aluminium alloys modified by chromium and niobium and method of preparation' US Patent 4879092.

(40) Lipsitt, H. A., and Dimiduk. D. M., (1985) 'Titanium aluminides – an overview'. Mat Res. Soc. Symposium Proceedings. 39. pp. 351-364.

(41) Lasalmonie, A., (2006). 'Intermetallics: Why is it so difficult to introduce them in gas turbine engines?'. Intermetallics. 14(10-11), pp. 1123-1129.

(42) Kelly, T, J., Weimer, M. J., Austin, C. M., Fink, P. J., Huang, H.-C., (1997). 'Method for heat treating gamma titanium aluminide alloys'. US Patent 5634992A.

(43) Bartolotta, P., Barret, J., Kelly, T., Smashey, R., (1997) 'The use of cast Ti-48Al-2Cr-Nb in jet engines', JOM 49. 48–76.

(44) Weimer, M., Kelly, T., (2008) 'Gamma TiAl Applications at GE Aviation, in: Structural Aluminides for Elevated Temperatures'

(45) Kenel C, Dawson K and Barras J, (2017): 'Microstructure and oxide particle stability in a novel ODS γ-TiAl alloy processed by spark plasma sintering and laser additive manufacturing'. Intermetallics, Volume 90, 2017, Pages 63-73, ISSN 0966-9795.

(46) Kenel C, Lis A, Dawson K and Barras J, (2017): 'Mechanical performance and oxidation resistance of an ODS γ-TiAl alloy processed by spark plasma sintering and laser additive manufacturing'. Intermetallics, Volume 91, 2017, Pages 169-180.

(47) M. H. Loretto, D. Horspool, R. Botten, D. Hu, Y. G. Li, D. Srivastava, R. Sharman, X. Wu, Controlling the properties of some ordered Ti-based alloys, Materials Science & Engineering A 329-331 (2002) 1–6.

(48) D. Srivastava, I. T. H. Chang, M. H. Loretto, The effect of process parameters and heat treatment on the microstructure of direct laser fabricated TiAl alloy samples, Intermetallics 9 (2001) 1003–1013.

(49) D. Srivastava, D. Hu, I. T. H. Chang, M. H. Loretto, The influence of thermal processing route on the microstructure of some TiAl-based alloys, Intermetallics 7 (1999) 1107–1112.

(50) Moll, J. H. B. J. McTiernan, PM (2000) 'TiAl alloys: the sky's the limit', Metal Powder Report 55. pp.18–22.

(51) X. D. Zhang, C. Brice, D. W. Mahaffey, H. Zang, K. Schwendner, D. J. Evans, H. L. Fraser, Characterization of laser-deposited TiAl alloys, Scripta Materialia 44 (2001) 2419–2424.

(52) W. Liu, J. Dupont, Fabrication of Carbide-Particle-Reinforced Titanium Aluminide-Matrix Composites by Laser-Engineered Net Shaping, Metallurgical and Materials Transactions A 35, 1133–1140,(2004).

(53) T. Vilaro, V. Kottman-Rexerodt, M. Thomas, C. Colin, P.Bertrand, L.Thivillon, S. Abed, V. Ji, P. Aubry, P. Peyre, T. Malot, Direct fabrication of a Ti-47Al-2Cr-2Nb alloy by selective laser melting and direct metal deposition processes, Advanced Materials Research 89-91, 586–591, (2010).

(54) L. Murr, S. Gaytan, A. Ceylan, E. Martinez, J. Martinez, Characterization of titanium aluminide alloy components fabricated by additive manufacturing using electron beam melting, Acta materialia 58, 1887–1894, (2010).

(55) S. Franzen, B. Karlsson, R. Dehoff, U. Ackelid, O. Rios, C. Parish, W. Peters, Microstructural Properties of Gamma Titanium Aluminide Manufactured by Electron Beam Melting, in: The Minerals, Metals & Materials Society, volume 3, pp. 455–462, (2011)

(56) S. Biamino, A. Penna, U. Ackelid, S. Sabbadini, O. Tassa, P. Fino, M. Pavese, P. Gennaro, C. Badini, Electron beam melting of Ti–48Al–2Cr–2Nb alloy: Microstructure and mechanical properties investigation, Intermetallics 19 776–781, (2011).

(57) J. Schwerdtfeger, C. Körner, Selective electron beam melting of Ti-48Al-2Nb-2Cr: Microstructure and aluminium loss, Intermetallics, 49 29–35, (2014).

(58) S. Biamino, B. Klöden, T. Weissgärber, B. Kieback, U. Ackelid, Titanium aluminides for automotive applications processed by electron beam melting, Technical Report, (2014).

(59) G. Baudana, S. Biamino, D. Ugues, M. Lombardi, P. Fino, M. Pavese, C. Badini, Titanium aluminides for aerospace and automotive applications processed by Electron Beam Melting: Contribution of Politecnico di Torino, Metal Powder Report (2016).

(60) H. Tang, G. Yang, W. Jia, W. He, S. Lu, M. Qian, Additive manufacturing of a high niobium-containing titanium aluminide alloy by selective electron beam melting, Materials Science and Engineering: A 636 103–107, (2015).

(61) L. Löber, F. P. Schimansky, U. Kühn, F. Pyczak, J. Eckert, 'Selective laser melting of a beta-solidifying TNM-B1 titanium aluminide alloy', Journal of Materials Processing Technology 214 1852–1860, (2014).

(62) P. Farahmand, S. Liu, Z. Zhang, R. Kovacevic, 'Laser cladding assisted by induction heating of Ni–WC composite enhanced by nano-WC and La2O3' Elsevier, Ceramics International, 15421-15438, (2014).

(63) W. Ya, B. Pathiraj, D.T.A. Matthews, M. Bright, S. Melzer, 'Cladding of Tribaloy T400 on steel substrates using a high power Nd:YAG laser', Elsevier, Surface & Coatings Technology, 323-333. (2018).

(64) ASTM 'standard test method for measuring abrasion using the dry sand/rubber wheel apparatus' G65-16, DOI: 10.1520/G0065-16R21, (2021).

(65) C. Zhong, A. Gasser, J. Kittel, 'Microstructures and tensile properties of Inconel 718 formed by high deposition-rate laser metal deposition', Journal of Laser Applications, Vol 28 (2016) doi: 10.2351/1.4943290

(66) ASTM G65-16e1, Standard Test Method for Measuring Abrasion Using the Dry Sand/Rubber Wheel Apparatus, ASTM International, West Conshohocken, PA, 2016, www.astm.org, DOI: 10.1520/G0065-16E01

(67) Navas C, Cadenas M, Cuetos J M and de Damborenea J, (2006): 'Microstructure and sliding wear behaviour of Tribaloy T-800 coatings deposited by laser cladding'. Wear, Volume 260, Issues 7–8, 2006, Pages 838-846, ISSN 0043-1648.

(68) Laserline GmbH, 2022, 'Laser cladding today: Status of technology', 20/12/2022. https://www.laserline.com/en-int/laser-cladding-today-status-of-technology-part-ii/

(69) Zhan, X. & Qi, Chaoqi & Gao, Zhuanni & Tian, Deyong & Wang, Zhengdong, 'The influence of heat input on microstructure and porosity during laser cladding of Invar alloy', Optics & Laser Technology, 113. 453-461, (2019).

(70) Yanjiao Hu, Zixuan Wang, Ming Pang, 'Effect of WC content on laser cladding Ni-based coating on the surface of stainless steel', Materials Today Communications, Volume 31, 103357, ISSN 2352-4928, https://doi.org/10.1016/j.mtcomm.2022.103357. (2022)

(71) Christoforou, P., Dowding, R., Pinna, C. et al., 'Two-layer laser clad coating as a replacement for chrome electroplating on forged steel', Proceedings of the Institution of Mechanical Engineers, Part C: Journal of Mechanical Engineering Science, 235 (23). pp. 7120-7138. ISSN 0954-4062. (2021)

(72) Liu, Yanhui & Li, J & Xuan, Fu-Zhen, 'Fabrication of TiC reinforced Ni based coating by laser cladding', Surface Engineering, 28. 560-563. 10.1179/1743294412Y.0000000026. (2012)

Appendix A

Powder Test Certificates

Tribaloy T800 and Tristelle 5183

FAX TRANSMISSION

Company: TWI Technology Centre (Yorkshire) Ltd	**Fax No.** 0114 269 9781
Attention: Josh Barras	**Date:** 20/03/2017
From: M. Tunnicliffe	**Customer Order No.** P765307
Page 1 of 1	**Lab. Request No.** 3701625
Comments:	**Email:** josh.barras@twi.co.uk

TEST REPORT TO FOLLOW WITH FULL ANALYSES DETAILS
Where UKAS Accreditation applies, this will be confirmed on the full analysis certificate

URGENT - TOP PRIORITY

TRIBALLOY T800 3705007		**TRISTELLE 5183** 3705008	
Al	<0.02 %	Al	<0.05 %
B	<0.02 %	Co	0.04 %
Co	50.80 By Diff %	Cr	21.70 %
Cr	17.52 %	Cu	0.10 %
Cu	0.06 %	Fe	55.38 By Diff %
Fe	0.07 %	Mn	0.13 %
Mn	<0.02 %	Mo	<0.02 %
Mo	28.43 %	Nb	7.35 %
Nb	<0.02 %	Ni	10.01%
Ni	0.14 %	P	0.006 %
P	0.013 %	Si	3.13 %
Si	2.86 %	Sn	<0.02 %
Sn	0.03 %	Ta	<0.02 %
Ta	<0.02 %	Ti	0.02 %
Ti	<0.02 %	V	0.02 %
V	<0.02 %	W	<0.02 %
W	<0.02 %	C	2.04 %
C	0.001%	S	0.006 %
S	0.001 %	N	0.045 %
N	0.020 %	O	0.022 %
O	0.014 %	H	3.3 ppm
H	2.3 ppm		

Analysis on 'As Received' Basis

Analysis on 'As Received' Basis

All analysis carried out to our terms and conditions

REGARDS

Fax Check Signature

SRJ

In the event of an incomplete transmission please contact laboratory administration on Extension 763

NiCrSiB Metco 12C

œrlikon
metco

Inspection Certificate
EN 10204 - 3.1

TWI LTD.
Wallis Way
Catcliffe
ROTHERHAM
South Yorkshire
S60 5TZ
GROßBRITANNIEN
Customer PO: P786171
PO: 200322107
Product: 1002519 12C / 5 KG
Quantity: 10.000 KG

Shipping Doc/Date
800549348 / 09.04.2019

Page
1

Lot No: 10201

Characteristic	Inspection Method	Value	Unit
Chemical Analysis			
B		1.65	WT%
C		0.24	WT%
Cr		7.48	WT%
Fe		2.47	WT%
Ni	Balance	84.64	WT%
Si		3.52	WT%
Sieve Size			
+100 mesh (150 µm)		0.0	WT%
-150 +125 µm		0.5	WT%
-125+45my	Balance	99.5	WT%
-325 mesh (45 µm)		0.0	WT%

Material was inspected and released by Oerlikon Metco Europe GmbH, Kelsterbach,unless otherwise stated.

It is hereby certified that the material described above has been inspected, and conforms to all applicable requirements of the contract order and specifications referenced on this certificate. This certificate shall not be reproduced except in full without the written approval of Oerlikon Metco. The recording of false, fictitous, or fraudulent statement or entries on this certificate may be punished as felony under the federal law. This material is being supplied in accordance with the Quality System at Oerlikon Metco Europe GmbH which is an ISO 9001:2008 Certified Vendor. This material is supplied according to the quality requirements of the customers purchase orders. This inspection certificate meets the requirements of EN10204:2005 3.1 (Inspection Certificate), 2.2 (Test Report) or 2.1 (Certificate of Compliance with the Order).

By _____
Quality Assurance Representative on behalf of
Joem Lindner

Table A1 Titanium Aluminide: Inclusion Powder Test

Test	Non-ODS 15-45µm	Non-ODS 45-106µm	ODS 0.6 wt.%, 45-106 µm
Oxygen, ppm	8006	1516	9995 (8788*)
Carbon, ppm	306	88	1104
B. Dens., g.cm^{-3}	1.69	2.23	1.77
Nitrogen, ppm	510	89	432
BET, m^2.g^{-1}	0.1367	0.0305	0.1972

*The bracketed oxygen value for the ODS material is a manually calculated normalisation, discounting the impact that the yttria has on the measured oxygen result.

Ni-WC powder

œrlikon
metco

Inspection Certificate
EN 10204 - 3.1

‖‖‖‖‖‖‖‖‖‖‖‖‖‖‖‖‖

Oerlikon Metco Europe GmbH
Spreestrasse 2
D-65451 KELSTERBACH
Phone: +49 6142 6033 0
Fax: +49 6142 6033 400

TWI LTD.
Wallis Way
Catcliffe
ROTHERHAM
South Yorkshire
S60 5TZ
GROßBRITANNIEN

Shipping Doc/Date	Page
800490948 / 14.08.2017	1

Customer PO: P769082
PO: 200286457
Product: 1075604 MetcoClad 52052 -106+45 µm 5 KG
Quantity: 15.000 KG

Lot No: 729-U-4

Characteristic	Inspection Method	Value	Unit
Particle size distribution analysis			
+150	ROTAP	0.0	%
+125	ROTAP	0.0	%
+106	ROTAP	0.6	%
+45	ROTAP	95.2	%
-45	ROTAP	4.2	%
Physical analysis			
AD		6.63	g/cm3
HF s/50g		9.2	s
Chemical analysis			
C		2.5	%
Cr		2.87	%
Ni		33.91	%
Fe		1.21	%
W		Balance	
B		0.65	%
Si		1.41	%
Others		0.07	%

ROTAP: The "Mass-%"-values are measured on each sieve.
MICROTRAC: Measured values (volume-%) are cumulative.

Material produced / packaged, inspected and released by Oerlikon Metco WOKA GmbH, Barchfeld-Immelborn unless otherwise stated.

By
Quality Assurance Representative on behalf of
Joern Lindner

Ni-WC oxidised powder

FAX TRANSMISSION

Company: TWI Technology Centre (Yorkshire) Ltd

Attention: Josh Barras

From: M. Tunnicliffe

Page 1 of 1

Comments: Re-analysed due to QC failure
✱

Fax No. 0114 269 9781

Date: 30/01/2018

Customer Order No. P773039

Lab. Request No. 3800349

Email: josh.barras@twi.co.uk

TEST REPORT TO FOLLOW WITH FULL ANALYSES DETAILS
Where UKAS Accreditation applies, this will be confirmed on the full analysis certificate

<u>URGENT - TOP PRIORITY</u>

LAM 10186
3801156

Al	<0.05 %
Ti	<0.05 %
V	<0.05 %
Cr	3.05 %
Mn	0.07 %
Fe	2.22 %
Co	<0.05 %
Ni	31.12 %
Cu	<0.05 %
Nb	<0.05 %
Mo	<0.05 %
Sn	<0.05 %
W	54.48 %
P	0.017 %
Mg	<0.05 %
Ca	<0.05 %
Zn	<0.05 %
Zr	<0.05 %
Hf	<0.05 %
Ta	<0.05 %
Pb	<0.05 %
C	1.60 %
Si	1.40 %
O ✱	5.87 %

Analysis on 'As Received' Basis

All analysis carried out to our terms and conditions

REGARDS

Fax Check Signature

In the event of an incomplete transmission please contact laboratory administration on Extension 763

Appendix B

Deposition images, Microstructural inspection and Test Data

Task 2.1: Tribaloy T800

Figure B1 Deposit sample 114
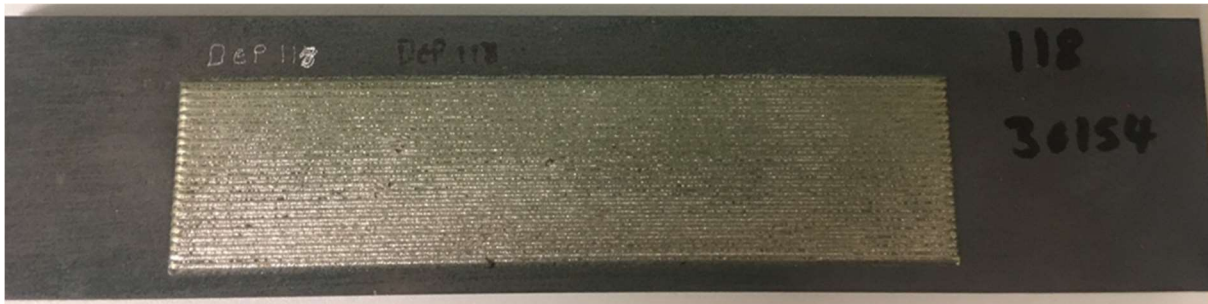
Figure B2 Deposit sample 118
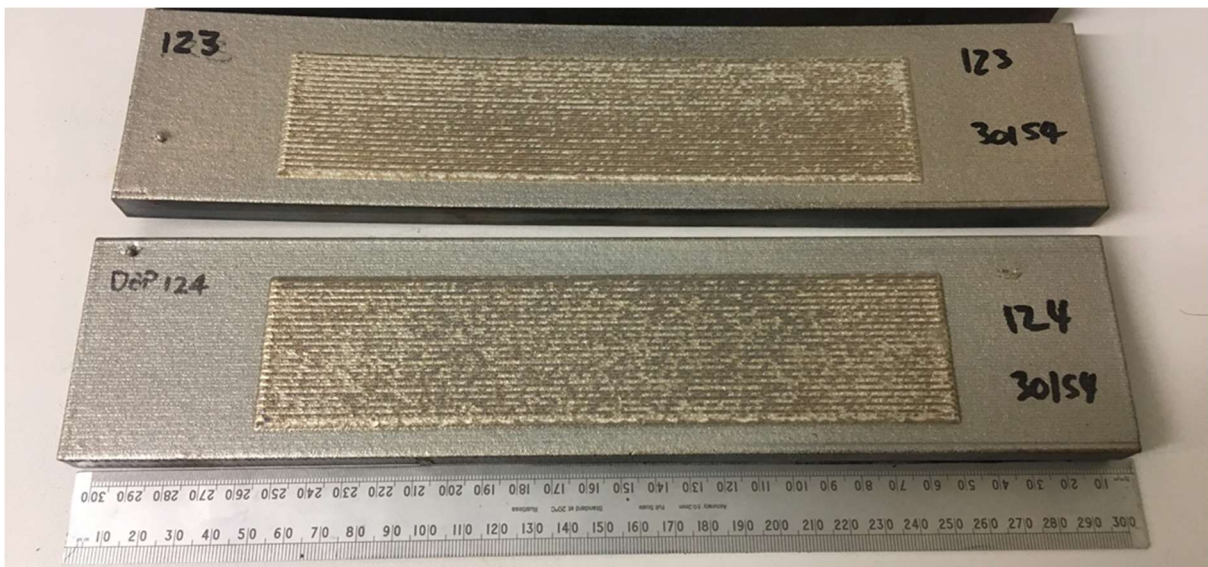
Figure B3 Deposit sample 123 and 124
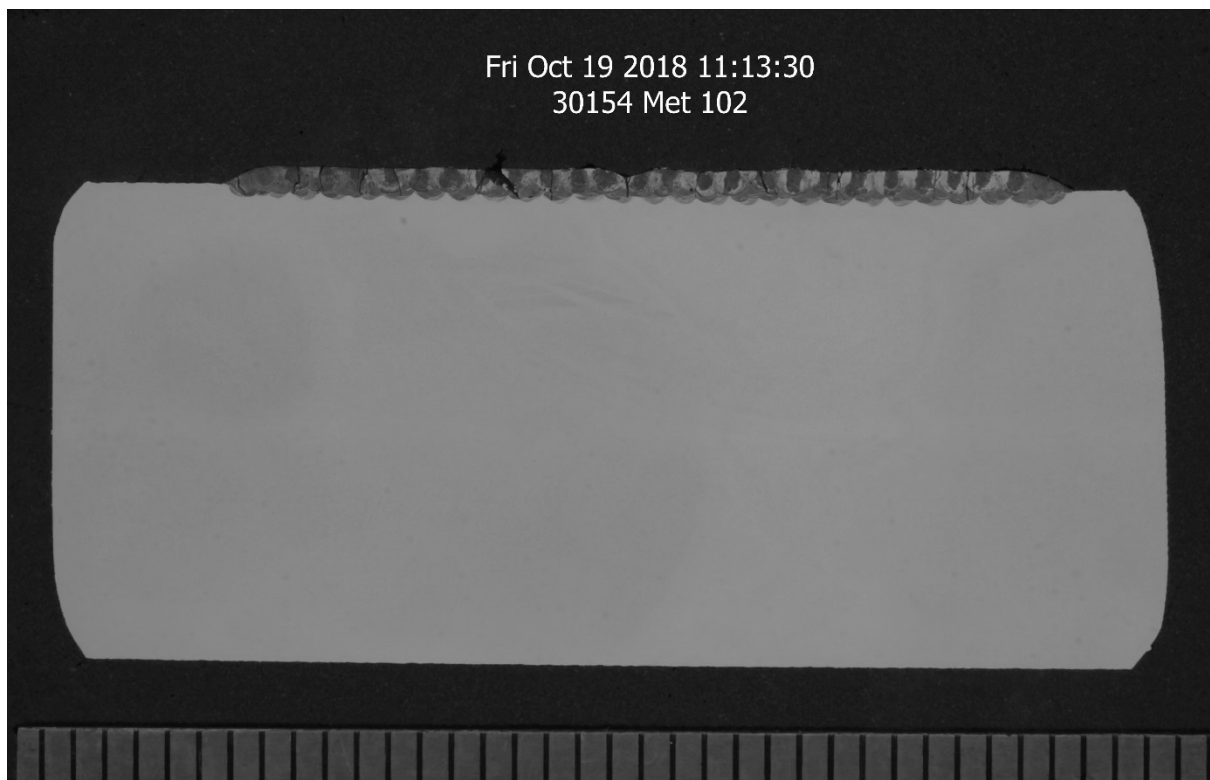
Figure B4 Deposit sample 102 (no pre heat and significant cracking)
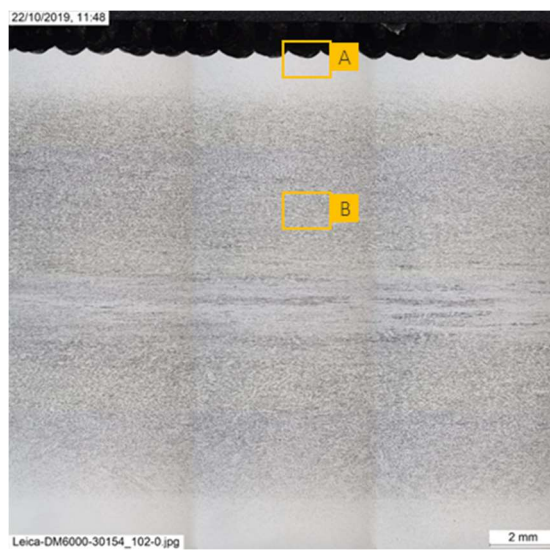
Figure B5 Deposit sample 102

(a)

(b)

(c)

(d)

Figure B6 Deposit sample 102.

Figure B7 deposit sample 118 (>850°C).

(a)

(b)

(c)

(d)

Figure B8 Deposit sample 118.
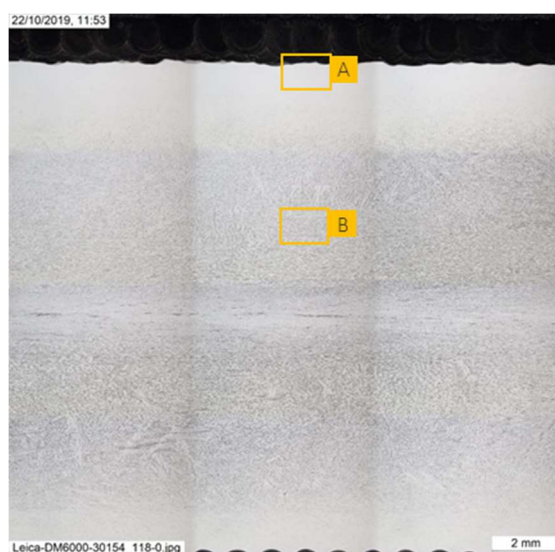
Figure B9 Deposit sample 124 (preheat 700°C and buffer layers).

(a)

(b)

(c)

(d)

Figure B10 Deposit sample 124

Table B1 Tribaloy T800 Chemical Analysis EDX

	Sample	Si	Mo	Cr	Mn	Fe	Co	Ni	Approx Depth from surface	Corrected Depth from surface
									mm	mm
102	102-1	2.5	20.8	17.2	0.5	23	32.5	3.6	0	0.1
	102-2	2.9	19.5	17.3	0.6	23.2	32.7	3.8	0.2855	0.3855
	102-3	2.5	20.8	17	0.5	23.5	32	3.8	0.571	0.671
	102-4	2.6	14.2	17.1	0.8	35.5	24.4	5.5	0.8565	0.9565
	102-5	1.6	7.6	17	1.1	52.6	12.3	7.8	1.42	1.42
	102-6	0.6	2.3	17.1	1.3	68.7		10		1.62
114	114-1	3.2	23.7	16.5	0.5	21.2	31.5	3.6	0	0.1
	114-2	2.5	20.6	17.3	0.6	24.5	30.8	3.9	0.39225	0.49225
	114-3	2.3	20.6	17.1	0.5	25	30.8	3.8	0.7845	0.8845
	114-4	1.8	13.9	17	0.8	41.3	19.4	5.9	1.17675	1.27675
	114-5	1.4	9.5	16.9	1	51.9	11.9	7.4	1.569	1.569
	114-6	0.6	2.3	17.1	1.3	69.2		9.5		1.769
118	118-1	2.6	21.5	17.2	0.6	23	31.5	3.6	0	0.1
	118-2	2.5	21.2	17	0.6	23.7	31.3	3.8	0.3565	0.4565
	118-3	2.5	21.4	17.1	0.5	23.8	31.2	3.6	0.713	0.813
	118-4	2.4	20.7	17.1	0.5	25.9	29.7	3.9	1.0695	1.1695
	118-5	1.8	13.6	16.9	0.9	41.9	18.8	6.2	1.426	1.426
	118-6	0.5	2	17	1.3	69.3		9.8		1.626
119	119-1	2.1	17.7	16.8	0.7	32.3	24.5	5	0	0.1
	119-2	2.2	17.7	17.2	0.6	32.3	25.1	5	0.356	0.456
	119-3	2.1	17.3	17	0.7	32.7	25.4	4.9	0.712	0.812
	119-4	1.9	17.2	17.3	0.8	32.9	24.9	5	1.068	1.168
	119-5	1.8	14.4	17	0.9	40.3	20	5.7	1.424	1.424
	119-6	0.5	2	17	1.3	69.3		9.9		1.624
120	120-1	2.5	16	15.8	0.5	27.2	21.6	16.4	0	0.1
	120-2	2.3	13.5	15.5	0.7	29.8	20.6	17.7	0.39775	0.49775
	120-3	2.4	14.8	15.7	0.6	28.8	20.5	17.2	0.7955	0.8955
	120-4	2.4	13.5	15.7	0.6	31.2	19.1	17.6	1.19325	1.29325
	120-5	1.9	9.6	15.8	0.8	39.5	12.4	20.1	1.591	1.591
	120-6	0.6	1.9	17.6	1.3	69.1		9.5		1.791
123	123-1	2.8	17.5	15.3	0.5	18.4	26.4	19.2	0	0.1
	123-2	2.7	17.5	15.5	0.5	18.2	26.7	19	0.24075	0.34075
	123-3	2.6	17.2	15.6	0.4	18.6	26.9	18.8	0.4815	0.5815
	123-4	2.5	12.5	14.8	0.5	26.8	17.7	25.3	0.72225	0.82225
	123-5	2.5	14.6	15.2	0.7	23.1	20.8	23.1	0.963	0.963
	123-6	0.7	1.8	17.3	1.4	68.4		10.4		1.163
124	124-1	3.2	21.4	15.3	0.4	11.1	31.9	16.8	0	0.1
	124-2	3	20.3	15.5	0.3	11.7	31.5	17.7	0.24075	0.34075
	124-3	3.2	20.9	15.1	0.3	12.1	29.8	18.7	0.4815	0.5815
	124-4	3.1	18.6	15	0.4	14.7	26.8	21.5	0.72225	0.82225
	124-5	2.7	14.7	15	0.5	24.5	20.9	21.7	0.963	0.963
										1.163
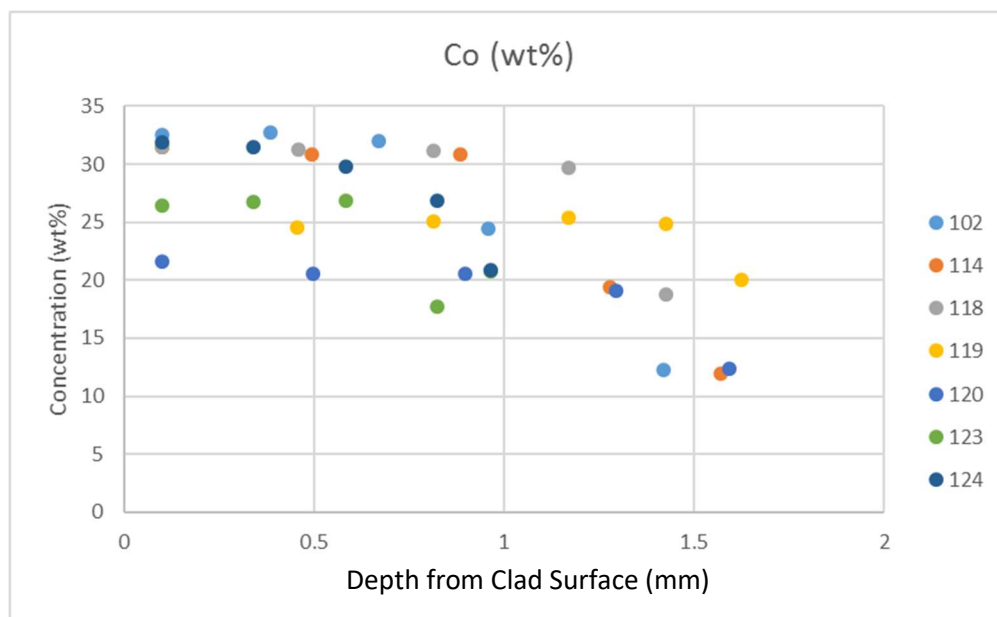
Figure B11 comparison of Cobalt content in Tribaloy deposits.
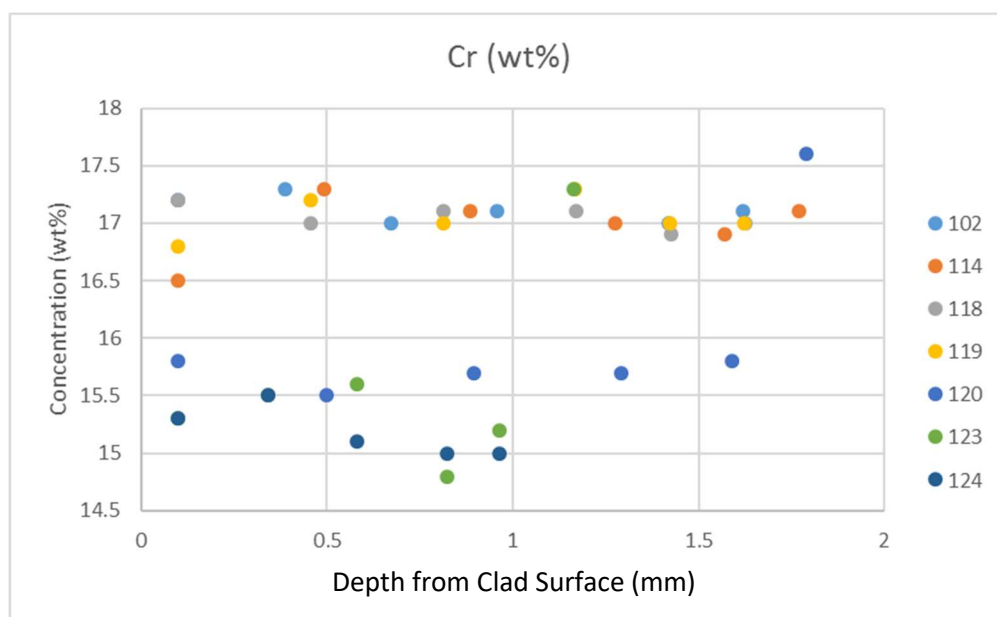
Figure B12 comparison of Chromium content in Tribaloy deposits.
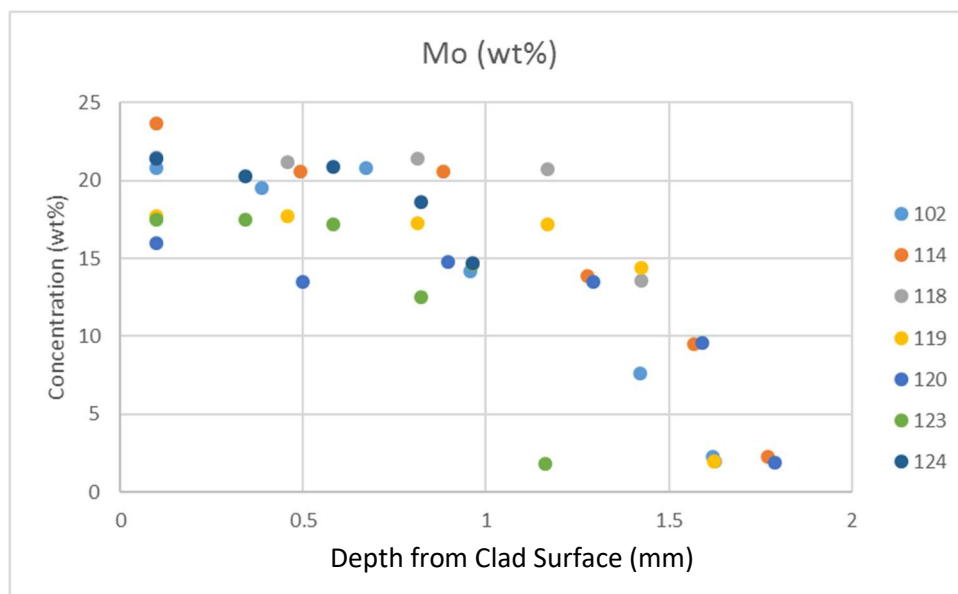
Figure B13 comparison of Molybdenum content in Tribaloy deposits.
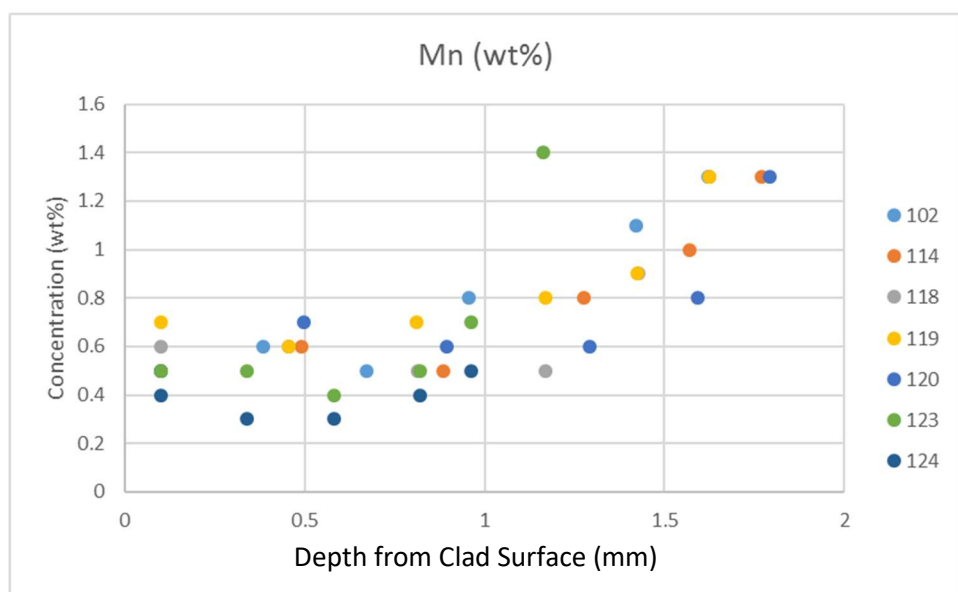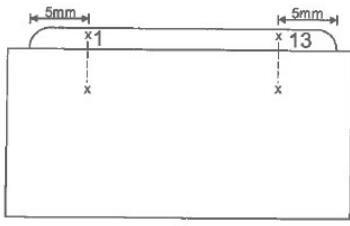
Figure B14 comparison of Manganese content in Tribaloy deposits.
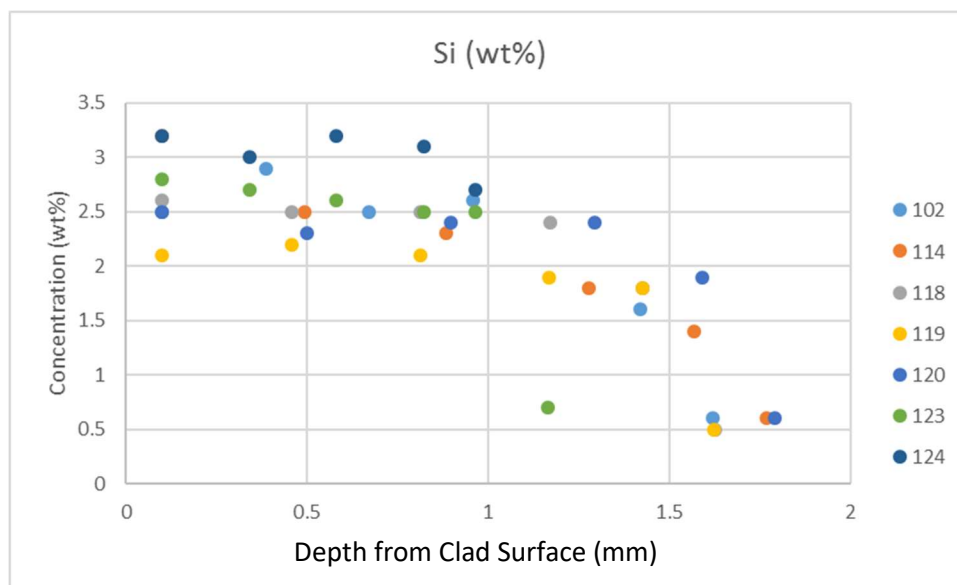
Figure B15 comparison of Silicon content in Tribaloy deposits.
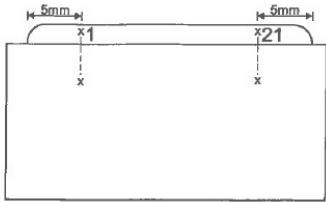
Vickers hardness test method TP08A, BS EN ISO 6507-2015.

Table B2 Sample 101 hardness results

Hardness Test	Method	Indentor		Load (kg)		
Mark No: 101	Vickers	Diamond Pyramid		1		
		Indent	Hardness	Indent	Hardness	Indent	Hardness

Indent	Hardness	Indent	Hardness	Indent	Hardness
1	560	16	495	31	–
2	536	17	567	32	–
3	575	18	385	33	–
4	547	19	556	34	–
5	582	20	202	35	–
6	532	21	204	36	–
7	217	22	210	37	–
8	218	23	214	38	–
9	212	24	215	39	–
10	210	25	–	40	–
11	205	26	–	41	–
12	215	27	–	42	–
13	573	28	–	43	–
14	627	29	–	44	–
15	527	30	–	45	–
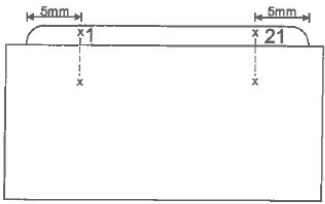
Room temperature during testing: 23.95°C.

Table B3 Sample 102 hardness results

Hardness Test	Method	Indentor		Load (kg)		
Mark No: 102	Vickers	Diamond Pyramid		1		
		Indent	Hardness	Indent	Hardness	Indent	Hardness

Indent	Hardness	Indent	Hardness	Indent	Hardness
1	887	16	205	31	663
2	903	17	211	32	296
3	953	18	208	33	211
4	942	19	207	34	203
5	856	20	215	35	207
6	815	21	797	36	207
7	805	22	931	37	214
8	682	23	780	38	210
9	721	24	862	39	209
10	692	25	798	40	205
11	559	26	803	41	-
12	231	27	856	42	-
13	200	28	782	43	-
14	212	29	825	44	-
15	207	30	721	45	-
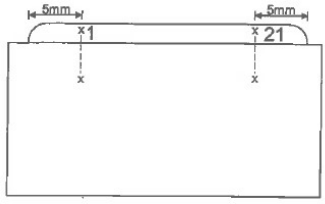
Room temperature during testing: 23.97C

Table B4 Sample 114 hardness results

Hardness Test	Method	Indentor		Load (kg)		
Mark No: 114	Vickers	Diamond Pyramid		1		

Indent	Hardness	Indent	Hardness	Indent	Hardness
1	725	16	177	31	743
2	848	17	170	32	*
3	924	18	179	33	371
4	853	19	189	34	456
5	860	20	201	35	196
6	832	21	*	36	181
7	893	22	614	37	180
8	755	23	*	38	179
9	810	24	899	39	197
10	712	25	465	40	198
11	759	26	898	41	-
12	474	27	583	42	-
13	503	28	701	43	-
14	524	29	486	44	-
15	218	30	890	45	-
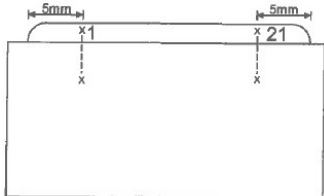
Room temperature during testing: 23.97C
Note: * - Invalid result due to cracks.

Table B5 Sample 118 hardness results

Hardness Test	Method	Indentor		Load (kg)		
Mark No: 118	Vickers	Diamond Pyramid		1		

Indent	Hardness	Indent	Hardness	Indent	Hardness
1	852	16	175	31	789
2	784	17	177	32	*
3	778	18	175	33	555
4	788	19	171	34	537
5	855	20	172	35	194
6	841	21	*	36	186
7	836	22	740	37	177
8	842	23	512	38	187
9	850	24	840	39	182
10	786	25	711	40	184
11	813	26	800	41	-
12	729	27	838	42	-
13	678	28	786	43	-
14	607	29	782	44	-
15	176	30	614	45	-
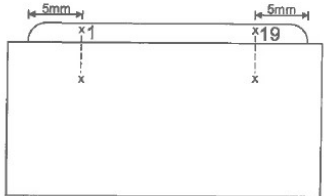
Room temperature during testing: 23.97C.
Note: * - Invalid result due to cracks.

Table B6 Sample 119 hardness results

Hardness Test	Method	Indentor			Load (kg)		
Mark No: 119	Vickers	Diamond Pyramid			1		
		Indent	Hardness	Indent	Hardness	Indent	Hardness
		1	544	16	169	31	634
		2	555	17	174	32	630
		3	567	18	167	33	675
		4	563	19	167	34	644
		5	566	20	165	35	428
		6	580	21	655	36	309
		7	596	22	645	37	158
		8	568	23	650	38	160
		9	562	24	660	39	160
		10	550	25	687	40	154
		11	561	26	677	41	-
		12	537	27	665	42	-
		13	174	28	631	43	-
		14	174	29	644	44	-
		15	171	30	673	45	-
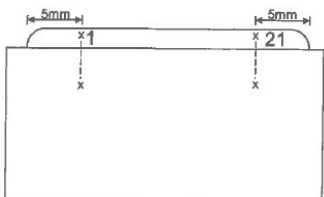
Room temperature during testing: 23.97C.

Table B7 Sample 120 hardness results

Hardness Test	Method	Indentor			Load (kg)		
Mark No: 120	Vickers	Diamond Pyramid			1		
		Indent	Hardness	Indent	Hardness	Indent	Hardness
		1	322	16	173	31	321
		2	341	i7	170	32	224
		3	234	18	172	33	175
		4	328	19	320	34	176
		5	331	20	344	35	173
		6	336	21	336	36	176
		7	339	22	343	37	-
		8	331	23	329	38	-
		9	351	24	338	39	-
		10	336	25	332	40	-
		11	373	26	337	41	-
		12	341	27	332	42	-
		13	342	28	346	43	-
		14	328	29	324	44	-
		15	184	30	357	45	-
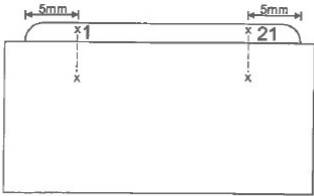
Room temperature during testing: 23.97C.

Table B8 Sample 121 hardness results

Hardness Test	Method	Indentor			Load (kg)		
Mark No: 121	Vickers	Diamond Pyramid			1		
		Indent	Hardness	Indent	Hardness	Indent	Hardness
		1	290	16	180	31	292
		2	285	17	177	32	294
		3	267	18	175	33	245
		4	290	19	174	34	175
		5	298	20	172	35	178
		6	287	21	305	36	183
		7	284	22	288	37	173
		8	289	23	309	38	166
		9	300	24	294	39	170
		10	293	25	298	40	170
		11	304	26	303	41	-
		12	288	27	286	42	-
		13	251	28	302	43	-
		14	178	29	303	44	-
		15	182	30	307	45	-
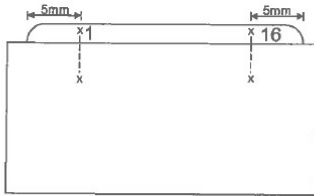
Room temperature during testing: 23.97C.

Table B9 Sample 122 hardness results

Hardness Test Mark No: 122	Method Vickers	Indentor Diamond Pyramid		Load (kg) 1		
Indent	Hardness	Indent	Hardness	Indent	Hardness
1	424	16	178	31	184
2	434	17	185	32	185
3	437	18	178	33	187
4	405	19	174	34	186
5	434	20	171	35	179
6	357	21	513	36	179
7	325	22	436	37	174
8	197	23	507	38	171
9	178	24	467	39	172
10	183	25	390	40	176
11	184	26	324	41	-
12	180	27	331	42	-
13	185	28	214	43	-
14	175	29	186	44	-
15	172	30	192	45	-
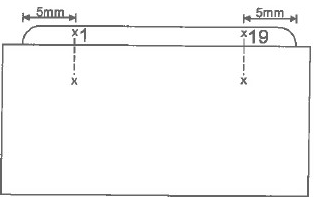
Room temperature during testing: 23.97C.

Table B10 Sample 123 hardness results

Hardness Test Mark No: 123	Method Vickers	Indentor Diamond Pyramid		Load (kg) 1		
Indent	Hardness	Indent	Hardness	Indent	Hardness
1	483	16	510	31	-
2	506	17	485	32	-
3	473	18	505	33	-
4	488	19	484	34	-
5	354	20	375	35	-
6	347	21	319	36	-
7	252	22	231	37	-
8	196	23	195	38	-
9	194	24	195	39	-
10	195	25	198	40	-
11	196	26	196	41	-
12	193	27	193	42	-
13	195	28	196	43	-
14	193	29	192	44	-
15	193	30	190	45	-

Room temperature during testing: 23.97C.

Table B11 Sample 124 hardness results

Hardness Test Mark No: 124	Method Vickers	Indentor Diamond Pyramid		Load (kg) 1		
Indent	Hardness	Indent	Hardness	Indent	Hardness
1	525	16	203	31	195
2	546	17	205	32	211
3	540	18	208	33	209
4	542	19	208	34	206
5	470	20	211	35	202
6	549	21	523	36	212
7	475	22	519	37	212
8	467	23	508	38	211
9	494	24	495	39	210
10	338	25	526	40	212
11	184	26	538	41	-
12	189	27	540	42	-
13	197	28	433	43	-
14	201	29	334	44	-
15	205	30	356	45	-

Room temperature during testing: 23.97C

Task 2.2. Tristelle 5183

Figure B16 overview image of Tristelle deposit.

Figure B17 G65 dry sand abrasion samples after testing, indicating good uniformity and therefore valid test results.

Table B18 Task 2c capability mapping DOE (+ indicates the parameter value for the trial no, and – means not applicable)

	30	35	40	45	50	2.25	1.5	1	0.5	0.35	0.2	0	800	1200	1600	2000	600	1200	1800	7	14	21	4	8
	Stand off Distance (mm)					Dial setting Motorised Optic Unit							Laser Power (W)				Traverse Speed (mm/min)			Powder (%RPM)			Nozzle Gas (l/min)	
Trial no.	1	2	3	4	5	6	7	8	9	10	11	12	13	14	15	16	17	18	19	20	21	22	23	24
1	+	-	-	-	-	+	-	-	-	-	-	-	+	-	-	-	+	-	-	+	-	-	+	-
2	+	-	-	-	-	+	-	-	-	-	-	-	+	-	-	-	-	+	-	+	-	-	+	-
3	+	-	-	-	-	+	-	-	-	-	-	-	+	-	-	-	-	+	-	+	-	-	-	+
4	+	-	-	-	-	+	-	-	-	-	-	-	+	-	-	-	-	+	-	-	+	-	-	+
5	+	-	-	-	-	+	-	-	-	-	-	-	+	-	-	-	-	-	+	-	+	-	-	+
6	+	-	-	-	-	+	-	-	-	-	-	-	-	+	-	-	+	-	-	+	-	-	+	-
7	+	-	-	-	-	+	-	-	-	-	-	-	-	+	-	-	+	-	-	+	-	-	-	+
8	+	-	-	-	-	+	-	-	-	-	-	-	-	+	-	-	+	-	-	-	+	-	-	+
9	+	-	-	-	-	+	-	-	-	-	-	-	-	+	-	-	-	+	-	-	+	-	-	+
10	+	-	-	-	-	+	-	-	-	-	-	-	-	+	-	-	-	-	+	-	+	-	-	+
11	+	-	-	-	-	+	-	-	-	-	-	-	-	+	-	-	-	-	+	-	-	+	-	+
12	+	-	-	-	-	+	-	-	-	-	-	-	-	-	+	-	+	-	-	-	+	-	-	+
13	+	-	-	-	-	+	-	-	-	-	-	-	-	-	+	-	-	+	-	-	+	-	-	+
14	+	-	-	-	-	+	-	-	-	-	-	-	-	-	+	-	-	-	+	-	+	-	-	+
15	+	-	-	-	-	+	-	-	-	-	-	-	-	-	+	-	-	-	+	-	-	+	+	-
16	+	-	-	-	-	+	-	-	-	-	-	-	-	-	+	-	-	-	+	-	-	+	-	+
17	+	-	-	-	-	+	-	-	-	-	-	-	-	-	-	+	+	-	-	-	+	-	-	+
18	+	-	-	-	-	+	-	-	-	-	-	-	-	-	-	+	-	+	-	-	+	-	-	+
19	+	-	-	-	-	+	-	-	-	-	-	-	-	-	-	+	-	-	+	-	+	-	-	+
20	+	-	-	-	-	+	-	-	-	-	-	-	-	-	-	+	-	-	+	-	-	+	+	-
21	+	-	-	-	-	+	-	-	-	-	-	-	-	-	-	+	-	-	+	-	-	+	-	+
22	+	-	-	-	-	-	+	-	-	-	-	-	+	-	-	-	+	-	-	+	-	-	+	-
23	+	-	-	-	-	-	+	-	-	-	-	-	+	-	-	-	-	+	-	+	-	-	+	-
24	+	-	-	-	-	-	+	-	-	-	-	-	+	-	-	-	-	+	-	+	-	-	-	+
25	+	-	-	-	-	-	+	-	-	-	-	-	+	-	-	-	-	+	-	-	+	-	-	+
26	+	-	-	-	-	-	+	-	-	-	-	-	+	-	-	-	-	-	+	-	+	-	-	+

	Stand off Distance (mm)					Dial setting Motorised Optic Unit							Laser Power (W)				Traverse Speed (mm/min)			Powder (%RPM)			Nozzle Gas (l/min)	
	30	35	40	45	50	2.25	1.5	1	0.5	0.35	0.2	0	800	1200	1600	2000	600	1200	1800	7	14	21	4	8
27	+	-	-	-	-	-	+	-	-	-	-	-	-	+	-	-	+	-	-	+	-	-	+	-
28	+	-	-	-	-	-	+	-	-	-	-	-	-	+	-	-	+	-	-	+	-	-	-	+
29	+	-	-	-	-	-	+	-	-	-	-	-	-	+	-	-	+	-	-	-	+	-	-	+
30	+	-	-	-	-	-	+	-	-	-	-	-	-	+	-	-	-	+	-	-	+	-	-	+
31	+	-	-	-	-	-	+	-	-	-	-	-	-	+	-	-	-	-	+	-	+	-	-	+
32	+	-	-	-	-	-	+	-	-	-	-	-	-	+	-	-	-	-	+	-	-	+	-	+
33	+	-	-	-	-	-	+	-	-	-	-	-	-	-	+	-	+	-	-	-	+	-	-	+
34	+	-	-	-	-	-	+	-	-	-	-	-	-	-	+	-	-	+	-	-	+	-	-	+
35	+	-	-	-	-	-	+	-	-	-	-	-	-	-	+	-	-	-	+	-	+	-	-	+
36	+	-	-	-	-	-	+	-	-	-	-	-	-	-	+	-	-	-	+	-	-	+	+	-
37	+	-	-	-	-	-	+	-	-	-	-	-	-	-	+	-	-	-	+	-	-	+	-	+
38	+	-	-	-	-	-	+	-	-	-	-	-	-	-	-	+	+	-	-	-	+	-	-	+
39	+	-	-	-	-	-	+	-	-	-	-	-	-	-	-	+	-	+	-	-	+	-	-	+
40	+	-	-	-	-	-	+	-	-	-	-	-	-	-	-	+	-	-	+	-	+	-	-	+
41	+	-	-	-	-	-	+	-	-	-	-	-	-	-	-	+	-	-	+	-	-	+	+	-
42	+	-	-	-	-	-	+	-	-	-	-	-	-	-	-	+	-	-	+	-	-	+	-	+
43	+	-	-	-	-	-	-	+	-	-	-	-	+	-	-	-	+	-	-	+	-	-	+	-
44	+	-	-	-	-	-	-	+	-	-	-	-	+	-	-	-	-	+	-	+	-	-	+	-
45	+	-	-	-	-	-	-	+	-	-	-	-	+	-	-	-	-	+	-	+	-	-	-	+
46	+	-	-	-	-	-	-	+	-	-	-	-	+	-	-	-	-	+	-	-	+	-	-	+
47	+	-	-	-	-	-	-	+	-	-	-	-	+	-	-	-	-	-	+	-	+	-	-	+
48	+	-	-	-	-	-	-	+	-	-	-	-	-	+	-	-	+	-	-	+	-	-	+	-
49	+	-	-	-	-	-	-	+	-	-	-	-	-	+	-	-	+	-	-	+	-	-	-	+
50	+	-	-	-	-	-	-	+	-	-	-	-	-	+	-	-	+	-	-	-	+	-	-	+
51	+	-	-	-	-	-	-	+	-	-	-	-	-	+	-	-	-	+	-	-	+	-	-	+
52	+	-	-	-	-	-	-	+	-	-	-	-	-	+	-	-	-	-	+	-	+	-	-	+
53	+	-	-	-	-	-	-	+	-	-	-	-	-	+	-	-	-	-	+	-	-	+	-	+
54	+	-	-	-	-	-	-	+	-	-	-	-	-	-	+	-	+	-	-	-	+	-	-	+

	Stand off Distance (mm)					Dial setting Motorised Optic Unit							Laser Power (W)				Traverse Speed (mm/min)			Powder (%RPM)			Nozzle Gas (l/min)	
	30	35	40	45	50	2.25	1.5	1	0.5	0.35	0.2	0	800	1200	1600	2000	600	1200	1800	7	14	21	4	8
55	+	-	-	-	-	-	-	+	-	-	-	-	-	-	+	-	-	+	-	-	+	-	-	+
56	+	-	-	-	-	-	-	+	-	-	-	-	-	-	+	-	-	-	+	-	+	-	-	+
57	+	-	-	-	-	-	-	+	-	-	-	-	-	-	+	-	-	-	+	-	-	+	+	-
58	+	-	-	-	-	-	-	+	-	-	-	-	-	-	+	-	-	-	+	-	-	+	-	+
59	+	-	-	-	-	-	-	+	-	-	-	-	-	-	-	+	+	-	-	-	+	-	-	+
60	+	-	-	-	-	-	-	+	-	-	-	-	-	-	-	+	-	+	-	-	+	-	-	+
61	+	-	-	-	-	-	-	+	-	-	-	-	-	-	-	+	-	-	+	-	+	-	-	+
62	+	-	-	-	-	-	-	+	-	-	-	-	-	-	-	+	-	-	+	-	-	+	+	-
63	+	-	-	-	-	-	-	+	-	-	-	-	-	-	-	+	-	-	+	-	-	+	-	+
64	+	-	-	-	-	-	-	-	+	-	-	-	+	-	-	-	+	-	-	+	-	-	+	-
65	+	-	-	-	-	-	-	-	+	-	-	-	+	-	-	-	-	+	-	+	-	-	+	-
66	+	-	-	-	-	-	-	-	+	-	-	-	+	-	-	-	-	+	-	+	-	-	-	+
67	+	-	-	-	-	-	-	-	+	-	-	-	+	-	-	-	-	+	-	-	+	-	-	+
68	+	-	-	-	-	-	-	-	+	-	-	-	+	-	-	-	-	-	+	-	+	-	-	+
69	+	-	-	-	-	-	-	-	+	-	-	-	-	+	-	-	+	-	-	+	-	-	+	-
70	+	-	-	-	-	-	-	-	+	-	-	-	-	+	-	-	+	-	-	+	-	-	-	+
71	+	-	-	-	-	-	-	-	+	-	-	-	-	+	-	-	+	-	-	-	+	-	-	+
72	+	-	-	-	-	-	-	-	+	-	-	-	-	+	-	-	-	+	-	-	+	-	-	+
73	+	-	-	-	-	-	-	-	+	-	-	-	-	+	-	-	-	-	+	-	+	-	-	+
74	+	-	-	-	-	-	-	-	+	-	-	-	-	+	-	-	-	-	+	-	-	+	-	+
75	+	-	-	-	-	-	-	-	+	-	-	-	-	-	+	-	+	-	-	-	+	-	-	+
76	+	-	-	-	-	-	-	-	+	-	-	-	-	-	+	-	-	+	-	-	+	-	-	+
77	+	-	-	-	-	-	-	-	+	-	-	-	-	-	+	-	-	-	+	-	+	-	-	+
78	+	-	-	-	-	-	-	-	+	-	-	-	-	-	+	-	-	-	+	-	-	+	+	-
79	+	-	-	-	-	-	-	-	+	-	-	-	-	-	+	-	-	-	+	-	-	+	-	+
80	+	-	-	-	-	-	-	-	+	-	-	-	-	-	-	+	+	-	-	-	+	-	-	+
81	+	-	-	-	-	-	-	-	+	-	-	-	-	-	-	+	-	+	-	-	+	-	-	+
82	+	-	-	-	-	-	-	-	+	-	-	-	-	-	-	+	-	-	+	-	+	-	-	+

	Stand off Distance (mm)					Dial setting Motorised Optic Unit							Laser Power (W)				Traverse Speed (mm/min)			Powder (%RPM)			Nozzle Gas (l/min)	
	30	35	40	45	50	2.25	1.5	1	0.5	0.35	0.2	0	800	1200	1600	2000	600	1200	1800	7	14	21	4	8
83	+	-	-	-	-	-	-	-	+	-	-	-	-	-	-	+	-	-	+	-	-	+	+	-
84	+	-	-	-	-	-	-	-	+	-	-	-	-	-	-	+	-	-	+	-	-	+	-	+
85	+	-	-	-	-	-	-	-	-	+	-	-	+	-	-	-	+	-	-	+	-	-	+	-
86	+	-	-	-	-	-	-	-	-	+	-	-	+	-	-	-	-	+	-	+	-	-	+	-
87	+	-	-	-	-	-	-	-	-	+	-	-	+	-	-	-	-	+	-	+	-	-	-	+
88	+	-	-	-	-	-	-	-	-	+	-	-	+	-	-	-	-	+	-	-	+	-	-	+
89	+	-	-	-	-	-	-	-	-	+	-	-	+	-	-	-	-	-	+	-	+	-	-	+
90	+	-	-	-	-	-	-	-	-	+	-	-	-	+	-	-	+	-	-	+	-	-	+	-
91	+	-	-	-	-	-	-	-	-	+	-	-	-	+	-	-	+	-	-	+	-	-	-	+
92	+	-	-	-	-	-	-	-	-	+	-	-	-	+	-	-	+	-	-	-	+	-	-	+
93	+	-	-	-	-	-	-	-	-	+	-	-	-	+	-	-	-	+	-	-	+	-	-	+
94	+	-	-	-	-	-	-	-	-	+	-	-	-	+	-	-	-	-	+	-	+	-	-	+
95	+	-	-	-	-	-	-	-	-	+	-	-	-	+	-	-	-	-	+	-	-	+	-	+
96	+	-	-	-	-	-	-	-	-	+	-	-	-	-	+	-	+	-	-	-	+	-	-	+
97	+	-	-	-	-	-	-	-	-	+	-	-	-	-	+	-	-	+	-	-	+	-	-	+
98	+	-	-	-	-	-	-	-	-	+	-	-	-	-	+	-	-	-	+	-	+	-	-	+
99	+	-	-	-	-	-	-	-	-	+	-	-	-	-	+	-	-	-	+	-	-	+	+	-
100	+	-	-	-	-	-	-	-	-	+	-	-	-	-	+	-	-	-	+	-	-	+	-	+
101	+	-	-	-	-	-	-	-	-	+	-	-	-	-	-	+	+	-	-	-	+	-	-	+
102	+	-	-	-	-	-	-	-	-	+	-	-	-	-	-	+	-	+	-	-	+	-	-	+
103	+	-	-	-	-	-	-	-	-	+	-	-	-	-	-	+	-	-	+	-	+	-	-	+
104	+	-	-	-	-	-	-	-	-	+	-	-	-	-	-	+	-	-	+	-	-	+	+	-
105	+	-	-	-	-	-	-	-	-	+	-	-	-	-	-	+	-	-	+	-	-	+	-	+
106	+	-	-	-	-	-	-	-	-	-	+	-	+	-	-	-	+	-	-	+	-	-	+	-
107	+	-	-	-	-	-	-	-	-	-	+	-	+	-	-	-	-	+	-	+	-	-	+	-
108	+	-	-	-	-	-	-	-	-	-	+	-	+	-	-	-	-	+	-	+	-	-	-	+
109	+	-	-	-	-	-	-	-	-	-	+	-	+	-	-	-	-	+	-	-	+	-	-	+
110	+	-	-	-	-	-	-	-	-	-	+	-	+	-	-	-	-	-	+	-	+	-	-	+

	Stand off Distance (mm)					Dial setting Motorised Optic Unit							Laser Power (W)				Traverse Speed (mm/min)			Powder (%RPM)			Nozzle Gas (l/min)	
	30	35	40	45	50	2.25	1.5	1	0.5	0.35	0.2	0	800	1200	1600	2000	600	1200	1800	7	14	21	4	8
111	+	-	-	-	-	-	-	-	-	-	+	-	-	+	-	-	+	-	-	+	-	-	+	-
112	+	-	-	-	-	-	-	-	-	-	+	-	-	+	-	-	+	-	-	+	-	-	-	+
113	+	-	-	-	-	-	-	-	-	-	+	-	-	+	-	-	+	-	-	-	+	-	-	+
114	+	-	-	-	-	-	-	-	-	-	+	-	-	+	-	-	-	+	-	-	+	-	-	+
115	+	-	-	-	-	-	-	-	-	-	+	-	-	+	-	-	-	-	+	-	+	-	-	+
116	+	-	-	-	-	-	-	-	-	-	+	-	-	+	-	-	-	-	+	-	-	+	-	+
117	+	-	-	-	-	-	-	-	-	-	+	-	-	-	+	-	+	-	-	-	+	-	-	+
118	+	-	-	-	-	-	-	-	-	-	+	-	-	-	+	-	-	+	-	-	+	-	-	+
119	+	-	-	-	-	-	-	-	-	-	+	-	-	-	+	-	-	-	+	-	+	-	-	+
120	+	-	-	-	-	-	-	-	-	-	+	-	-	-	+	-	-	-	+	-	-	+	+	-
121	+	-	-	-	-	-	-	-	-	-	+	-	-	-	+	-	-	-	+	-	-	+	-	+
122	+	-	-	-	-	-	-	-	-	-	+	-	-	-	-	+	+	-	-	-	+	-	-	+
123	+	-	-	-	-	-	-	-	-	-	+	-	-	-	-	+	-	+	-	-	+	-	-	+
124	+	-	-	-	-	-	-	-	-	-	+	-	-	-	-	+	-	-	+	-	+	-	-	+
125	+	-	-	-	-	-	-	-	-	-	+	-	-	-	-	+	-	-	+	-	-	+	+	-
126	+	-	-	-	-	-	-	-	-	-	+	-	-	-	-	+	-	-	+	-	-	+	-	+
127	+	-	-	-	-	-	-	-	-	-	-	+	+	-	-	-	+	-	-	+	-	-	+	-
128	+	-	-	-	-	-	-	-	-	-	-	+	+	-	-	-	-	+	-	+	-	-	+	-
129	+	-	-	-	-	-	-	-	-	-	-	+	+	-	-	-	-	+	-	+	-	-	-	+
130	+	-	-	-	-	-	-	-	-	-	-	+	+	-	-	-	-	+	-	-	+	-	-	+
131	+	-	-	-	-	-	-	-	-	-	-	+	+	-	-	-	-	-	+	-	+	-	-	+
132	+	-	-	-	-	-	-	-	-	-	-	+	-	+	-	-	+	-	-	+	-	-	+	-
133	+	-	-	-	-	-	-	-	-	-	-	+	-	+	-	-	+	-	-	+	-	-	-	+
134	+	-	-	-	-	-	-	-	-	-	-	+	-	+	-	-	+	-	-	-	+	-	-	+
135	+	-	-	-	-	-	-	-	-	-	-	+	-	+	-	-	-	+	-	-	+	-	-	+
136	+	-	-	-	-	-	-	-	-	-	-	+	-	+	-	-	-	-	+	-	+	-	-	+
137	+	-	-	-	-	-	-	-	-	-	-	+	-	+	-	-	-	-	+	-	-	+	-	+
138	+	-	-	-	-	-	-	-	-	-	-	+	-	-	+	-	+	-	-	-	+	-	-	+

	Stand off Distance (mm)					Dial setting Motorised Optic Unit							Laser Power (W)				Traverse Speed (mm/min)			Powder (%RPM)			Nozzle Gas (l/min)	
	30	35	40	45	50	2.25	1.5	1	0.5	0.35	0.2	0	800	1200	1600	2000	600	1200	1800	7	14	21	4	8
139	+	-	-	-	-	-	-	-	-	-	-	+	-	-	+	-	-	+	-	-	+	-	-	+
140	+	-	-	-	-	-	-	-	-	-	-	+	-	-	+	-	-	-	+	-	+	-	-	+
141	+	-	-	-	-	-	-	-	-	-	-	+	-	-	+	-	-	-	+	-	-	+	+	-
142	+	-	-	-	-	-	-	-	-	-	-	+	-	-	+	-	-	-	+	-	-	+	-	+
143	+	-	-	-	-	-	-	-	-	-	-	+	-	-	-	+	+	-	-	-	+	-	-	+
144	+	-	-	-	-	-	-	-	-	-	-	+	-	-	-	+	-	+	-	-	+	-	-	+
145	+	-	-	-	-	-	-	-	-	-	-	+	-	-	-	+	-	-	+	-	+	-	-	+
146	+	-	-	-	-	-	-	-	-	-	-	+	-	-	-	+	-	-	+	-	-	+	+	-
147	+	-	-	-	-	-	-	-	-	-	-	+	-	-	-	+	-	-	+	-	-	+	-	+

Appendix C

Co-authored Papers relating to this work

Paper 1

CrossMark

Microstructure and oxide particle stability in a novel ODS γ-TiAl alloy processed by spark plasma sintering and laser additive manufacturing

C. Kenel[a,b], K. Dawson[c], J. Barras[d], C. Hauser[d], G. Dasargyri[a], T. Bauer[e], A. Colella[f], A.B. Spierings[e], G.J. Tatlock[c], C. Leinenbach[a,*], K. Wegener[b]

[a] Empa - Swiss Federal Laboratories for Materials Science and Technology, Überlandstrasse 129, 8600, Dübendorf, Switzerland
[b] ETH Zürich, IWF - Institute for Machine Tools and Manufacturing, Leonhardstrasse 21, Zurich, Switzerland
[c] Centre for Materials and Structures, School of Engineering, University of Liverpool, Brownlow Hill, Liverpool, L69 3GH, UK
[d] TWI Technology Centre Yorkshire, Advanced Manufacturing Park, Wallis Way, Catcliffe, Rotherham, S60 5TZ, UK
[e] Inspire AG, icams, Lerchenfeldstrasse 5, St. Gallen, Switzerland
[f] MBN Nanomaterialia S.p.A., Via G. Bortolan 42, 31050, Vascon di Carbonera (TV), Italy

ARTICLE INFO

ABSTRACT

In this work, a novel oxide dispersion strengthened titanium aluminide alloy (Ti-45Al-3Nb- $< 0.2Y_2O_3$ at.%) was developed for powder-based processing technologies with a focus on spark plasma sintering and additive manufacturing. Titanium aluminides are promising structural intermetallics for weight reduction and an increased performance of high temperature components. The alloy design and selection process was supported by computational thermodynamics based on the CALPHAD approach, taking into account requirements for processing as well as long term alloy behavior under service conditions. Processing trials using spark plasma sintering, direct metal deposition and selective laser melting were conducted to study the alloy behavior, microstructure formation and introduction as well as stability of the ODS particles. Additionally, thermal annealing on the sintered and laser consolidated material was performed. Conventional dual phase α_2-Ti_3Al and γ-TiAl duplex and near-lamellar microstructures were obtained from the processed material. The ODS particles were homogeneously distributed in the alloy matrix after processing in the liquid state. For the direct metal deposition process, the novel alloy was compared to the established GE48-2-2 alloy (Ti-48Al-2Cr-2Nb) in terms of phases, microstructure and texture after processing. A significantly reduced texture formation was observed with the novel alloy. The hardness of the consolidated material shows superior properties for ODS-containing TiAl compared to ODS-free material. This work provides a first step towards tailored alloys for AM and the production of ODS TiAl alloys.

1. Introduction

Titanium aluminides are promising candidates for high temperature capable light-weight materials to increase efficiency and performance in aerospace and automotive applications [1,2]. In recent years, additive manufacturing (AM) has become an interesting alternative to conventional processing like sintering or casting, providing additional geometrical freedom and optimized components with higher complexity, fewer joints and reduced weight. Titanium aluminides are also increasingly processed using powder bed fusion by selective laser melting (SLM) [3–5] and electron beam melting [6–8] as well as directed energy and blown-powder based laser metal deposition (DMD) [5,9,10]. Beside the potentially increased geometrical complexity, AM also allows the production of novel alloys and composites directly in the manufacturing process [9]. The non-equilibrium processing conditions involving high cooling rates create a need for detailed studies in order to develop and select alloys for AM. In this work, the alloy design route is based on previous studies on the influence of cooling rate and composition on the microstructures in rapidly solidified binary Ti-Al and higher-order TiAl alloys [11,12]. Recent *in situ* rapid solidification studies using synchrotron X-ray diffraction could also show the non-equilibrium solidification path in rapidly solidified Ti-48Al [13].

Oxide dispersion strengthened (ODS) alloys have been produced for decades due to their beneficial properties at high temperature as strength retention and creep resistance. Due to particle coarsening, agglomeration and slag-off during casting, powder metallurgical methods, such as sintering, are usually applied for the manufacturing of ODS alloys. Recent studies on Fe-based ODS alloys have proved the

possibility to process ODS alloys using liquid state AM technologies and retaining a small dispersoid size by taking advantage of the high solidification and cooling rate inherent to the process [14]. The combination of ODS alloys with AM processing technologies opens a new field for the production of parts with complex shapes, directly from powder. In this work, this approach is expanded to the promising TiAl alloys to produce ODS TiAl alloys by liquid state AM and solid state spark plasma sintering (SPS). This emerging sintering technique has been successfully applied to produce geometrically simple as well as near-net shape parts from titanium aluminides [15,16]. While other aluminide systems have been modified to yield ODS alloys, e.g. ODS FeAl, only a few attempts at ODS TiAl alloys are reported. Er and Gd have been added to the melt to form the corresponding oxides *in situ*, but the particles were not homogeneously distributed [17,18]. Mechanically alloyed Ti-48Al-2Cr-2Nb with Y addition formed Al-Y-O complex oxides after hipping [19]. Grain growth retention up to 1423 K was reported together with no losses in ductility or fracture toughness due to particle formation. To the authors knowledge, no attempts to combine ODS TiAl alloys with AM have been performed so far.

In this work a novel ODS β-solidifying γ-TiAl was studied for powder-based consolidation based on computational thermodynamics and experimental work and taking into account service and processing conditions. The results from consolidation tests by SPS, SLM and DMD are compared in terms of the resulting microstructures, their evolution upon thermal annealing and size of the incorporated dispersoids. Finally, the influence of the processing energy density on dispersoid size and processability of the alloy are discussed. This novel class of material is foreseen to enhance the high temperature capabilities of titanium aluminides by oxide dispersion strengthening combined with geometrical freedom of additive manufacturing.

2. Alloy design and selection

The selection of the alloy serving as matrix for oxide particle strengthening and the second phase itself is dictated by various factors related to service conditions, processing technology and material compatibility. Naturally, a low density and high strength is desired for TiAl alloys to provide high density-normalized specific properties and save weight in structural components. Additional technical requirements in this work were a high chemical homogeneity, a homogeneous distribution of the incorporated oxide particles and microstructural stability at elevated temperatures. From a processing point of view, low anisotropy in as-processed parts is desired and the compatibility of the alloy and the particles for powder-based sintering and AM technologies as SLM and DMD is required. Based on the technical requirements, specific alloy requirements can then be formulated. In modern TiAl alloys enhanced strength is achieved by the stabilization of a higher phase fraction of α_2-Ti$_3$Al of 20–30% [2,20]. This is typically achieved by a lower Al content of 43–45 at.% compared to earlier Al-rich TiAl alloys, as for example in the Ti-48Al-2Cr-2Nb alloy. Additionally, Nb is commonly added to enhance oxidation resistance and high temperature strength. Regarding the oxidation resistance, the Al content should be maximized at the same time, which is a competing requirement to β-solidification and a high fraction of α_2. So the selected alloy should contain an enhanced fraction of α_2 combined with moderate Nb additions and maximum Al content to ensure oxidation stability under operation conditions. The most beneficial properties in terms of balanced creep resistance, strength and toughness is then typically achieved with lamellar or near-lamellar microstructures consisting of alternating plates of α_2-Ti$_3$Al and γ-TiAl [1]. Additionally, Ti-Al alloys solidifying solely by the β-phase were found in Ref. [2] to strongly reduce texture and segregation in cast parts. In studies on rapidly solidified binary Ti-Al and ternary Ti-Al-Nb it was found, that these alloys also show strongly reduced segregation behavior under non-equilibrium conditions involving high cooling rates [11,12]. In Al-rich alloys strong segregation of Al was observed, forming a highly Al-enriched liquid
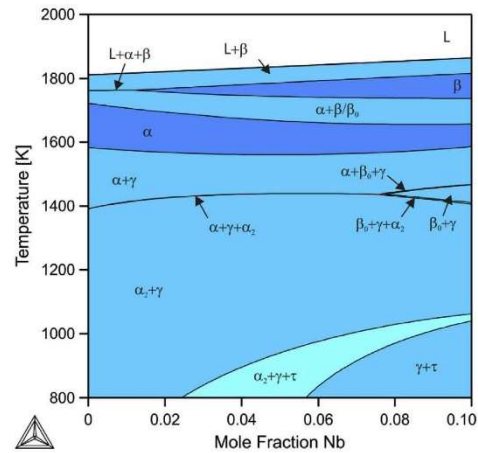
Fig. 1. Calculated isopleth Ti-45Al-(0–10)Nb using a published assessment [22]. Solid single phase (dark), dual phase (intermediate) and triple phase fields (bright) are indicated. The liquid phase field is shown in white. The disordered α-Ti and β-Ti phases, the ordered variants α_2-Ti$_3$Al and β_0/B2 as well as the γ-TiAl and τ-Ti$_4$NbAl$_3$ phases are shown.

towards the final stage of solidification, while Al-lean alloys show only slight changes in Al and Nb content throughout the metastable α_2-rich microstructure. The formation of a supersaturated metastable phase can then later be exploited to produce fine structured material by heat treatments. Based on these findings, the Ti-45Al-xNb system was chosen as a basis for the further alloy selection process.

Supporting thermodynamic calculations were performed based on the CALPHAD approach (CALculation of PHAse Diagrams) using Thermo-Calc 2015a [21] in combination with a published assessment of the Ti-Al-Nb system [22]. Fig. 1 shows a calculated isopleth along Ti-45Al-(0–10)Nb. With increasing Nb additions, the alloy changes from the (quasi-)peritectic solidification type to full β-solidification. At the same time the γ-solvus temperature is slightly decreased and the α → α_2 + γ decomposition temperature is increased. The former reduces the necessary temperature for solution heat treatments in the α-phase field, while the latter defines the theoretical upper temperature limit of the fully intermetallic structure. At lower temperatures a ternary phase, τ-Ti$_4$NbAl$_3$, is predicted to be stable above 2.25 at.% Nb at 800 K. In this work, this phase is considered as an unwanted constituent. However, Nb diffusion is rather slow at low temperatures and thus its formation is expected to be suppressed also at higher Nb content. Under non-equilibrium conditions, extended β-solidification was observed in binary Ti-45Al and ternary Ti-45Al-Nb [12]. For simultaneously Al- and Nb-rich β-solidifying alloys the formation of large amounts of massively transformed γ_m was observed. Consequently, a slight stabilization of the β-phase is sufficient to ensure the desired solidification path. Based on the data in Fig. 2, no substantial changes are achieved in the γ-solvus and α → α_2 + γ decomposition temperature beyond alloying levels of 3 at.% Nb.

For processing of ODS alloys maintaining a homogeneous particle distribution is crucial. This problem becomes substantial, when the alloy is processed in the liquid state. ODS alloys are generally not processable by casting due to particle agglomeration and coarsening. Consequently, ODS alloys are typically processed in the solid state using powder metallurgical methods such as sintering and extrusion. In AM, the high solidification and cooling rates enable the retention of homogeneously distributed particles in Fe-base alloys [14]. It can be expected, that a strongly segregating Ti-Al alloy may also show local particle trapping in inter-dendritic spaces and agglomeration of
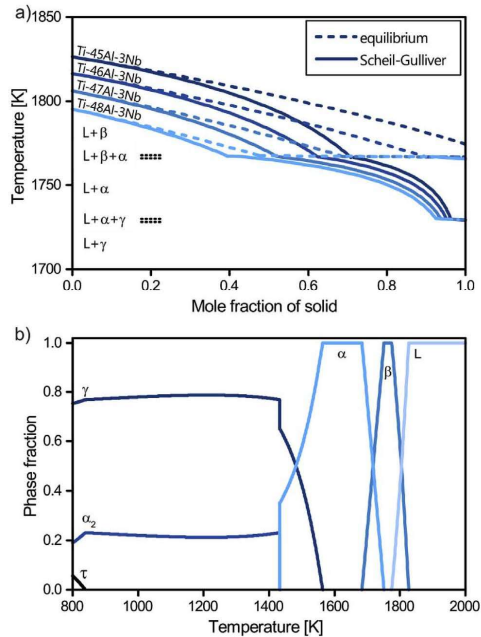
Fig. 2. a) Calculated solidification path of Ti-(45–48)Al-3Nb assuming equilibrium (dashed) and non-equilibrium conditions according to the Scheil-Gulliver model (solid) and b) calculated phase fractions versus temperature for Ti-45Al-3Nb using published data [22]. The stable phases and the fractions of the α, β, α₂, γ and τ phases are indicated.

particles in the remaining melt. If particles are pushed instead of incorporated by the proceeding solidification front, segregation and the formation of a persistent liquid phase prolonging solidification allow for longer time for dispersoid coarsening as well as agglomeration in the inter-dendritic spaces. Additionally, the size of the oxide particles is ideally kept as small as possible to ensure good mechanical and creep properties. This requires a short lifetime of the melt pool, which translates to a low melting range for the chosen alloy. Fig. 3a shows the calculated solidification paths for Ti-(45–48)Al-3Nb for equilibrium and non-equilibrium Scheil-Gulliver conditions. Under equilibrium conditions, only the Ti-45Al-3Nb alloy is expected to solidify solely by the β-phase. Applying the Scheil-Gulliver model, all compositions are predicted to show substantial segregation and final solidification by direct formation of γ from a highly Al-enriched melt. As indicated before, β-solidifying alloys were found to show low segregation under near-equilibrium conditions [23,24] as well as at high cooling rates [12].

Consequently, the effective solidification path follows more closely the equilibrium curve for Ti-45Al-3Nb, while it is better described by the Scheil-Gulliver model for the Al-rich Ti-48Al-3Nb. This discrepancy between the straight-forward application of a simple model and real behavior can be explained by the different diffusivities in the α and β phases. While α has a dense hexagonal close-packed structure, β is body-centered cubic with reduced packing density. Combined with the higher temperature at which β is stable, (back-)diffusion in the β-phase is fast enough to ensure full solidification by β, without the formation of an Al-enriched liquid.

Based on the discussed considerations, Ti-45Al-3Nb was selected as the base alloy for oxide particle incorporation. Fig. 3b shows the calculated phase fractions of the stable phases versus temperature in this alloy. After solidification by β, the alloy crosses the α single phase field before forming γ and finally α₂ and γ become the stable phases. The α₂-fraction is stable above 20% and almost independently from temperature. This ensures additional microstructural stability if components are subjected to varying temperature as both, α₂ and γ, remain stable at the same amount. At low temperatures, a small amount of τ is predicted. However, its solvus temperature is lower than the operation temperature limit and consequently no formation of τ is expected.

3. Experimental

3.1. Powders

Ti-45Al-3Nb and Ti-45Al-3Nb- < 0.2Y₂O₃ (at.% and mol.%, respectively, for all compositions in this work) intermetallic powders (hereafter named OX 45-3 and OX 45-3 ODS) used for consolidation were produced by mechanical alloying and were supplied by MBN Nanomaterialia S.p.A., Italy. High-energy ball milling (HEBM) of the elemental and oxide powders, as described by Suryanarayana and Froes [18], was performed in equipment made from Ti and under protective atmosphere to avoid contamination in the proprietary Mechanomade® process specifically developed by MBN for the manufacture of TiAl-based ODS material for AM. HEBM was performed with a Ball to Powder Ratio (v/v) 10:1 and with a specific energy of 10.5 kWh/kg. Loading and downloading of the powder from the reactor was made under protective atmosphere (Argon) to prevent oxidation. Other processing details are courtesy of MBN. From the yttria-containing variant, two size fractions with 10–45 μm and 46–106 μm particle size were obtained by sieving (Table 1). From the yttria-free reference alloy only the finer fraction was retrieved for comparative SPS consolidation. The powders produced by HEBM have a globular but irregular shape and a fine structure of typically sub-micrometer thin Nb-rich flakes is visible (Fig. 3a and b). Internal porosity is also observed. For comparative DMD processing trials, a gas-atomized Ti-48Al-2Cr-2Nb (GE48-2-2) powder with a particle size of 46–106 μm was sourced from LPW Technology, UK. This powder is spherical with little internal porosity and has a fine microstructure consisting of equiaxed γ and α₂ lamellae (Fig. 3c).
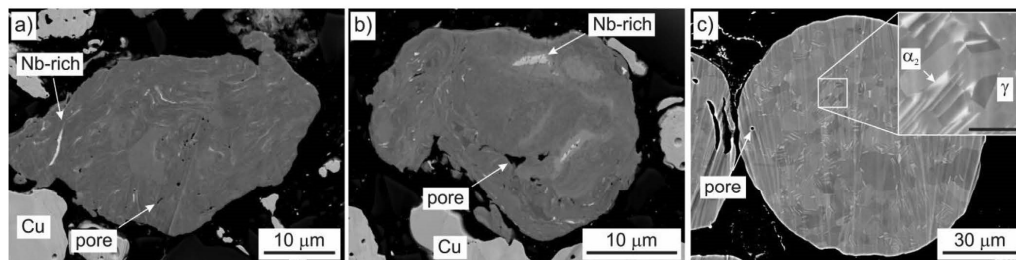
Fig. 3. BSE SEM micrographs of a) OX 45–3, b) OX 45-3 ODS and c) GE48-2-2 (inset: Scale bar is 5 μm). The bright Cu particles in a) and b) are part of the used embedding material.

Table 1
Alloy designation, composition, particle sizes and applied consolidation technology of the studied alloys.

Alloy	Composition (at.%, mol. %)	Particle sizes (µm)	Consolidation
OX 45-3	Ti-45Al-3Nb	10–45	SPS
OX 45-3 ODS	Ti-45Al-3Nb- < 0.2Y₂O₃	10-45 and 46-106	SPS, SLM, DMD
GE48-2-2	Ti-48Al-2Cr-2Nb	46–106	DMD

3.2. Consolidation

Solid state sintering was performed by SPS on a HP D 10 commercial setup (FCT Systeme GmbH, Germany) in a cylindrical graphite die lined with graphite sheets. Sintering of the 10 mm high billets was performed at a pressure of 50 MPa under vacuum in pulsed current mode with 12 pulses of 3 ms followed by a waiting time of 6 ms with zero current. The heating rate was 100 K/min up to the maximum temperature of 1598 K with a 2 min holding stage before cooling. Heating parameters were adapted from Molénat et al. [15]. In order to compare different laser processing technologies, the area and volume energies E_a and E_v were calculated according to

$$E_a = \frac{P}{v \cdot h}, \quad E_v = \frac{P}{v \cdot h \cdot d} \tag{1}$$

where P is the laser power, v is the scanning speed, h is the hatch distance and d is the layer thickness. SLM was performed on a ConceptLaser M2 (ConceptLaser GmbH, Germany) equipped with a fiber laser operated at 1070 nm in continuous wave mode with a maximum power output of 200 W and a diameter of 100 µm at the focal plane. The powder layer thickness was 50 µm and E_a and E_v were 4.5 J/mm² and 90 J/mm³, respectively. The selected parameters are the result of a study on SLM processing of complex geometries from the OX 45-3 ODS alloy which will be presented in a further paper. The sample geometry is a cuboidal 5 × 5x1.6 mm³ build consisting of 32 individual layers (see Supplementary Fig. S1a). A unidirectional cross-hatched exposure strategy was applied to ensure a homogeneous energy input. Ar 4.8 was used as processing gas and the oxygen content was controlled to be below 0.1%. DMD was performed using a tri-beam coaxial powder delivery head with a TruDisk 8002 laser source (Trumpf Laser GmbH, Germany) with a maximum power output of 5.3 kW and a spot size of 1.3 mm. For precise mounting, the deposition head is mounted on a Reis RV60-40 robot (Reis Robotics, Germany). He was used as transport gas, Ar 4.8 was as applied as shielding gas during processing. The build geometry of OX 45-3 ODS is a cuboid with 20 × 20 × 1.4 mm³ consisting of 5 layers (Fig. S1b). GE48-2-2 has been deposited as a 14 layer 20 × 15 × 5 mm³ block (Fig. S1c). For GE48-2-2 the base plate was inductively preheated to 973 K to reduce residual stress formation and cracking. In order to reduce the thermal impact on the dispersoids, the ODS alloy was processed without preheating and at lower energy input. The applied E_a and E_v for OX 45-3 ODS and GE48-2-2 were 120 J/mm², 179 J/mm³ and 444 J/mm³, 484 J/mm³, respectively. Both alloys were processed with a bi-directional deposition strategy. The base plates for SLM and DMD were produced from Titanium grade 2.

3.3. Thermal annealing

Short term and high temperature annealing of SPS, SLM and DMD processed specimens were conducted in an induction furnace (in-house developed at Empa, Switzerland) under 5 mbar of Ar 6.0 to avoid excessive elemental losses due to evaporation. The specimen temperature is directly controlled by a ratio pyrometer (QKTR 1085-1, Maurer, ± 1 K). Thermal annealing below 1273 K was performed in a full metal-lined high vacuum furnace (Cambridge, UK) at pressures < 10⁻⁵ mbar. The specimen temperature was controlled by calibrated thermocouples placed next to the specimen.

3.4. Characterization

For the microstructural analysis the specimens were embedded into epoxy resin and polished using diamond suspensions from 9 to 1 µm. The final polishing step was performed using a non-crystallizing silica solution (20 nm) with H₂O₂ addition. To remove the remaining surface deformation layer present after the final polishing step, Ar ion beam polishing was applied using a Hitachi IM4000 ion beam polisher at 4 kV acceleration voltage and an incident beam angle of 80° to the surface normal direction. After surface preparation, the specimens were investigated using scanning electron microscopy using a Hitachi S3700N equipped with BSE and EDX detectors (EDAX) for imaging and a Hitachi S4800 for high resolution imaging and particle measurements in SLM and DMD processed specimens.

On selected specimens X-ray diffraction (XRD) and XRD pole figure measurements were performed with Cu Kα radiation using a Bruker D8 DISCOVER equipped with a LynxEye 1D detector. The measurement conditions were 40 kV and 40 mA with a step size of 0.02° (2Θ). XRD pole figure data was corrected for defocusing effects and normalized to yield multiples of random distribution (m.r.d.) using the MULTEX software package of Bruker. Additional pinhole snouts were used to restrict the beam diameter to the area of the specimens.

Solid state SPS sintered material was analyzed using transmission electron microscopy (TEM) and scanning transmission electron microscopy (STEM) on an aberration-corrected JEOL 2100FCs S/TEM operating at 200 kV. The electron-transparent lamellas were prepared using a FEI Helios 600i dual beam focused ion beam (FIB) instrument. Specimens were prepared by the lift out method and low energy (2 kV) polishing was applied as final step.

The size of the lamellar colonies and γ-TiAl grains in SPS sintered and heat treated material was determined using the line intersection method on 2560 × 1920 pixel BSE SEM micrographs recorded at 2000× magnification along a rectangular line grid. The fraction of lamellar colonies was determined by their area fraction on the same micrographs. The size distribution of the ODS particles in SPS material was measured on 1024 × 1024 pixel bright-field STEM micrographs at 20′000× magnification using the maximum particle diameter ($n_{SPS} = 1718$). The fewer and larger ODS particles after SLM and DMD processing were measured on a series of high-resolution SEM micrographs at up to 4096 × 3200 pixels and 32′000× magnification ($n_{SLM} = 386$ and $n_{DMD} = 391$). Particle densities were estimated from the same micrographs assuming particle detection in a 2D plane yielding the area number density N/A with N the number of particles and A the area. The volume particle density is then calculated as

$$\frac{N}{V} = \left(\frac{N}{A}\right)^{\frac{3}{2}} \tag{2}$$

with V being the volume. The mean particle center distance l_c can then be estimated as

$$l_c = \left(\frac{3 \cdot V}{4 \cdot \pi \cdot N}\right)^{\frac{1}{3}} \tag{3}$$

assuming a spherical volume element centered at the particle position. Using the median size of the particles d_{median} the inter-particle distance l can be calculated simply as

$$l = l_c - d_{median} \tag{4}$$

For TEM lamellae with a certain thickness, the particle volume density is clearly overestimated by Equation (2). However, the error of this estimation can be neglected in this case where the order-of-magnitude differences in between the different consolidation methods are of interest.

The fraction of retained dispersoids f is calculated using the determined median dispersoid size and volume number densities according to

$$f = \frac{N}{V} \cdot \frac{4 \cdot \pi}{3} \cdot \left(\frac{d_{median}}{2} \right)^3 \qquad (5)$$

Vickers hardness (HV) was measured using a Fischerscope HM2000 (Fischer, Germany) on polished specimens prepared for microscopic investigation. The indentation with the Vickers diamond tip was performed with a maximum load of 400 mN and a load increase time of 20 s. For bulk material a minimum of 25 indentations with a spacing larger than 50 μm were measured to ensure statistical relevance of the data. For SPS specimens the hardness was measured perpendicular to the pressing direction, for SLM and DMD the measurements were performed on the z-y plane where z is the build direction. The machine is calibrated using standards to ensure data repeatability and create the necessary correction functions. The typical indentation diameter is in the order of 10 μm.

4. Processing results and discussion

In this section the results from solid and liquid state powder processing are shown. Sintered material was used to study the formed microstructure and its stability upon high temperature annealing. SLM and DMD were applied to test the alloy behavior under AM processing conditions and evaluate microstructure formation, texture and the possibility to achieve a desired microstructure by thermal annealing. Additional TEM investigations provide information about the size and distribution of the oxide particles in the alloy matrix. Finally, the particle incorporation is compared for solid state SPS and liquid state additive SLM and DMD.

4.1. Spark plasma sintering

Solid state consolidation using SPS was successful in producing dense material from the OX 45-3 ODS powder. Fig. 4a shows the fine grained duplex microstructure consisting of lamellar colonies and equiaxed γ and α_2 grains in the as SPS state. After the SPS consolidation, the specimen cools down with a maximum cooling rate of 9 K s^{-1}. Consequently, the specimen contains a high fraction of α_2 phase around 49% and is in a metastable state. For any application, the microstructure needs to be stabilized closer to its equilibrium state. Additionally, fast non-homogeneous cooling gives rise to residual stresses in the as SPS consolidated material. To achieve the stabilization a thermal annealing at 1123 K for 12 h in vacuum was performed. Fig. 4b shows the resulting structure with γ and α_2 fractions of around 75% and 25%, respectively, and a lamellar fraction of 26%. Comparing these results to the calculated phase fractions shown in Fig. 3b, the obtained state is close to equilibrium. Note that the consolidation by SPS was performed at 1598 K, which is in the α phase field for the chosen alloy. So already during consolidation, the formation of a coarse grained lamellar microstructure would be expected. Conventional heat treatments to obtain lamellar microstructures for TiAl alloys typically involve a high temperature treatment in or close to the α phase field at temperatures around 1573 K–1673 K, depending on the composition. Fig. 4c and d shows the resulting microstructures after two step thermal annealing involving a high temperature step at 1573 K or 1673 K for 15 min and the stabilization treatment described before. The two temperatures were selected based on the calculated phase fractions and are close to the lower and upper boundary of the calculated α phase field for this alloy (1563 K–1683 K). The obtained microstructures are very similar to the one obtained by the stabilization annealing only. The measured intersection length of the equiaxed γ grains was determined as 1.4 $\pm$ 0.8 μm for the stabilized state and 1.5 $\pm$ 1 μm and 1.3 $\pm$ 0.6 μm after the thermal annealing at 1573 K and 1673 K, respectively. The fraction of lamellar grains increased from 26% to 36%
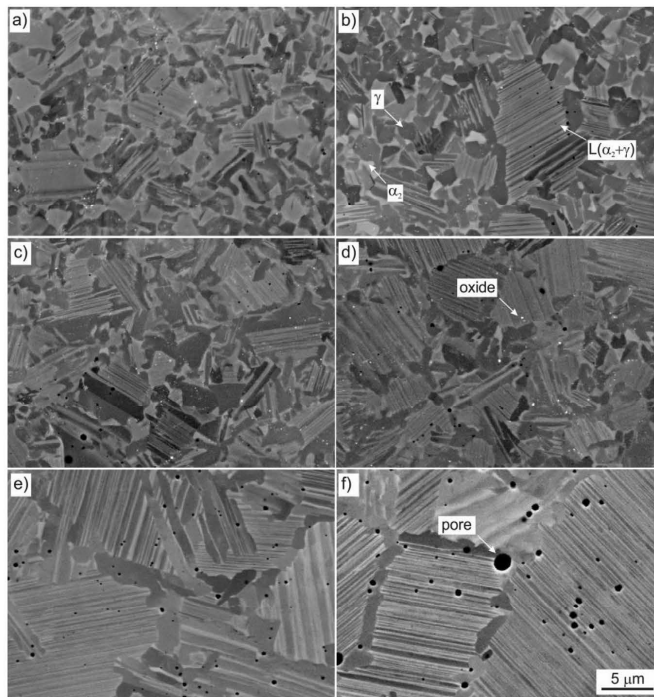
Fig. 4. BSE SEM micrographs of SPS (a–d) OX 45-3 ODS and (e, f) ODS-free OX 45-3 a) in the as SPS state, and after thermal annealing of (b, e) 1123 K/12 h, c) 1573 K/15 min + 1123 K/12 h and (d, f) 1673 K/15 min + 1123 K/12 h. The α_2 (light grey) and γ (dark grey) phases, pores (black) and Y-based oxides (white) are indicated as well as the lamellar colonies formed of $\gamma + \alpha_2$. The scale bar in f) applies for all micrographs.
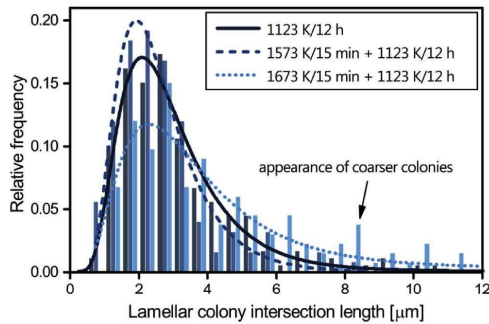
Fig. 5. Distribution of the measured intersection length of lamellar colonies in SPS OX 45-3 ODS after different thermal annealing. Least-square-fitted log-normal distribution curves are shown overlaid.

after 1573 K and to 63% after 1673 K. Fig. 5 shows the distribution of the measured intersection lengths of lamellar colonies after the various thermal annealings for OX 45-3 ODS. Independently from the chosen thermal annealing, the peak values are obtained around 2 μm due to the presence of very small colonies. The mean intersection lengths of lamellar colonies for thermal annealing at 1123 K for 12 h, 1573 K or 1673 K for 15min and the stabilization treatment are 3.2 ± 2.2 μm, 2.6 ± 1.4 μm and 4.4 ± 3.1 μm, respectively. After 1673 K for 15 min the fraction of larger colonies starts to increase, which is also evident from Fig. 4d. At this temperature, the γ grains are slowly dissolving in the disordered α matrix resulting in larger lamellar colonies in the final microstructure. With increasing temperature this process is expected to occur faster as it is observed in the SPS material. Fig. 4e shows the microstructure of the OSD-free variant OX 45-3 after SPS and 1123 K for 12 h. Large lamellar colonies are formed with γ at the colony boundaries along with a multitude of sub-micrometer pores. After a high temperature anneal at 1673 K for 15 min and the stabilization treatment, the microstructure is further coarsened. The mean intersection length of the lamellar colonies after 1123 K for 12 h and 1673 K for 15min plus 1123 K for 12 h are 10.9 ± 8.9 μm and 11.0 ± 8.2 μm, respectively. After high temperature annealing, larger pores appear in the γ-seams along the colony boundaries (Fig. 4f). This pore expansion is explained by a combination of high temperature, absence of strengthening particles and a high internal pressure in the pores. During SPS the pores and any contained gas are compressed with 50 MPa. This is equivalent to an overpressure of 500 bar inside the pores assuming residual gas pores with atmospheric pressure contained in the powder. As the alloy is later annealed, the high internal pressure leads to deformation of the surrounding matrix and an increased pore size. The appearance of the largest pores in the γ-seams further strengthens this argument, as the lamellar structure is expected to have superior creep resistance compared to the γ-phase. Additionally, dissolved gas may be liberated and further contribute to pore expansion. It has to be noted, that the observed pore size is expected to be an overestimate of the true

pore size, as chemo-mechanical final polishing is applied. Thus the material is attacked and exposed pores are expected to increase in size.

The observed behavior upon consolidation and thermal annealing shows an exceptional microstructural stability of the produced SPS ODS alloy variant at high temperatures during consolidation and following thermal annealing. The increased microstructural stability of the SPS material can be directly related to the presence of the ODS particles in the alloy matrix. With the possibility to produce near-net shape turbine blades by SPS the newly developed OX 45-3 ODS alloy or similar ODS TiAl alloys have potential applications as solid state sintered component in high temperature environments in the future. Additionally, microstructural stability is a crucial factor for application of SPS consolidated alloys [16]. The introduction of dispersoids effectively limits colony coarsening and allows production of alloy with colony sizes around 5–10 μm promising interesting mechanical properties at high temperatures.

4.2. Selective laser melting

Liquid state consolidation using SLM was successful in creating test parts with low porosity (Fig. 6). Fig. 6a shows the observed microstructure in the as-processed state. In the as-processed state, the major constituent is a metastable α_2 phase which forms during rapid cooling [12]. Starting from the melt pool boundary, a grain selection process takes place producing a gradient in grain size. Subsequent laser scans partly re-melt the previously deposited material and eliminate the very coarse grains. Again, selected grains continue to grow. Consequently, the deposited material contains fine grained former melt pool boundaries and coarser bulk regions. In the material close to the former melt pool boundary a fine structure is visible originating from the primary β cells later transformed to α are visible. Residual porosity below 5 μm is also observed. Based on the spherical shape it is proposed, that these are caused by the entrapped gas from powder production or processing. Material from the same specimen was subjected to a thermal annealing at 1123 K for 12 h similar to the SPS consolidated material. Fig. 6b shows the obtained near-lamellar microstructure consisting of lamellar $\gamma + \alpha_2$ colonies in a size range of 5–30 μm and sub-micrometer γ and α_2 grains formed at the colony boundaries. These grains show an elongated shape and are oriented typically parallel with respect to each other and to one of the adjacent colonies (inset Fig. 6b). This bimodal lamellar structure, fine inside the colonies and coarse at the boundary in between, can be explained by the kinetics of the phase transformation. First, fast decomposition of the former α grains into primary $\gamma + \alpha_2$ colonies takes place upon thermal annealing. The size and shape of the primary lamellar colonies is similar to the α_2-grains observed in the as processed material. This indicates a direct decomposition of the metastable microstructure upon thermal annealing. Later a slow decomposition of the fine structure into a coarser lamellar structure by discontinuous coarsening starts. This requires diffusion over greater length. At 1123 K the diffusion in TiAl alloys is expected to be rather slow based on their intermetallic ordered structure. Consequently, this second transformation is observed in its initial stage after the thermal annealing. Inside the colonies finely distributed dispersoids are visible
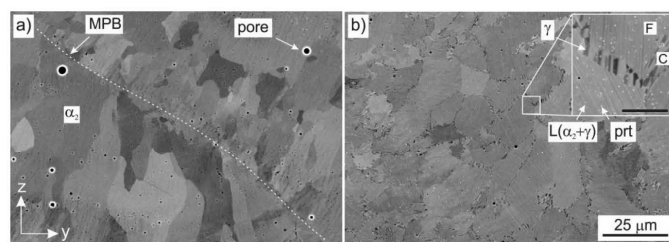

Fig. 6. BSE SEM micrographs of SLM processed OX 45-3 ODS ($E_a = 4.5$ J/mm²) in a) as processed state and b) after thermal annealing at 1123 K for 12 h (inset: scale bar = 4 μm). The observed phases, pores, melt pool boundary (MPB), coarse (C) and fine lamellar (F) regions and dispersoids (prt) are indicated. The scale bar in b) applies for both micrographs. The build direction (z) and the beam translation (y) are shown. The scanning direction (x) is out-of-plane.

as bright spots due to the mass contrast of the yttrium-based oxides (inset Fig. 6b). It needs to be pointed out, that the applied thermal annealing temperature is far below conventional heat treatment temperatures to obtain near-lamellar microstructures. In cast parts of similar composition, temperatures as high as 1653 K in the α-field are applied [23]. This is more than 500 K higher than the thermal annealing which was applied in this work. The formation of a supersaturated metastable microstructure during rapid solidification enables such low heat treatment temperatures and phase decomposition.

The obtained results clearly show that the OX 45-3 ODS alloy can be consolidated using laser processing and be transformed into conventional microstructures afterwards. This opens the space to complex shaped ODS TiAl alloys for highly loaded applications. Detailed studies on suitable processing parameter windows and part integrity are needed in the future to enable the application ODS TiAl alloys.

4.3. Direct metal deposition

Compared to the powder-bed based SLM technique, blown-powder based DMD provides higher deposition rates at higher energy densities. In this work, the applied area energy densities for DMD were a factor of 27 higher than for SLM. Fig. 7 shows the observed microstructures for OX 45-3 ODS and GE48-2-2 in the as-processed and annealed state. The Al-rich GE48-2-2 forms a dendritic microstructure consisting of lamellar $\gamma + \alpha_2$ colonies and inter-dendritic γ phase. The Al-leaner OX 45-3 ODS forms a columnar grained structure consisting mainly of the α_2 phase with some spurious γ. The largest dispersoids are visible as white spots in the SEM micrograph. After a thermal annealing at 1123 K for 12 h both alloys start to recrystallize (Fig. 7c and d). While GE48-2-2 retains
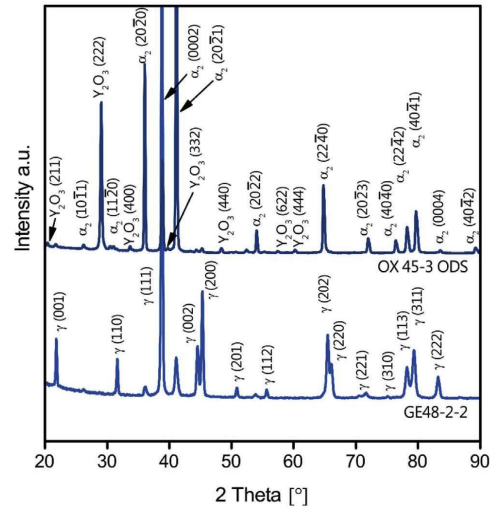
Fig. 8. XRD spectra of DMD processed OX 45-3 ODS (top) and GE48-2-2 (bottom). Peaks of the intermetallic α_2 and γ phases and of Y_2O_3 are indicated.
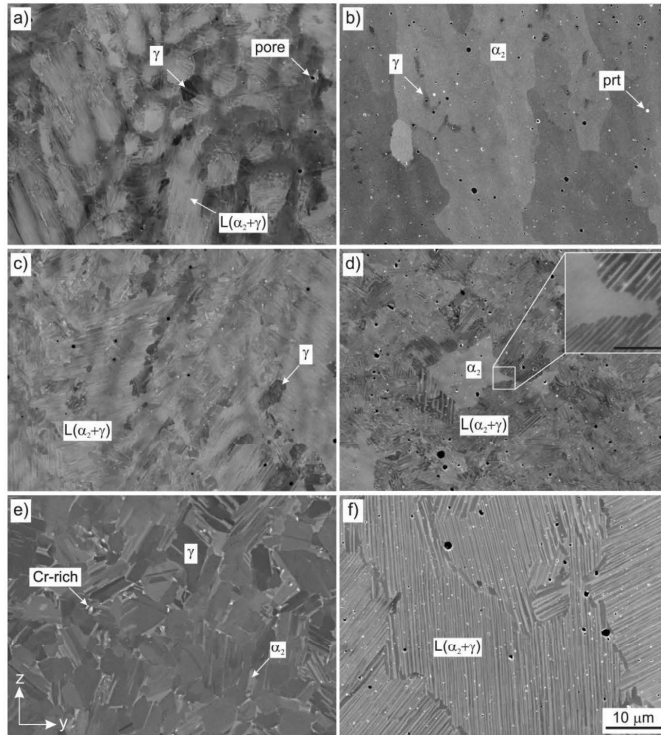
Fig. 7. BSE SEM micrographs of DMD processed a, c, e) GE48-2-2 (E_a = 179 J/mm^2) and b, d, f) OX 45-3 ODS (E_a = 120 J/mm^2). (a, b) in the as processed state and after thermal annealing of (c, d) 1123 K/12 h and (e, f) 1573 K/15 min + 1123 K/12 h. The α_2 and γ phase, pores and dispersoids (prt) are indicated. Bright spots in e) correspond to Cr-rich areas. The scale bar in f) applies for all micrographs (inset: scale bar = 2 μm). The build direction (z) and the beam translation (y) are shown. The scanning direction (x) is out-of-plane.

its fine lamellar structure with equiaxed γ, OX 45-3 ODS decomposes into small lamellar γ + α$_2$ colonies. Residual areas between the colonies still resemble the α$_2$ structure observed in the as processed state. The presence of a dual phase structure in these areas with a very fine lamellar spacing would be expected based on the results of annealed SLM-consolidated material (Fig. 6b). If present, the resolution of the SEM or compositional difference and thus contrast was not high enough to resolve this structure. After annealing at 1573 K for 15 min and 1123 K for 12 h, GE48-2-2 is fully transformed into a duplex structure with an increased amount of γ. This is in agreement with established phase diagram data on Ti-48Al-2Cr-2Nb predicting 1573 K to be in the α + γ two phase field and consistent with observations on DMD of similar alloys [5]. OX 45-3 ODS forms a fully lamellar microstructure with ragged colony boundaries, as the chosen temperature is in the α single phase field. Fig. 8 shows XRD spectra of DMD processed OX 45-3 ODS (top) and GE48-2-2 (bottom). The ODS alloy contains a large fraction of α$_2$ with a minor γ content. Additionally, Y$_2$O$_3$ is clearly observed which is enriched at the surface due to partial slagging-off of the oxide particles in the last deposited layer during processing. The GE48-2-2 alloy contains mainly γ together with α$_2$ based on the relative intensities of the γ(111) and α$_2$ (20$\bar{2}$1) peaks. This different behavior is explained by the dependence of the solidification path on alloy composition. OX 45-3 ODS is fully β-solidifying, while GE48-2-2 is forming primary β, undergoes a peritectic reaction and then solidifies by α under equilibrium conditions. Recent *in situ* XRD experiments on Ti-48Al at high cooling rates by Ref. [13] show that the formation of β-phase is suppressed at high cooling rates and the alloy forms primary α phase. Additionally, it is presented in Ref. [11] that Al-rich alloys typically show much stronger segregation than Al-lean alloys. Consequently, GE48-2-2 shows a fine structure dominated by the solidification of the α phase, whereas OX 45-3 ODS shows a coarse structure originating from the primary β phase. Beside the phase fractions and segregation, the texture is also strongly influenced by the alloy composition. Fig. 9 shows XRD pole figures for DMD processed GE48-2-2 (top) and OX 45-3 ODS (bottom) for the γ(111)/α$_2$(0002) reflection (left) and the α$_2$ (20$\bar{2}$1) reflection (right). For GE48-2-2 a fiber texture is observed for both reflections while OX 45-3 ODS is much less textured based on the intensity

distributions. No distinct alignment of the principal peaks of α$_2$ and γ was observed with the out-of-plane direction in the center of the pole figures. Based on the observed intensity distributions, γ(111)/α$_2$(0002) is slightly oriented towards the in-plane direction, whereas α$_2$(20$\bar{2}$1) is observed more frequently at lower angles to the surface normal direction. The distinct ring shape for the α$_2$(20$\bar{2}$1) pole figure of GE48-2-2 is formed by the other planes of the α$_2${20$\bar{2}$1} family of planes rotated around the out-of-plane direction. The calculated ideal inter-planar angles between α$_2$(20$\bar{2}$1) and α$_2$(20$\bar{2}$1) and between α$_2$(20$\bar{2}$1) and α$_2$(20$\bar{2}$1) are of 52.32° and 56.31°, respectively. These angles agree well with the observed ring shape between 50 and 70° taking into account the spread of the central peak of ± 11° and ± 9° parallel and perpendicular to the laser scan direction, respectively. This spread indicates a misalignment of the α$_2$ phase with the out-of-plane direction and is caused by slightly different crystal orientation depending on the position in the overlapping melt pools. Consequently, the ring shape of the α$_2${20$\bar{2}$1} plane family is also spread. The different phase fractions of γ and α$_2$ in the two studied alloys have to be taken into account when interpreting the pole figure data for γ(111)/α$_2$(0002). In GE48-2-2 the resulting pole figure is dominated by the principal orientation of the γ phase as the main component. On the contrary, the pole figure of the same reflection for OX 45-3 ODS reflects the orientation of mainly α$_2$(0002), as only a minor fraction of γ is present in this alloy. The difference in data smoothness for the two alloys is explained by the different grain sizes of the formed microstructures. GE48-2-2 formed a very fine microstructure providing a multitude of different grains that simultaneously fulfill the diffraction conditions. The coarser structure in OX 45-3 ODS provides only a reduced number of grains that can contribute to diffracted intensity in a certain direction. Thus a speckle-like intensity distribution is observed in the pole figures of OX 45-3 ODS. However, these differences related to the dual phase microstructures of the alloys do not the change the fact, that the overall degree of texture after DMD processing is significantly reduced in the β-solidifying OX 45-3 ODS alloy. As observed from the orientations of the lamellar colonies after annealing, there seems to be also no preferential lamellar orientation after thermal annealing (Fig. 7d and f).

The results clearly show the possibility to consolidate OX 45-3 ODS using DMD. Furthermore, the chosen β-solidifying alloy induces significantly reduced texture in as-processed parts. Finally, the obtained microstructure can be transformed to a conventionally applied one by adapted thermal annealing (see Section 4.2). The compatibility of the developed ODS alloy with DMD opens possibilities to produce larger complex shaped ODS TiAl components which cannot be efficiently produced by powder-bed based methods as SLM or have too intricate features to be just produced by solid state sintering. Furthermore, the geometrical freedom in DMD processing facilitates controlled preheating to avoid the formation of large residual stresses, part deformation and potentially cracking.

4.4. ODS particle incorporation

It was shown that the OX 45-3 ODS alloy can be consolidated using solid state and additive liquid state processing technologies. In ODS alloys, the size and distribution of the ODS particles is crucial for the desired properties. Based on the well-known Orowan-relation

$$\sigma_{or} = M\frac{Gb}{2(l - r)} \tag{6}$$

where M = 3 is the conversion factor between shear and normal stress, G is the shear modulus, b is the Burgers vector, the stress σ_{or} is increased with smaller particle diameter r and smaller inter-particle distance l for non-cuttable particles. For dispersion strengthened ordered intermetallics more complex models are applied in order to account for detachment of the dissociated dislocations from the embedded particles [25]. The optimum dispersoid diameter d is then related to the dissociation width w by $w/d \approx 0.6$. As the involved energies of the formed

Fig. 9. XRD pole figures of DMD processed GE48-2-2 (top) and OX 45-3 ODS (bottom) for the most intense reflections γ(111)/α$_2$(0002) (left) and α$_2$(20$\bar{2}$1) (right). The coloring corresponds to low (blue) to high (red) values of m.r.d. The laser scan direction is horizontal for all subfigures. The part top surface normal is out-of-plane and in the center of the pole figures. (For interpretation of the references to colour in this figure legend, the reader is referred to the web version of this article.)
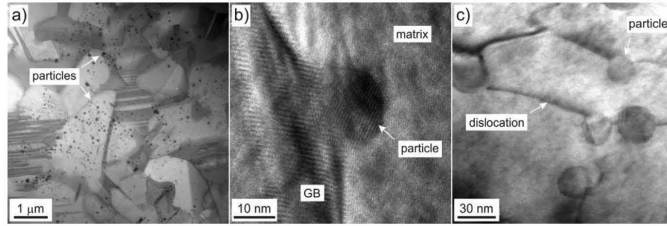
Fig. 10. Microstructure of SPS OX 45-3 ODS stabilized at 1123 K for 12 h a) STEM bright-field micrograph showing the distribution of fine ODS particles, b) HRTEM micrograph of an ODS particle pinning a grain boundary (GB) in the intermetallic matrix, c) TEM micrograph of ODS particles interacting with dislocations.

faults in TiAl alloys are comparably high, the corresponding dislocation dissociation width is typically less than 8 nm [26]. Consequently, the most effective dispersoid size for enhanced creep strength in ODS TiAl alloys is around 13 nm or less. For the dissociated super-dislocations the slightly larger particles are more effective while ordinary dislocations are more effectively hindered in their movement by smaller dispersoids. Fig. 10a shows the distribution of fine dispersoids throughout the intermetallic matrix in SPS OX 45-3 ODS stabilized at 1123 K for 12 h. The median particle size and volume number density were determined as 29 nm and $4.4 \cdot 10^{20}$ m^{-3}. The calculated median particle interspacing is 134 nm. The dispersoids are present in the equiaxed grains as well as in the lamellar colonies. The obtained particle sizes are comparable to the particle sizes in recrystallized PM2000, an established ODS Fe-base alloy [14,27]. Already in the stabilized state, grain boundary pinning was observed (Fig. 10b). The particles stop grain boundary movement and effectively retain a fine microstructure and also seem to slow down the $\gamma \rightarrow \alpha$ phase transformation as discussed in section 4.1. It is observed, that the particles interact with dislocations in the material (Fig. 10c). Dislocation pinning at the particles and bowing in between is evident. During service at elevated temperature these effects can be exploited to retain a desired microstructure - i.e. coarse grains for creep loading - for enhanced mechanical properties and long term stability. Fig. 11a shows the observed particle size distributions for solid state and additive liquid state processing. Fitted log-normal distribution curves are shown overlaid. Comparing these results it is evident, that liquid state processing leads to a certain degree of particle coarsening due to the high temperature and the presence of a liquid phase allowing fast diffusion of the elements necessary for particle growth. The diffusion of Y and O is limiting the growth of pure Y_2O_3 particles. The formation of higher-order oxides containing Ti and/or Al and having various crystal structures has been described earlier for Al-containing ODS alloys [27]. Specifically for TiAl alloys, the formation of Y-Al-O particles has been observed [19]. Consequently, the particle coarsening is not limited only by the diffusion of Y anymore and rapid growth can occur in the liquid state by incorporation of Ti and/or Al. After SPS and stabilization at 1123 K for 12 h a rather sharp size distribution with a median size of 29 nm is preserved. In SLM processed material a slightly broader distribution with a median size of 82 nm is observed. The volume number density is decreased to $7.4 \cdot 10^{18}$ m^{-3}. Consequently, the median particle interspacing is increased to 554 nm. DMD processing leads to a very broad size distribution ranging from sub-50 nm dispersoids to particles with a diameter of several hundreds of nanometers. These large particles are recognizable due to their high Y-content in BSE SEM micrographs (Fig. 7d). In accordance with the coarsening also the volume number density is reduced to $1.1 \cdot 10^{18}$ m^{-3}. The calculated median particle interspacing becomes relatively large with 1043 nm. Comparing the different consolidation methods, reducing the energy input in the material during processing clearly reduces the preserved oxide particle size. The two applied liquid state processing technologies SLM and DMD have greatly different heat input and melt pool sizes based on their laser spot diameters and area energy densities of 100 μm and 1.3 mm, and 4.5 J/mm^2 and 120 J/mm^2, respectively. Fig. 11b shows the correlation of oxide particle size
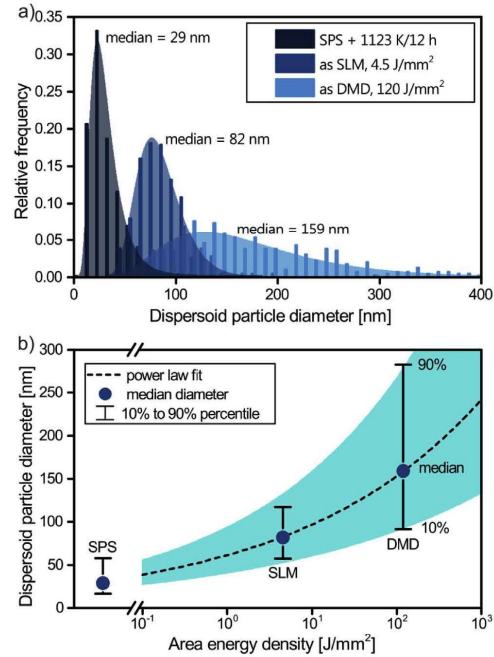

Fig. 11. a) Size distribution of ODS particles in solid state SPS sintered and stabilized, SLM and DMD processed OX 45-3 ODS. Least-square-fitted log-normal distribution curves are shown overlaid as well as the corresponding median value. b) Correlation of median ODS particle diameter and area energy in laser processing. The value for SPS sintered material is shown for comparison. A power law fit and the estimated 10%–90% percentile range are shown overlaid.

distribution and applied area energy density. The results from solid state SPS are shown for comparison. Overlaid is a power law fit of the median particle size according to

$$d = a \cdot E_a^{\frac{1}{m}} \tag{7}$$

where d is the median oxide particle diameter, a is the proportionality constant, E_a is the area energy density and m is the growth exponent. Simulations on melt pool life times in SLM show an approximately linear dependence on applied area energy density [28] (Supplementary Fig. S2). This allows applying a conventional parabolic diffusion-dominated growth model with $d \sim t^{\frac{1}{m}}$ where $t \sim E_a$ is the time and linear proportional to the area energy density E_a. The data and the fitted curve indicate that the energy input would need to be decreased to very low and finally unreasonable values to obtain similar particle sizes by liquid state processing as in solid state SPS material. It also

Table 2
Vickers hardness (HV ± 1σ) of SPS and DMD consolidated ODS-containing OX 45-3 ODS and ODS-free OX 45-3 and DMD consolidated GE48-2-2.

Process and Material	Condition	HV ± 1σ
SPS OX 45-3	1123 K/12 h	441 ± 29
	1673 K/15 min + 1123 K/12 h	409 ± 26
SPS OX 45-3 ODS	as SPS	505 ± 18
	1123 K/12 h	477 ± 16
	1573 K/15 min + 1123 K/12 h	471 ± 23
	1673 K/15 min + 1123 K/12 h	485 ± 15
DMD OX 45-3 ODS	as DMD	564 ± 61
	1123 K/12 h	546 ± 38
	1573 K/15 min + 1123 K/12 h	469 ± 25
DMD GE48-2-2	as DMD	512 ± 45
	1123 K/12 h	410 ± 19
	1573 K/15 min + 1123 K/12 h	358 ± 15

shows the limited effect of slight parameter variations in process control, as area energy input between SLM and DMD in this work differs by a factor of ~ 27, while the median dispersoid size is only increased by a factor of 2. However, if liquid state AM technologies based on very fine focused beams at low power and high scanning speeds are applied, particle sizes comparable to SPS seem to be possible. Generally, the life time of the melt pool needs to be minimized to yield the smallest particles.

The retained fraction of dispersoids after SLM and DMD processing is decreased to 38% and 41%, respectively, compared to SPS material. Slagging-off due to relatively low scanning speeds and slow solidification in DMD explains the observed losses and is confirmed by Y_2O_3 forming on the surface. Generally, a reduction of particles after SLM and DMD processing can be explained by a combination of slagging-off, dissolution and potentially also formation of dispersoids below the detection limit. No Y_2O_3 was observed on the surface of SLM processed material, indicating that the latter two processes play a dominant role. Future work will be dedicated to study the dispersoid size, stability and composition after processing.

4.5. Hardness of consolidated material

The hardness of SPS and DMD consolidated material was measured to analyze the effects of ODS incorporation and different consolidation methods on the mechanical properties (Table 2). Comparing the ODS-containing and ODS-free SPS consolidated alloy a beneficial effect of the yttria addition is evident. After a stabilization annealing at 1123 K for 12 h the ODS-free variant has 441 ± 29 HV, while OX 45-3 ODS has 477 ± 16 HV. This difference gets accentuated after high temperature annealing at 1673 K. The hardness of OX 45-3 is reduced to 409 ± 26 HV, while it is increased in OX 45-3 ODS to 485 ± 15 HV. DMD processed material has a high hardness in the as-processed state due to a high fraction of α_2 (Figs. 7 and 8) After thermal annealing at 1123 K for 12 h the hardness is slightly reduced to 546 ± 38 HV but still significantly higher than for SPS material annealed similarly. After high temperature annealing at 1573 K for 15 min and 1123 K for 12 h, similar hardness values are obtained for SPS and DMD processed OX 45-3 ODS, 471 ± 23 and 469 ± 25 HV, respectively. The DMD processed GE48-2-2 material shows lower hardness after processing and after all thermal annealing compared to OX 45-3 ODS. The similarity of hardness of annealed SPS and DMD material has extensive implications, as the microstructure of SPS and DMD material is different. In SPS material a fine duplex microstructure is observed, while DMD produces first a columnar structure of mainly α_2 that decomposes into a near-lamellar microstructure during thermal annealing (Figs. 4 and 7). Naturally, the finer SPS structure would be expected to provide the higher hardness due to a strength increase according to a Hall-Petch relation. Such behavior is observed when comparing SPS consolidated OX 45-3 and OX 45-3 ODS. The high hardness of DMD processed material indicates that

the size of the lamellar colonies is not the factor determining increased hardness. Although the effect can be attributed to the introduction of the dispersoids, it remains unclear if it is only the presence of the particles or if the dispersoids are partly dissolved in the melt leading to a doping effect of the matrix. Given the reactivity of TiAl alloy melts and the associated problems of finding suitable ceramics for crucibles such a mechanism has to be considered. Despite the hardness cannot be directly used as a measure for the mechanical performance of TiAl alloys, the measurements indicate that the mechanical properties in OX 45-3 ODS are increased by the introduction of Y-based dispersoids. These effects are also observed after liquid phase AM processing by DMD. A more detailed study of the mechanical properties of the consolidated ODS material will be reported in a separate paper.

5. Summary and conclusions

- SPS OX 45-3 ODS has superior microstructural stability up to 1573 K compared to the ODS-free variant. The median particle size is 29 nm at a volume number density of $4.4·10^{20}$ m^{-3}.
- SLM produces a coarse grained α_2-rich microstructure with a median dispersoid size of 82 nm at a volume number density of $7.4·10^{18}$ m^{-3}. Upon annealing at 1123 K for 12 h, microstructural refinement into fine lamellar material is demonstrated. The retained fraction of dispersoids is 38% compared to SPS material.
- After DMD also a coarse grained α_2-rich microstructure is formed. Fine grained material is obtained after heat treatment at 1123 K for 12 h. Coarse grained material for enhanced creep resistance is observed after a two-step heat treatment at 1573 K/15 min + 1123 K/ 12 h. Incorporated particles have a median size of 159 nm at a number density of $1.1·10^{18}$ m^{-3}. The as processed material shows significantly reduced texture and more evenly distributed intensity for the measured $\gamma(111)/\alpha_2(0002)$ and $\alpha_2(2021)$ reflections compared to DMD GE 48-2-2 alloy (Ti-48Al-2Cr-2Nb). The retained fraction of dispersoids is 41% compared to SPS material.
- Hardness measurements show superior values for SPS OX 45-3 ODS compared to its non-ODS counterpart.

From the obtained results it can be concluded that ODS TiAl alloys can be successfully produced by mechanical alloying and be consolidated by SPS, SLM and DMD. Especially the incorporation of small oxide particles using liquid state AM processing based on rapid solidification is a novel approach in TiAl alloys and was here reported for the first time according to the authors' knowledge. The compatibility of the developed Ti-45Al-3Nb ODS alloy with different processing technologies is foreseen to allow the use of solid state sintering and liquid state AM technologies to produce complex components using multi-step manufacturing taking advantage of the individual processing characteristics. The same alloy can then be used for a geometrically simple, sintered support structure with smaller oxides, combined with highly complex features produced by AM on top containing larger particles.

Acknowledgement

Appendix A. Supplementary data

Supplementary data related to this article can be found at http://dx.doi.org/10.1016/j.intermet.2017.07.004.

References

[1] Y.-W. Kim, Ordered intermetallic alloys, Part III: gamma titanium aluminides, JOM 46 (1994) 30–39.

[2] H. Clemens, S. Mayer, Design, processing, microstructure, properties, and applications of advanced intermetallic TiAl alloys, Adv. Eng. Mater 15 (2013) 191–215.

[3] L. Löber, F.P. Schimansky, U. Kühn, F. Pyczak, J. Eckert, Selective laser melting of a beta-solidifying TNM-B1 titanium aluminide alloy, J. Mater. Process. Technol. 214 (2014) 1852–1860, http://dx.doi.org/10.1016/j.jmatprotec.2014.04.002.

[4] J. Gussone, Y.-C. Hagedorn, H. Gherekhloo, G. Kasperovich, T. Merzouk, J. Hausmann, Microstructure of γ-titanium aluminide processed by selective laser melting at elevated temperatures, Intermetallics 66 (2015) 133–140, http://dx.doi.org/10.1016/j.intermet.2015.07.005.

[5] T. Vilaro, V. Kottman-Rexerodt, M. Thomas, C. Colin, P. Bertrand, L. Thivillon, S. Abed, V. Ji, P. Aubry, P. Peyre, T. Malot, Direct fabrication of a Ti-47Al-2Cr-2Nb alloy by selective laser melting and direct metal deposition processes, Adv. Mater. Res. 89–91 (2010) 586–591.

[6] S. Franzen, B. Karlsson, R. Dehoff, U. Ackelid, O. Rios, C. Parish, W. Peters, Microstructural properties of gamma titanium aluminide manufactured by electron beam melting, Min. Met. Mater. Soc. (2011) 455–462.

[7] J. Schwerdtfeger, C. Körner, Selective electron beam melting of Ti-48Al-2Nb-2Cr: microstructure and aluminium loss, Intermetallics 49 (2014) 29–35.

[8] L.E. Murr, S.M. Gaytan, A. Ceylan, E. Martinez, J.L. Martinez, Characterization of titanium aluminide alloy components fabricated by additive manufacturing using electron beam melting, Acta Mater 58 (2010) 1887–1894.

[9] W. Liu, J.N. Dupont, Fabrication of carbide-particle-reinforced titanium aluminide-matrix composites by laser-engineered net shaping, Metall. Mater. Trans. A 35 (2004) 1133–1140.

[10] D. Srivastava, I.T.H. Chang, M.H. Loretto, The effect of process parameters and heat treatment on the microstructure of direct laser fabricated TiAl alloy samples, Intermetallics 9 (2001) 1003–1013.

[11] C. Kenel, C. Leinenbach, Influence of cooling rate on microstructure formation during rapid solidification of binary TiAl alloys, J. Alloys Compd. 637 (2015) 242–247, http://dx.doi.org/10.1016/j.jallcom.2015.03.016.

[12] C. Kenel, C. Leinenbach, Influence of Nb and Mo on microstructure formation of rapidly solidified ternary Ti-Al-(Nb, Mo) alloys, Intermetallics 69 (2016) 82–89, http://dx.doi.org/10.1016/j.intermet.2015.10.018.

[13] C. Kenel, D. Grolimund, J.F. Fife, V.A. Samson, H. Van Swygenhoven, C. Leinenbach, Combined in situ synchrotron microXRD and high-speed imaging on rapidly heated and solidified Ti-48Al under additive manufacturing conditions, Scr. Mater. 114 (2016) 117–120.

[14] T. Boegelein, S.N. Dryepondt, A. Pandey, K. Dawson, G.J. Tatlock, Mechanical response and deformation mechanisms of ferritic oxide dispersion strengthened steel structures produced by selective laser melting, Acta Mater 87 (2015) 201–215, http://dx.doi.org/10.1016/j.actamat.2014.12.047.

[15] G. Molénat, M. Thomas, J. Galy, A. Couret, Application of spark plasma sintering to titanium aluminide alloys, Adv. Eng. Mater 9 (2007) 667–669.

[16] T. Voisin, J.-P. Monchoux, L. Durand, N. Karnatak, M. Thomas, A. Couret, An innovative way to produce γ-TiAl blades: spark plasma sintering, Adv. Eng. Mater 17 (2015) 1408–1413, http://dx.doi.org/10.1002/adem.201500019.

[17] D.S. Schwartz, P. Fraundorf, S.M.L. Sastry, TEM study of B- and Er-containing dispersoids in rapidly solidified dispersion-strengthened titanium aluminide alloys, Ultramicroscopy 37 (1991) 310–317.

[18] C. Suryanarayana, F.H. Froes, Mechanical alloying of titanium-base alloys, Adv. Mater 5 (1993) 96–106.

[19] P.B. Trivedi, E.G. Baburaj, A. Genc, L. Ovecoglu, S.N. Patankar, F.H. Froes, Grain-size control in Ti-48Al-2Cr-2Nb with yttrium additions, Metall. Mater. Trans. A 33A (2002) 2729–2736.

[20] H. Clemens, W. Wallgram, S. Kremmer, V. Güther, A. Otto, A. Bartels, Design of novel β-solidifying TiAl alloys with adjustable β/B2-phase fraction and excellent hot-workability, Adv. Eng. Mater 10 (2008) 707–713.

[21] J.O. Andersson, T. Helander, L. Höglund, P.F. Shi, B. Sundman, Thermo-Calc, DICTRA, Computational tools for materials science, Calphad 26 (2002) 273–312.

[22] V.T. Witusiewicz, A.A. Bondar, U. Hecht, T.Y. Velikanova, The Al-B-Nb-Ti system IV. Experimental study and thermodynamic re-evaluation of the binary Al-Nb and ternary Al-Nb-Ti systems, J. Alloys Compd. 472 (2009) 133–161.

[23] F. Appel, J.D.H. Paul, M. Oehring (Eds.), Gamma Titanium Aluminide Alloys, Wiley-VCH, 2011.

[24] J. Zollinger, V. Witusiewicz, A. Drevermann, D. Daloz, U. Hecht, Solidification of high Nb containing TiAl based alloys, Int. J. Cast. Met. Res. 22 (2009) 339–342, http://dx.doi.org/10.1179/136404609X368163.

[25] E. Arzt, E. Göhring, A model for dispersion strengthening of ordered intermetallics at high temperatures, Acta Mater 46 (1998) 6575–6584.

[26] S.H. Whang, D.P. Pope, C.T. Liu, High temperature aluminides and intermetallics, Proceedings of the Second International ASM Conference on High Temperature Aluminides and Intermetallics, September 16-19, 1991, Elsevier, San Diego, CA, USA, 2013.

[27] C. Capdevila, G. Pimentel, M.M. Aranda, R. Rementeria, K. Dawson, E. Urones-Garrote, G.J. Tatlock, M.K. Miller, Role of Y-Al oxides during extended recovery process of a ferritic ODS alloy, JOM 67 (2015) 2208–2215, http://dx.doi.org/10.1007/s11837-015-1559-5.

[28] Y. Li, D. Gu, Parametric analysis of thermal behavior during selective laser melting additive manufacturing of aluminum alloy powder, Mater. Des. 63 (2014) 856–867, http://dx.doi.org/10.1016/j.matdes.2014.07.006.

Paper 2

Mechanical performance and oxidation resistance of an ODS γ-TiAl alloy processed by spark plasma sintering and laser additive manufacturing

C. Kenel[a,b], A. Lis[a,c], K. Dawson[d], M. Stiefel[a], C. Pecnik[a], J. Barras[e], A. Colella[f], C. Hauser[e], G.J. Tatlock[d], C. Leinenbach[a,*], K. Wegener[b]

[a] Empa - Swiss Federal Laboratories for Materials Science and Technology, Überlandstrasse 129, 8600, Dübendorf, Switzerland
[b] ETH Zürich, IWF - Institute for Machine Tools and Manufacturing, Leonhardstrasse 21, Zurich, Switzerland
[c] Division of Materials and Manufacturing Science, Graduate School of Engineering, Osaka University, Suita, Japan
[d] Centre for Materials and Structures, School of Engineering, University of Liverpool, Brownlow Hill, Liverpool, L69 3GH, UK
[e] TWI Technology Centre Yorkshire, Advanced Manufacturing Park, Wallis Way, Catcliffe Rotherham, S60 5TZ, UK
[f] MBN Nanomaterialia S.p.A., Via G. Bortolan 42, 31050, Vascon di Carbonera (TV), Italy

ARTICLE INFO

ABSTRACT

In this work, the influence of Y_2O_3 additions on the mechanical properties and oxidation resistance of a Ti-45Al-3Nb (at.%) alloy have been studied. In particular, the mechanical properties from 293 K to 1073 K and oxidation resistance at 1073 K of spark plasma sintered and direct metal deposited material have been examined. At room temperature, higher yield stress (+34%) and ultimate tensile strength (+14%) at reduced ductility (−17%) is observed for the oxide dispersion strengthened variant compared to its non-strengthened counterpart. The strengthened variant shows superior strength retention up to 1073 K. Strengthened direct metal deposited material shows similar deformation characteristics as sintered material but suffers from premature fracture due to residual porosity. The addition of Y_2O_3 increases the oxidation resistance of both sintered and direct metal deposited material. Parabolic growth constants are decreased by −49% and −75% in sintered and direct metal deposited material, respectively. In sintered material the dispersoid size shows only slight changes from 29 nm to 26 nm at 923 K after 987 h and to 32 nm at 1073 K after 924 h demonstrating the high stability of the added particles. TEM analysis reveals abundant grain boundary pinning by the particles contributing to microstructural stability. The results show the potential of oxide dispersion strengthening in titanium aluminides for conventional sintering as well as for additive manufacturing processing routes.

1. Introduction

Composite materials based on a TiAl matrix have been considered for high temperature applications since the development of the first TiAl alloys [1]. Regarding the coefficient of thermal expansion (CTE), the oxides Al_2O_3, Y_2O_3 and ZrO_2 are similar to the TiAl matrix while SiC and Si_3N_4 have significantly smaller CTEs [2]. Chemical compatibility with the matrix is essentially stability against the aggressive TiAl melt. Only a handful of materials is more stable than the reaction products of Ti and Al with O and N. Minimal reactivity is observed for rare earth oxides of group III of the periodic table of the elements and Al with the M_2O_3 stoichiometry [3]. Additions of oxide particles to intermetallics have been proposed early on for the FeAl, NiAl and TiAl systems [5]. The oxide dispersion strengthened (ODS) systems NiAl and FeAl have been studied in detail using Y_2O_3 as the dispersed phase [5,6]. While the addition of hard and stable particles to TiAl has been studied by

several researchers [7–9], ODS TiAl alloys have not been reported in the literature. ODS TiAl has theoretical advantages over ODS NiAl in terms of compatibility with the strengthening particles and a higher melting point of the matrix [3]. Early attempts using B and Er additions were published in 1991 by Schwartz et al. [10]. Suryanarayana and Froes [11] later reviewed the addition of Er and Gd to a $(\alpha_2 + \beta)$ Ti-25Al-10Nb-3V-1Mo alloy to form the corresponding oxides as fine particles. Uniform particle dispersion could not be obtained. However, the reported results indicated enhanced hardness without excessive embrittlement of the alloys. Later studies by Trivedi et al. [12] used Y additions in GE48-2-2 to form an ODS material by mechanical alloying and hipping. In the studied alloy the particles restricted grain growth up to 1423 K. These results indicate superior properties of ODS titanium aluminides compared to their non-strengthened parent alloy regarding low and high temperature strength without losses in fracture toughness and ductility. Recently, the fabrication of *in situ* TiAl/Al_2O_3 composites

was reported [13,14]. The resulting strengthening effects could be attributed to the presence of the oxide particles and the reduced grain size. Only a few studies have been published on ODS TiAl despite the potential to provide superior properties compared to established ODS intermetallics.

The beneficial effects upon addition of rare earth elements on oxidation resistance and the associated rare earth effect (REE) are well known and exploited in many state-of-the-art alloy systems, especially in Ni- and Fe-based alloys [15]. In alumina-forming alloys, the elements Y and Hf were found to be equally effective [16]. Later work, as reviewed by Pint [17], provided estimations for suitable addition levels and element combinations in alumina formers. The combination of Y with Hf or Zr provides the highest oxidation resistance, but as a single addition Y is more effective than the other elements. It was also observed that ideally Hf and Zr levels around 0.05 at.% are applied, while slightly higher Y contents in the range of 0.1 at.% provide the best results.

While the REE can increase oxidation resistance in alumina-forming alloys by more than one order of magnitude, its effect on marginal alumina-forming alloys is much lower. TiAl alloys and other aluminides are an example of such alloys, as they tend to form mixed scales consisting of Al_2O_3 and TiO_2 instead of the desired pure alumina scale [18]. For TiAl alloys, the effects of Y addition on the oxidation resistance have been classified as beneficial, neutral or even detrimental in the past. Taking into account the specifics of the REE, in the case of additions exceeding a 1 at.% over-doping leads to a similar or inferior oxidation resistance compared to the un-doped base alloy [17,18]. However for low Y levels in the alloy or applied as a coating, beneficial [19–24], detrimental and neutral effects have been described [20,21,25,26]. The beneficial effects refer to reduced scale growth rates and increased scale adherence, while the observed detrimental effects are internal oxidation of Y forming locally Y_2O_3 or only limited protection due to Y depletion in the case of coatings. However, several studies focusing on a range of compositions with a rare earth level below 1 at.% confirm the existence of the REE also for TiAl alloys upon addition of Y [23,24] and Hf [27].

This manuscript is part of our work on the development of ODS TiAl and its consolidation by spark plasma sintering (SPS), selective laser melting (SLM) and laser direct metal deposition (DMD). In a first paper, the microstructure and Y_2O_3 particle stability after processing and thermal treatment were characterized [28]. In this work, the effect of Y_2O_3 addition to spark plasma sintered (SPS) and direct metal deposited (DMD) TiAl alloys on the mechanical properties and oxidation resistance are described.

2. Experimental

2.1. Material

The studied materials are SPS Ti-45Al-3Nb (at.%), and SPS and direct metal deposited (DMD) Ti-45Al-3Nb+ < 0.2Y_2O_3 (at.%, mol.%). Hereafter the two alloys are called OX 45-3 and OX 45-3 ODS. The bulk material is consolidated from mechanically alloyed powder supplied by MBN Nanomaterialia, Italy. After obtaining the non-ODS OX 45-3 alloy in a size fraction of 10 μm–45 μm for SPS, Y_2O_3 is added upon high energy ball milling to form the ODS variant. Powder fractions in the size ranges of 10–45 μm and 46–106 μm are retrieved for SPS and DMD consolidation, respectively. The details of consolidation have been described in Ref. [28]. In brief, SPS consolidation of cylindrical billets (d = 50 mm) is performed at 50 MPa and 1598 K with a dwell time of 2 min using a HP D 10 commercial setup (FCT Systeme GmbH, Germany). A combination of a tri-beam coaxial powder delivery head with a TruDisk 8002 laser source (Trumpf Laser GmbH, Germany) mounted on a Reis RV60-40 robot (Reis Robotics, Germany) is used for DMD. The material is deposited in a (15 × 70 × 15) mm³ cuboid with a bidirectional strategy at a volume energy density of 120 J/mm³. All material

is heat treated at 1123 K for 12 h in vacuum. Cast TNB-V5 (Ti-45Al-5Nb-0.2C-0.2B) supplied by the Helmholtz-Zentrum Geesthacht, Germany, was used as reference for oxidation testing.

2.2. Mechanical testing

Mechanical testing in the range of 293 K–1073 K was performed with a tensile/compression module developed by Kammrath & Weiss, Germany (F_{max} = ± 5 kN). All room temperature tests were performed in air, while the experiments at elevated temperatures were conducted at $2 \cdot 10^{-5}$ mbar in a vacuum setup. The specimen geometry is a flat dog bone shape with a nominal gauge length of 10 mm, a width of 3 mm and a thickness of 1 mm (Supplementary Figs. S1 and S2). Prior to machining the bulk material was heat treated at 1123 K for 12 h in vacuum for stress relief. Specimens were produced from bulk material by electro-discharge machining (EDM) and ground to P600 using SiC grinding paper. Grinding was performed parallel to the testing direction to avoid stress concentration at surface flaws. Tests at room temperature are performed with an extensometer attached to the specimen (EXA10-1x, Sandner, Germany, ± 0.1 μm) while the load is measured by a load cell (± 0.5 N). For tests at elevated temperature a ceramic heating element covered with a W plate was mounted directly to the specimen with W springs. Temperature was measured by a thermocouple in the W plate close to the specimens interface and actively controlled ± 1 K. Prior to testing the setup was heated with 40 K/min from room temperature to the test temperature to allow thermal equilibration of the specimen. The thermal expansion and developing compressive stress were compensated using the load control mode of the module maintaining an effective load of 0 ± 5 N during heating. After reaching the target temperature and a dwell time of 2 min the specimen was loaded in tensile mode with 5 N/s until fracture. Due to geometric restrictions the extensometer could not be mounted for the high-temperature experiments. Consequently, only the machine elongation and load were measured for these experiments. We assume that the machine stiffness is, in good approximation, independent of the testing temperature (only the gauge length of the specimen is actively heated) and that the same specimen geometry is applied. Hence, the machine elongation e_m and specimen elongation e_s are correlated by

$$e_s = c(F) \cdot e_m \tag{1}$$

where c is a function of the applied load F, which was determined based on the room temperature experiments, where both e_m and e_s were simultaneously measured. This procedure allows the estimation of the fracture strain ε_f and yield stresses for different temperatures. As the ε_f of titanium aluminides is typically one order of magnitude lower than in conventional Ti alloys, the yield stress at 0.1% plastic strain, $Rp_{0.1}$, is used in this work.

2.3. Oxidation resistance

The degradation behavior of consolidated TiAl alloys was measured at 923 K and 1073 K in static laboratory air. The tests were performed in an air furnace equipped with $MoSi_2$ heating elements (Nabertherm, Switzerland). The temperature was measured by a K-type thermocouple (Labfacility Ltd, UK, ± 2.5 K) placed directly beneath the alumina test containers. The setup consisted of an alumina crucible (Almath Crucibles Ltd, UK) with the specimen suspended by Pt-Rh wire from an alumina bar (Supplementary Fig. S3). This ensured access of air to all surfaces of the specimen while the specimen was irradiated only by the surrounding alumina crucible separating it from the hot heating filaments. The specimen geometry was a (10 × 10 x 1) mm³ platelet, ground up to a P1200 SiC paper (15.3 μm average particle diameter) and cleaned in acetone in an ultrasonic bath. Prior to and after testing the specimen size was measured with calipers (Mitutoyo CD-15DC, ± 0.01 mm) and the weight was determined on a precision balance (ALJ 120-4, Kern & Sohn, Germany, ± 0.1 mg). Gaussian error propagation

was applied to estimate the errors introduced by the uncertainties of specimen size and weight. These errors are later shown as error bars with the data points. In order to compare the observed oxide scale growth rates of the different studied alloys, a parabolic growth model according to

$$\left(\frac{\Delta m}{A}\right)^2 = k_p \cdot t \tag{2}$$

where t is the time, m is the mass, A is the surface area and k_p is the parabolic growth constant, was fitted to the data.

2.4. Characterization

Scanning electron microscopy (SEM) using a Philips XL30 ESEM, equipped with a secondary electron (SE) and a backscattered electron imaging (BSE) detector, was applied to the specimen facture surfaces and oxide scales. Oxide cross-sections and energy dispersive X-ray (EDX) scans thereof for qualitative compositional analysis were prepared by focused ion beam milling (FIB) using a FEI Helios 660 G3 UC equipped with an Oxford Instruments X-Max 150 EDX detector and an in-column detector (ICD) providing compositional contrast. Electron transparent lamellae for transmission electron microscopy (TEM) investigations were prepared by FIB on a dual beam FEI Helios 600i using the lift out technique and a final polishing step at 2 kV was applied. The prepared lamellae were analyzed by scanning transmission electron microscopy (STEM) on an aberration-corrected JEOL 2100FCs S/TEM operating at 200 kV.

X-ray diffraction (XRD) measurements were performed using a Bruker D8 DISCOVER (Bruker, Germany) equipped with a LynxEye 1D detector. Measurements were performed with Cu K_α radiation at 40 kV and 40 mA with a step size of $0.02° \pm 0.0001°$ (2Θ).

3. Results and discussion

3.1. Alloy microstructure

Fig. 1 shows the microstructure of the studied materials. SPS OX 45-3 has a near-lamellar structure with a large fraction of lamellar colonies of γ-TiAl and α_2-Ti$_3$Al phases, γ-phase located at the colony boundaries and residual porosity can be observed (Fig. 1a). Upon addition of Y$_2$O$_3$ in SPS OX 45-3 ODS the microstructure is refined yielding smaller colony sizes around 5 μm–10 μm and an increased fraction of equiaxed γ phase as well as α_2 phase (Fig. 1b). In DMD OX 45-3 ODS a fine structure consisting predominantly of lamellar colonies around 5 μm, coarsened oxide particles and residual pores are observed (Fig. 1c).

3.2. Mechanical performance

The addition of ODS particles has a clear influence on the tensile properties of ternary Ti-45Al-3Nb at room temperature. Fig. 2a shows the tensile stress-strain curves for SPS OX 45-3 and OX 45-3 ODS tested until fracture at room temperature. The ODS variant has a higher yield point Rp$_{0.1}$ of 794 $\pm$ 12 MPa ($+34\%$) and higher ultimate strength Rm of 856 $\pm$ 0.1 MPa ($+14\%$) but a lower total fracture strain ε_f of 0.76 $\pm$ 0.04% (-17%) compared to the ODS-free variant with 593 $\pm$ 10 MPa, 751 $\pm$ 8 MPa and 0.91 $\pm$ 0.03%, respectively. The Young's modulus of both variants is close to 170 GPa based on the linear elastic part of the stress-strain curve. Only small scatter is observed between the individual specimens, selected randomly from different regions in the consolidated billet. This indicates good microstructural homogeneity throughout the SPS consolidated material. The mechanical performance of SPS OX 45-3 ODS remains superior to the ODS-free variant up to 1073 K. Fig. 2b shows the evolution of Rp$_{0.1}$, Rm and ε_f for both variants after testing at 293 K, 873 K, 973 K and 1073 K. The Rp$_{0.1}$ of SPS OX 45-3 ODS is slightly reduced at 873 K compared to its maximum value at room temperature before increasing again at 973 K
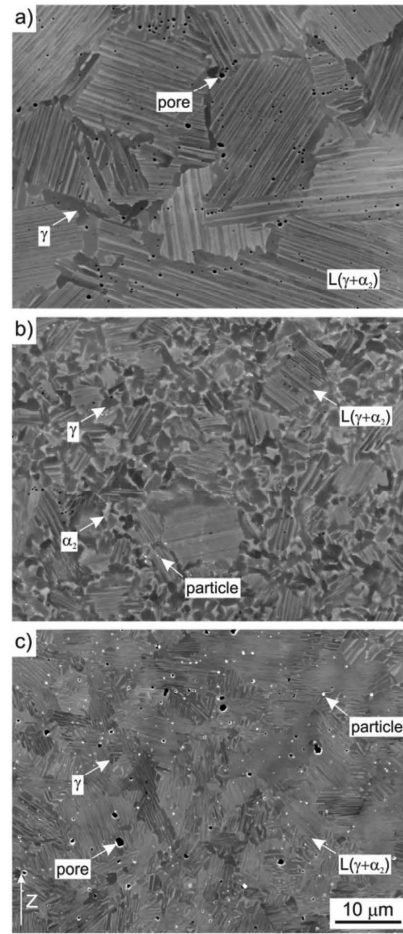

Fig. 1. Microstructures of a) SPS OX 45-3, b) SPS OX 45-3 ODS and c) DMD OX 45-3 ODS after heat treatment at 1123 K for 12 h. Microstructural features as well as the build direction in DMD (z) are indicated. The scale bar in c) is valid for all micrographs.

and 1073 K. The Rm shows a similar behavior with an initial decrease and later recovery. The very similar evolution of Rm and ε_f indicates a critical strain based failure mechanism leading to premature fracture and lower Rm at intermediate temperatures. This is also evident from the increased standard deviation of Rm at 973 K, which is caused by a strong scattering of the obtained values for four specimens. This high standard deviation is unusual for this alloy comparing all the other data. Detailed analysis shows that the measured values of Rm at 973 K are 747 MPa, 755 MPa, 775 MPa and 856 MPa. At the same time the Rp$_{0.1}$ value shows only little scattering. The maximum strain at fracture is 0.77% for 856 MPa while the minimum observed strain is 0.61% for 755 MPa.

In the ODS-free variant SPS OX 45-3 the Rp$_{0.1}$ first increases at 873 K before it strongly decreases at 973 K and increases again at 1073 K. The Rm and ε_f show a similar evolution which is inverse to the trends of the Rp$_{0.1}$. First, both values decrease when tested up to 873 K. At 973 K the Rm recovers to 734 $\pm$ 22 MPa while ε_f reaches its
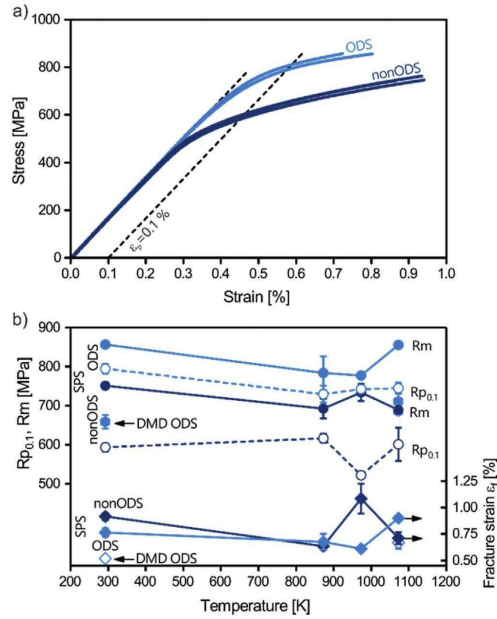
Fig. 2. a) Tensile stress-strain curves for SPS OX 45-3 (nonODS, n = 3) and OX 45-3 ODS (ODS, n = 2) at room temperature. b) Mechanical performance of non-ODS OX 45-3 and SPS and DMD OX 45-3 ODS from 293 K to 1073 K. DMD data is shown as hexagons for Rm and Rp$_{0.1}$ and open diamonds for ε$_f$.

maximum of 1.08 ± 0.14%. At 1073 K both values decrease again. The mechanical properties of DMD OX 45-3 at 293 K and 1073 K exceed the values of ODS-free SPS OX 45-3 but remain inferior to SPS OX 45-3 ODS (Fig. 2b). All mechanical data is reported in Supplementary Table S1.

To understand the differences in mechanical performance and the cause of failure, the fracture surfaces are examined by SEM. Fig. 3 shows the characteristic features observed in SPS OX 45-3 ODS after fracture at 293 K, 873 K, 973 K and 1073 K. The insets show the region of the crack origin as identified by the typical star-like crack pattern forming around it. Three main failure modes are observed: *trans*-lamellar (TL), inter-granular (IG) and "feathery" *trans*-lamellar (FTL) fracture. The *trans*-lamellar modes are observed in the lamellar colonies of α$_2$ + γ. The TL mode shows a ragged crack surface following the lamellar interfaces before crossing individual lamellae. The FTL mode crosses several lamellae without directional change along the interfaces. The IG mode is observed in the equiaxed region following the grain boundaries of the γ phase. It is evident from the micrographs that SPS OX 45-3 ODS shows a very similar fracture mode at all temperatures. The origin of the crack is related to a cleavage fracture of the intermetallic matrix. Based on the size of these cleaved regions it is believed that is related to the lamellar colonies in the material. No mass contrast between the crack origin and the surrounding matrix is observed, indicating intrinsic crack initiation in the microstructure. At room temperature a small inclusion is observed close to the cleaved region. Although probably responsible for initiation of final fracture its influence on the mechanical performance though appears to be minimal based on the superior strength of the material. Fig. 4 shows the fracture surfaces of SPS OX 45-3 after testing at 293 K–1073 K. The same three fracture modes as in the ODS-variant are observed, including the additional inter-lamellar (IL) mode. The IL mode is observed in the lamellar colonies and separates the individual lamellae, leading to large planar features. At 293 K the predominant fracture mode is the TL mode (Fig. 4a). The IG and FTL modes are also observed in the γ-rich regions and across lamellae, respectively. At 873 K the FTL mode appears on larger areas while the equiaxed γ shows very distinct inter-granular fracture with no apparent ductility (Fig. 4b). At 973 K the IL mode is
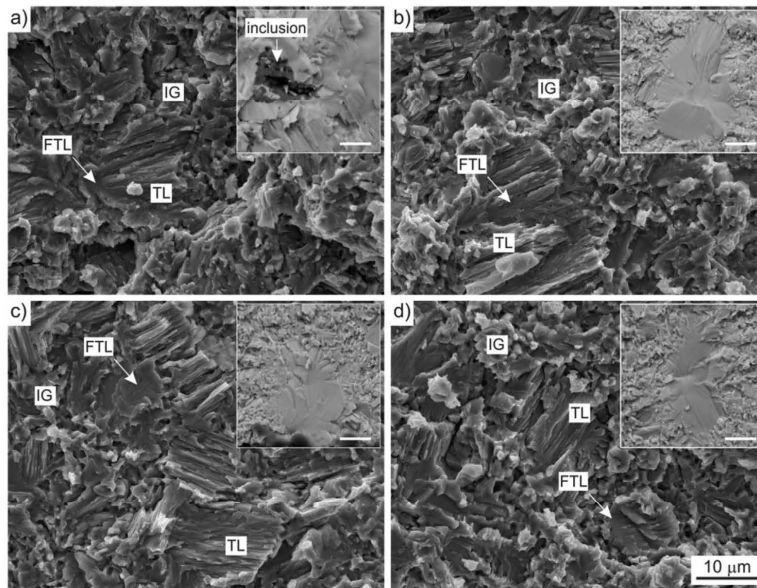

Fig. 3. SE SEM micrographs of the fracture surface of OX 45-3 ODS tensile tested at a) 293 K, b) 873 K, c) 973 K and d) 1073 K. Insets: BSE SEM micrographs of the origin of fracture. The characteristic fracture modes *trans*-lamellar (TL), feathery *trans*-lamellar (FTL) and inter-granular (IG) are indicated. The scale bar in d) applies for a-d). Insets: scale bar = 10 μm.
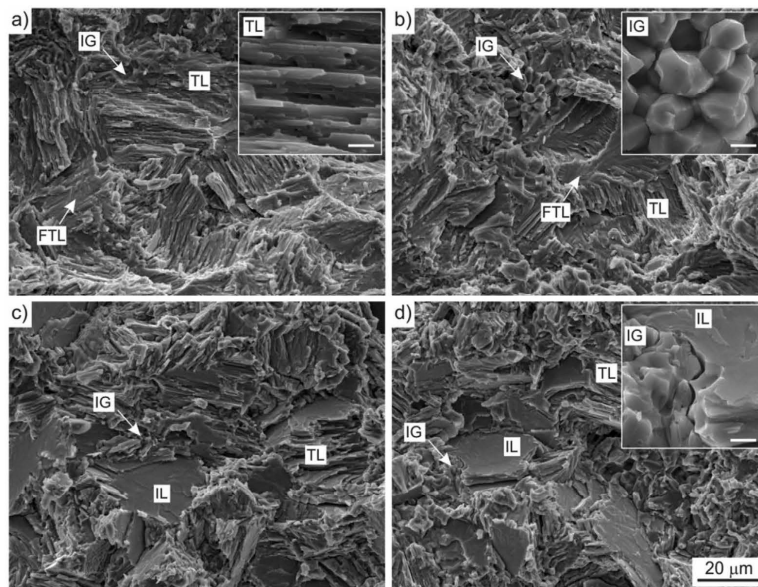
Fig. 4. SE SEM micrographs (SE contrast/image) of the fracture surface of OX 45-3 tensile tested at a) 293 K, b) 873 K, c) 973 K and d) 1073 K. The characteristic fracture modes TL, FTL, inter-lamellar (IL) and IG are indicated. The scale bar in d) applies for a-d). Inset a): scale bar = 1 μm, insets b), d): scale bar = 2 μm.
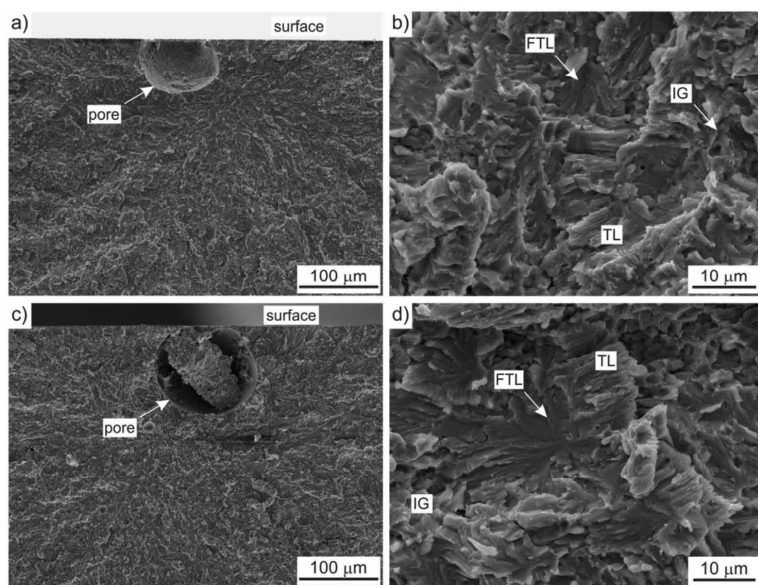

Fig. 5. SE SEM micrographs (SE contrast/image) of the fracture surface of DMD OX 45-3 ODS tensile tested at a, b) 293 K and c, d) 1073 K. The characteristic fracture modes TL, FTL and IG are indicated.

observed, thereby completely changing the appearance of the fracture surfaces. At the same time the FTL mode vanishes (Fig. 4c). The fracture surface at 1073 K is similar to the one observed at 973 K showing TL, IG and IL modes (Fig. 4d). The inset shows also separation cracks forming in between the IG and IL zones in the equiaxed γ and lamellar colonies. The change in fracture mode between 873 K and 973 K is accompanied with a strong increase in ductility and reduced yield strength (Fig. 2b).

This indicates that the IL mode is actually a ductile fracture mode compared to the brittle IG and TL modes. The replacement of the FTL mode by the IL mode could indicate that the FTL mode is also a ductile fracture mode. However, based on the macroscopic ductility this cannot be confirmed due to its limited occurrence within the fracture surface.

Also the ODS-variant shows an increased ductility at high temperature with abundance of the FTL mode (Fig. 3d). This indicates that
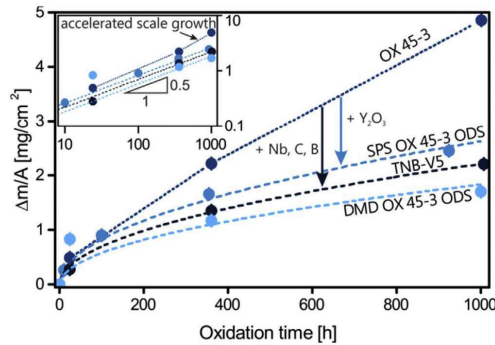
Fig. 6. Weight gain of OX 45-3, SPS and DMD OX 45-3 ODS and TNB-V5 at 1073 K in static laboratory air. For OX 45-3 ODS and TNB-V5 fitted parabolic curves are shown (- -). The data points for OX 45-3 have been connected to guide the reader's eye (·).

Table 1
Parabolic growth rates k_p for OX 45-3, OX 45-3 ODS and TNB-V5 at 1073 K.

Alloy	$k_p \cdot 10^{-10}$ (kg^2 m^{-4} s^{-1})	Evaluated time t (h)	Reference
SPS OX 45-3	3.7	0 < t < 360	This work
SPS OX 45-3 ODS	1.9	0 < t < 924	This work
DMD OX 45-3 ODS	0.9	0 < t < 1000	This work
TNB-V5	1.4	0 < t < 1001	This work
	1.1	0 < t < 62	[32]

indeed the FTL mode is a sign of ductility in the lamellar colonies and can explain the increased strain at fracture. Furthermore, the IL and FTL modes appear to be strongly related with the direction of the crack growth changing from *trans*-lamellar at low temperature to inter-lamellar in the IL mode at high temperature in the ODS-free variant while the predominant direction remains *trans*-lamellar in the ODS-variant. Consequently, the IL mode is not observed in this sample.

Fig. 5 shows the fracture surfaces of DMD OX 45-3 ODS tested at 293 K and 1073 K. At both temperatures the origin of fracture is a pore close to the specimen surface with a diameter of around 100 µm (Fig. 5a and c). This explains the lower Rm and ε_f observed in DMD material compared to its SPS counterpart. Due to stress concentration and a reduction of the load bearing area, the DMD specimens fail at lower macroscopic stresses and strains. A close examination of the fracture surface reveals a similar fracture surface as in SPS material (Fig. 5b and d). At room temperature fracture occurs predominantly with the TL and IG modes with little occurrence of the FTL mode. At 1073 K all three fracture modes persist with increased fraction of the FTL mode. This indicates a similar deformation and fracture mechanism for the OX 45-3 ODS material processed by SPS or DMD.

The significant increase in yield point of the ODS-variant can be attributed to the addition of dispersoids. However, the underlying mechanism for the higher yield point is not only depending on the presence of the dispersoids and their interaction with dislocations. A second and very important contribution is from the microstructure itself: the ODS-variant has a fine microstructure with equiaxed γ phase between small lamellar colonies forming a duplex to near-lamellar alloy. The ODS-free alloy has less γ surrounding larger lamellar colonies and is thus closer to a near-lamellar alloy. It is well known that in TiAl alloys all constituents, equiaxed γ, lamellar colonies and the lamellar structure itself follow a Hall-Petch relationship with increased strength with reduced feature size [29]. Duplex microstructures combining lamellar colonies and a significant fraction of equiaxed γ have typically already high strength, but are inferior to near-lamellar microstructures providing the highest strength in TiAl alloys [30]. Taking into account these findings, the microstructure of the ODS-free variant should actually provide the higher strength than the structure richer in equiaxed γ found in the ODS-variant based on its general microstructure. A refinement effect upon ODS addition of each microstructural feature can however lead to significantly enhanced strength as the Hall-Petch constants of TiAl alloys for lamellar microstructures have been found to be unusually high up to 5 MPa m$^{1/2}$ compared to common metals with values close or below unity [29]. Separation of the individual effects, however, remains difficult as microstructure, properties and alloy composition are intertwined in TiAl alloys. At elevated temperature the abnormal mechanical behavior of the intermetallic phases contributes
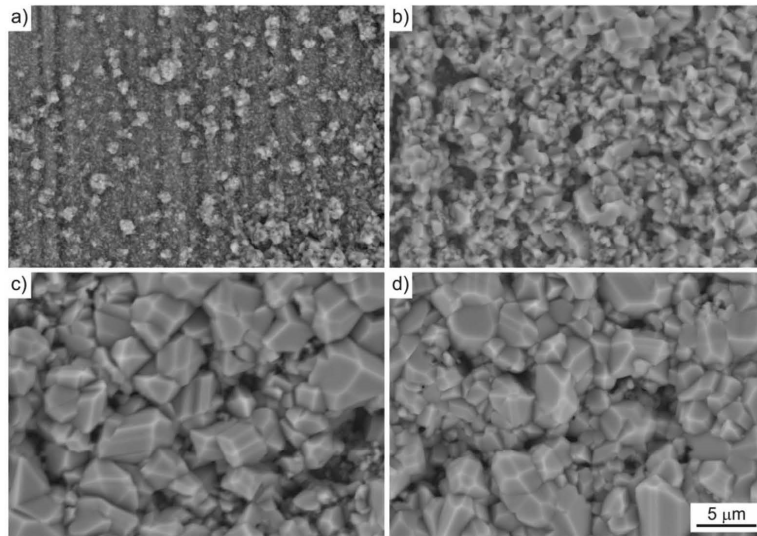

Fig. 7. BSE SEM top-view micrographs of OX 45-3 ODS after a) 10 h, b) 100 h, c) 354 h and d) 924 h at 1073 K in air. The scale bar in d) is valid for a-d).
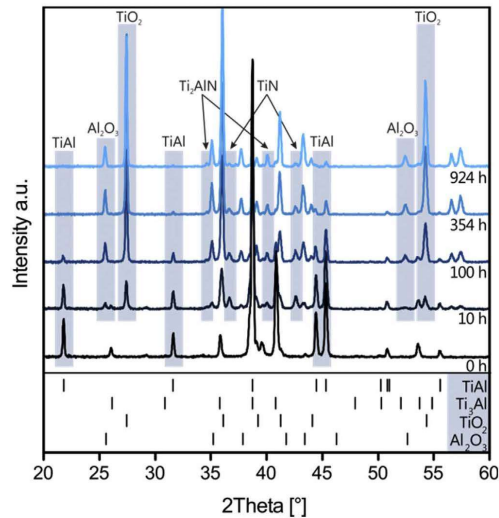
Fig. 8. XRD spectra of oxidized OX 45-3 ODS at 1073 K. The peak positions of the major phases γ TiAl, α_2 Ti$_3$Al, TiO$_2$ (rutile) and a-Al$_2$O$_3$ (corundum) are indicated as well as the evolution of their prominent peaks. Traces of TiN and Ti$_2$AlN peaks are marked with arrows ($\downarrow$).

to the strength retention. The single-crystalline γ and α_2 show an abnormal strength increase with increasing temperature with their maximum yield stress around 873 K and 1173 K, respectively [31]. In technical alloys this leads to a ductile-to-brittle transition around 923 K–1073 K, as γ starts to soften. This is in agreement with the observations in the ODS-free OX 45-3 alloy. The addition of dispersoids suppresses the softening reaction found in OX 45-3 which is a clear benefit for the ODS variant providing stable yield stress for all tested temperatures. The softening is explained by increased mobility of

previously dissociated and locked super-dislocations recombining due to thermal activation [31]. While the dissociating contribution disappears, the dispersoids remain stable and continue to hinder dislocation movement. Consequently, superior yield stress is maintained to higher temperature in ODS TiAl alloys.

3.3. Oxidation resistance

3.3.1. Weight gain

Fig. 6 shows the weight gain per unit area for ODS-free SPS OX 45-3, SPS and DMD OX 45-3 ODS and TNB-V5. Comparing the ODS-free and ODS-containing variant processed by SPS a reduced weight gain is clearly observed upon addition of the Y$_2$O$_3$. SPS OX 45-3 ODS shows a parabolic growth of the oxide scale up to the maximum tested time of 924 h. At this point spallation is observed at the edges of the specimens. Over the complete duration of the oxidation test, the parabolic growth mode is maintained which is also seen by the data points lying on a line with a slope of 0.5 on a logarithmic scale (inset Fig. 6). The ODS-free OX 45-3 alloy shows initially parabolic growth up to 360 h. For longer test duration accelerated growth is observed which is also evident from an increased slope on the logarithmic scale. Consequently, no fitted parabolic growth model is shown for OX 45-3. However, the data up to 360 h follows a parabolic model and is thus included in Table 1 for comparison. The fitted k_p value for the OX 45-3 ODS variant is about half the value of the ODS-free alloy with $1.9 \cdot 10^{-10}$ kg^{2}m^{-4}s^{-1} and $3.7 \cdot 10^{-10}$ kg^{2}m^{-4}s^{-1}, respectively. For DMD processed OX 45-3 ODS another reduction is observed to $0.9 \cdot 10^{-10}$ kg^{2}m^{-4}s^{-1}. It is hypothesized that this is an effect of compositional homogenization during DMD as well as potential doping effects by Y due to particle dissolution.

Comparing the oxidation resistance of OX 45-3 ODS to TNB-V5, the SPS material is slightly inferior and the DMD material is superior. The reference alloy TNB-V5 is also a Ti-Al-Nb based alloy with additions of B and C, containing an increased amount of Nb compared to OX 45-3 (ODS). Upon the addition of the elements Nb, C, and B, to TiAl alloys increased oxidation resistance has been observed [18]. In the case of Ti-Al-Nb alloys additions exceeding 5 at.% Nb have been found to have significantly increased oxidation resistance [19]. The difference in composition thus explains the increased oxidation resistance of TNB-V5
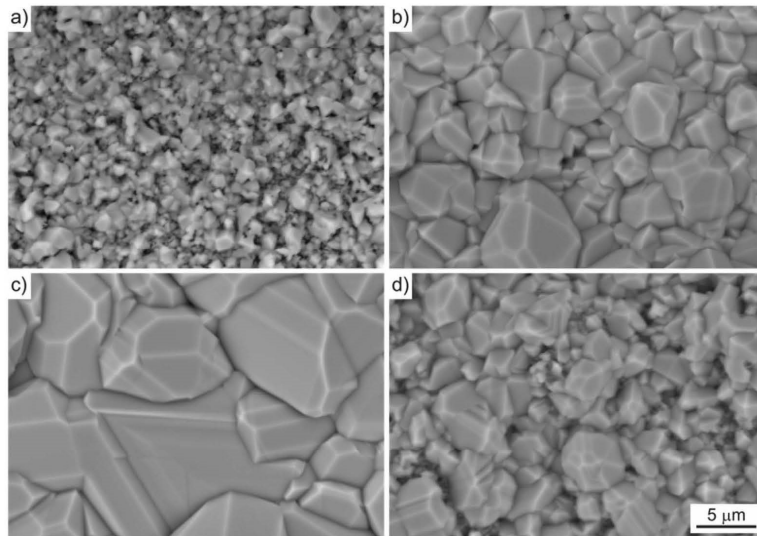

Fig. 9. BSE SEM top-view micrographs of a-c) OX 45-3 and d) TNB-V5 after a) 24 h, b) 360 h, and c, d) 1001 h at 1073 K in air. The scale bar in d) is valid for a-d).
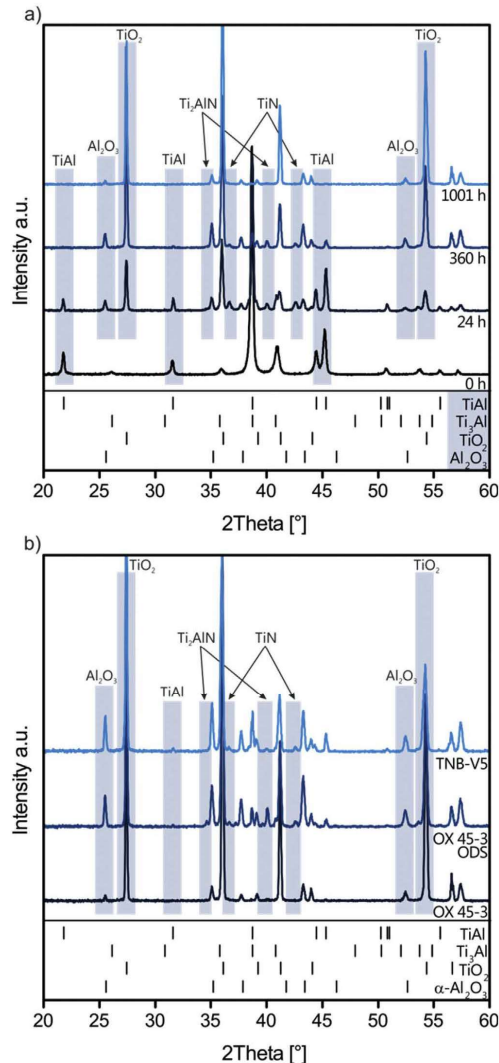
a)

TiO$_2$ Ti$_2$AlN   TiN   TiO$_2$

TiAl   Al$_2$O$_3$ TiAl   TiAl   Al$_2$O$_3$

Intensity a.u.

1001 h

360 h

24 h

0 h

TiAl
Ti$_3$Al
TiO$_2$
Al$_2$O$_3$

20   25   30   35   40   45   50   55   60

2Theta [°]

b)

TiO$_2$ Ti$_2$AlN   TiN   TiO$_2$

Al$_2$O$_3$ TiAl   Al$_2$O$_3$

Intensity a.u.

TNB-V5

OX 45-3
ODS

OX 45-3

TiAl
Ti$_3$Al
TiO$_2$
α-Al$_2$O$_3$

20   25   30   35   40   45   50   55   60

2Theta [°]

Fig. 10. XRD spectra of a) oxidized OX 45-3 at 1073 K and b) OX 45-3 (bottom), OX 45-3 ODS (center) and TNB-V5 (top) oxidized at 1073 K for 1001 h, 924 h and 1001 h, respectively.

compared to OX 45-3. It is an important observation that the addition of < 0.2 mol.% Y$_2$O$_3$ leads to a similar oxidation resistance to an increased Nb alloying level by 2 at.% plus the addition of C and B. The k_p value for TNB-V5 determined in this work for a test duration of 1001 h is increased by $0.3 \cdot 10^{-10}$ kg^{2}m^{-4}s^{-1} compared to the value reported by Masset and Schütze for 62 h [32] (Table 1). However, the weight gain at 24 h of TNB-V5 observed in this work is overestimated by the fit over the complete test duration (see inset Fig. 6). Consequently, a lower k_p is determined for short-term testing and explains the slight difference between reported values and the ones obtained in this work.

3.3.2. Morphology and phase evolution of the formed oxide scale

The evolution of the morphology of the oxide scale on OX 45-3 ODS at 1073 K initially shows the formation of a fine grained, Al$_2$O$_3$-rich scale after 10 h (Fig. 7a). Some coarsened oxides appear, being TiO$_2$ based on their composition. According to XRD, the scale after 10 h consists of TiO$_2$ (rutile) and α-Al$_2$O$_3$ (corundum) and trace amounts of TiN and Ti$_2$AlN (Fig. 8). After 100 h exposure the TiO$_2$ covers most of the surface with only a few spots left where the fine grained Al$_2$O$_3$-layer remains visible (Fig. 7b). This is also represented by a strong increase in TiO$_2$ peak intensities in XRD. The reflections of the TiN-phase decrease in intensity, indicating its formation in the initial stages of oxidation and its location close to the alloy-scale interface. After 354 h of oxidation the scale surface shows mainly coarse, faceted TiO$_2$ crystals with a lateral size below 5 µm (Fig. 7c). Upon exposure for 924 h no significant changes of the oxide scale surface morphology are observed (Fig. 7d). The scale continues to increase in thickness and mass, as it is evident from Fig. 6 but also from vanishing substrate and TiN signal intensities in XRD (Fig. 8).

In order to elucidate the effect of the Y$_2$O$_3$ addition in OX 45-3 ODS, the morphology evolution of the ODS-free variant OX 45-3 and TNB-V5 is studied. OX 45-3 shows accelerated degradation compared to the ODS-variant. After 24 h exposure of OX 45-3 at 1073 K the surface is already covered by TiO$_2$ (Fig. 9a). XRD also indicates the presence of α-Al$_2$O$_3$ as well as traces of TiN and Ti$_2$AlN (Fig. 10a). Upon 1001 h of exposure, the surface structure is coarsened with large TiO$_2$-crystals forming with lateral sizes exceeding 10 µm (Fig. 9c)., XRD indicates fast and predominant formation of TiO$_2$. The scale formed on the reference alloy TNB-V5 after 1001 h at 1073 K consists out of coarse, faceted TiO$_2$ as well as fine-grained regions in between them (Fig. 9d). Comparing the morphologies of the formed scale after similar exposure time on OX 45-3, OX 45-3 ODS and TNB-V5 shows a very similar behavior of the latter two. Both form a scale with a bimodal grain size distribution of coarser TiO$_2$ and finer TiO$_2$ + Al$_2$O$_3$ in between. This similarity also observed in the XRD spectra after the maximum test time (Fig. 10b). While the spectra for OX 45-3 ODS and TNB-V5 are virtually the same, showing the presence of a significant fraction of Al$_2$O$_3$ beside the major TiO$_2$, the spectrum of OX 45-3 is dominated by the presence of TiO$_2$. Beside this difference, the general phase evolution appears to be similar for all alloys.

Fig. 11 shows a comparison of FIB cross-section across the oxide scale in OX 45-3, OX 45-3 ODS and TNB-V5 after exposure at 1073 K. As indicated by the weight gain, OX 45-3 forms a thicker scale compared to OX 45-3 ODS and TNB-V5 (Fig. 11a–c). Despite the change in thickness, the micrographs show a similar multiphase, layered and complex scale structure. As evident from the XRD measurements, the outermost region consists of a coarse TiO$_2$ layer. EDX line-scans across the scale confirm a region consisting of fine grained Al$_2$O$_3$ + TiO$_2$ below the surface layer (Fig. 12). Towards the base material, the Al$_2$O$_3$ phase disappears leaving behind a region of predominantly TiO$_2$ phase. At the alloy-scale interface bulky Al$_2$O$_3$-rich phases are observed together with a thin layer enriched in Ti, Al and N as well as Nb-rich phases (Fig. 11d–f). Below the alloy-scale interface, Ti-depletion is observed in the base material. Simultaneously, Nb is enriched in this region with its maximum concentration directly below the oxide scale. Nb is also incorporated into the first TiO$_2$-rich zone, but is absent in the outer Al$_2$O$_3$ + TiO$_2$ and surface TiO$_2$-layer. OX 45-3 shows internal degradation with the formation of N-rich phases and small Al-oxides along grain boundaries (Fig. 11d). Consistently, EDX shows signal variations for N and O in the subsurface zone (Fig. 12a). The internal degradation is clearly attenuated in OX 45-3 ODS with much less penetration depth into the subsurface zone (Fig. 10e). TNB-V5 shows no internal degradation (Fig. 11f).

The general behavior of the three studied alloys is schematically summarized in Fig. 13. In the initial state, the alloy has a thin native oxide layer due to the high affinity of Ti and Al to oxidize. After exposure to air (< 24 h at 1073 K), the surface is covered with fine
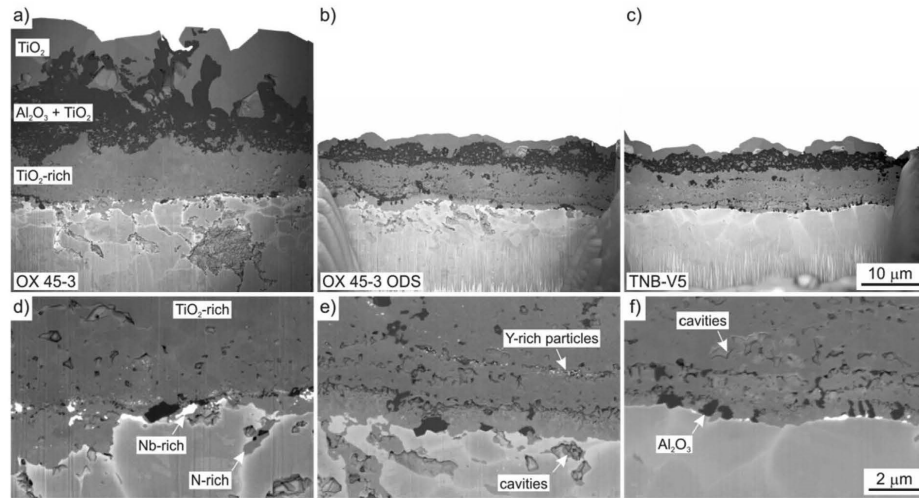
Fig. 11. FIB ICD SEM (Z-contrast) cross-sections of OX 45-3 (a, d) after 1001 h, OX 45-3 (b, e) ODS after 924 h and TNB-V5 after 1001 h exposure to air at 1073 K (c, f). The scale bar in c) is valid for a-c), the scale bar in f) for d-f).
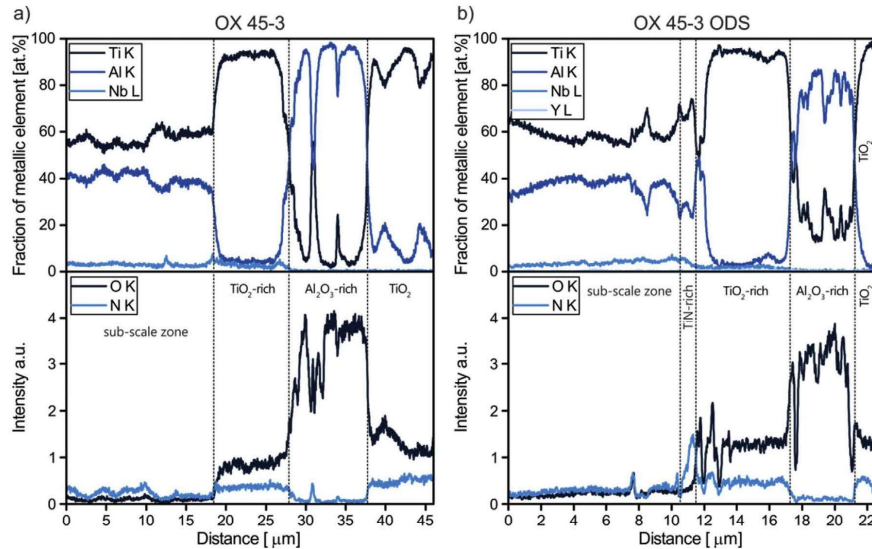

Fig. 12. EDX line scans across the formed oxide scales in a) OX 45-3 after 1001 h and b) OX 45-3 ODS after 924 h exposure to air at 1073 K showing the atomic percentage of the main metallic elements (top) and the intensity of the light elements O and N (bottom).

grained Al_2O_3 and TiN as well as dispersed coarser TiO_2 crystals. Upon prolonged exposure to air, TiO_2 starts to overgrow the fine grained Al_2O_3-rich layer as TiO_2 provides a fast diffusion path for oxygen. Additionally, N diffuses towards the alloy, forming various nitride phases. Ti and Al diffuse into the scale and form new oxides, which leads to a multiphase structure. Nb as a slowly diffusing element enriches at the lower interface, forming Nb-rich phases. After long term exposure of 1000 h the final layered oxide structure is formed with TiO_2 as the outermost layer. The underlying fine grained Al_2O_3-rich layer controls

the diffusion of oxygen and thus scale growth. Toward the alloy-scale interface a mixed layer of Ti- and Al-oxides is formed. The interface itself consists of a mixture of nitrides, Al-oxides, and Nb-rich phases. Enhanced diffusion of N along grain boundaries favors the formation of nitrides in the sub-scale zone. Due to selective oxidation of Ti and Al these elements are depleted leaving behind a Nb-enriched zone with typically higher α_2 content due to compositional shifts towards higher Ti content.

While all three alloys show a similar scale evolution in terms of the
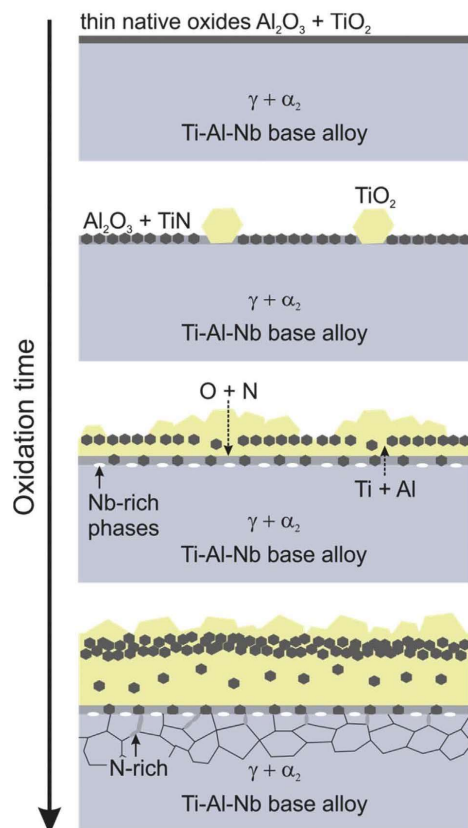
Fig. 13. General oxidation processes and structural evolution upon oxidation of the studied Ti-Al-Nb base alloys at 1073 K a) native state, b) short term exposure up to 24 h, c) intermediate stage (24 h < t < 1000 h), d) final state after 1000 h.

sequence of the formed phases, their weight gains have been found to be very different, where the ODS-containing variant and the Nb-richer TNB-V5 show similarly low growth kinetics. In the past the beneficial effect of Nb and the similar elements Mo and W have been attributed to the stabilization of Al_2O_3 forming in a sub-surface barrier layer as well as in the inner TiO_2-rich region [18]. Consequently, inward transport of oxygen along the TiO_2 is strongly reduced and higher oxidation resistance is achieved. Similar effects on the stability of Al_2O_3 have been described for Y-doped TiAl alloys [24]. Comparing the results for OX 45-3 and OX 45-3 ODS, this effect is also triggered by additions of Y_2O_3 in the form of finely distributed dispersoids (Fig. 11e). Unlike in elemental addition, the Y is concentrated in the stable dispersoids avoiding detrimental effects as formation of large internal Y_2O_3-particles, as observed by Haanappel et al. [25]. This effect is not observed in this work by the addition of Y in the form of a stable dispersion of Y-based oxides.

3.3.3. Size evolution of the dispersoids at high temperature

The stability of the dispersoids and their size evolution is determined for the OX 45-3 ODS variant after exposure to air at 923 K and 1073 K after 987 h and 924 h, respectively (Fig. 14). After testing at both temperatures, the dispersoids remain stable and well distributed

throughout the intermetallic matrix (Fig. 14a and c). The particles are observed in the equiaxed region consisting of γ and α_2 as well as in the lamellar $\alpha_2 + \gamma$ colonies, where no preference for either phase is found. The dispersoids are globular and partly faceted, with diameters between sub-10 nm up to 150 nm. In both conditions a multitude of dispersoids is found on phase or grain boundaries, indicating a strong pinning effect by the dispersoids and consequently reduced grain growth due to their presence in the ODS-variant (Fig. 14b and d). Coarser dispersoids exert a high enough pinning force, which leads to locally curved grain boundaries. This clearly indicates the beneficial effects of a portion of larger particles on the microstructure stability at high temperatures. A similar effect has also been observed at short term annealing at high temperatures in OX 45-3 ODS [28]. Upon exposure to air at 923 K and 1073 K the dispersoids show little change in their size distribution. Fig. 15 shows the size distributions after both exposure conditions as well as the initial state in the stabilized OX 45-3 ODS alloy. After consolidation by SPS, the following stress relief and microstructural stabilization annealing at 1123 K for 12 h, the resulting mean dispersoid diameter is 29 nm. The log-normal shape of the distribution indicates the highest fraction of particles at a slightly smaller diameter of around 23 nm. The number density of particles is $4.4 \cdot 10^{20}$ m^{-3}. Upon exposure at 923 K for 987 h the resulting size distribution is shifted to 26 nm with its maximum relative frequency in the size class of 15–20 nm with a particle number density of $5.3 \cdot 10^{20}$ m^{-3}. A similar oxidation time at 1073 K leads to a slight particle coarsening, shifting the size distribution to a median of 32 nm at a particle number density of $4.4 \cdot 10^{20}$ m^{-3}. While the relative frequency of the fine dispersoids is reduced, a larger amount of coarser ones appears simultaneously indicating continued growth of particles of all sizes. The appearance of a high fraction of dispersoids with submedian size after oxidation at 923 K could be attributed to fast coarsening of very fine precipitates or re-precipitation from the matrix. In the present case the latter appears to be the case, as the fraction of small dispersoids after consolidation appears not to be high enough to explain such behavior. The increased number density also suggests the formation of new particles. But it has also to be noted that the measurement of particles below 5 nm is difficult based on their low contrast to the surrounding matrix. The re-precipitation mechanism can be understood taking into account the production route of the alloy. Upon high-energy ball milling the added Y_2O_3 is finely dispersed and potentially partially dissolved into the matrix alloy. After precipitation and growth upon SPS consolidation and annealing, the formed particles are in a metastable equilibrium with the matrix, based on the relative stabilities of the phases involved. It was shown in the past that even in equilibrium a portion of the initially added dispersoid material remains in solution [4]. This leads to a doping of the TiAl alloy matrix with Y and O in the case of Y_2O_3 addition. Upon long-term oxidation at moderate temperature, the formation of new particles appears to be faster than the growth of the existing ones, leading to an effective shift of the total size distribution towards smaller diameters. At higher temperature this effect is not observed. Additional effects may be chemistry changes of the particles formed. Changing from a Y-rich to a Y-lean phase, new particles can be formed by incorporation of the abundant Ti and Al as well as O. To unambiguously determine such an effect a large amount of measurements on the formed particles is needed to ensure statistical meaning which is not the goal of the presented study. However, this remains an important topic for future studies of this class of intermetallics. Apart from the discussion about the underlying cause of the observed shifts in the particle size distribution by a few nanometers, it can be clearly stated that the particles in OX 45-3 ODS exhibit a low coarsening tendency and are stable at 1073 K for 1000 h.

4. Summary and conclusion

- At room temperature, SPS OX 45-3 ODS has a 34% higher yield point, 14% higher ultimate tensile strength at a reduction in fracture
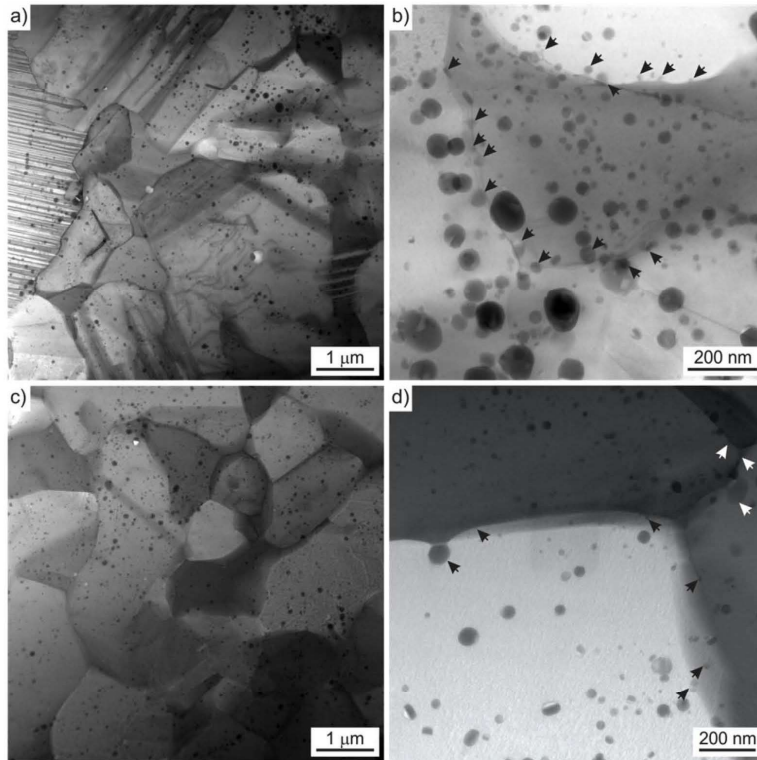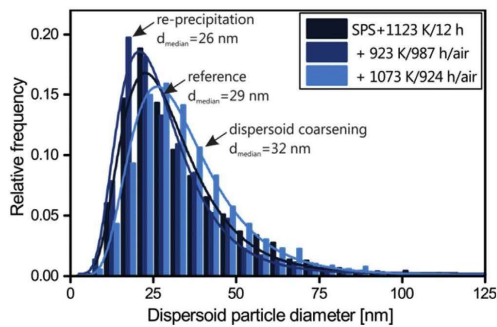
Fig. 15. Size distribution of ODS particles in solid state SPS sintered and stabilized material after exposure for 987 h at 923 K and 924 h at 1073 K. Least-square-fitted log-normal distribution curves are shown overlaid.

strain of 17% compared to SPS OX 45-3. The ODS variant retains its superior yield point and ultimate strength up to 1073 K.

- The ultimate strength of DMD specimens is limited by the presence of pores leading to premature fracture.
- The fracture surfaces of OX 45-3 show increased tendency for interlamellar failure at high temperatures. SPS and DMD OX 45-3 ODS shows similar fracture surfaces from 293 K to 1073 K with preferred *trans*-lamellar fracture.

- The addition of Y_2O_3 increases the oxidation resistance of mechanically alloyed and SPS sintered Ti-45Al-3Nb at 1073 K by a factor of two compared to the ODS-free variant. DMD material is superior to SPS material.
- Upon oxidation at a complex oxide scale is formed. XRD shows the presence of TiO_2, Al_2O_3 and TiN and Ti_2AlN nitride phases, where TiO_2 forms the outermost layer. All alloys form protective Al_2O_3 as part of their oxide scales.
- The Y-based dispersoids remain stable at 923 K and 1073 K up to 1000 h with minimal changes in median size from 29 nm in the initial state to 26 nm at 923 K and 32 nm at 1073 K, respectively. Increased number densities from 4.4 to $5.3 \cdot 10^{20}$ m^{-3} indicate precipitation of new particles at 923 K.

The achieved oxidation behavior is comparable to a commercial TNB-V5 alloy richer in Nb and additionally alloyed with C and B. The addition of < 0.2 mol.% Y_2O_3 provides similar resistance as the effects of additional 2 at.% Nb and 0.2 at.% C and B. The addition of dispersed Y_2O_3 opens a new possibility to further enhance the oxidation resistance of TiAl alloys alloyed already to their maximum allowable contents of Nb or other elements as W and Mo based on the desired set of phases. Based on the presented results, the addition of ODS particles is considered a promising way to further enhance the properties of TiAl alloys. In the future, detailed creep studies are needed to explore the limits of the ODS approach in TiAl material.

Acknowledgement

Appendix A. Supplementary data

Supplementary data related to this article can be found at http://dx. doi.org/10.1016/j.intermet.2017.09.004.

References

[1] F.H. Froes, C. Suryanarayana, D. Eliezer, Synthesis, properties and applications of titanium aluminides, J. Mater. Sci. 27 (1992) 5113–5140, http://dx.doi.org/10.1007/BF00553381.

[2] K.S. Kumar, G. Bao, Intermetallic-matrix composites: an overview, Compos. Sci. Technol. 52 (1994) 127–150.

[3] A.V. Antonova, K.B. Povarova, A.A. Drozdov, Composite materials with an inter-metallic matrix based on nickel and titanium monoaluminides hardened by oxide particles or fibers, Russ. Metall. Met. 2011 (2012) 853–864, http://dx.doi.org/10.1134/S0036029511090023.

[4] M. Grujicic, S. Arokiaraj, Chemical compatibility between zirconia dispersion and gamma titanium aluminide matrix, Calphad 17 (1993) 133–140, http://dx.doi.org/10.1016/0364-5916(93)90013-2.

[5] C.C. Koch, Intermetallic matrix composites prepared by mechanical alloying—a review, Mater. Sci. Eng. A 244 (1998) 39–48.

[6] O.A. Skachkov, K.B. Povarova, A.A. Drozdov, A.E. Morozov, S.V. Pozharov, Deformation and heat treatment of NiAl-Y2O3-based powder alloys: I. Deformation and production of various pressed sections, Russ. Metall. 3 (2013) 217–219.

[7] S.L. Kampe, J.D. Bryant, L. Christodoulou, Creep deformation of TiB2-reinforced near-γ titanium aluminides, Metall. Trans. A 22 (1991) 447–454.

[8] F.H. Froes, Titanium aluminides: science, technology, applications and synthesis by mechanical alloying, J. Mater. Chem. Sci. Technol. 10 (1994) 251–262.

[9] W. Liu, J.N. Dupont, Fabrication of carbide-particle-reinforced titanium aluminide-matrix composites by laser-engineered net shaping, Metall. Mater. Trans. A 35 (2004) 1133–1140.

[10] D.S. Schwartz, P. Fraundorf, S.M.L. Sastry, TEM study of B- and Er-containing dispersoids in rapidly solidified dispersion-strengthened titanium aluminide alloys, Ultramicroscopy 37 (1991) 310–317.

[11] C. Suryanarayana, F.H. Froes, Mechanical alloying of titanium-base alloys, Adv. Mater 5 (1993) 96–106.

[12] P.B. Trivedi, E.G. Baburaj, A. Genc, L. Ovecoglu, S.N. Patankar, F.H. Froes, Grain-size control in Ti-48Al-2Cr-2Nb with yttrium additions, Metall. Mater. Trans. A 33A (2002) 2729–2736.

[13] Z.W. Li, W. Gao, D.L. Zhang, Z.H. Cai, High temperature oxidation behaviour of a TiAl-Al2O3 intermetallic matrix composite, Corros. Sci. 46 (2004) 1997–2007, http://dx.doi.org/10.1016/j.corsci.2003.10.026.

[14] K. Zhang, W. Fen, J. Zhu, H. Wu, Mechanical properties and microstructure of Al2O3/TiAl in situ composites doped with Cr and V2O5, Sci. Sinter. 44 (2012) 73–80.

[15] D.P. Whittle, J. Stringer, Improvements in high temperature oxidation resistance by additions of reactive elements or oxide dispersions, Philos. Trans. R. Soc. Lond. Math. Phys. Eng. Sci. 295 (1980) 309–329, http://dx.doi.org/10.1098/rsta.1980.0124.

[16] J. Stringer, Proceedings of the 2nd international symposium on high temperature corrosion of advanced materials and coatings the reactive element effect in high-temperature corrosion, Mater. Sci. Eng. A 120 (1989) 129–137, http://dx.doi.org/10.1016/0921-5093(89)90730-2.

[17] B.A. Pint, Progress in understanding the reactive element effect since the Whittle and Stringer literature review, Proc John Stringer Symp. High Temp. Corros. ASM International, 2003, pp. 9–19.

[18] Y. Shida, H. Anada, The effect of various ternary additives on the oxidation behavior of TiAl in high-temperature air, Oxid. Met. 45 (1996) 197–219.

[19] J.W. Fergus, Review of the effect of alloy composition on the growth rates of scales formed during oxidation of gamma titanium aluminide alloys, Mater. Sci. Eng. A 338 (2002) 108–125, http://dx.doi.org/10.1016/S0921-5093(02)00064-3.

[20] W. Zhang, G. Chen, Z. Sun, Oxidation of ternary Ti–18Nb–48Al and Ti–10Nb–45Al alloys, Scr. Metall. Mater 28 (1993) 563–567, http://dx.doi.org/10.1016/0956-716X(93)90197-Z.

[21] A. Gil, B. Rajchel, N. Zheng, W.J. Quadakkers, H. Nickel, The influence of implanted chromium and yttrium on the oxidation behaviour of TiAl-based intermetallics, J. Mater. Sci. 30 (1995) 5793–5798, http://dx.doi.org/10.1007/BF00356723.

[22] J.P. Kim, H.G. Jung, K.Y. Kim, Al + Y codeposition using EB-PVD method for im-provement of high-temperature oxidation resistance of TiAl, Surf. Coat. Technol. 112 (1999) 91–97, http://dx.doi.org/10.1016/S0257-8972(98)00787-7.

[23] K. Kasahara, Y. Ikeda, T. Kimura, T. Tsujimoto, Effects of additions of Y and rare-earth metals on the cyclic oxidation of TiAl alloys, J. Jpn. Inst. Met. (1996) 907–913.

[24] Y. Wu, S.K. Hwang, Microstructural refinement and improvement of mechanical properties and oxidation resistance in EPM TiAl-based intermetallics with yttrium addition, Acta Mater 50 (2002) 1479–1493, http://dx.doi.org/10.1016/S1359-6454(02)00006-X.

[25] V.A.C. Haanappel, H. Clemens, M.F. Stroosnijder, The high temperature oxidation behaviour of high and low alloyed TiAl-based intermetallics, Intermetallics 10 (2002) 293–305.

[26] M.K. Lei, X.P. Zhu, X.J. Wang, Oxidation resistance of ion-implanted γ-TiAl-base intermetallics, Oxid. Met. 58 (2002) 361–374, http://dx.doi.org/10.1023/A:1020162922745.

[27] S. Taniguchi, T. Shibata, Influence of additional elements on the oxidation behaviour of TiAl, Intermetallics 4 (1996) 85–S93, http://dx.doi.org/10.1016/0966-9795(96)00017-9.

[28] C. Kenel, K. Dawson, C. Hauser, J. Barras, G. Dasargyri, T. Bauer, A. Colella, A.B. Spierings, G.J. Tatlock, C. Leinenbach, K. Wegener, Microstructure and Oxide Particle Stability in a Novel ODS γ-TiAl Alloy Processed by Spark Plasma Sintering and Laser Additive Manufacturing Submitted, (2017).

[29] D.M. Dimiduk, P.M. Hazzledine, T.A. Parthasarathy, M.G. Mendiratta, S. Seshagiri, The role of grain size and selected microstructural parameters in strengthening fully lamellar TiAl alloys, Metall. Mater. Trans. A 29 (1998) 37–47, http://dx.doi.org/10.1007/s11661-998-0157-3.

[30] Y.-W. Kim, Ordered intermetallic alloys, Part III: gamma titanium aluminides, JOM 46 (1994) 30–39.

[31] S. Djanarthany, J.-C. Viala, J. Bouix, An overview of monolithic titanium alumi-nides based on Ti3Al and TiAl, Mater. Chem. Phys. 72 (2001) 301–319.

[32] P.J. Masset, M. Schütze, Oxidation tests with untreated and F-Treated TNBV5 al-loys, ECS Trans. 25 (2010) 45–56, http://dx.doi.org/10.1149/1.3315795.

Paper 3
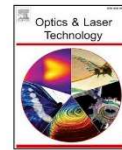
Full length article

The influence of key process parameters on melt pool geometry in direct energy deposition additive manufacturing systems

Robert Sampson[a], Robert Lancaster[b,*], Mark Sutcliffe[a], David Carswell[a], Carl Hauser[a], Josh Barras[a]

[a] TWI Granta Park, Great Abington, Cambridge CB21 6AL, UK
[b] Swansea University, Bay Campus, Fabian Way, Swansea SA1 8EN, UK

HIGHLIGHTS

- Directional emittance algorithm successfully used to perform a detailed parametric study.
- Increasing powder mass flow rate widens the resultant melt pool.
- When using high laser power settings, a larger body of molten material is formed.
- Increasing PMFR at low laser power settings does not influence melt pool width.
- Increasing path velocity reduces melt pool width for all laser power settings.

ARTICLE INFO

ABSTRACT

The measurement of melt pool width has proven to be critical in the development of advanced control systems, defect detection algorithms and understanding the influence of parameter changes on build quality in additive manufacturing processes. Parametric studies are performed on new materials and builds to help identify optimal parameter settings for final components. Many parametric iterations are often required to produce optimal components, which requires in-depth process/material knowledge from highly skilled engineers. Having fundamental knowledge of parametric interaction and melt pool mechanics is key in developing state of the art additive manufacturing components. This paper addresses the need for complex parametric interaction understanding in additive manufacturing processes by providing a detailed parametric study using directional emittance melt pool edge detection techniques.

1. Introduction

Additive Manufacturing (AM) is a progressive technology that is currently being utilised in multiple industries including the aerospace, automotive and medical sectors. AM is a family of manufacturing technologies that fabricate components by adding material, as opposed to conventional subtractive techniques such as milling and lathing. The umbrella term AM can be broken down into seven subcategories: vat photopolymerisation, material extrusion, material jetting, binder jetting, Powder Bed Fusion (PBF), Direct Energy Deposition (DED) and sheet lamination. DED is a powder blown technique that induces a laser beam onto a substrate and injects powder into the molten metal pool (melt pool) formed to enlarge it. Melt pools can be controlled by robotic manipulators to form complex near net shape structures. This paper focuses on the implementation of Melt Pool Monitoring (MPM) techniques into DED processes. Whilst specific focus has been placed on DED, it should be noted that MPM advancements made for DED systems can be transferred or adapted into PBF systems and vice versa.

MPM systems have been used in AM processes for many years to develop defect detection capabilities, control systems and better understand process parameters. A more holistic understanding of input parameters can benefit AM research organisations, as it allows for good manufacturing practices and optimum component quality.

Key process parameter knowledge allows skilled engineers to manually manipulate parameters to produce high quality components. Meriaudeau & Truchetet [1] determined key process variables by integrating multiple cameras into PBF systems to measure powder distribution, track surface temperature and track geometry. They

determined that the Powder Mass Flow Rate (PMFR) affects track height and suggested that PMFR, laser power and beam diameter can affect bonding quality. Renier, Meriaudeau, & Truchetet [2] further studied the influence of welding temperature on track deposition using image processing techniques. This knowledge was used to optimise industrial weld applications, with their studies identifying melt pool temperature to be a key process parameter. Meriaudeau et al. [3] subsequently developed image-based powder particle speed measurement techniques and identified Powder Mass Flow Rate (PMFR) as a key process variable that influences both the melt pool and AM process. Hua et al. [4] developed a temperature measurement system using a two-colour infrared thermometer to investigate the influence of process parameters (including PMFR, scanning velocity and laser power) on melt pool temperature. They concluded that increasing PMFR decreases melt pool temperature, increasing scanning velocity decreases melt pool temperature and increasing laser power increases melt pool temperature. Sun & Hao [5] studied the influence of changing PMFR, laser power and scanning speed on both track geometry and dilution (the relation between the melted area of the substrate and the amount of added material). They discovered that PMFR is the dominant factor that affects both the width and height of the track, whilst scanning speed has the most effect on molten depth of substrate. Cheng et al. [6] studied the influence of changing path velocity on melt pool geometry and identified it as a key process variable that influences both melt pool and component. They found that increasing path velocity results in a decrease in melt pool width. The effects of thermal behaviour, or the evolution of temperature during PBF, on the melt pool and part quality is studied in detail by Yan et al. [7]. They concluded that the thermal behaviour from the process and melt pool mechanics influence residual stress, deformation, microstructure and defects. Yao et al. [8] performed a parametric study using a DED system and identified that laser energy density is positively correlated to part density. They found that the key parameters to influence energy density are laser power, path velocity and PMFR.

Melt pool behaviour is influenced by many parameters within AM processes. Hooper [9] studied the effects of geometry and scan path on the melt pool's temperature gradients and cooling rates. Hooper determined that events such as beginning scans, ending scans and turning during hatching affect temperature gradients, cooling rates and melt pool stability. Hooper's results displayed fluctuations in both temperature gradients and cooling rates during multiple events. Hooper concluded that a deeper understanding of process fundamentals can accelerate and refine process parameter development to provide improved component quality. Craeghs et al. [10] studied changes in melt pool behaviour with overhanging structures. They discovered a novel way of presenting thermal data and determined that overhang structures (geometry) can have a major influence on the melt pool. Results from Craeghs et al. [10] show that increasing the amount of support structures on layers prior to building overhanging features causes more uniform heat dissipation and reduced overheating of powder, due to the supports acting as a heat sink. Kledwig et al. [11] used an MPM system in a DED process to identify the minimum energy required to produce stable melt pools. They used optical monitoring systems and a pixel counting method to identify the melt pool area. The study was able to determine influences of laser power, PMFR and path velocity on melt pool area. It identified parametric boundaries for the material X2CrNiMol7-12-2 such as the minimum required specific energy (18 J/mm^2). Furumoto et al. [12] used high-speed imaging and studied the influence of surface temperature and build sequence on resultant formation and spatter particles. They determined that substrate temperature influences melt pool behaviour and spatter patterns. Manvatkar and DebRoy [13] created a three-dimensional transient heat transfer and fluid flow model to determine changes in melt pool geometry and cooling rates across different heights layers in build cycles. They determined that peak temperature and melt pool dimensions increase and cooling rates decrease as build layers are added.

Melt pool behaviour has been linked with both process parameters and the integrity of the manufactured component. Direct input parameters such as laser power, PMFR and path velocity can be used to influence the melt pool and improve part quality. Dai et al. [14] identified a new scan strategy to greatly improve component quality. They increased part density and improved tensile properties by remelting previous layers using a higher laser volume energy density. This liberated entrapped gas, promoting the formation of high densification. Fiegl et al. [15] established that the position and orientation of components within build chambers influences surface roughness, porosity levels and tensile strength of built parts. They discovered that increasing the distance between the component and zero-point (directly below the laser), resulted in an increased surface roughness and porosity, and decreased tensile strength and elongation. Ding et al. [16] studied the process parameters from the Electron Beam Melting (EBM) process and successfully linked resultant microstructure, melt pool geometry and input parameters together. They discovered that increasing line energy resulted in an increase in melt pool width and depth. During this process they identified that the shape of the melt pool progressed from semi-elliptical to semi-circular and then to conical. Colodrón et al. [17] measured melt pool width using emissivity-based image processing techniques and determined it to be a good indication of process status. They discovered that melt pool width could be correlated to dilution. In a subsequent study, Colodrón et al. [18] then used melt pool width calculations to improve part quality by creating a control system to regulate laser power. They found that control systems are useful for components with complex geometries, where individual cladding tracks are non-continuous and short. A similar technique was developed by Hofman et al. [19], who successfully used a CMOS camera and software to calculate melt pool geometry. They regulated melt pool width by using a control system to alter laser power throughout the build. They discovered that a constant laser power leads to excessive dilution and reduced hardness. By controlling the laser power, and thus melt pool width, they reduced dilution in DED processes. Sun et al. [20] developed a melt pool dimensioning system that can accurately predict melt pool width and shape in DED processes. They discovered that melt pool boundary shape can be used to predict the crystal growth direction in manufactured components.

Research has shown that MPM systems can be used in a range of applications to improve AM processes and components. This research aims to utilise a previously documented melt pool dimensioning technique, developed by Sampson et al. [21], to better understand process parameters for subjective build optimisation decisions.

This study focuses on the influence of two major parameters in DED processes – PMFR and path velocity. These parameters have been selected from experience of DED processes and are supported by literature. Meriaudeau et al. [3] identified PMFR as a major influence on the melt pool and process. Cheng et al. [6] studied the influence of path velocity on melt pool width and identified it as a parameter that influences both melt pool and component. Yan et al. [7] provided a recent parametric study to identify both PMFR and path velocity as key processing parameters in DED processes.

PMFR and path velocity changes can have both positive and negative effects on melt pool stability and build quality. High speed deposition and low powder wastage can be achieved by optimising parameters. Manufacturing outside of a material's parametric envelopes however can cause melt pool instability, and defects such as lack of fusion and keyhole porosity. Often material parameter envelopes are not understood, and no guidance is provided for the distribution of powder material for DED processes. This study aims to utilise advanced MPM techniques by Sampson et al. [21], to better understand the complex interaction of laser power, PMFR and path velocity parameters when manufacturing with the steel alloy, EN25.

2. Melt pool monitoring system

The MPM system used in this research has been previously disseminated in a paper by Sampson et al. [21]. The MPM system can provide accurate melt pool width calculations without the need for emissivity values. The technique uses improved machine vision techniques to highlight features that best indicate the true melt pool edge when depositing with EN25.

2.1. Adaptive exposure times

Adaptive exposure times are used to achieve high-quality melt pool images over a range of parameter settings. To calibrate exposure times for EN25, a series of scans were produced to identify the best exposure time for various laser power settings. The laser power and exposure times are correlated subjectively by the operator to increase the directional emittance phenomenon. The experimental procedure used to create Eq. (1) is detailed within a paper previously disseminated by Sampson et al. [21]. Eq. (1) is used to identify the optimum exposure time for laser power settings between 600 and 1200 W.

$$E = -6.0 \times 10^{-4} \cdot P + 0.9192\# \tag{1}$$

where E is the exposure time setting to be used, and P is the laser power setting being used when depositing EN25 powder. Fig. 1 shows the melt pool images captured using optimum exposure times over multiple laser power settings. The images illustrate melt pool edge features and have low levels of saturation.

2.2. Directional emittance phenomena

Emissivity describes a surface's ability to emit radiation. Emittance is the radiation mismatch between a real surface and a blackbody of that material. A blackbody is an idealistic surface that absorbs all incident light, independent of both wavelength and direction, and neither reflects nor transmits. Real surfaces almost never have properties of a blackbody. The surface of a real body is one that only partially emits radiation compared with a blackbody at the same temperature and wavelength. A real body does not emit radiation equally for all wavelengths in all directions.

As described by Meola [22], the directional emittance phenomenon occurs in melt pool images when using optimised exposure times as a result of real body radiation not emitting equally in all directions. This results in part of the substrate emitting stronger radiation in the direction of the sensor even though the surface temperature is lower.

Radiation emitted from the melt pool in the direction of the sensor is dependent on the melt pool's surface angle. Measured intensity is reduced at the edges of the melt pool due to higher surface angles. Higher emission levels are measured from the substrate due to low surface angles. This is referred to as the directional emittance phenomenon throughout this paper and results in images with true melt pool edge features. Fig. 2 is a schematic representation of the emission theory.

2.3. Melt pool width extraction

The melt pool image processing algorithm used in this study was discussed previously by Sampson et al. [21]. The image processing algorithm uses the directional emittance phenomena and optimised melt pool images to extract melt pool width measurements. The contrast between the melt pool edge and brightly lit substrate provides a unique feature that can be extracted using image processing techniques. Cross-sectional signals are extracted, averaged and differentiated to expose edge locations. Locations of the melt pool's edges are then used to calculate melt pool width. Fig. 3 displays melt pool width calculations using the directional emittance technique.

2.4. Melt pool width track averages

To directly compare width measurement signals (extracted from melt pool video recordings of different tracks) for parametric studies, snippets are extracted from the original full track deposition data. Taking snippets from recordings allows for an easier comparison as fluctuations in the acceleration/stabilisation and deceleration/destabilisation stages of deposition are eradicated.

For data collection, snippet lengths are half that of the original signals. The deposition start point is determined when the first melt pool measurement was recorded for each individual track. The starting point for snippet extraction began after 25% of the track length had passed and finished before the last 25% of the track length. This resulted in signals that were not clouded by the unstable nature of the melt pool in the acceleration/stabilisation and deceleration/destabilisation stages of deposition. Fig. 4 presents an original melt pool signal, with guidelines to display the extraction process. The frame numbers on the extracted signal are not carried over from the original signal and are reset.

3. Experimental configuration

3.1. Equipment set-up

In this research a Trumpf Trudisk 8002 5.3 kW disc laser DED system was used with a TruControl 1000 controller. Trumpf BEO D70 processing optics with a motorised collimation laser deposition head were employed with a Reis RV60-40 robot, a Reis RDKVv05 two axis manipulator and a Sulzer Metco 10-C powder feeder with a dual 1.5 kg hopper arrangement.

A NIR CMOS machine vision camera (U3-3240ML-NIR-GL) was installed to improve melt pool imaging and was combined with a UV/VIS cut off imaging filter with a 135 nm notch. The filter had an optical density of 3.0 for wavelengths of 200–750 nm and 4.0 for wavelengths of 1000–1200 nm. The notch filter and NIR CMOS camera were coaxially installed into the laser deposition head for a clear birds-eye view of the melt pool.

3.2. Material

The deposition material for this study was the steel alloy EN25. The composition is presented in Table 1. It should be noted that powder from different manufacturers and even different batches of powder can cause changes in melt pool characteristics.

3.3. Method

Single line tracks with lengths of 150 mm were deposited onto a 15 mm thick stainless steel 316L substrate plate for all experiments. Two separate parametric experiments were conducted, each consisting of 45 cladding tracks. Substrate temperatures were measured before each cladding track was deposited to ensure that heat accumulation did not affect results. Cladding tracks were deposited with enough distance separation so that previous tracks did not interfere with further deposition. Fig. 5 displays schematically how tracks were deposited. The direction of travel was fixed, the carrier gas was set to 3.5 L/min, the shielding gas was set to 6 L/min, the laser spot size was 1.5 mm, and three laser power settings of 750, 900 and 1050 W were used. All these settings remained consistent throughout the experiment. Two separate trials were conducted, to determine the influence of both PMFR and path velocity on melt pool width. The PMFR setting was iterated from 3.70 to 5.29 g/min. PMFR is controlled by an opening on the hopper, with a percentage value indicating how much the hopper is open. This value was changed from 9 to 12.5% on the machine using 15 increments of 0.25% to achieve the described PMFR. The path velocity setting was iterated from 9.5 to 13 mm/s with a total of 15 increments
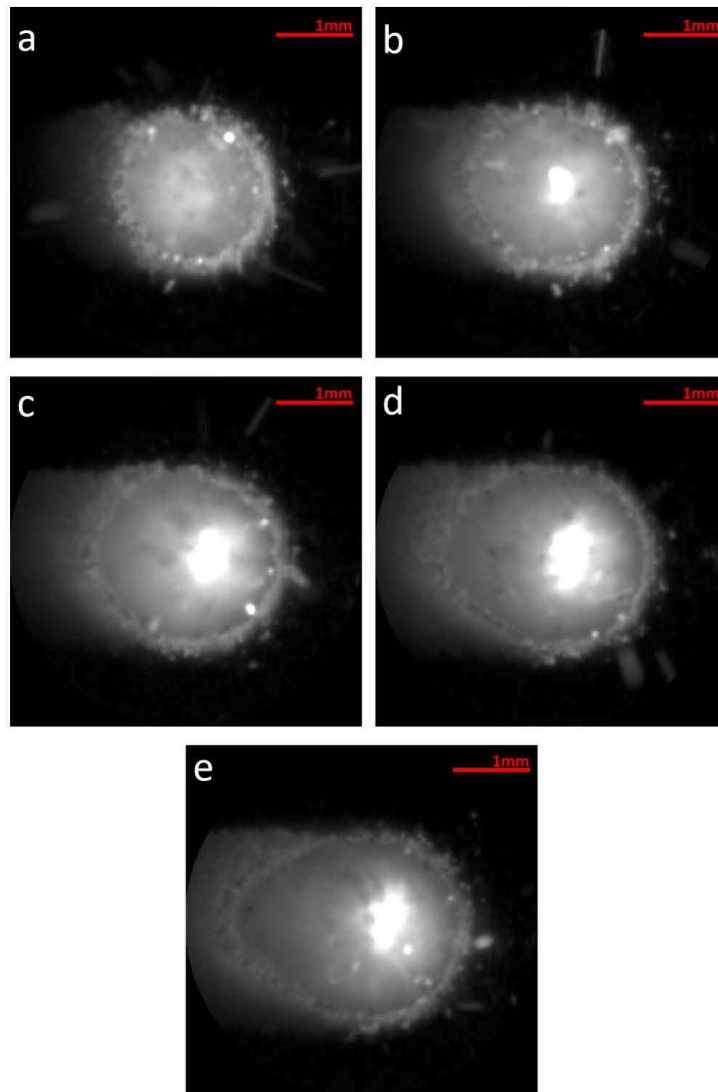
Fig. 1. A series of melt pool images for various laser powers taken using adaptive exposure times. The laser power settings are: (a) 600 W (b) 750 W (c) 900 W (d) 1050 W and (e) 1200 W.

(0.25 mm/s). The matrices of parameters used for the experiments are displayed in Tables 2 and 3. All values were selected within the parameter envelope of EN25 and are known to produce quality tracks with good mechanical properties and reduced defects. Parameters outside these ranges are known to produce poor quality deposition for EN25.

Using standard recording software (distributed with the U3-3240ML-NIR-GL camera), a total of 90 videos were recorded for the entire track lengths. The melt pool width average for each track was extracted from the corresponding videos in the manner described within this paper.

4. Results

This section is presented in two separate subsections, describing results for the PMFR and path velocity experiments separately. Each experiment consisted of 45 individual cladding tracks, which were deposited on substrates as depicted in Fig. 5. The large amount of data collected has been collated into single graphs for each experiment to allow for comprehensive analysis. Figs. 6 and 7 represent the coalesced data for the PMFR and path velocity experiments respectively. Each data point on the graph represents a melt pool width average for a
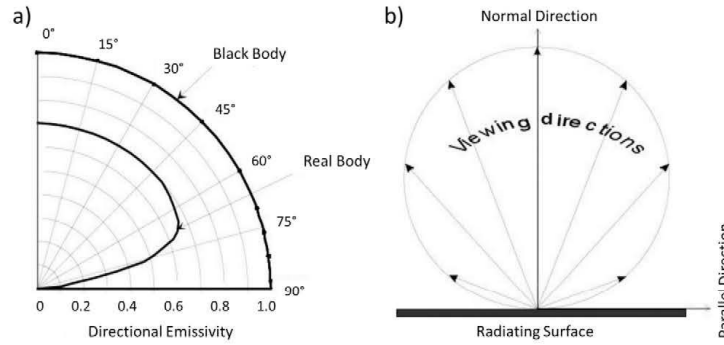
Fig. 2. (a) Directional emittance of a blackbody and real body. (b) A schematic representation of directional emittance from a flat surface. Documented by Meola [22].
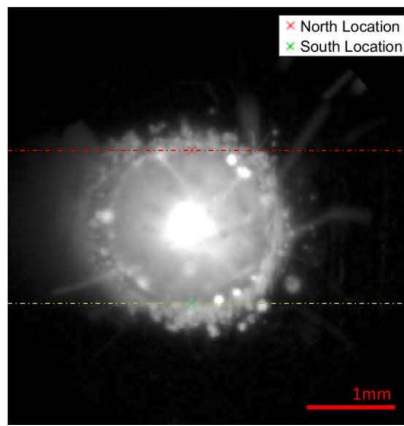

Fig. 3. An image showing the north and south locations calculated using the directional emittance technique.

single clad track, calculated using the melt pool width extraction and track averaging technique outlined within this paper.

4.1. Powder mass flow rate

Results from the PMFR parametric experiment detailed in Table 2 were plotted on a single graph, as depicted in Fig. 6.

The results have shown that the effects of changing PMFR on the melt pool width is dependent on the laser power, and it cannot simply be assumed that the melt pool width increases with increasing PMFR. For the highest laser power setting used in this experiment (1050 W) the melt pool width did increase when an increasing PMFR was used. Having a high laser power setting means that there is more energy to melt powder and increasing the PMFR in this scenario resulted in more powder being absorbed into the melt pool. This in turn led to an increase in melt pool width.

For the mid (900 W) laser power setting this was again true. Having a relatively high laser power setting resulted in more powder being melted and accepted into the molten melt pool when the PMFR was increased.

The gradients of the lines for both the mid and high laser power settings differ. The tracks with a mid laser power setting showed a shallower increase in melt pool width for the same increase in PMFR. This is most likely due to there being insufficient energy to melt excess powder as effectively.

The gradient of the line of best fit for the low (750 W) laser power setting is close to zero. Results showed that increasing the PMFR for a low laser power setting did not increase the size of the melt pool. The average melt pool width stayed constant as the PMFR was increased. For tracks deposited using the lower laser power, there is larger deviation of calculated melt pool width values from the line of best fit. Using a low laser power setting showed more variance between melt pool width calculations which indicated melt pool instability.

Results have indicated that increasing PMFR does not always increase melt pool width. This behaviour cannot be assumed for all parameter settings. The effects that increasing/decreasing the PMFR has on the melt pool is dependent on other parameter settings used.

4.2. Path velocity

Results from the path velocity parametric experiment described in Table 3 were plotted on a single graph, as depicted in Fig. 7.

The results from this plot provide information regarding the influence that the path velocity setting has on calculated melt pool widths. For all laser power settings, the average melt pool width decreased when the path velocity was increased. The melt pool width increases when the laser power setting is increased due to a higher energy density melting more blown powder and substrate material.

Increasing the path velocity results in a decrease in energy density, which in turn results in less energy being available to melt the molten powder and substrate in an instance. In addition, higher translation speeds reduce the interaction time between the laser and powder, resulting in less powder absorption into the melt pool. Both factors likely result in a reduction of melt pool width. The gradients of the three lines of best fit have also been displayed on the graph. The lines of best fit all show a negative gradient of similar values. This said, performing the cladding tracks at a laser power of 900 W produced the shallowest gradient. The difference between this gradient and the other two could be a result of the complex interactions that occur between different parameters. Increasing the path velocity could have different results on the melt pool geometry depending on other parameters that are used in the process. However, before conclusions are drawn more research should be performed to further increase understanding.

5. Discussion

This research aimed to provide a detailed understanding of how changes in AM parameters can affect melt pool geometry. Studies have
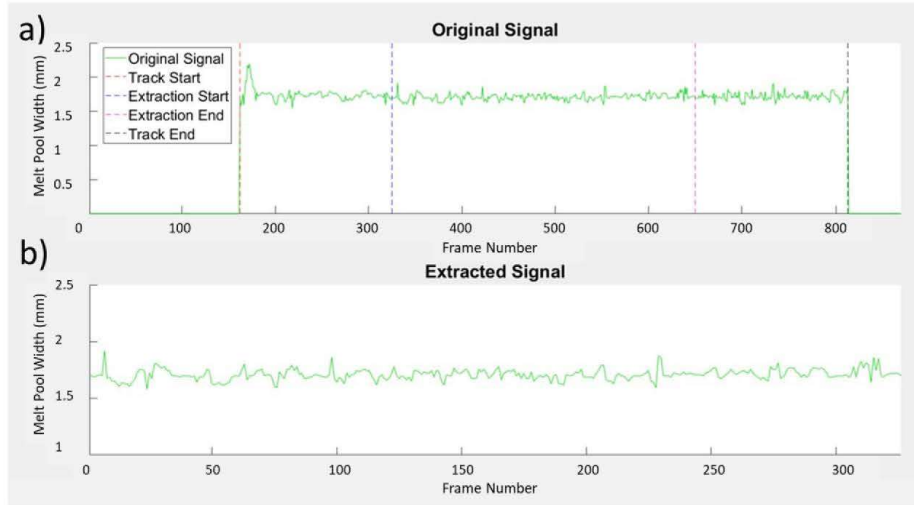
Fig. 4. (a) An original signal of the melt pool width calculations for a recording of a track deposition. (b) The extracted signal used for melt pool dimensioning comparison.

Table 1
The chemical composition of the EN25 powder used for experimental deposition (wt%).

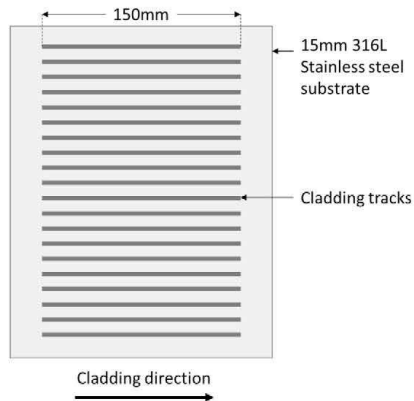| Al	Cr	Cu	Mn	Mo	Ni	P	Si	C
0.003	0.69	0.006	0.64	0.59	2.66	0.004	0.26	0.32
S	O	N	Fe	TAO	B	Mg	Zr	Co
0.003	0.02	0.003	Bal	0.01	< 0.001	< 0.001	< 0.01	0.01

Fig. 5. A schematic representation of the cladding tracks deposited on the stainless-steel plate substrates.

shown that PMFR is a parameter known to greatly affect DED processes, with Meriaudeau et al. [3] and Yao et al. [8] concluding that it majorly influences both melt pool behaviour and part quality. This research has highlighted that changes in PMFR greatly affects melt pool width, and that these changes can be accurately measured using the directional

emittance technique outlined be Sampson et al. [21]. This research extends knowledge contributed by Meriaudeau et al. [3] and Yao et al. [8] by providing a detailed study on the interaction between melt pool width, laser power and PMFR. This information can provide users with greater process understanding, which can subsequently lead to higher quality deposition.

Sun & Hao [5] and Meriaudeau et al. [3] both explored the effects of PMFR on solidified track dimensions and stated that PMFR is one of the dominant features affecting these. Their research shows that increasing the PMFR simply increases the size of the track width, but they do not detail the size of the melt pool throughout the process. Results from this paper detail the effects of changing PMFR on melt pool width and expose a complex relationship. Although melt pool width and track width are positively correlated, there are subtle differences between these dimensions due to shrinkage in material during solidification. Previous research from Sampson et al. [21] shows that both melt pool and track width increase with increasing laser power. They do however highlight that changes in shrinkage rates are apparent for different laser power settings. Sampson et al. [21] conclude that whilst melt pool width and track width are related, shrinkage rates are influenced by laser power and likely other parameters. Future work should look to explore the complex relationships between melt pool width and track width for varying PMFR settings.

Meriaudeau et al. [3] details the effects that path velocity has on solidified track width and reports that increasing path velocity results in a decrease in track width. Although this study measures the effects of path velocity on solidified track width, melt pool width and track width are undoubtedly linked. Previous work from Sampson et al. [21] has shown that whilst shrinkage rates can change for different parameters, the melt pool width and track width are positively correlated. Results for the path velocity experiment within this paper compliment those that were published by Meriaudeau et al. [3].

Hua et al. [4] details the effects that path velocity has on melt pool temperature and layer thickness. Their results show that increasing the path velocity reduces the temperature of the melt pool during manufacturing. Comparing results shows that increasing path velocity reduces both the melt pool width and temperature. This compliments the statement that increasing path velocity reduces the energy density for a

Table 2
The matrix of parameters used in the PMFR experiment.

Laser Power (W)	PMFR (g/min)	Laser Power (W)	PMFR (g/min)	Laser Power (W)	PMFR (g/min)
750	3.70	900	3.70	1050	3.70
750	3.81	900	3.81	1050	3.81
750	3.93	900	3.93	1050	3.93
750	4.04	900	4.04	1050	4.04
750	4.15	900	4.15	1050	4.15
750	4.27	900	4.27	1050	4.27
750	4.38	900	4.38	1050	4.38
750	4.49	900	4.49	1050	4.49
750	4.61	900	4.61	1050	4.61
750	4.72	900	4.72	1050	4.72
750	4.83	900	4.83	1050	4.83
750	4.95	900	4.95	1050	4.95
750	5.06	900	5.06	1050	5.06
750	5.17	900	5.17	1050	5.17
750	5.29	900	5.29	1050	5.29

Table 3
The matrix of parameters used in the path velocity experiment.

Laser Power (W)	Path Vel. (mm/s)	Laser Power (W)	Path Vel. (mm/s)	Laser Power (W)	Path Vel. (mm/s)
750	9.5	900	9.5	1050	9.5
750	9.75	900	9.75	1050	9.75
750	10	900	10	1050	10
750	10.25	900	10.25	1050	10.25
750	10.5	900	10.5	1050	10.5
750	10.75	900	10.75	1050	10.75
750	11	900	11	1050	11
750	11.25	900	11.25	1050	11.25
750	11.5	900	11.5	1050	11.5
750	11.75	900	11.75	1050	11.75
750	12	900	12	1050	12
750	12.25	900	12.25	1050	12.25
750	12.5	900	12.5	1050	12.5
750	12.75	900	12.75	1050	12.75
750	13	900	13	1050	13

specific instance, resulting in lower temperature melt pools and less powder being able to be absorbed.

Cheng et al. [6] detailed the effects of path velocity on melt pool width and indicated that increasing path velocity results in a decrease in melt pool width. The experiments conducted by Cheng et al. [6] were performed on a PBF machine using Inconel 718 powder. Despite differences in both the AM technique and material used, the same results were evident within this paper.

This paper demonstrates that the directional emittance algorithm can be used to effectively study parameter interaction. Results have provided a deeper understanding of the interaction between PMFR and melt pool width for multiple laser power settings. This research has solidified the understanding that increasing path velocity decreases melt pool width. Future work should look to further study the relationship between melt pool width, temperature and solidified track measurements, for various parameter settings. Having a deeper understanding of the influences of parameters on both the melt pool and formed track will help develop advanced material understanding and improve build quality.

6. Conclusion

This paper implemented a previously published directional emittance image processing technique to further understand process parameter interactions in DED processes. Two separate parameter trials were conducted to determine how both the PMFR and path velocity influence the melt pool's width.

Increasing the PMFR when there is excess energy available (using higher laser power settings) results in the melt pool width increasing as more powder is melted by the excess energy. When using high laser power settings (1050 W), a larger body of molten material was formed. This was evident on the mid laser power settings (900 W), but the influence that increasing PMFR had on the melt pool width was reduced. Deposition using a low laser power setting (750 W) showed results that have not been documented previously and increasing the PMFR at this laser power setting resulted in no increase in melt pool width. Low energy levels were not able to melt the extra powder that was introduced and resulted in the melt pool not growing.

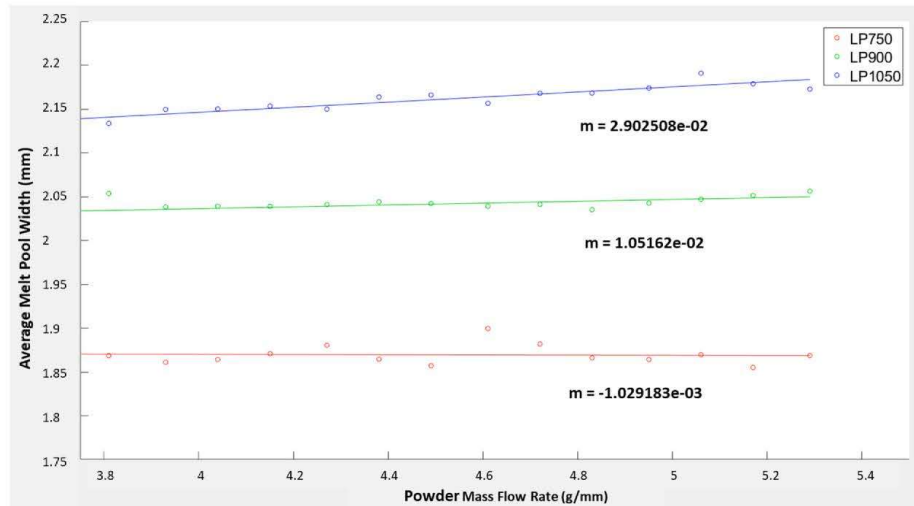Increasing the path velocity showed a decrease in melt pool width

Fig. 6. Graph representing all calculated average melt pool values for various parameter settings used in the PMFR experiment.
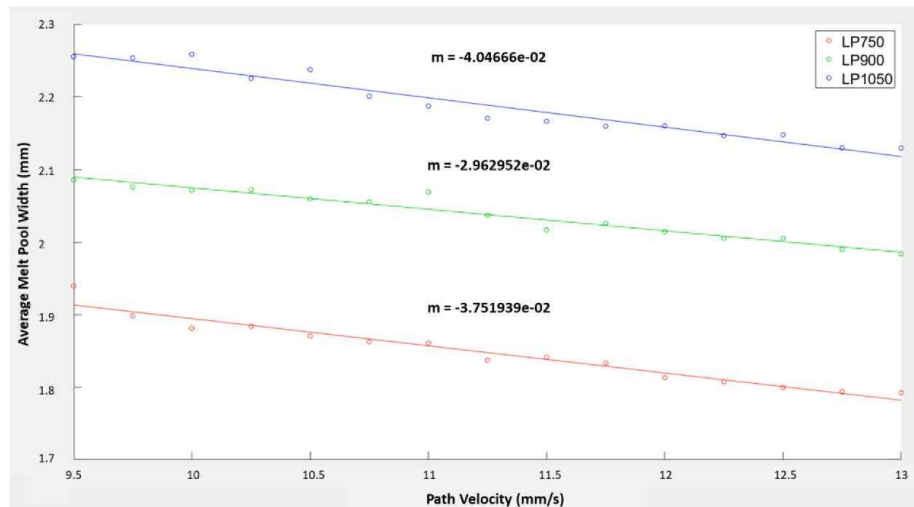
Fig. 7. A graph representing all calculated average melt pool values for various parameter settings used in the path velocity experiment.

for all laser power settings. Some variances in laser power settings resulted in changes to the rate of melt pool width decreasing, but the differences were not as prominent as those displayed in the PMFR study. No conclusion could be drawn from the three laser power settings used in this study and the subtle differences between them. The conclusion drawn from this experiment is that increasing path velocity results in the melt pool width decreasing. This compliments previous findings.

The directional emittance algorithm has been successfully used to better understand the complex DED process and has uncovered how certain parameters influence the melt pool in more detail. Results show that laser power, PMFR and path velocity have complex interactions and changing one can directly influence how the melt pool reacts to further parameter changes. The directional emittance algorithm has been successfully used to perform a detailed parametric study.

CRediT authorship contribution statement

The work presented in this paper was carried out as a collaboration between all authors. The research theme was defined by Robert Sampson, Robert Lancaster, Mark Sutcliffe and Carl Hauser. Robert Sampson, Robert Lancaster, Mark Sutcliffe, David Carswell, Carl Hauser and Josh Barras prepared the scientific manuscript, with Robert Sampson, Robert Lancaster, Mark Sutcliffe and David Carswell deriving the monitoring methodology. Robert Lancaster, Mark Sutcliffe and Carl Hauser secured the relevant funding to enable the research programme to take place and provided the supervision of the project. All authors have contributed to, seen and approved the final manuscript.

Declaration of Competing Interest

The authors declare that they have no known competing financial interests or personal relationships that could have appeared to influence the work reported in this paper.

Acknowledgements

Data Availability Statement

The raw/processed data required to reproduce these findings cannot be shared at this time as the data also forms part of an ongoing study.

References

[1] F. Meriaudeau, F. Truchetet, Control and optimization of the laser cladding process using matrix cameras and image processing, J. Laser Appl. 8 (1996) 317–324, https://doi.org/10.2351/1.4745438.

[2] E. Renier, F. Meriaudeau, F. Truchetet, CCD Technology Applied To Industrial Welding Applications, Melecon 96 (1996) 1335–1338.

[3] F. Meriaudeau, D. Truchetet, A. Grevey, B. Vannes, Lasercladding processandimage processing, J. Lasers Eng. 6 (1997) 161–187.

[4] T. Hua, C. Jing, L. Xin, Z. Fengying, H. Weidong, Research on molten pool temperature in the process of laser rapid forming, J. Mater. Process. Technol. 198 (1–3) (2008) 454–462, https://doi.org/10.1016/j.jmatprotec.2007.06.090.

[5] Y. Sun, M. Hao, Statistical analysis and optimization of process parameters in Ti6Al4V laser cladding using Nd:YAG laser, Opt. Lasers Eng. 50 (7) (2012) 985–995, https://doi.org/10.1016/j.optlaseng.2012.01.018.

[6] B. Cheng, J. Lydon, K. Cooper, V. Cole, P. Northrop, K. Chou, Melt pool sensing and size analysis in laser powder-bed metal additive manufacturing, J. Manuf. Processes 32 (November 2017) (2018) 744–753, https://doi.org/10.1016/j.jmapro.2018.04.002.

[7] Z. Yan, W. Liu, Z. Tang, X. Liu, N. Zhang, M. Li, H. Zhang, Review on thermal analysis in laser-based additive manufacturing, Opt. Laser Technol. 106 (2018) 427–441, https://doi.org/10.1016/j.optlastec.2018.04.034.

[8] Y. Yao, Y. Huang, B. Chen, C. Tan, Y. Su, J. Feng, Influence of processing parameters and heat treatment on the mechanical properties of 18Ni300 manufactured by laser based directed energy deposition, Opt. Laser Technol. 105 (2018) 171–179, https://doi.org/10.1016/j.optlastec.2018.03.011.

[9] P.A. Hooper, Melt pool temperature and cooling rates in laser powder bed fusion, Addit. Manuf. 22 (May) (2018) 548–559, https://doi.org/10.1016/j.addma.2018.05.032.

[10] T. Craeghs, S. Clijsters, J.-P. Kruth, F. Bechmann, M.-C. Ebert, Detection of process failures in layerwise laser melting with optical process monitoring, Phys. Procedia 39 (2012) 753–759, https://doi.org/10.1016/j.phpro.2012.10.097.

[11] C. Kledwig, H. Perfahl, M. Reisacher, F. Brückner, J. Bliedtner, C. Leyens, Analysis of melt pool characteristics and process parameters using a coaxial monitoring system during directed energy deposition in additive manufacturing, Materials 12 (2) (2019), https://doi.org/10.3390/ma12020308.

[12] T. Furumoto, K. Egashira, K. Munekage, S. Abe, Experimental investigation of melt pool behaviour during selective laser melting by high speed imaging, CIRP Ann. 67 (1) (2018) 253–256, https://doi.org/10.1016/j.cirp.2018.04.097.

[13] V. Manvatkar, A. De, T. DebRoy, Spatial variation of melt pool geometry, peak temperature and solidification parameters during laser assisted additive

manufacturing process, Mater. Sci. Technol. 31 (8) (2015) 924–930, https://doi.org/10.1179/1743284714Y.0000000701.

[14] D. Dai, D. Gu, H. Zhang, J. Xiong, C. Ma, C. Hong, R. Poprawe, Influence of scan strategy and molten pool configuration on microstructures and tensile properties of selective laser melting additive manufactured aluminum based parts, Opt. Laser Technol. 99 (2018) 91–100, https://doi.org/10.1016/j.optlastec.2017.08.015.

[15] T. Fiegl, M. Franke, C. Körner, Impact of build envelope on the properties of additive manufactured parts from AlSi10Mg, Opt. Laser Technol. 111 (June 2018) (2019) 51–57, https://doi.org/10.1016/j.optlastec.2018.08.050.

[16] X. Ding, Y. Koizumi, D. Wei, A. Chiba, Effect of process parameters on melt pool geometry and microstructure development for electron beam melting of IN718: A systematic single bead analysis study, Addit. Manuf. 26 (December 2018) (2019) 215–226, https://doi.org/10.1016/j.addma.2018.12.018.

[17] P. Colodrón, J. Fariña, J.J. Rodríguez-Andina, F. Vidal, J.L. Mato, Á. Montealegre, Performance improvement of a laser cladding system through FPGA-based control, IECON Proceedings (Industrial Electronics Conference), 2011, pp. 2814–2819, , https://doi.org/10.1109/IECON.2011.6119758.

[18] P. Colodrón, J. Fariña, J.J. Rodríguez-Andina, F. Vidal, J.L. Mato, M.Á. Montealegre, FPGA-based measurement of melt pool size in laser cladding systems, in: Proceedings – ISIE 2011: 2011 IEEE International Symposium on Industrial Electronics, 2011, pp. 1503–1508. https://doi.org/10.1109/ISIE.2011.5984383.

[19] J.T. Hofman, B. Pathiraj, J. van Dijk, D.F. de Lange, J. Meijer, A camera based feedback control strategy for the laser cladding process, J. Mater. Process. Technol. 212 (11) (2012) 2455–2462, https://doi.org/10.1016/j.jmatprotec.2012.06.027.

[20] Z. Sun, W. Guo, L. Li, In-process measurement of melt pool cross-sectional geometry and grain orientation in a laser directed energy deposition additive manufacturing process, Opt. Laser Technol. 129 (April) (2020) 106280, , https://doi.org/10.1016/j.optlastec.2020.106280.

[21] R. Sampson, R. Lancaster, M. Sutcliffe, D. Carswell, C. Hauser, J. Barras, An improved methodology of melt pool monitoring of direct energy deposition processes, Opt. Laser Technol. 127 (December 2019) (2020), https://doi.org/10.1016/j.optlastec.2020.106194.

[22] C. Meola, Infrared Thermography : Recent Advances And Future Trends, January, 2016.